NATIONAL TECHNICAL UNIVERSITY OF ATHENS
SCHOOL OF NAVAL ARCHITECTURE & MARINE ENGINEERING
DIVISION OF MARINE ENGINEERING

SPRAY BREAKUP MODELING TAKING INTO ACCOUNT ASYMMETRIC FLOW CONDITIONS

A Dissertation submitted for the degree of
Doctor of Philosophy

Presented by
IMRE GERGELY NAGY
(MSc. Mechanical Engineer Budapest University of Technology and Economics BME)

Born 13.01.1988
Citizen of Hungary
Resident of Switzerland

PhD Advisory Committee

Lambros Kaiktsis, Professor, N.T.U.A. (Supervisor)
Maria Founti, Professor, N.T.U.A.
George S. Triantafyllou, Professor, N.T.U.A.

2021

Persistence

ABSTRACT

Emission regulations and requirements for increased economic operation of marine Diesel engines have become compulsory in modern engine design. Emission and fuel consumption reductions are currently the primary goals in marine Diesel engine development. Recent studies show that the contribution of ships to global emissions of CO_2, NOx, and SOx is substantial, corresponding to about 2.5%, 10-15%, and 3-7%, respectively (Eyring *et al.* (2007) [1], ABS (2018) [2], United Nations (2019) [3]). The international shipping industry is facing an increasingly tighter regulatory frame, with strong pressure from policymakers, especially in terms of limits imposed upon emissions to the atmosphere. Diesel engines are still the main prime movers of ships, while there is at present a broad discussion regarding alternative fuels and ship propulsion technologies (DNV GL (2018) [4]; Wik & Niemi (2016) [5]). In all cases, marine engines and aftertreatment systems should be optimized to meet legislation requirements, while minimizing fuel consumption. To decrease fuel consumption and emission, it is indispensable to optimize the combustion process. The overall performance of marine Diesel engines depends critically on the injection system and the resulting fuel atomization.

Several studies have described the symmetric spray formation and influence of fuel injection processes on combustion. However, in marine Diesel engines, it is typical for orifices to be arranged eccentrically with respect to the central bore axis of the injector, thus creating a highly asymmetric spray structure. The widely-used models in the automotive sector give an indication regarding marine Diesel engine processes. Nonetheless, the spray dynamics in a marine compression-ignition engine differs substantially from automotive engines; thus the existing models cannot comprehensively describe the spray processes. The literature on modeling high-pressure non-symmetric Diesel sprays is still extremely limited.

The present dissertation is thus an attempt to characterize in detail asymmetric sprays for conditions representative of large marine Diesel engines, using Computational Fluid Dynamics, with a focus on nonevaporating conditions. A new methodology for modeling Diesel sprays in large 2-stroke marine Diesel engines is proposed. The study is supported by experiments. Three representative nozzle layouts are considered: a noneccentric nozzle, a nozzle of medium eccentricity, and a highly eccentric nozzle.

First, RANS and LES simulations were performed for different large two-stroke marine Diesel engine atomizer geometries, analyzing the in-nozzle flow. The influence of time discretization and of the initial and boundary conditions on the computed flow field was assessed. A description of the grid requirements and generation was provided, and the importance of proper resolution in LES was discussed. Simulations predicted non-uniform velocity magnitude distribution in the nozzle bores for all nozzle geometries investigated. Consequently, the spray primary breakup zone was analyzed by coupled RANS - LES simulations. Simulation results revealed a highly asymmetric spray behavior for the different nozzle layouts. The resulting spray structures were analyzed, and it was illustrated that the eccentric arrangement of the nozzle results in a deflection normal to the main spray direction. The deflection was found to increase with nozzle eccentricity. The present results also showed that the spray was not just deflected in the spanwise direction, but it also deviated from its symmetry line upwards, in the radial direction.

Next, the phenomenon of cavitation was considered in the in-nozzle flow, for different nozzle geometries. Earlier investigations have shown that the strongly asymmetrically and eccentrically arranged nozzle bores of the fuel injectors of large two-stroke marine Diesel engines can lead to undesirable spray deflections that provoke increased levels of component temperature, emissions, and fuel consumption. To investigate the origin of these spray deviations, experiments were performed with diesel fuel in a constant volume spray combustion chamber at Winterthur Gas & Diesel Ltd. Impingement measurements were executed to characterize the nozzle performance and validate CFD simulations. Computational results for the cavitating in-nozzle flow and the evaluated momentum flux were compared against experiments, demonstrating a good qualitative agreement in terms of the cavitation patterns and differences lower than 6% for the momentum flux.

A method to investigate the spray structures in primary breakup was introduced. The effect of the role of liquid core on the droplet formation was assessed. A new droplet identification method was introduced, to analyze the droplets that appeared in the vicinity of the core during primary breakup. β-PDF functions were generated for droplet location, velocity, and mass, in properly defined segments, in order to be used as an input in CFD simulations of the spray secondary breakup, in a Lagrangian description of droplets. In the LES simulations of primary breakup, the droplets generated by different atomizer layouts were identified; it was found that the conventional noneccentric nozzle generated the highest number of droplets, while the most eccentric nozzle yielded the smallest number of parent droplets. The droplets resulting from the nozzle of medium eccentricity were characterized by the highest values of Sauter Mean Diameter (SMD); similar SMD values were calculated for the other two nozzles.

To further understand and characterize the spray structure and dynamics during the primary breakup, a 3-D Proper Orthogonal Decomposition (POD) analysis was implemented. Characterization, employing the velocity and fuel concentration fields of the asymmetric spray jets emanating from large two-stroke marine Diesel engine injectors calculated by LES, was performed. Hereby, the "method of snapshots" was applied. Simulation results enlightened the role of Kelvin-Helmholtz instabilities in disintegrating the spray liquid core, generating ligaments and large droplets during the primary breakup. The first POD mode qualitatively provided a very good estimate of the flow pattern of the ensemble average. The results demonstrated that the flow dynamics can be represented by a few dominant modes; thus, the flow field can be reconstructed by including the 4-5 most energetic modes of a spatial structure reflecting the asymmetric character of the spray flow. Analysis of time coefficients of the POD modes has shown that they are characterized by dominant frequencies representative of turbulent axisymmetric jets.

The β-PDF functions generated by analyzing the LES results of primary breakup for the one noneccentric and the two eccentric nozzles were used as input for the spray secondary breakup calculations. CFD results were compared against experiments in the large spray combustion chamber, as well as with CFD simulations using a conventional (URANS-only) approach. The computational results using the present approach illustrate the asymmetric structure of sprays, even for the case of noneccentric nozzle, which is associated with a nonaxisymmetric flow at the nozzle tip, and is the outcome of in-nozzle flow. In all cases, the results properly accounted for the spray

morphology and yielded good predictions of important quantities, such as the spray penetration length, and the spray cone and deflection angles, as verified by comparison with experiments. The results were superior to those of a conventional (URANS-only) approach (which cannot account for nonaxisymmetric spray structure). The present computational study has shown that spray deflection increased with nozzle eccentricity. Furthermore, the spray cone angle also increased with nozzle eccentricity. This resulted in a higher effective spray area, yielding an increased intensity of spray breakup, and thus a decreased penetration length. Overall, the CFD approach of the present study accurately predicted asymmetric sprays of large marine engines, while maintaining the computational cost at an affordable level.

An approach for extending the applicability of the new computational framework was introduced and tested at different injection pressure levels. In particular, LES results at a given injection pressure are properly adapted for another pressure, and are used as input for secondary breakup URANS simulations of nonevaporating sprays. The comparison between CFD and experimental results has shown a good agreement regarding the spray tip penetration, for all nozzle layouts investigated. At each pressure level, the new approach outperformed the conventional approach of URANS-only simulations, improving important global parameters as the spray cone angle, quantified both at the horizontal and at the vertical mid-surface.

In a final step, the new CFD simulation approach developed in this study was applied for reactive sprays, and first results were compared against new experiments in the spray combustion chamber, in terms of ignition delay. For that, the experimental setup was properly modified, and experiments with injection from a single hole were performed. The present experiments have shown that the reactive sprays exhibited deflections in their structure, similar to those of nonevaporating sprays. The predicted values of ignition delay time exhibited the same trends as those of the experiments.

The presentation of work is organized in 12 chapters:

Chapter 1 discusses the present status regarding emissions, emission regulations and alternative fuels pertinent to the marine industry, and provides a general introduction to the technology of large 2-stroke marine Diesel engines. A detailed discussion on governing equations and modeling of turbulent flows is given in **Chapter 2**. In **Chapter 3,** the physics and simulation techniques of Diesel sprays are discussed. **Chapter 4** summarizes the in-nozzle flow and spray primary breakup simulation results. Computational results for cavitating in-nozzle flow are presented in **Chapter 5**. A detailed characterization of spray structure in the primary breakup regime is presented, on the basis of LES results, in **Chapter 6**. Results of 3-D Proper Orthogonal Decomposition (POD) analysis of spray flow in the primary breakup zone are presented and discussed in **Chapter 7**. **Chapter 8** presents computational results of spray secondary breakup, utilizing proper input from the LES primary breakup results. Spray characterization uses calculation of proper global parameters, and comparison of their values against experiments. Furthermore, an approach for extending the applicability of the present modeling framework is presented. Experiments and first simulation results of reactive spray flow are discussed in **Chapter 9**. The novelty of the present Thesis is highlighted in **Chapter 10**. In **Chapter 11**, the main conclusions of the present study are summarized. Suggestions for future work are presented in **Chapter 12**. Finally, the list of references is provided.

ACKNOWLEDGEMENTS

This research has received funding from the People Programme (Marie Curie Actions) of the European Union's Seventh Framework Programme FP7/2007-2013/ under REA grant agreement n° 607214. The current work has been done at Winterthur Gas & Diesel Ltd, Department of Engine Performance in Switzerland, and at the National Technical University of Athens, School of Naval Architecture and Marine Engineering, under the supervision of Professor Lambros Kaiktsis.

I would like to express my gratitude and thanks to Professor Kaiktsis, for his support and patience during the entire thesis project. His optimistic attitude provided me the courage to finish my thesis. His guidance helped me to deliver a structured and high-quality work. Finally, I am more than grateful to him for arranging all details of my stay, for more than one semester, in Athens.

I am thankful to Professor Maria Founti for all of her support during the project. I would also like to thank the third member of the advisory committee, Professor George Triantafyllou, for his support and suggestions.

I would also like to thank the other members of the examination committee, Professors D. Bouris, N. Kyrtatos, C. Papadopoulos and A. Tomboulides.

My honest and deep honor goes to Dr. Sebastian Hensel, for trusting and supporting me with this extremely demanding topic. He provided me the knowledge that I needed to get on the right path.

My special thanks go to my workmates at Winterthur Gas and Diesel Ltd., Dr. Matthias Brunner, Cakir Ertugrul, Ourania Voutsi, Jan Smit, Dr. Ilias Dodoulas, Dr. Marios Ioannou, Dr. Andreas Schmid, Julian Gehrdau, Matthieu Akrour, and Pietro Scrocco. This extraordinary team has given me technical support and invaluable knowledge. They have become my friends for a lifetime and made me feel at home in Switzerland. In particular, I would like to thank Naoki Yamada for his support with the experiments of reactive spray flow.

I cannot forget expressing my deepest appreciation to Mr. Alexandros Panagoulias (Siemens Industry Software GmbH) for being my support engineer. We have faced countless challenges, but no single occasion has happened that we could not find an innovative solution. Thank you for your honest interest and for being a friend of mine.

I would like to congratulate the entire ECCO-MATE team, for forming a great community, and completing this project successfully. We have given everything and had some great fun.

Finally, I would like to thank my family and friends for standing always behind me during these years.

Many thanks to all of you.

…….**.....** Athens, Greece

Nagy Imre Gergely June 2021

DECLARATION

I hereby certify that this report is my own work except where otherwise indicated. I have identified my source of information and, in particular, have put in quotation marks any passages that have been quoted word for word, and identified their origins.

……..... Athens, Greece

Nagy Imre Gergely June 2021

Contents

This page is intentionally left blank.

List of Figures

This page is intentionally left blank.

List of Tables

This page is intentionally left blank.

1 CHAPTER: Introduction

1.1 Air pollution from shipping

Shipping is a key component of the global economy, representing 85% of the global trade [1]. Sea transport emits less carbon dioxide per tonne-km compared to all other forms of transport [7-9], but given its sheer scale, the maritime sector is a large contributor to global ecological impacts [10]. Today's maritime industry is driven by environmental protection, in terms of both meeting legislative requirements intended to safeguard marine life and reduce emissions, and in ensuring a sustainable future for our planet. Human society, in general, is becoming increasingly aware of sustainability issues, while investors are showing an interest in these areas, including the need for a social return on investment. Shipping plays a key role in connecting countries and markets, and leads the market of international trading, while the global cruise industry continues to grow rapidly. The maritime industry bears the responsibility to minimize exhaust gas emissions and other forms of pollution caused by shipping.

The international shipping industry is facing an increasingly tight regulatory environment, with strong pressure from policymakers, especially in terms of limits imposed upon emissions to air. Environmental concerns have led to increasingly more stringent emission legislation. What started as an onshore industry regulatory development is now also influencing the shipping industry [11-12].

1.2 Marine engine emissions and legislation

Main emissions from marine engines include carbon dioxide (CO_2), sulphur oxides (SOx), nitrogen oxides (NOx) and particulate matter (PM); they depend on the engine type and operating point, as well as on the fuel used.

1.2.1 CO_2 emissions

CO_2 emissions are the main global source of greenhouse gas (GHG) emissions, resulting in global warming. Actual CO_2 emissions from marine engines have been continuously reduced over the past decades. As ships are also getting larger and more efficient, CO_2 emissions per unit of useful transport work (cargo tonne-miles) are also decreasing. Nonetheless, after 2030, new propulsion concepts (dual-fuel engines, gas engines) will have to be widely adopted in order for the maritime sector to be able to maintain a stable 2.2-3%, of global CO_2 emissions; in the same frame, the development of alternative fuels will also have to be accelerated [13-18].

1.2.2 SO_x emissions

SO_x (sulphur oxides) emissions mainly consist in sulphur dioxide (SO_2) and sulphur trioxide (SO_3). SO_x are toxic compounds, with SO_3 being a precursor to the formation of sulfuric acid. Present regulations of the International Maritime Organization (IMO) pertinent to SO_x impose limits on the allowed sulphur content of marine fuels. The global Sulphur Cap of 0.5%, limiting the sulphur content of marine fuels, was implemented in 2020. To produce low sulphur content marine fuels, blending Heavy Fuel Oil (HFO) with Marine Gas Oil (MGO) would increase fuel prices. Low Sulphur HFO (LSHFO) is now available in the shipping market. MGO can be used in Sulphur

Emission Control Areas (SECAs) for SO_x, meeting the requirement for a maximum sulphur content of 0.1%. Finally, HFO of a high sulphur content (up to 3.5%) can still be used in ships retrofitted with scrubber installations.

1.2.3 NOx emissions

The combustion of fossil fuels is the dominant source of NOx emissions, mainly consisting of nitric oxide (NO) and nitric dioxide (NO_2). The emitted NOx contributes to acid deposition and eutrophication, which as a result can lead to changes in soil and water quality. The impacts of acid deposition can be significant, including adverse effects on aquatic ecosystems. Marine Diesel engines can meet the Tier III limits by aftertreatment systems utilizing catalysts, i.e. Selective Catalytic Reduction (SCR) units, while another alternative is Exhaust Gas Recirculation (EGR) [13-17]. Both strategies have initiated demanding development projects by main marine engine manufacturers, and new engines are finding a position in the global market.

1.2.4 Particulate matter

Black carbon is a major contributor to shipping's climate impacts. Following CO_2, black carbon (BC) contributes most to the climate impact of shipping, representing 7% of total shipping CO_2 equivalent emissions on a 100-year timescale and 21% of CO_2 equivalent emissions on a 20-year time scale [19].

1.2.5 Emission legislation and Emission Control Areas

The International Maritime Organization's (IMO) Tier III limits for NOx and a part of the MARPOL Annex VI regulations governing marine emissions became significantly stricter. According to these regulations, ships that are keel-laid after January 1st, 2016, and are operating in the North American and U.S. Caribbean Sea Emission Control Areas (ECAs), must comply with Tier III emission limits, dictating a reduction of NOx emissions by about 80% compared to a Tier I compliant engine. In the North and Baltic Seas, Tier III limits are applicable for ships keel-laid after January 1st, 2021 [20-23]. As indicated above, Sulphur Emission Control Areas (SECAs) have also been defined, with an upper limit in sulphur content of 0.1%; they are presented in **Figure 1**.

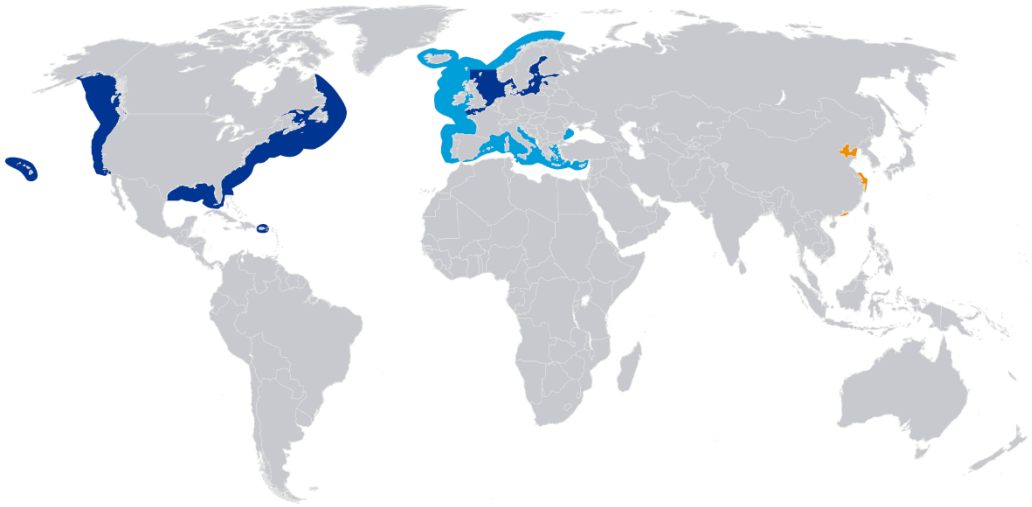

○ 0.5% Global limit (MARPOL, 2020)
● 0.1% Emission Control Areas (MARPOL, 2015)
● 0.1% EU ports (EU Sulphur Directive, 2010)
● 0.5% Selected areas in China/Hong Kong (2016-2019)*

*Note that China and Hong Kong may go down to 0,1% before 2020.

Area	Sulphur limit	Scrubbers
Global	0,5% (2020)	yes
Sulphur	0,1% in all ports	yes
EU	0,1% in selected areas	open-loop restricted in some countries
China	0,5% in selected areas	yes
California	0,1% within 24 nm	no, only through research exemption

Figure 1 - Global and regional sulphur content limits and corresponding Emission Control Areas (ECAs) [11].

1.3 Decarbonization and alternative fuels

The shipping industry is experiencing a constantly increasing pressure to decarbonize its operations and reduce emissions to the atmosphere. In April 2018, the IMO adopted an ambitious strategy to decarbonize shipping and decrease associated greenhouse gas (GHG) emissions. With 2008 as the baseline year, this strategy aims to reduce global emissions from shipping by at least 30% by 2030 and 50% by 2050. Considering the increase in global trade by shipping, these reductions correspond to reductions in the average carbon intensity (CO_2 per tonne-mile) of at least 40% by 2030 and 70% by 2050 [24]. The roadmap of the GHG emission reduction is shown in **Figure 2**.

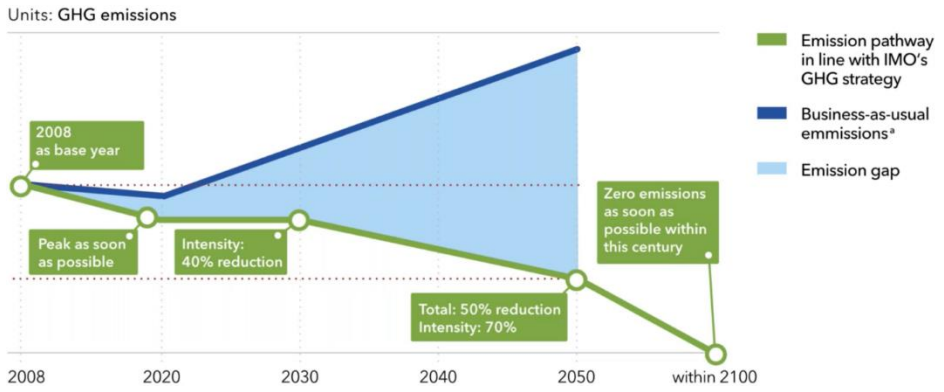

Figure 2 - Pathway of Greenhouse gas emissions.[24].

The above decarbonization targets pose significant challenges for a range of stakeholders, from ship owners, charterers, and cargo owners, to shipbuilders, designers, engine manufacturers, fuel suppliers, financiers, and policymakers. Reaching these targets will require the application of technology that is currently under development, acceptance of lower speed, and availability of large volumes of zero-carbon or carbon-neutral sustainable fuels. A summary of the decarbonization options for shipping is provided in **Figure 3**. It is underlined that engine optimization will remain a key element towards reducing GHG emissions. Further information, elaborating on the decarbonization options presented in **Figure 3**, also including the outcome of a survey among shipping stakeholders, is presented in **Figure 4**.

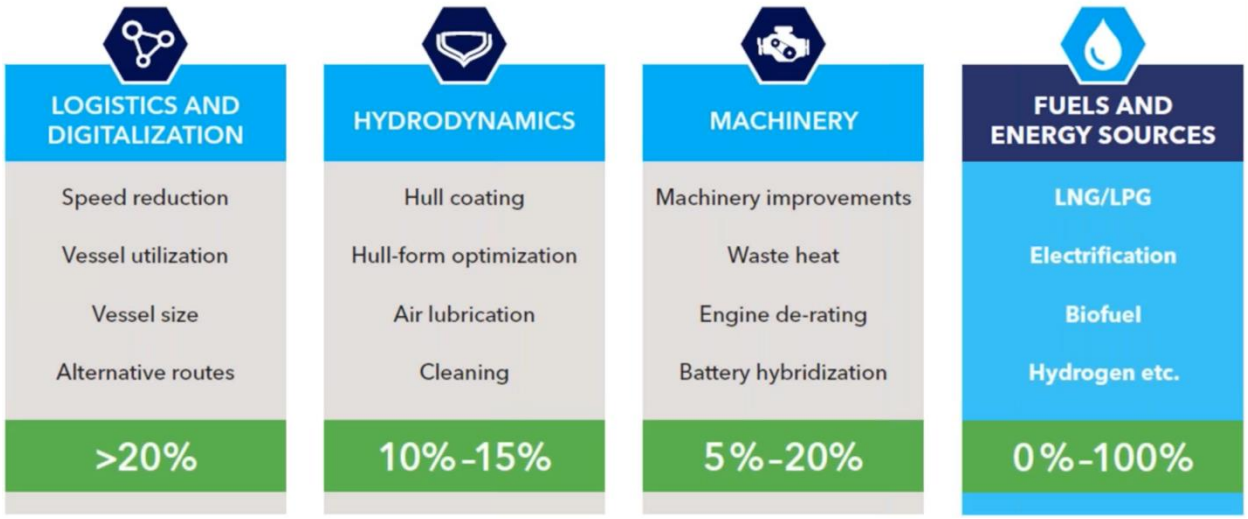

Figure 3 - Decarbonization options for shipping [25].

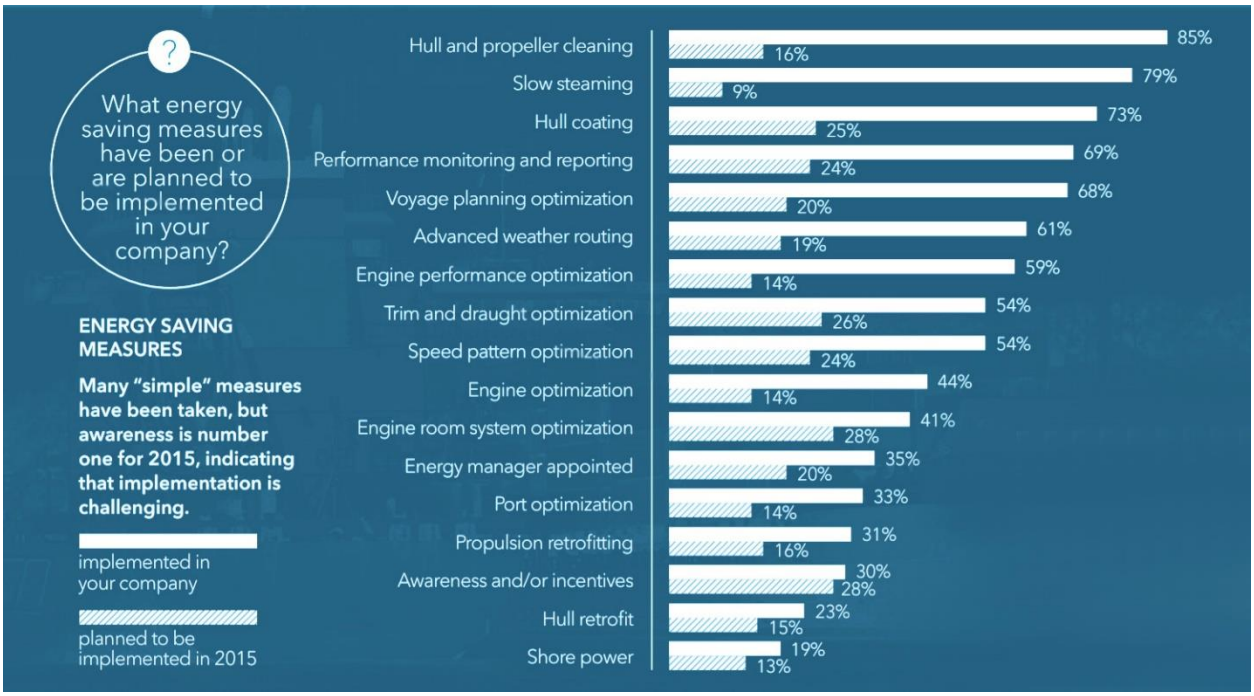

Figure 4 - Potential energy-saving areas [26].

The IMO's GHG strategy has also introduced a list of short-term, mid-term, and long-term measures. Short-term measures include the evaluation and improvement of vessels' energy efficiency requirement (EEDI - Energy Efficiency Design Index, SEEMP - Ship Energy Efficiency Management Plan), the application of technical efficiency measures for existing ships (EEXI - Energy Efficiency Existing Ship Index), and the introduction and regulation of carbon intensity (CII - Carbon Intensity Index) for ships in operation. Mid-term and long-term measures include developing an implementation program for alternative low/zero-carbon fuels, adoption of other possible innovations in emission reduction mechanism(s), and Market-Based Measures (MBMs) to encourage GHG emission reduction [27,28].

1.3.1 EU strategy on decarbonisation

The EU has launched the "European Green Deal" plan, including the marine industry, to achieve a climate-neutral Europe by 2050. This strategy also strongly supports including shipping in the European Trading System (ETS), while a CO_2 tax is also being considered [27,28].

1.3.2 Challenges for shipowners

Shipowners have to consider both existing and new build vessels. This includes availability of alternative fuels, and associated prices. Vessel owners also have to consider vessel speed reduction or different retrofitting options. As for the new build vessels, shipowners should consider which equipment is currently under development and could be delivered within 2-3 years [27,28].

1.3.3 Alternative fuels

LNG

The main component of liquefied natural gas (LNG) is methane (CH_4), characterized by the lowest carbon content (percentage) among all hydrocarbons, and thus by the highest potential to reduce CO_2 emissions. However, methane is a potent greenhouse gas, and therefore methane slip must be kept under control to ensure reductions in GHG emissions when using LNG.

The technology required for employing LNG as ship fuel is available. Engines operating with LNG include low- and high-pressure 2-stroke and 4-stroke engines. Accordingly, several LNG storage tank types, as well as process equipment, are also commercially available. LNG must be stored in insulated tanks, to ensure cryogenic operation. This equipment comes at a substantially higher cost, relative to conventional petroleum-operated fuel storage and supply systems.

By 2022, the LNG consumption is estimated to increase by nearly a factor of 3, in comparison to 2020. Currently, mainly the small passenger ships use LNG as fuel. Nonetheless, the new orders regarding very large container ships, tankers, as well as large cruise ships, show that the tendency of using LNG as fuel expands towards large vessels. This is also supported by the development of LNG bunker vessels [27,28].

LPG

Liquefied Petroleum Gas (LPG) is by-product of the production of natural gas. It mainly consists of propane (C_3H_8) and butane (C_4H_{10}), typically of a percentage of 60% and 40%, respectively. It is associated with a low production and overall capital cost (close to that of LNG), making it financially attractive. However, the operational experience for ship propulsion is limited. In addition, the lack of bunkering infrastructure is at present a barrier to using LPG as an alternative marine fuel. Moreover, a major downside to LPG as an alternative fuel is its environmental performance when produced from fossil sources [27,28].

Ammonia

Ammonia has the potential to become a carbon-free energy carrier, as it is associated with a volumetric energy density higher to that of other alternative fuels, as hydrogen. However, there is at present no experience with using ammonia for marine production, while green ammonia is expensive. Further, the lack of a bunkering infrastructure forms a barrier in using ammonia as an alternative marine fuel, and will require time before it is developed. In a lifecycle context, GHG emissions from ammonia remain high with the current production, using fossil energy sources. The maritime projects opting for ammonia may ensure the use (and contribute to increased production) of ammonia produced from renewables, at the expense of a higher cost and likely slower uptake compared to existing alternatives, as LNG. It should also be noted that costs for required safety systems and mitigating measures (considering the toxicity of ammonia) are not quantified explicitly in the literature, and may cause further delay in the adoption of ammonia [27,28].

Hydrogen

The main advantage of hydrogen is the prospect of being a zero-emission fuel, if produced from renewables. Further, future hydrogen production demand fits well with the anticipated energy transition to renewable energy production on land. The most prominent challenges for hydrogen are the costs and the lack of bunkering infrastructure. Hydrogen will mainly be produced from natural gas, until the transition to renewable power production is well underway. With current technology, hydrogen seems limited to shortsea shipping, considering the current costs of tanks and fuel cells maximum power. Other technical considerations are associated with the explosive characteristics of hydrogen. The costs for required hydrogen safety systems and mitigating measures are not quantified explicitly in the literature, and could be substantial [27,28].

Methanol

The main upside for methanol is the relatively good performance and immediate applicability, as it can be utilized with existing marine engine, with low-cost tanks, which translates into low-capital costs. A major downside to methanol as an alternative fuel is its environmental performance when produced from fossil sources. Methanol is priced close to or higher than MGO in today's market, therefore a limited uptake as an alternative fuel is expected [27,28].

Advanced Biodiesel, Hydrotreated Vegetable Oil (HVO)

Biodiesel is an alternative for ship propulsion. In particular, HVO, produced by hydrotreatment of vegetable oils and/or animal fats, could fit well as an alternative fuel, since it is a direct substitute for conventional petroleum-based fuels. On the other hand, HVO is expensive, and there is currently limited production capacity and bunkering availability, which raises the question of whether it can be a scalable marine fuel. In addition, the use of exhaust gas treatment systems to address the issue of NOx and PM emissions, necessary to meet current and future emission requirements, must be considered [27,28].

1.3.4 Fuel energy density

The energy density of a fuel can be specified both in terms of its volumetric storage energy density (energy content per unit volume) and gravimetric energy density (energy content per unit mass). High volumetric and gravimetric densities imply that, to meet a certain energy requirement, the fuel requires less storage space and a lower stored mass, which is advantageous for using the fuel onboard a vessel.

In **Figure 5**, the volumetric and gravimetric energy densities are specified for various fuels. The figure shows that LNG has a volumetric energy density which is lower to that of diesel fuel by about 40%, and is comparable to that of LPG. Liquid hydrogen, ammonia, and methanol have even lower volumetric energy densities. However, the additional volume needed for a storage system of methanol is lower, bringing its effective volumetric density closer to that of LNG.

Regarding storage, ammonia is normally stored in pressurized 'type C' tanks, i.e., spherical, or cylindrical pressure vessels, as in LNG storage systems, giving an affordable impact on actual ship space utilization. Considering the substantially lower storage volumetric efficiency of hydrogen,

it is evident that storing it effectively onboard will be a major challenge. LPG is currently stored both in prismatic tanks (cooled) and in cylindrical tanks (pressurized), similarly as for LNG. Finally, biodiesel has a significantly higher volumetric energy density than LNG, with levels almost as high as diesel fuel [27].

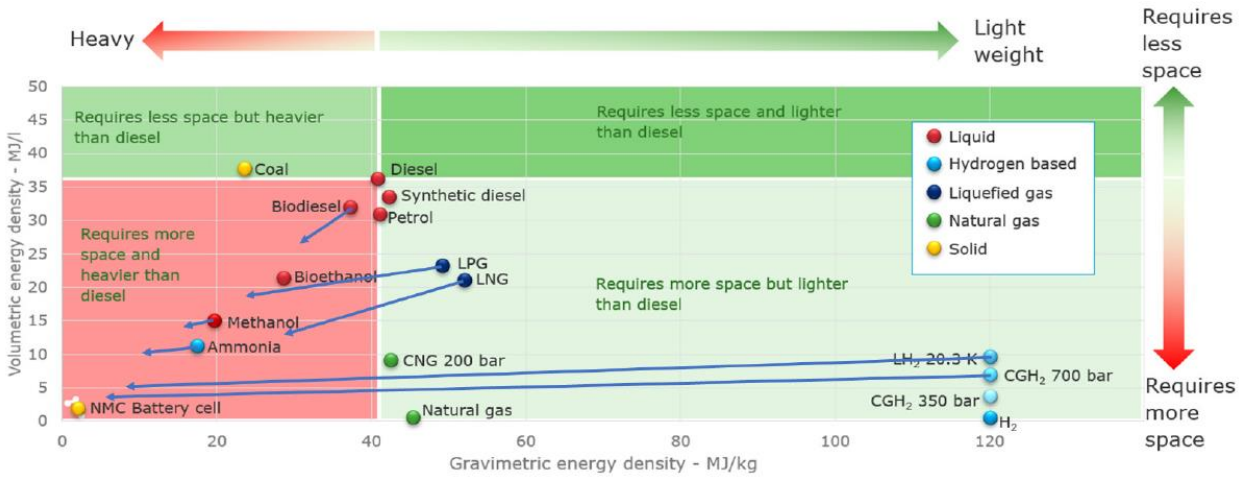

Figure 5 - Energy densities for different fuels. The arrows represent the impact on density when considering the storage systems for the different fuels (indicative values) [27].

1.3.5 Fuel prices

The price of fuel is a key component regarding its adoption by the shipping industry. It is proper to express fuel price per unit chemical energy. In this context, **Figure 6** presents the history of different fuel prices over the past seven years; the data correspond to a quarterly average, and are given in USD/MWh. With a few exceptions, the statistics of **Figure 6** reflect confirmed orders. The LNG statistics are primarily compiled from publicly available information, supplemented with data directly from stakeholders [29].

Figure 6 demonstrates that, in terms of energy cost, LNG and LPG are competitive in comparison to HFO, while biodiesel is significantly more expensive. Methanol and ammonia are substantially more expensive. The significant variations in time suggest the high uncertainty of the fuel market. Regarding prices of hydrogen, limited information is at present available; nonetheless, some sources indicate that, in comparison to hydrogen produced from natural gas, hydrogen from renewables may be more expensive, by about 50% [27].

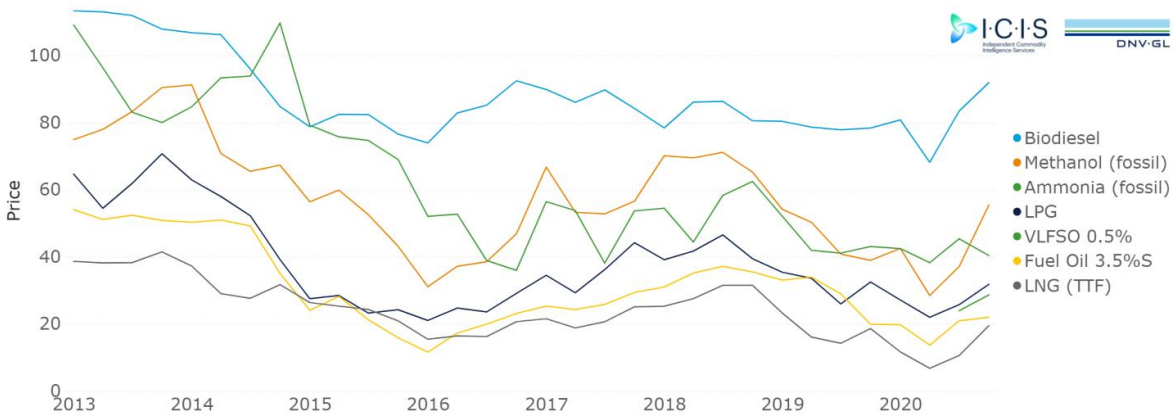

Figure 6 – Price of different fuels [USD/MWh] versus time [29].

In **Figure 7**, the estimated costs of a 23.000 TEU vessel versus time are shown, taking into account LSFO (green line), HFO with scrubber (blue line), and LNG with MGO pilot fuel injection (red line). The initial price for LNG is higher because of the high initial investment cost (for the engine). Operating the existing Diesel engine with LSFO satisfies the sulphur regulations, and no additional investment is required; however, the total cost is higher on the long term. For the case of using HFO and a scrubber, an initial (relatively low) cost associated with the scrubber installation is involved; however, the total cost becomes higher in comparison to LNG after approximately 11 years.

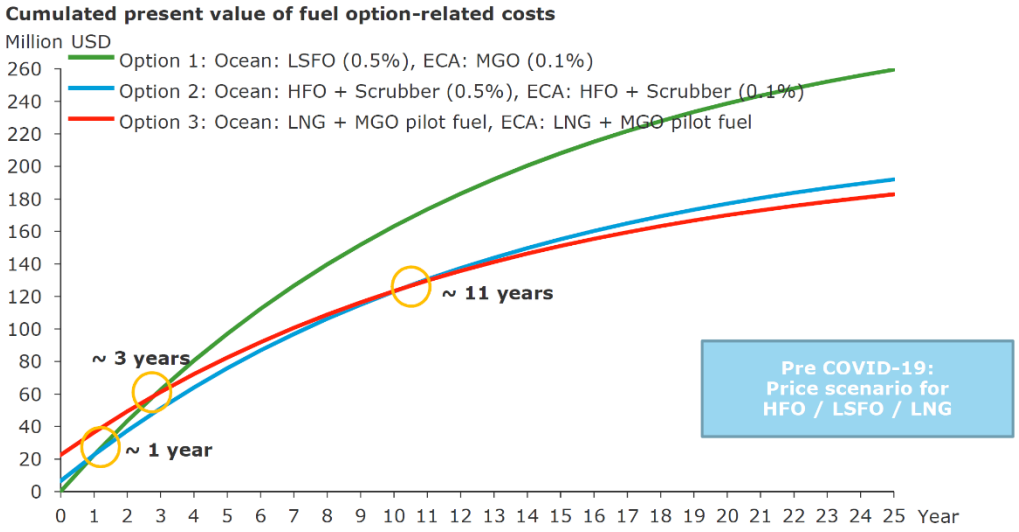

Figure 7 - Fuel example on a 23.00 TEU container ship: Comparison study for HFO/LSFO/LNG [25].

1.3.6 Availability of alternative fuels

Apart from its price, a future fuel must be available to the market in sufficient quantity. For all alternative fuels, with the exception of LNG, a rapid rise in demand would require massive investments, to increase production volume. In principle, a switchover of the entire global fleet to LNG would be possible today, since the current LNG production is higher than the shipping

industry's energy requirement, and the share of LNG in the shipping market is less than 10% (**Figure 8**).

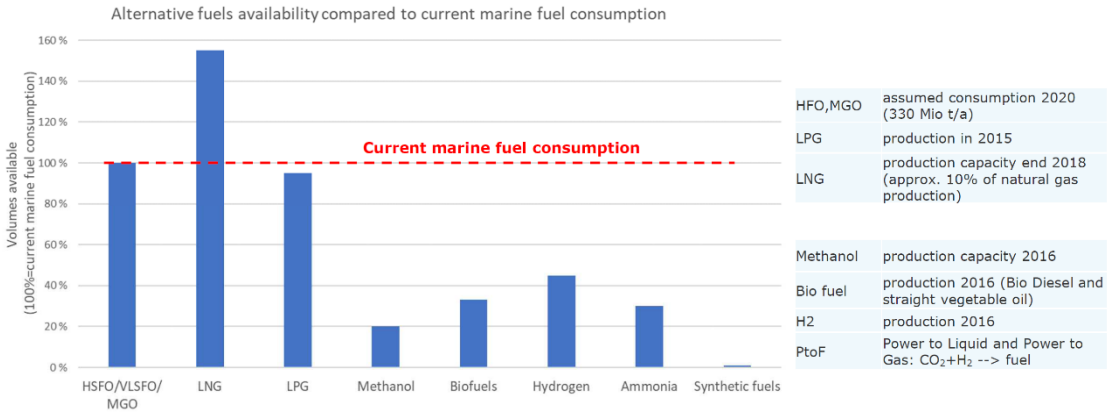

Figure 8 – Availability of alternative fuels compared to current marine fuel consumption [25].

LPG could also cover the energy need of the global fleet; however, no amount of LPG would have been left for other users. For all other fuels, the current infrastructure is either lacking or limited (Figure 8). Clearly, the total worldwide production of methanol, hydrogen, ammonia, biofuels, and synthetic fuels is not sufficient to consider any of them as a viable alternative at present.

Results of two surveys (of 2019 and 2021) considering the uptake of alternative fuels by 2030/2050, and involving stakeholders of the maritime industry, are presented in **Figure 9**. LNG, hydrogen, ammonia, biofuels, and hybrid systems and/or fully electric applications with battery are predicted to gain more popularity in the future. An important outcome of the two surveys is that the community conceives LNG as an intermediate fuel towards carbon free fuels and propulsion solutions.

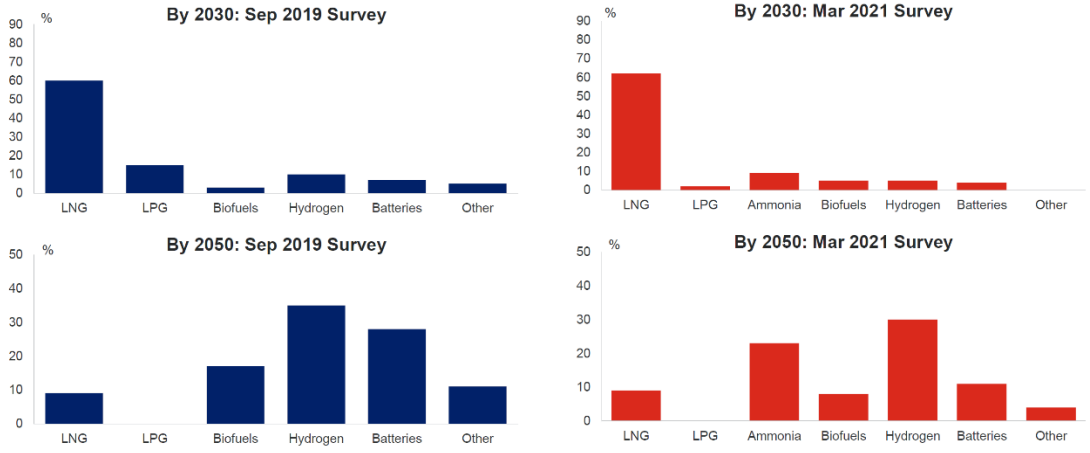

Figure 9 - Uptake of alternative fuels by 2030/2050: results of two surveys, 2019/2021. Source: Clarksons Research [30].

1.4 Present status and prospects of marine Diesel engine

1.4.1 Present of marine Diesel engines

Today, heavy fuel oil (HFO) and distillates (e.g. marine diesel oil - MDO) still account for more than 90% of the energy consumption by international shipping. HFO is a residual product after crude oil has been refined to jet oil and gas oils.

The availability of HFO compared to that of alternative fuels is substantially higher. The major downside of using HFO is its poor environmental performance. In particular, HFO has a high sulphur content, which results in high SOx, mainly SO_2 emissions. Because of the high C content, it causes high CO_2 emissions, while it also results in high levels of emitted NOx and PM. There are investment costs and operational costs associated with using scrubbers, but these are low compared to costs associated with alternative fuels. Historical data and near-future estimates of the world fleet fuel consumption over time are presented in **Figure 10**, from Clarksons Research, demonstrating the dominance of liquid fuels.

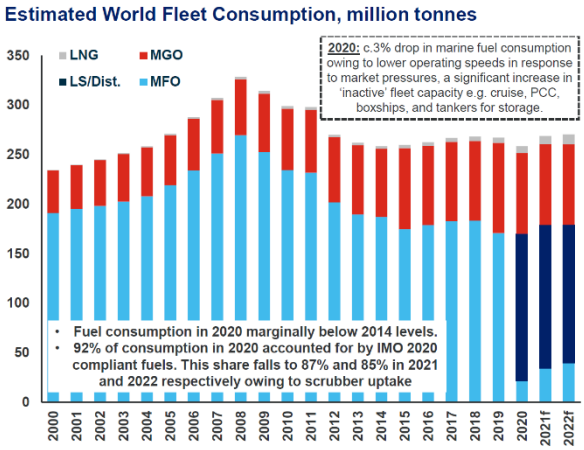

Figure 10 - Estimated yearly world fleet consumption in million tonnes over time. (Source: Clarksons Research [30]).

Figure 11 depicts the number of projects associated with alternative fuels or technologies, including confirmed orders up to 2027 (data by 04.2021). Clearly, the number of projects involving installation of scrubbers is dominant.

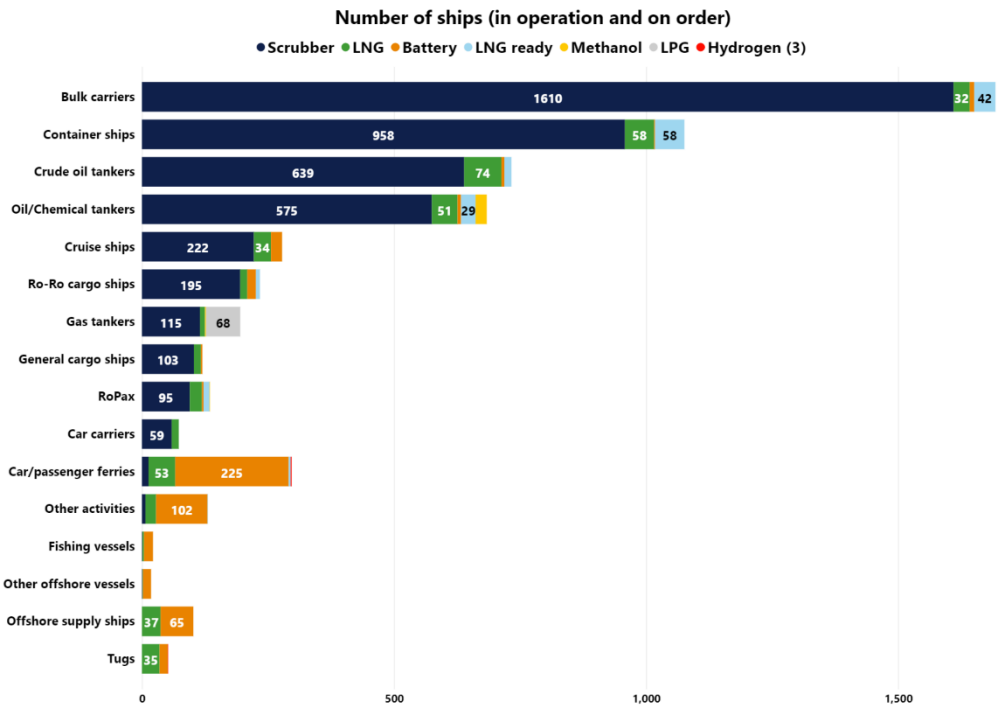

Figure 11 - Number of projects involving alternative fuels or technologies [29].

Focusing on the two-stroke marine engine segment, the number of ships younger than 5 years is presented in **Figure 12** (left), in which the market share of gas-fuelled engines is also given (right). **Figure 12** verifies that currently only 7% of the global fleet operates on gas (LNG and LPG), while the major share of the market still uses liquid fossil fuels.

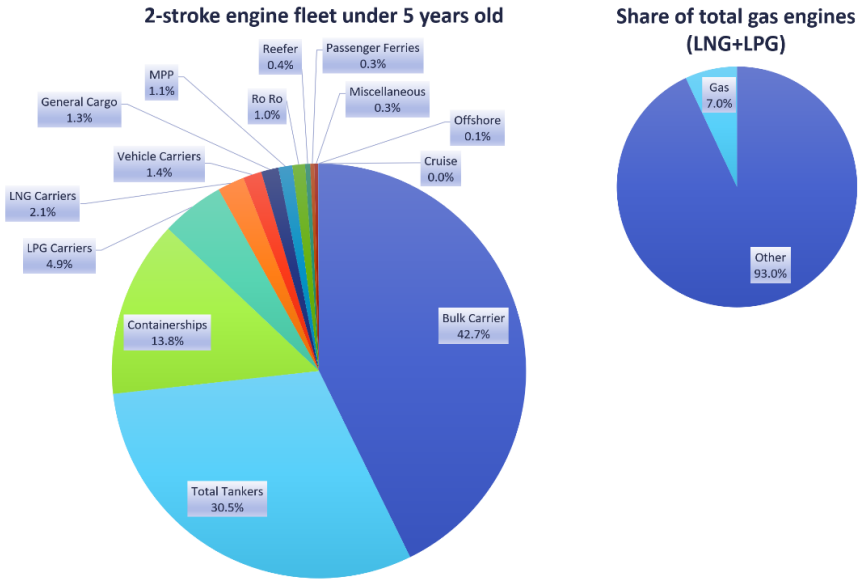

Figure 12 – Ships younger than 5 years: global distribution of ship types with two-stroke marine engines (left), and corresponding share of gas fuelled ships (right) . (Data source: World Fleet Register, Clarksons Research [30]).

The current market share of different fuel types in two-stroke marine engines is presented in **Figure 13** (left); the number of engines using gas and alternative fuels is less than 1%. The corresponding share for vessels on order is presented on the right part of **Figure 13**; a substantial increase in alternative fuels is demonstrated, which is very pronounced for LNG (15%) and LPG (4%), while it also shows the initiation of the interest in methanol as a marine fuel.

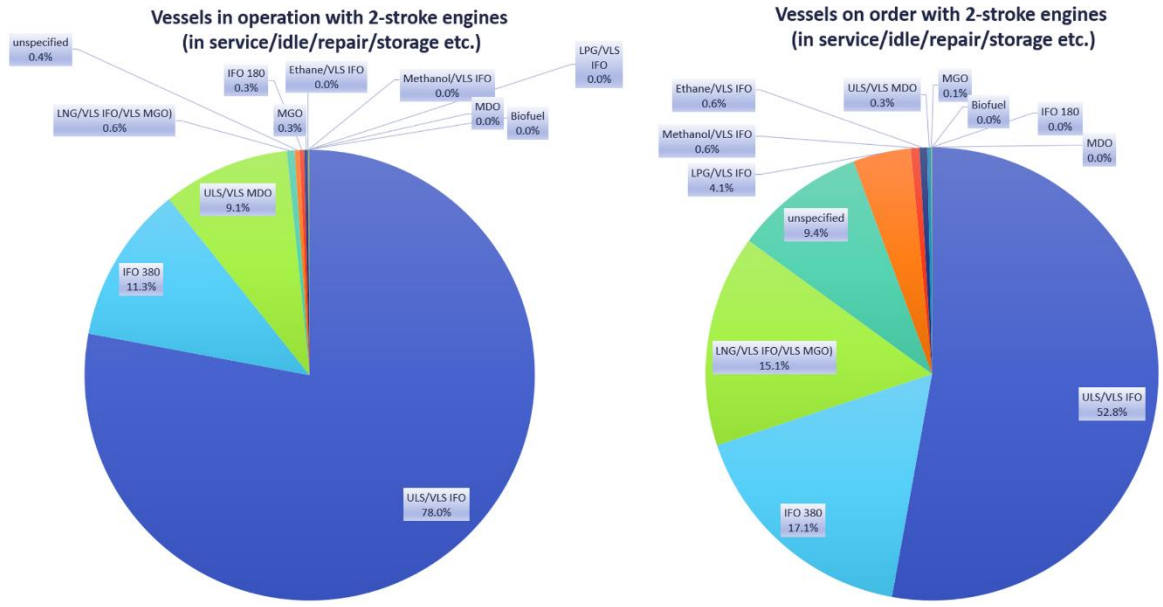

Figure 13 - Market share of different types of fuel used in two-stroke marine engines, for existing vessels (left), and for vessels on order (right). (Data source: World Fleet Register, Clarksons Research [30]).

1.4.2 Future of marine Diesel engines

By 2030, alternative fuels will have to replace by large HFO in the marine industry, contributing to a low share in global emissions. HFO will mainly be replaced by low sulphur alternatives (MDO/MGO or LSHFO) and LNG.

In [31], three different scenarios have been used to assess on the state of the future global fleet as a function of fuel used. These scenarios depend on major global drivers, such as economic and population growth, demand of resources, new technological advances, the rise in consumer demand, as well as the rate of further urbanization in large emerging countries. The three outcomes considered were the following:

1. ‘Status Quo’ scenario:
   In this scenario, long-term economic growth and an increase in global challenges are expected. There will be no single dominant trade power (state), but a collection of powers, trying to support current world orders and systems, to advance their interests. Worldwide demand for ship propulsion power continues to grow. Energy demands increase offshore investment.

2. ‘Global Commons’ scenario:
   Here, the global economic growth is even more pronounced. The scenario foresees major agreements on international trade, climate change, and environmental protection measures.

Globalization is clearly expanding, with strong international institutions regulating international affairs. Global demand for ship propulsion is rising. Compared to the previous scenario, the offshore power demand is rising even more rapidly.

3. ‘Competing Nations’ scenario:
   In this scenario, the shipping community will shrink from the potential roll-back of globalization and a rise in protectionism, which will encourage local production and consumption. Shipping will thus acquire a more ‘local’ presence, in a more complex global frame of strong national interests. Regarding shipping, the increase of demand for local services and decrease of associated demand for global services will have an overall negative effect.

In the ‘Status Quo’ and ‘Competing Nations’ scenarios, a relatively low technological take-up is present, and will reflect in a reduction of energy requirements for shipping, also supported by the reductions in ship design speed. Higher reductions in installed power are associated with the ‘Global Commons’ scenario, due to the combination of design speed reductions and the technological advancements regarding ship efficiency. Under the same scenario, the installed power is operated at the high end of the engine load, resulting in an overall efficient operation of the propulsion system.

The outcome of the three scenarios regarding the adoption of different fuels by 2030 by the shipping sector is presented in **Figure 14**; it should be considered with caution, as it was generated in 2015, i.e., some of the current developments and regulations are not accounted for. **Figure 14** indicates that, in any case, liquid fuels will maintain a major market share by 2030.

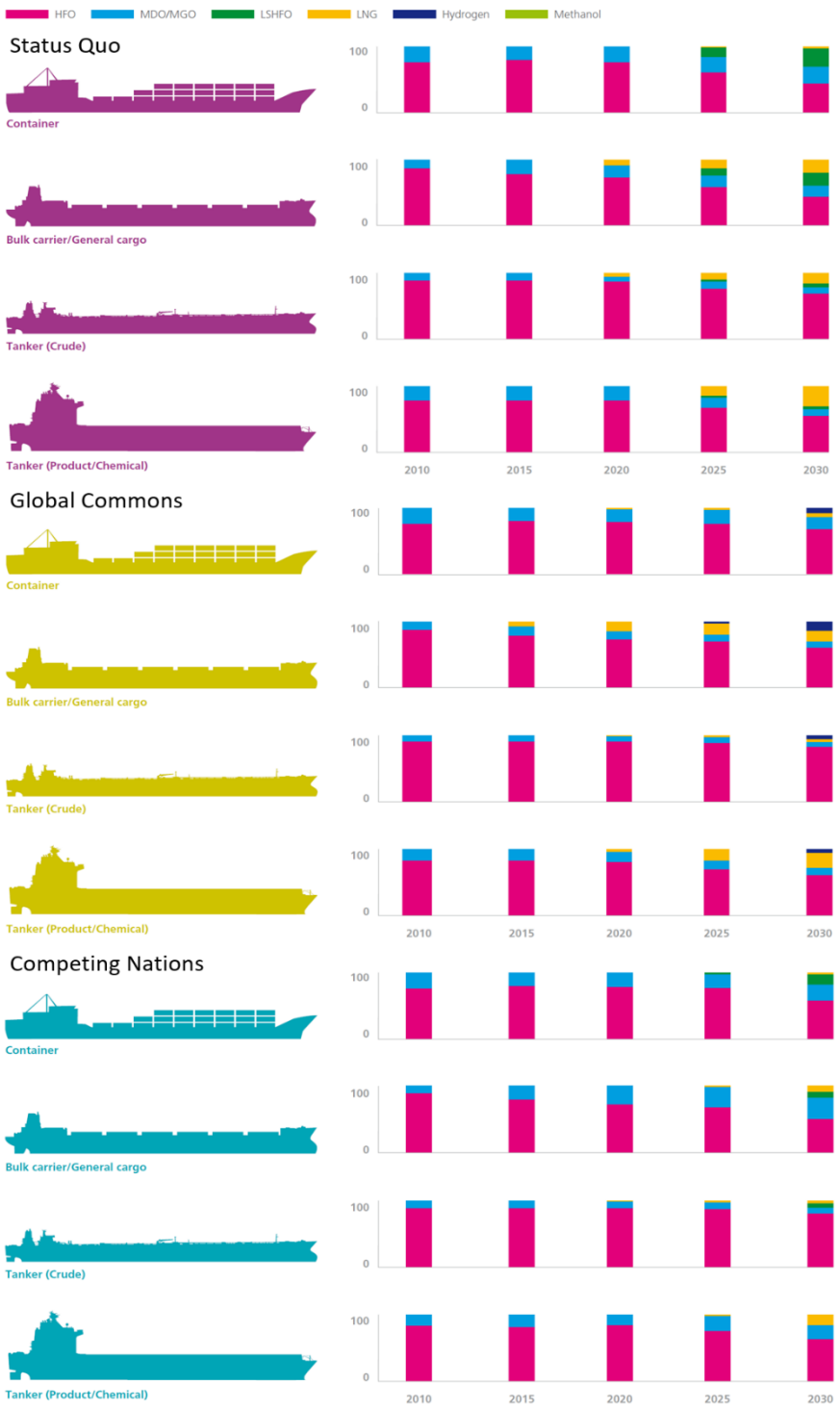

Figure 14 - Fuel mix for containerships, bulk carrier/general cargos, tankers (crude and product/chemical) (%) [31].

It is further noted that, even in the case of a very strong adoption of dual fuel engines, which mainly use LNG, i.e., methane, for operation in the gas mode, there will still be a significant time percentage of operation in the Diesel mode, while pilot injection will remain a key feature of gas mode operation. An example of a state-of-the-art ship which uses a dual-fuel two-stroke engine as

prime mover is CC Jacques Saade of the CMA CMG Group, currently the world's largest container vessel (23.000 TEU), with a WinGD X92DF engine, operating on LNG. **Figure 15** presents statistics regarding the use of fuel over a journey of 135 days, indicating that the engine was running, for a substantial percentage of time, using MDO.

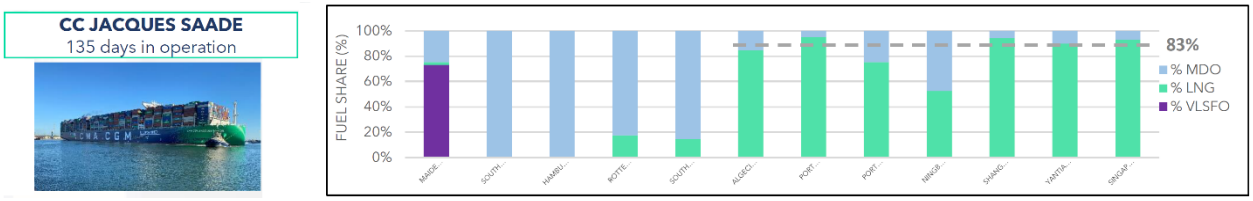

Figure 15 - Fuel share of the CC Jacques Saade container vessel over its 135-day operation [32].

1.5 Large two-stroke marine Diesel engines and fuel injection

The prime mover of merchant ships has been for more than a century the marine Diesel engine, which is nowadays predominantly a low-speed, two-stroke, crosshead-type, uniflow-scavenged, turbocharged, electronically controlled engine. The low-speed engine is, because of its size, the most efficient thermal machine and, due to its fewer moving parts, particularly reliable. The two-stroke cycle is applied to maximize the power to weight ratio, and minimize engine size. To minimize losses and increase scavenging efficiency, the marine engine features a very high stroke-to-bore ratio, which in turn is the main reason for the crosshead design. All two-stroke engines are nowadays turbocharged. Finally, the demand for flexible engine tuning, optimized throughout the load range, dictates the use of electronic engine control.

The market requirements for two-stroke marine Diesel engines differ profoundly from those of smaller engines in other segments. The engine designer is obliged to properly select the power output and the speed of the engine, considering that the engine is directly connected to the propeller, without a gearbox. This attribute of the low-speed engine, together with the low production volumes characteristic of the merchant shipbuilding market, makes the low-speed engine a highly customized product, tailor-made for each application [33-35].

The two-stroke engine's main feature, derived directly from market requirements (power and speed), is the layout field. It is limited by four lines, in a power-speed diagram, which represent the major design limitations; they are shown in **Figure 16** and analyzed below [33-35].

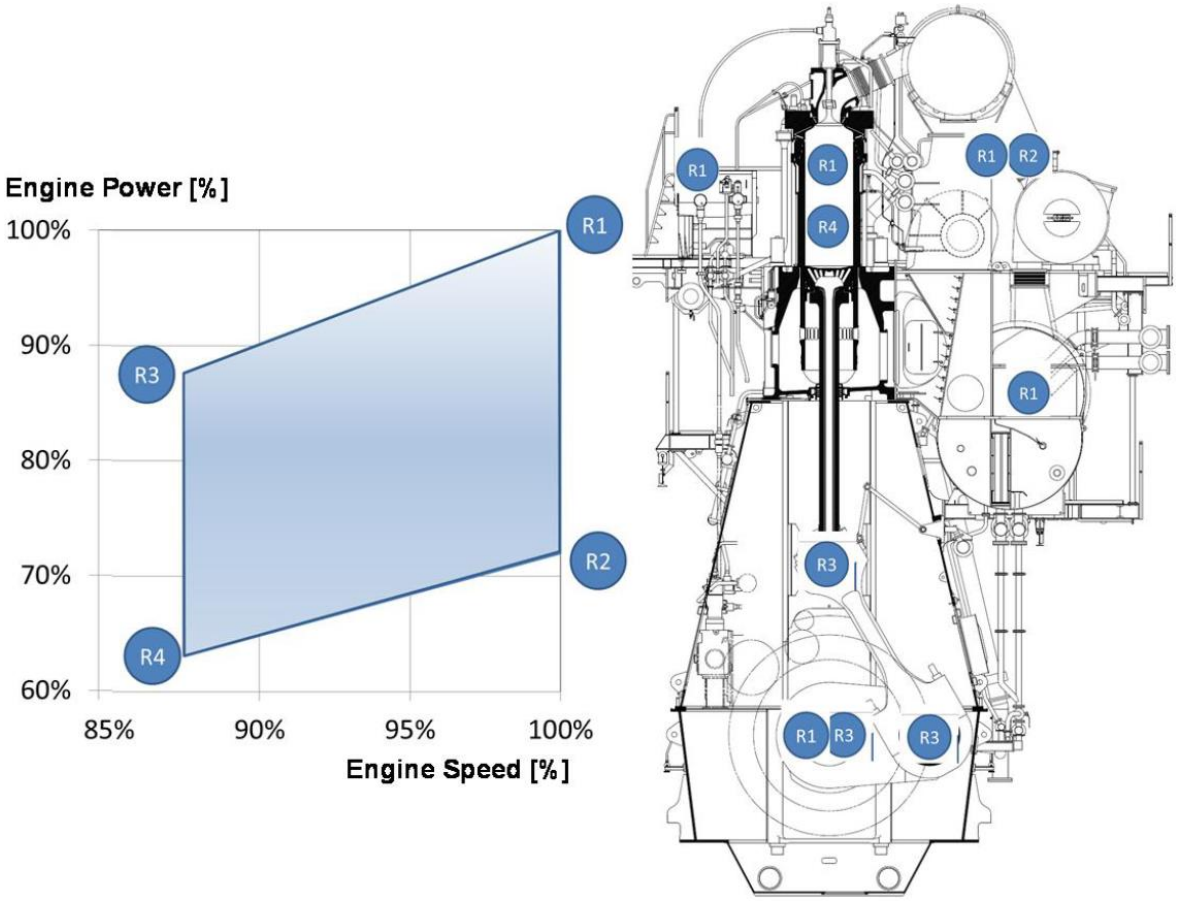

Figure 16 - Two-stroke engine layout field and associated important components affecting basic engine dimensions and design [33].

a) **Torque limit (R1-R3):** a constant Mean Effective Pressure (MEP) line, which determines the dimensioning of the crankshaft (mean & dynamic torque), main bearing and hot parts.
b) **Speed limit (R1-R2):** line of highest permissible speed, limited by tribological impacts of piston motion (Mean Piston Speed (MPS) close to 9.5 m/s in modern marine engines) and rotating masses, also affecting the size of the main bearing.
c) **Bearing layout limit (R3-R4):** line of minimum speed, associated with crosshead bearing and crank-pin bearing layout at maximum firing pressure.
d) **Scavenging limit (R2-R4):** constant MEP line, which represents the lower layout field limit due, associated with thermodynamic and scavenging effects.

The stroke-to-bore ratio is a principal parameter that is derived from the layout field, and determines the engine's main dimensions. To optimize propulsion efficiency and reduce propeller speed, recent development of two-stroke marine engines aims at increasing stroke-to-bore ratios and mean piston speed. This leads, in principle, above a certain value of stroke-to-bore ratio, to a compromise in Specific Fuel Consumption (SFC), due to increasing scavenging (throttling) losses, friction (mainly piston rings), and heat losses. However, the tendency for increased SFC is compensated by designs characterized by increased Maximum Cylinder Pressure (MCP) and MEP, consistently adopted by engines designers over the past decades.

Figure 17 gives an overview of the engine components of a two-stroke marine Diesel engine, namely the Wärtsilä 6-cylinder X62 engine.

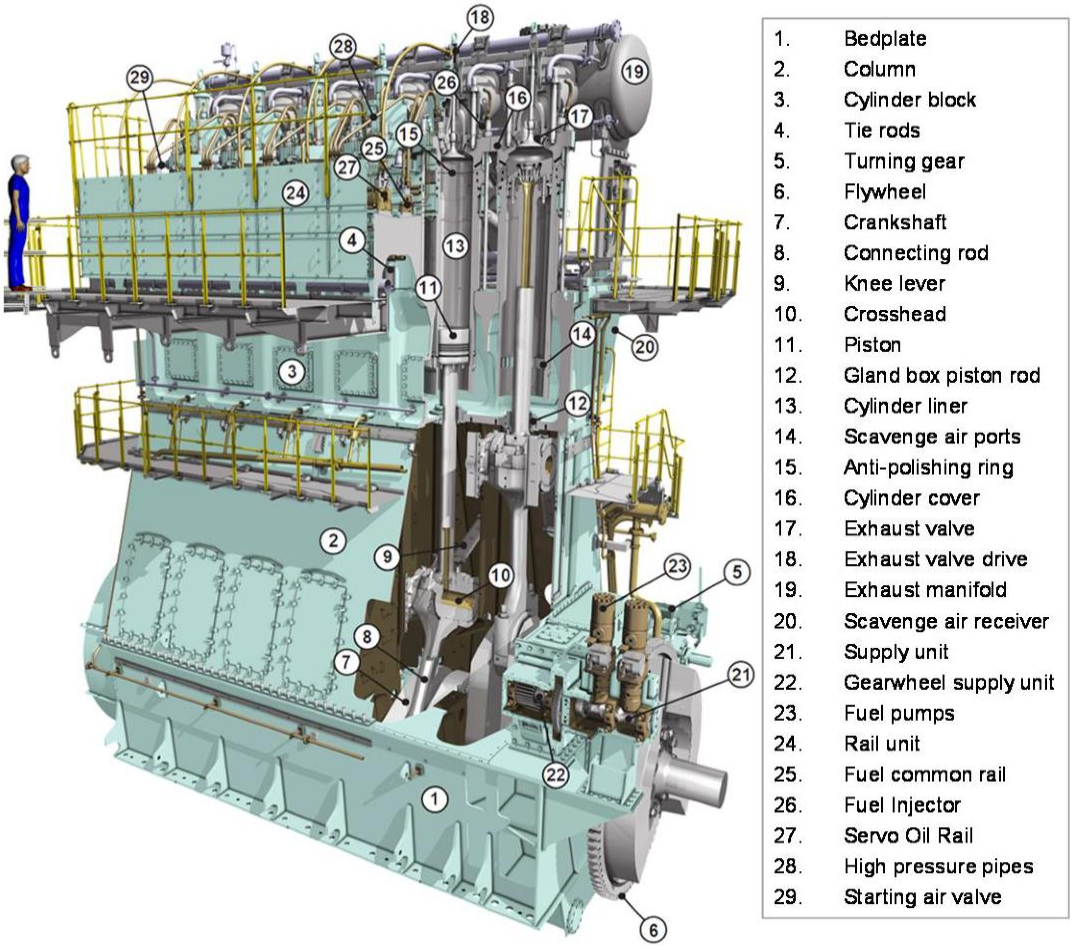

Figure 17 - Overview of the basic components the Wärtsilä 6-cylinder X62 engine [33].

1.5.1 Injection parameters

The fuel injection system and its controls represent the heart of the Diesel engine, and require the highest precision of manufacturing and operation timing. The optimal matching between the injection system and the engine is key for an effective performance. Diesel engine combustion is affected by the design of the chamber geometry, fuel injection, and air intake. Evidently, the fuel injection system plays a crucial role in mixture formation and combustion. Fuel injection systems are extremely important in reducing emissions and meeting emission standards, as well for meeting other performance requirements, as fuel economy and combustion noise. In addition to adjustments in injection timing and injection pressure, rate shaping can improve emissions, noise, and torque. Multiple injections, including pilot injection, and post-injection, possibly in more than one stages, are widely used techniques to control PM and NOx emissions, noise and to manage aftertreatment [36]. CFD-based studies aiming at optimizing of BSFC and emissions in large two-strokes marine Diesel engines using split injection strategies are reported in [37,38]. Split injection is now feasible due to the installation of common rail systems in marine engines, as analyzed below.

1.5.2 Common rail Diesel injection system

The present section contains a brief introduction to the common rail Diesel injection system, nowadays being a part of large two-stroke marine Diesel engines. Main components of the system include the supply unit, the rail unit, and the electronic controls. An overview of the system is presented in **Figure 18**.

In the computer-controlled common-rail concept, the camshaft and its gear drive, characteristic of the mechanically-driven injection of traditional engines, are not present. Instead, an electronically control system is present, including a fuel rail, where fuel is stored at nearly constant pressure. The control system determines fuel injection characteristics from each individual injector. Actuation of the exhaust valve is enabled by means of servo oil, stored in a corresponding rail. Finally, a starting air system is included (**Figure 18**).

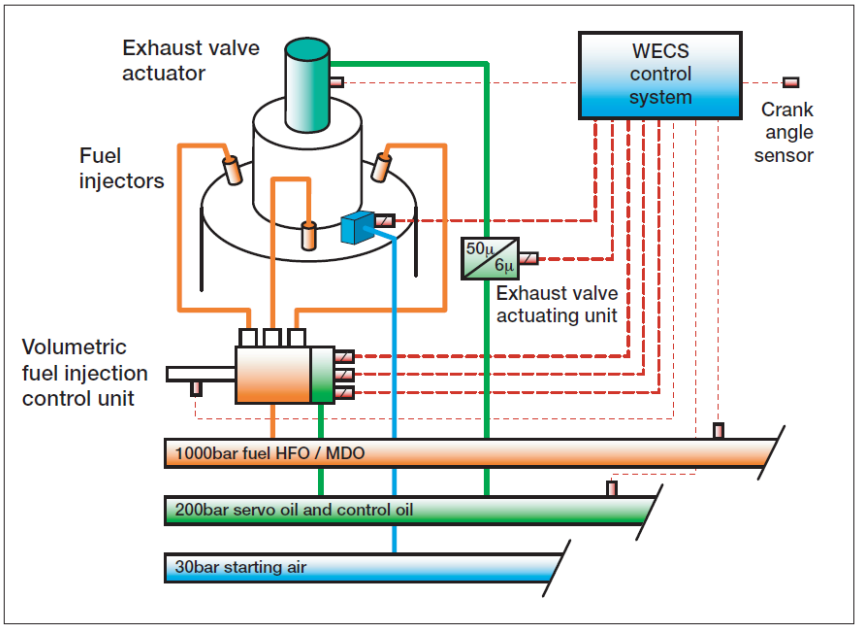

Figure 18 - Sketch of common rail system in a large two-stroke marine Diesel engine [41].

The fuel injection valves are individually controlled. Commonly, there are three or two fuel injection valves in each cylinder cover. The application of a fully-integrated electronic control enables improved low-speed operation, engine acceleration, the balance between cylinders, load control, and longer times between overhauls. These also ensure improved combustion at all operating speeds and loads, resulting in lower fuel consumption, lower exhaust emissions in terms of both smokeless operation at all operating speeds and decreased NOx emissions, as well as a cleaner engine internally, with decreased deposits of combustion residues. Engine diagnostics are built into the system, improving engine monitoring, reliability, and data availability [41]. A sketch of a large two-stroke engine, including main elements of its common rail system, is presented in **Figure 19**. Key components of the common rail system are highlighted next.

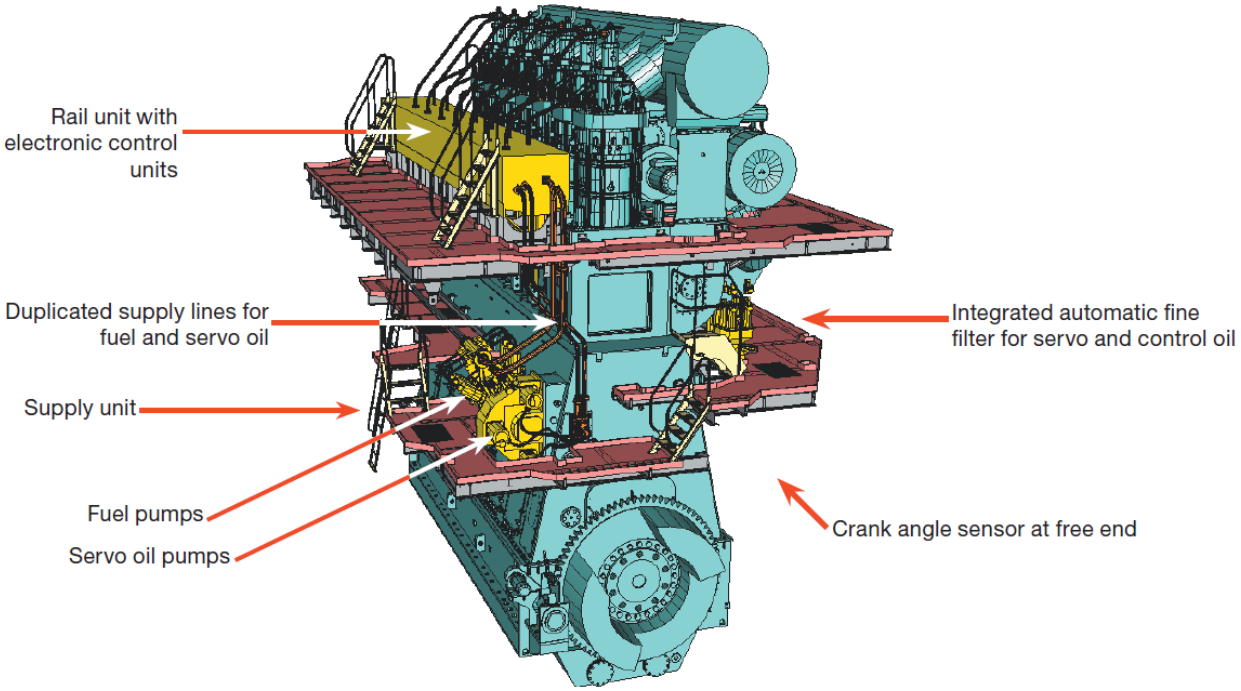

Figure 19 - A schematic of a large two-stroke marine Diesel engine, including main elements of the common rail injection system [41].

Supply unit

The supply unit driven utilizing gearing from the engine crankshaft. The supply unit is located on the front of the engine (on the same side as the rail unit) and at about mid-height (**Figure 19**). The supply unit is naturally at the location of the gear drive: at the driving end for five to seven-cylinder engines, and at the mid gear drive for a higher cylinder number. The fuel and the servo oil are delivered to the common rail system from the supply unit. The fuel supply pumps are arranged on one side of the drive gear, and the hydraulic servo-oil pumps are on the other side. This pump arrangement allows a very short, compact supply unit, with reasonable service access. The numbers, size, and arrangement of pumps are adapted to the engine type and the number of engine cylinders. The fuel supply pumps are driven through a camshaft with three-lobe cams [41].

Servo oil

Servo oil is used for exhaust valve actuation and control. It is supplied by many swashplate-type axial piston hydraulic pumps mounted on the supply unit. The pumps are of standard proprietary design, and are driven at a suitable speed through a step-up gear. The working pressure is controllable, to allow the pump power consumption to be reduced. The nominal operating pressure is up to 200 bar. The number and size of servo oil pumps on the supply unit depend on the engine output or the number of engine cylinders. There are between three and six servo oil pumps. The oil used in both the servo and control oil systems is standard engine system lubricating oil, and is simply taken from the delivery to the engine lubrication system. The oil is drawn through a six-micron automatic self-cleaning fine filter, to minimize wear in the servo oil pumps and to prolong

component life. After the fine filter, the oil flow is divided, one branch leading to the servo oil pumps and the other one to the control oil pumps [41].

Control oil

Control oil is supplied at a constant pressure of 200 bar, at all engine speeds, by two electrically-driven oil pumps, one active and the other on standby. These pumps are equipped with pressure-regulating and safety valves. The control oil system involves only a small flow quantity of the fine filtered oil. The control oil serves as the working medium for all rail valves of the injection control units (ICUs). The working pressure of the control oil is maintained constant, to ensure precise timing in the ICU [41].

Rail unit

The rail unit is located at the engine's top platform level, just below the cylinder cover level. It includes the rail pipes and associated equipment for the fuel, servo oil, and control oil systems, excluding the starting air system. For engines equipped up to eight cylinders, the rail unit is assembled as a single unit. In the case of higher number of cylinders, the rail unit is in two sections, according to the position of the mid-gear drive in the engine. The fuel common rail provides storage volume for the fuel oil, and dampens the pressure waves. The volume of the fuel rail and the supply rate from the fuel supply pumps are such, that a negligible pressure drop within the rail results after each injection event. The high-pressure pipe for the fuel rail is modular, including sections for each cylinder, which are flanged to the individual injection control units of each cylinder [41].

Injection control unit (ICU)

Fuel is delivered from the rail to the injection valves through a separate injection control unit (ICU) for each engine cylinder, sketched in **Figure 20**. The ICU precisely regulates the timing of fuel injection, accurately controls the volume of fuel injected, and sets the shape of the injection pattern. The ICU has an injection control valve and an electro-hydraulic rail valve for each fuel injection valve. The rail valves receive control signals for the start and end of injection from the respective electronic unit. The engines are normally equipped with two or three fuel injection valves in each engine cylinder. The fuel injection valves are hydraulically operated by the high-pressure fuel oil. All injection valves normally act in unison, and can be programmed to achieve separate operation (**Figure 20**).

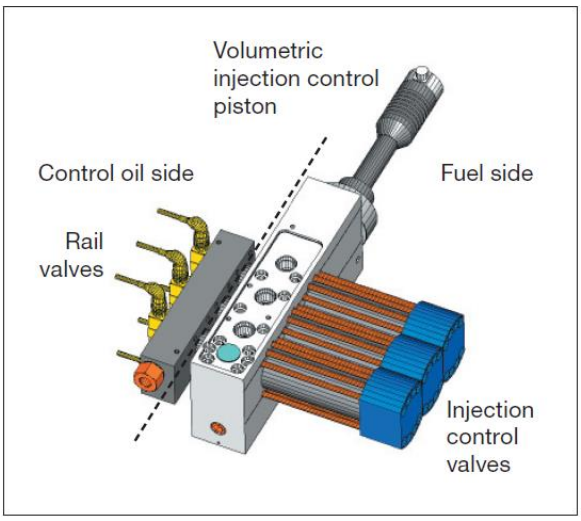

Figure 20 - Injection Control Unit [41].

Exhaust valve control

The hydraulic oil pressure opens the exhaust valve, while it is closed by an air spring with mechanical camshafts. The energy is provided by the servo oil rail. For each cylinder, there is one exhaust valve actuator. Valve actuation is driven by the servo oil acting on the underside of a free-moving actuator piston with normal system oil above the actuator piston. The rail valve activates the hydraulic control slide, which controls the flow of the servo oil to the actuator piston, thus ensuring the precise opening and damped closing of the exhaust valve. The exhaust valve operation is monitored by two position sensors located on the top of the valve spindle [41,42].

Schematics of the common rail injection system applied in large and small bore engines are presented in **Figure 21**.

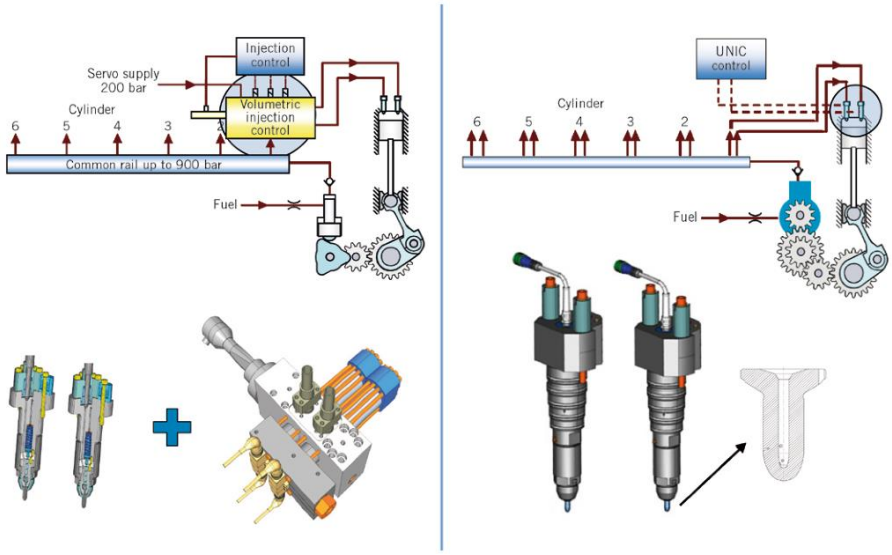

Figure 21 - Common rail fuel injection system with volumetric control for large bore engines (left) and with time control for small bore engines (right) [34].

1.6 Application of CFD in engine development

Conventional internal combustion engine design is mainly based on experimental techniques. The traditional experimental methods provide useful quantitative information, but they are often affected by the engine size, environment, personnel safety, cost, and accuracy considerations. Computational analysis by means of Computational Fluid Dynamics (CFD) can support the early evaluation of alternative solutions at a lower cost, as well as the interpretation of physical processes.

CFD can thus be crucial for understanding flow, thermal and chemical processes in internal combustion engine cylinders. In engine applications, CFD codes can be coupled to simpler 1-D modules, to account for processes as scavenging and injector flows. CFD engine simulations are nowadays still heavily based on Reynolds-Averaged Navier-Stokes (RANS), an approach supported by extensive modeling work (turbulence, spray, and combustion models) over the last decades. It is noted that the volume of data generated by CFD simulations make data analysis (and storage) a challenging task. CFD-based optimization studies of engine performance and emissions have been rather recently reported, including large marine engine applications [37,38]. Important current issues pertinent to engine CFD analysis are discussed in [43,44].

1.7 Background and objectives of the present study

In large two-stroke marine Diesel engines, the injector geometry differs substantially from the configurations used in most other Diesel engine applications. The injectors (commonly two or three) are located on the periphery of the cylinder head, and can inject a high range of fuel qualities (HFO, MDO, MGO, LFO, and alternative fuels) into a swirling air flow within the combustion chamber. The injector orifices are distributed in a highly asymmetric layout, aiming at a proper fuel dispersion. Typically, large marine engine atomizers have a number of orifices, ranging from 5 to 7. Orifice size is typically three orders of magnitude smaller than the cylinder bore [45], i.e., in large marine engines orifice diameters are of the order of 1 mm.

A large scale optically accessible constant volume combustion chamber (Spray Combustion Chamber – SCC) was developed in Oberwinterthur, Switzerland, in the frame of the HERCULES EU project [46-49]; further details on the experimental setup developed are provided in section 3.4 of the present Thesis. The chamber dimensions are representative of smaller two-stroke as well as larger four-stroke marine Diesel engines. In an extensive experimental campaign carried out in 2013, Schmid *et al.* [50] used single hole nozzles, of different eccentricity (**Figure 22**) to characterize spray formation and development. The results presented in [50] demonstrate the strong asymmetry of large marine engine sprays.

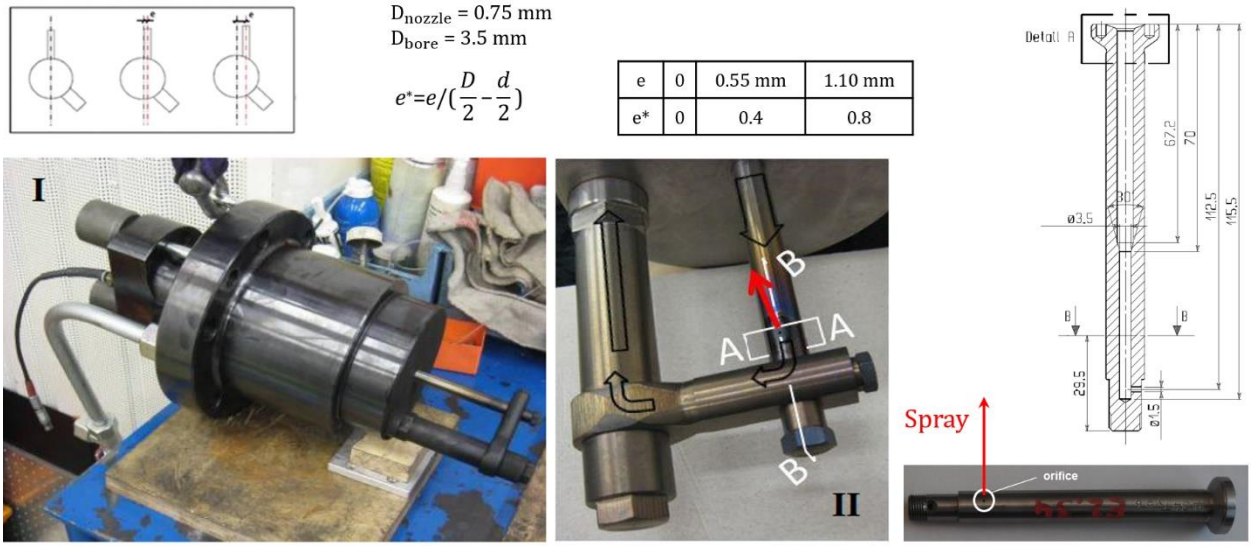

Figure 22 - Injector case (bottom-left), special single hole nozzle with bypass (middle), elongated nozzle design (right) and the three nozzle designs with different eccentricities tested. Definition of normalized eccentricity and its values are depicted.

In more detail, the experimental results reported in [50] indicate a complex three-dimensional structure of marine diesel sprays, with the flow asymmetry increasing with nozzle eccentricity. Nozzle eccentricity was shown to affect spray tip penetration, spray cone angles, and deflections of spray orientation with respect to the injection direction (**Figure 23**). The experimental results of [50] form the main reference data set for validating the CFD results of the present Thesis.

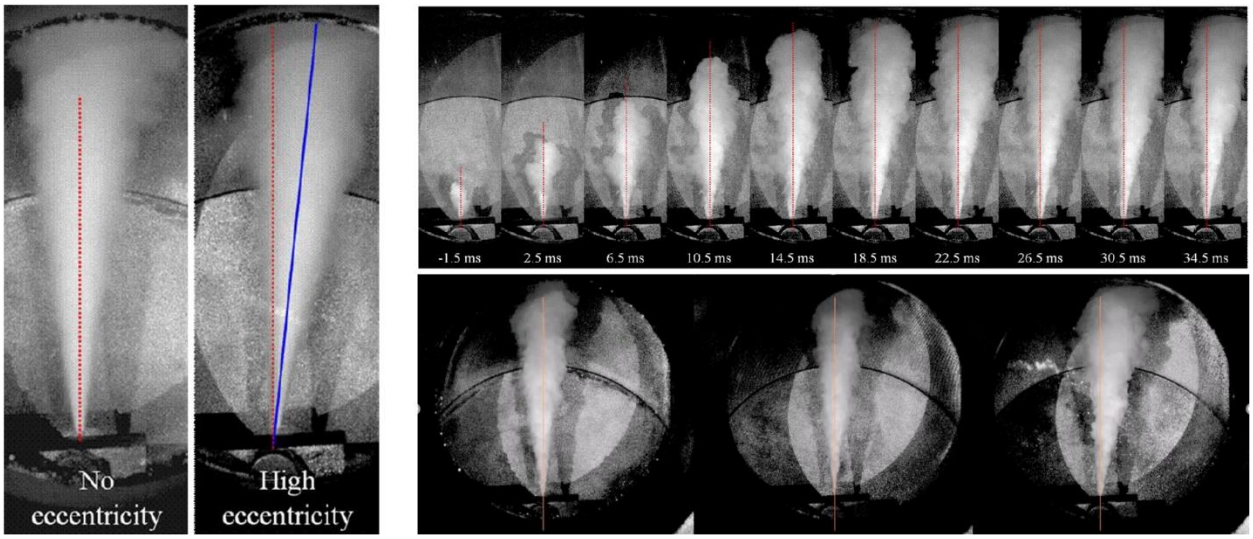

Figure 23 – Spray visualizations as reported in [50]. Upper right: temporal evolution of spray from the high eccentricity nozzle. Low right: Instantaneous images of noneccentric, medium eccentricity and high eccentricity nozzles.

Thus, in large marine Diesel engine injectors, the eccentric placement of orifices with respect to the injector bore axis, and possibly details of in-nozzle flow, cause a strongly asymmetric spray structure. It is underlined that the open literature reports no previous studies accounting for the asymmetry of spray mean flow. The lack of modeling approaches considering this principal spray characteristic is reflected in the frame of setting-up a spray simulation offered by major CFD codes,

applicable to engine CFD. **Figure 24** presents the input panels regarding spray modeling of the four state-of-the-art commercial codes used for engine CFD, namely CONVERGE CFD, STAR-CD, ANSYS FLUENT and STAR-CCM+. As shown in **Figure 24**, CFD codes can provide (in addition to basic data as the orifice diameter) the possibility of prescribing a spray cone angle, thus resulting in an axisymmetric spray structure, to be calculated. An even more basic approach consists in prescribing the injection velocity (for example, using the Bernoulli equation for a given pressure difference with the atomizer), and calculating, in a URANS framework, the spray jet with an Eularian approach using the Volume of Fluid (VOF) method, the breakup into droplets using proper modeling, and the secondary breakup using a Discrete Phase Modeling (DPM) approach. Evidently, in all cases, an axisymmetric spray structure is calculated.

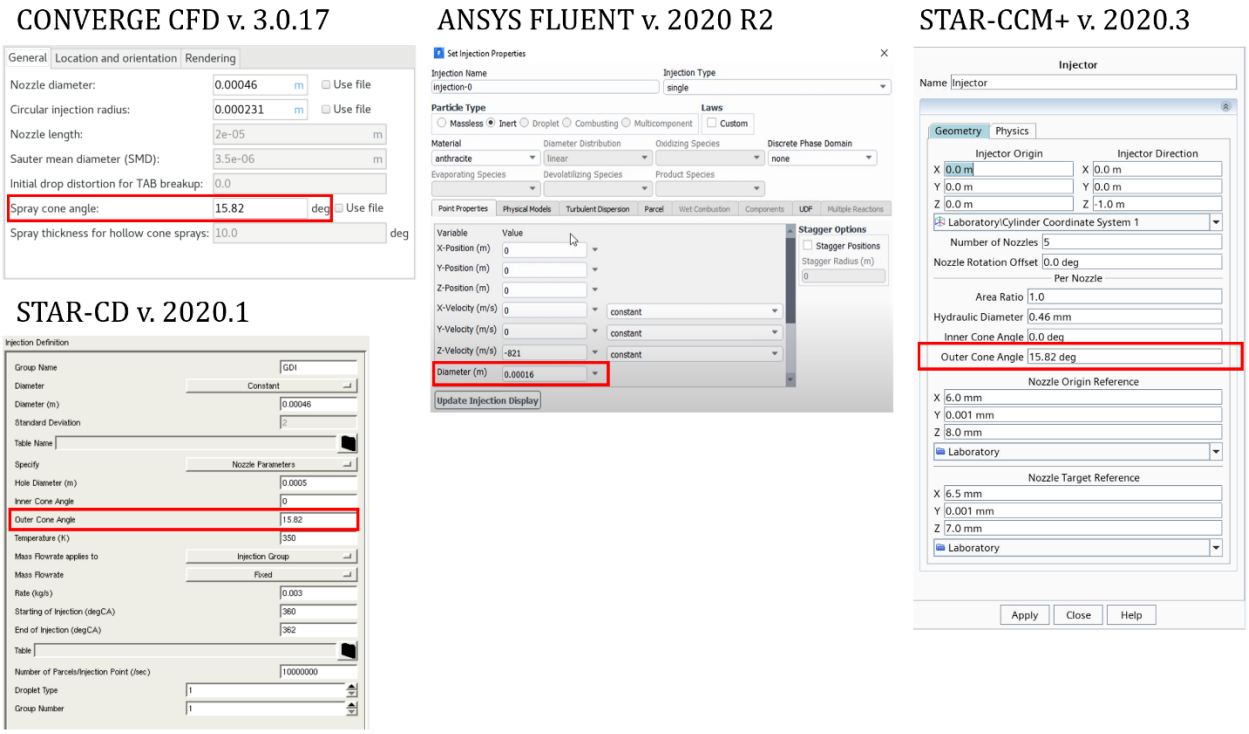

Figure 24 - Spray panels of the currently available state-of-the-art CFD software. CONVERGE CFD (top-left) (Source: CONVERGE CFD v3.0.17), STAR-CD (bottm-left) (Source: STAR-CD v.2020.1), Ansys Fluent (middle) (Source: ANSYS Fluent v.2020 R2) and Star-CCM+ (right) (Source: STAR-CCM+ v.2020.3).

The present dissertation is thus an attempt to characterize in detail the physics of asymmetric sprays for conditions representative of large marine Diesel engines, using Computational Fluid Dynamics, focusing on nonevaporating conditions. A new methodology for modeling sprays in large 2-stroke marine Diesel engines is proposed. The present computational study is supported by existing experimental data (Schmid *et al*. (2013) [50]), as well as new experiments performed for reactive spray flow. Three representative nozzle layouts are considered: a noneccentric nozzle, a nozzle of medium eccentricity, and a highly eccentric nozzle.

The main objectives of the present Thesis can thus be summarized as follows.

- Develop an integrated framework for modeling asymmetric sprays, representative of large two-stroke marine Diesel engines. Since the experimental studies of [50] have demonstrated a strongly asymmetric flow structure, the asymmetry is expected to arise from a corresponding flow asymmetry at the nozzle exit. Calculating in-nozzle flow is thus crucial, as it could provide the proper inflow conditions of spray simulations. To this end, calculation of in-nozzle flow, including cavitation, in a URANS framework, is deployed, and its accuracy is tested against LES calculations. An important expected outcome is thus a characterization of in-nozzle cavitation, and of its effects on overall flow development.
- Accurately calculate spray primary breakup, and characterize flow structure and dynamics. For that, LES calculations are deployed, and the results are analyzed, to provide proper input for secondary breakup calculations. Flow characterization is supported by Proper Orthogonal Decomposition (POD) analysis.
- Calculate spray secondary breakup, and validate results against experiments. To this end, the primary breakup results are used, in conjunction with validated secondary breakup models.
- Compare the overall accuracy of the present approach against the conventional (RANS-only) approach of the open literature.
- Demonstrate the overall accuracy of the present approach in terms of a first comparison of simulation results of reactive flow against experiments.

2 CHAPTER: Turbulent Flow and Simulation Approaches

2.1 Governing equations of fluid flows

Fluid flow and heat transfer are described by conservation equations. These laws can be expressed as follows [51-52]:

Conservation of mass
$$\frac{\partial \rho}{\partial t} + \frac{\partial (\rho u_i)}{\partial x_i} = 0 \quad (1)$$

Momentum equation
$$\frac{\partial (\rho u_i)}{\partial t} + \frac{\partial (\rho u_i u_j)}{\partial x_j} - \frac{\partial \tau_{ij}}{\partial x_j} - \rho g_i = 0 \quad (2)$$

Stress tensor component
$$\tau_{ij} = -p\delta_{ij} + \mu\left(\frac{\partial u_j}{\partial x_i} + \frac{\partial u_i}{\partial x_j} - \frac{2}{3}\delta_{ij}\frac{\partial u_k}{\partial x_k}\right) \quad (3)$$

Energy conservation
$$\frac{\partial (\rho h)}{\partial t} + \frac{\partial (\rho u_j h)}{\partial x_j} - \frac{\partial p}{\partial t} - \tau_{ij}\frac{\partial u_i}{\partial x_j} - \dot{q} + \frac{\partial q_j}{\partial x_j} = 0 \quad (4)$$

Equation of state
$$f(p, \rho, T) = 0 \quad (5)$$

where,
t is the time
x_i is the cartesian spatial coordinate (i = 1,2,3)
ρ is the fluid density
u_i is the absolute fluid velocity component in the coordinate direction x_i
τ_{ij} is the stress tensor
p is the pressure
g_i is the external force per unit mass in the coordinate direction x_i
μ is the dynamic viscosity
δ_{ij} is the Kronecker delta
h is the specific enthalpy
q̇ is source term (heat source such as radiation or spark plug)
q_j is the diffusive flux in the coordinate direction x_j
R is the specific gas constant
T is the absolute temperature.

2.2 Turbulence

In most engineering applications the flow is turbulent, with laminar flow being the exception. In laminar flows, the fluid moves in ordered layers driven by pressure gradients and deformed by the shear stresses. On the other hand, in turbulent flows, the fluid motion is chaotic, and the flow field is characterized by a wide range of length and time scales, and an energy cascade. The high mixing rates in turbulent flow are reflected in the turbulent diffusivity (turbulent viscosity), which is proportional to the product of integral length scale and a characteristic velocity fluctuation intensity. Turbulent flow originates due to the more pronounced presence of flow instabilities at increasing the flow critical parameter, which is commonly the Reynolds number. Turbulent flows

are three-dimensional and occur at large Reynolds numbers. Turbulence intensity can be expressed in terms of velocity or vorticity fluctuations. All turbulent flows are dissipative because of the work of the viscous stresses at the level of small scales. As a result, in the absence of a turbulence sustaining mechanism, the internal energy increases while the kinetic energy of turbulence decreases, i.e., turbulent flows require a continuous supply of energy to maintain an equilibrium state [51-52].

In turbulent flow, flow quantitates (velocity, density, pressure, etc.) vary irregularly as function of time and space. The time average of these quantities can be separated from the fluctuating part, and describes the mean (time-averaged) flow field. An instantaneous flow quantity can thus be considered as the sum of the mean and a fluctuating value (Reynolds decomposition), shown in Equation (*6*) on the example of a velocity component.

Reynolds decomposition

$$u_i(x,t) = \overline{U}_i(x,t) + u_i'(x,t) \tag{6}$$

where,
u_i is the instantaneous velocity
$\overline{U}_i$ is the mean (time-average) velocity component
u_i' is the fluctuating velocity component.

2.3 Turbulence lengthscales

Turbulent flows at high Reynolds numbers are characterized by fluid motions with different lengthscales. In highly turbulent flows a wide range of scales exists, from the large scales (eddies), of dimensions of the order of a characteristic geometrical length, to the smallest turbulent scales (eddies). The size of large eddies is represented by the *integral lengthscale* (l_0), and their motion is associated with a characteristic mean flow velocity (u_0). The smallest eddies of turbulence are represented by the *Kolmogorov lengthscale* (h).

The motions of small scales are also associated with small time scales, and thus they are assumed to be statistically independent of the relatively slow larger turbulence scales and mean flow. Therefore, the small-scale motion depends only on the rate of energy provided from the mean flow and the kinematic viscosity. According to the energy equilibrium, the rate of energy delivered to the small-scale motions is assumed to be equal with the rate of dissipation at the level of small scales [51-52].

In Kolmogorov's first similarity hypothesis, the small-scale turbulent motions have a universal form, which is determined by the kinematic viscosity (ν) and the rate of energy dissipation (ε). According to the assumed equilibrium, the local rate of production of turbulent kinetic energy is equal to the local rate of dissipation. Dimensional analysis leads to estimates of the characteristic scales for length, velocity, and time, at the level of small scales of turbulence [52]:

Length scale

$$h = (\nu^3/\varepsilon)^{1/4} \tag{7}$$

Velocity scale

$$u_h = (\varepsilon \cdot \nu)^{1/4} \tag{8}$$

Time scale

$$t_h = (\nu/\varepsilon)^{1/2} \tag{9}$$

The turbulent energy spectrum is used to characterize the energy cascade in a turbulent flow field, and is usually presented in terms of energy density (E) versus wavenumber (k) in a log-log diagram (**Figure 25**), in which three different sets of lengthscales can be distinguished:

- The energy containing range (largest scales).
- The inertial range, where energy is transferred from the large scales to the small scales, and is characterized by the Kolmogorov's -5/3 law.
- The dissipation range, where energy is dissipated at small scales.

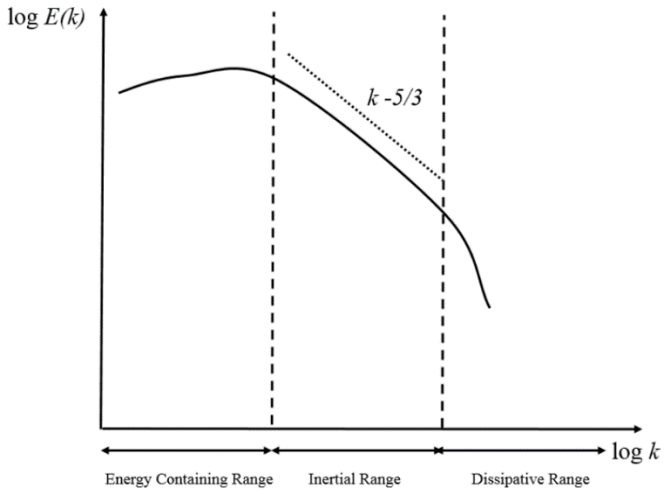

Figure 25 - Representation of the turbulent energy spectrum.

2.3.1 Two-point correlations

Two-point correlation are used in characterizing turbulent flow. This correlation function represents the relation between two points of the same field. A two-point correlation for the velocity fluctuation, $R(x, r)$, can be expressed as follows.

Two-point correlation $$R(x, r) = < u_i'(x, t)u_i'(x + r, t) >$$ (10)

where,
x is the spatial coordinate of the reference point
r is the distance between the two points in space
t is the time
$u_i'(x, t)$ is the instantaneous velocity fluctuation at the first point
$u_i'(x + r, t)$ is the instantaneous velocity fluctuation at the second point.

Commonly, velocity fluctuations are normalized by a corresponding RMS fluctuation intensity, to yield a nondimensional correlation function. Two-point correlations can be used to calculate flow lengthscales [52].

2.3.2 Integral lengthscale

From the two-point correlation, it is possible to define an integral lengthscale as follows [52,53]; separate calculations can be considered for computing the integral lengthscale in the longitudinal and transverse direction.

Integral lengthscale $$l_0(\mathrm{x}) = \int_0^{\infty} \mathrm{R}(\mathrm{x},\mathrm{r})\mathrm{dr} \quad (11)$$

where,
x is the reference point spatial coordinate
r is the distance of an arbitrary point from the reference point
R(x,r) is the correlation coefficient associate with an arbitrary point as above
$l_0(\mathrm{x})$ is the integral lengthscale associate with the reference point.

For high Reynolds number flows, the integral lengthscale can be estimated using Equation (*12*).

Integral lengthscale $$l_0 = \frac{\mathrm{k}^{3/2}}{\varepsilon} \quad (12)$$

where,
k is the turbulent kinetic energy per unit mass
ε is its dissipation rate.

2.3.3 Taylor microscale

The Taylor microscale is a lengthscale between the integral and the Kolmogorov scale (**Figure 26**). It can be associated with the strain rate in the mean flow, and calculated from the second derivative of the autocorrelation function as follows [52,53]; again, separate calculations can be considered in the longitudinal and transverse direction.

Taylor microscale $$\lambda = \left[-\frac{1}{2}f''(0,t)\right]^{-1/2} \quad (13)$$

where,
t is a considered time separation
f (0,t) is the autocorrelation function
λ is the resulting Taylor microscale.

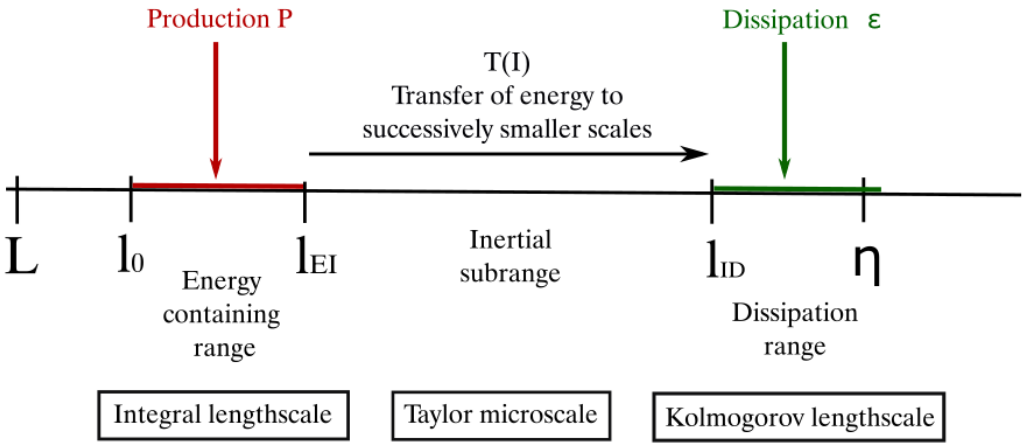

Figure 26 - Sketch of energy cascade of turbulence and correspondence to lengthscales.

The Taylor microscales can be calculated using Equation (*14*) in the case of homogeneous isotropic turbulence (HIT) [53].

Taylor microscale

$$\lambda = \sqrt{15 \cdot \frac{< u_i' \cdot u_i' > \cdot \nu}{\varepsilon}} \tag{14}$$

Where u_i' denotes a fluctuation of the velocity component in the direction i.

2.4 Reynolds-Averaged Navier-Stokes (RANS)

If the information contained in the smallest size eddies is not significant from an applications point of view, then the turbulent flow can be modeled by using the Reynolds-Averaged Navier-Stokes (RANS) equations. The RANS approach is widely used in industrial applications, since it provides simulation results at a reduced time and cost calculations, with acceptable accuracy. RANS methods solve the time-averaged conservation equations for mass, momentum, energy, and species. With the application of the Reynolds decomposition (Equation (*6*)) on the flow quantities, the conservation equations for the time averaged quantities are derived, which for mass and momentum conservation take the form:

Conservation of mass

$$\frac{\partial \bar{\rho}}{\partial t} + \frac{\partial (\overline{\rho u_i})}{\partial x_i} = 0 \tag{15}$$

Navier-Stokes

$$\frac{\partial (\overline{\rho u_i})}{\partial t} + \frac{\partial (\overline{\rho u_i u_j})}{\partial x_j} = \frac{\partial \overline{\tau_{i,j}}}{\partial x_j} + \bar{\rho} g_i \tag{16}$$

The RANS equations contain unknown terms, which for the momentum equation are the Reynolds stresses, $(\overline{u_i' u_j'})$. As a consequence, the equations must be closed in terms of proper turbulence modeling. The most popular closures for the RANS equations are the following:

- Algebraic models
- One-Equation models
- Two-Equation models

- Standard k – ε
- Standard k - ω
- RNG k - ε

➢ Reynolds Stress models.

Further information on turbulence modeling can be found in [52].

2.5 Large-Eddy Simulation

Large Eddy Simulation (LES) has recently gained popularity in more practical CFD applications of turbulent flow, including fuel atomization and fuel-air mixing in Diesel engines. Several engine research studies using LES have been reported. Examples of such studies related to in-cylinder flow and spray formation include the works of Dodoulas (2015) [54], Naitoh *et al*. (1992) [55], and Fukuda (2012) [56].

In LES, the Navier-Stokes equations are filtered at each time step with a low-pass filter. For a reliable LES, it is required that at least 80% of the total kinetic energy is resolved, thus the influence of small-scale motions is removed from the equations by the filtering operation. Sub-grid scale (SGS) models are applied to account for the influence of the small-scale motions. To determine a proper spatial discretization, knowledge of the kinetic energy and dissipation are needed. The filter corresponds to a cut-off wavenumber, which lies in the inertial subrange. Since LES results are highly dependent on spatial resolution, their quality must be ensured by generating numerical grids of a proper resolution.

2.5.1 LES filtering techniques

In LES, a spatial filter function $G(x - x'; \Delta(x))$ is used, with a proper filter width, $\Delta(x)$, and is applied to the Navier-Stokes equations, thus separating the large, energy containing scales from the small scales. The low-pass filter removes all finer fluctuations; therefore, the governing equations only describe filtered fields. The filtering operation is used in the entire flow domain, and is defined locally as follows [52,53-58]:

Local filtering
$$\bar{f}(x,t) = \oint_V G(x - x')f(x',t)dx' \quad (17)$$

where,
$f(x,t)$ is a flow variable (velocity component, pressure, etc.)
G is the filtering function
V is the volume determined by the filter width, Δ.

An instantaneous flow quantity can thus be decomposed into a filtered value and a fluctuation: $f(x,t) = \bar{f}(x,t) + f'(x,t)$. The approaches regarding LES filtering can be categorized into two groups:

1. Implicit filtering: the numerical grid is taken as the low-pass filter, and the filter width is directly related to the cell size, via the cell volume:

Filter width $$\bar{\Delta} = \sqrt[3]{V_{cell}} \quad (18)$$

The filter width can thus vary when nonuniform grids are used, possibly causing aliasing errors. Implicit filtering is the basic reference for the LES approach of the present study.

2. Explicit filtering: the filter width is independent of the grid spacing, and can be fixed for the entire numerical grid. Commutation and truncation errors are of the same order, and the aliasing errors can be controlled. The most known filters are the Gaussian filter, the box filter, and the sharp cut-off. Explicit filtering is computationally more expensive than implicit filtering. More information on explicit filtering can be found in [57,58], including a discussion on the effects of different filters on the resolved kinetic energy of turbulence.

2.5.2 Sub-Grid-Scale (SGS) modeling

There are two main categories of sub-grid scale models: the universal coefficient models, and the dynamic models. In the case of the universal coefficient models, the model constant value(s) must be specified, depending on the flow and/or grid resolution. The appropriate value of the model coefficient is normally determined by comparing numerical simulations to experimental data.

A different approach to model the sub-grid scale stresses was developed by Germano et al. (1991) [60], where the model coefficient is determined dynamically as a function of space and time from the resolved field. This approach assumes an equilibrium between resolved and subgrid scales. Dynamic models thus do not require a priori specifications of model constant value(s). Dynamic models have become widely used and proven to be sufficiently accurate.

In compressible flow, filtering to obtain the LES equations is weighted with the fluid density (Favre-filtering) [59].

Favre-filtering:

Similarly, to the Reynolds decomposition approach, one can decompose the turbulent field as follows [59]. An instantaneous flow quantity is thus decomposed into the filtered one and a fluctuation:

LES decomposition $$f = \bar{f} + f' \quad (19)$$

where,
$\bar{f}$ is the spatially filtered value
f' is the sub-grid contribution.

Favre-filtering applied as follows:

Favre-filter $$\tilde{f} = \frac{\overline{\rho \cdot f}}{\bar{\rho}} \quad (20)$$

Filtered Navier-Stokes equations:

Filtered continuity equation

$$\frac{\partial \bar{\rho}}{\partial t} + \frac{\partial (\bar{\rho} \tilde{u}_j)}{\partial x_j} = 0 \tag{21}$$

Filtered momentum equation

$$\frac{\partial (\bar{\rho} \tilde{u}_i)}{\partial t} + \frac{\partial (\bar{\rho} \widetilde{u_i u_j})}{\partial x_j} = -\frac{\partial \bar{p}}{\partial x_i} + \frac{\partial}{\partial x_j}\left[\bar{\mu}\left(\frac{\partial \bar{u}_j}{\partial x_i} + \frac{\partial \bar{u}_i}{\partial x_j} - \frac{2}{3}\frac{\partial \overline{u_k}}{\partial x_k}\delta_{ij}\right)\right] + \bar{\rho} g_i \tag{22}$$

Equation (*22*) is attained using the Favre-filter relation and assuming that the sub-grid stresses associated with molecular viscosity are negligible. LES filtering results in an unknown contribution, the sub-grid stress tensor.

SGS stress tensor

$$t_{ij}{}^{SGS} = \widetilde{u_i \cdot u_j} - \tilde{u}_i \cdot \tilde{u}_j \tag{23}$$

Combining Equations (*23*) and (*22*), the Favre-filtered LES momentum equation is derived, presented in Equation (*24*).

Filtered LES momentum equation

$$\frac{\partial (\bar{\rho} \tilde{u}_i)}{\partial t} + \frac{\partial (\bar{\rho} \tilde{u}_i \tilde{u}_j)}{\partial x_j} = -\frac{\partial \bar{p}}{\partial x_i} + \frac{\partial}{\partial x_j}\left[\bar{\mu}\left(\frac{\partial \tilde{u}_j}{\partial x_i} + \frac{\partial \tilde{u}_i}{\partial x_j} - \frac{2}{3}\frac{\partial \widetilde{u_k}}{\partial x_k}\delta_{ij}\right) - t_{ij}{}^{SGS}\right] + \bar{\rho} g_i \tag{24}$$

SGS stress modeling

The SGS models reintroduce the missing effect of the small turbulent scales into the spatially filtered LES equations, since these are removed by the filtering process, and therefore a closure is required. In this context, the most commonly used models are the eddy viscosity models. At the scale of small eddies, turbulent energy is dissipated by viscous stresses. In the eddy viscosity approaches, an additional turbulent viscosity (ν_t) is used in the SGS tensor, accounting for the viscous subgrid effects. These models remove energy from the grid scales without energy backscatter from the sub-grid to the resolved scales [52]. Equation (*25*) provides the relation to close the SGS tensor, where $\bar{S}_{ij}$ denotes the filtered rate of strain tensor, defined in Equation (*26*).

SGS stress tensor closure

$$t_{ij}{}^{SGS} - \frac{1}{3} \cdot t_{kk}{}^{SGS} \cdot \delta_{ij} = -2 \cdot \nu_t \cdot \bar{S}_{ij} \tag{25}$$

Filtered rate of strain tensor

$$\bar{S}_{ij} = \frac{1}{2} \cdot \left(\frac{\partial \tilde{u}_j}{\partial x_i} + \frac{\partial \tilde{u}_i}{\partial x_j}\right) \tag{26}$$

Zero-equation sub-grid models:

1. Smagorinsky model:

   The most commonly used SGS modeling technique is the constant Smagorinsky-model. The SGS eddy turbulent viscosity (ν_t) is used to relate the SGS stress ($t_{ij}{}^{SGS}$) to the filtered strain rate (Equation (*(27)*)). In this model, the Smagorinsky constant, C_s, is proportional to the local numerical grid spacing (grid filter width, $\bar{\Delta}$), and, can be determined from turbulence theory, from measurements or DNS data. The Smagorinsky constant commonly takes values between 0.05 and 0.2, but higher values can also be found in the literature [52].

Eddy-viscosity $$\nu_t = (C_s \cdot \overline{\Delta})^2 \cdot \sqrt{2 \cdot \overline{S}_{ij} \cdot \overline{S}_{ij}} \quad (27)$$

The standard Smagorinsky model has limitations in accuracy for transitional flows, where the C_s coefficient should be a function of time and space. Furthermore, the Smagorinsky model predicts nonvanishing SGS eddy viscosity in the regions where the flow is laminar, or the eddy viscosity should be zero [61-63].

2. Dynamic Smagorinsky model:

In the dynamic Smagorinsky model [60], the model coefficient, C_s, is dynamically determined as a function of space and time using an equilibrium between the SGS dissipation and the viscous dissipation at the same physical location. Germano *et al.* (1991) [60] proposed a method for evaluating the instantaneous local value of C_s from information contained in the resolved field. To this end, a second spatial filter (test filter) is applied on top of the original filter (see in **Figure 27**), to minimize errors of the computed flow, and C_s is defined from the resolved flow field. Both of these filters produce resolved flow fields. The difference between the two resolved fields is the contribution of the small scales, whose size falls between the grid filter and the test filter.

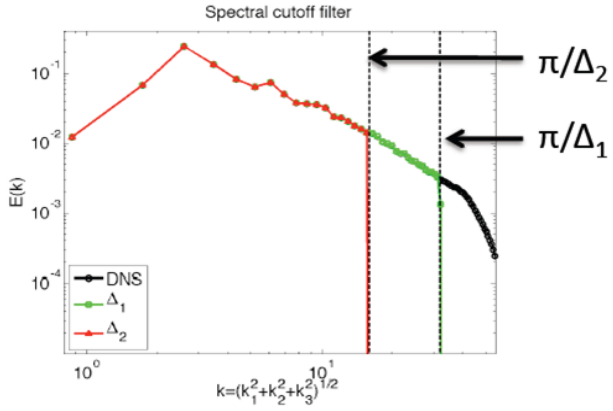

Figure 27 – Sketch of filtering approach used in the dynamic Smagorinsky model [64].

With the variation of C_s in time and space, a more accurate approximation of the resolved field is enabled, including more accurate simulations for the case of transition from laminar to turbulent flow. The resulting values of C_s can be both positive or negative. The negative values correspond to energy backscatter (from small to larger scales). To avoid numerical instability problems, a range of maximum and minimum values of C_s should be assigned. An accurate dynamic calculation of C_s, in the context of minimizing the difference between the resolved and the modelled SGS stresses, was proposed by Lilly (1992) [65]. Detailed information regarding the dynamic model is provided in [63-71].

3. Upwind LES model:

This model employs a dissipative upwind differencing scheme as an alternative to modeling the sub-grid tensor. It requires a sub-grid kinetic energy, k, or a sub-grid dissipation rate, ε.

These values can be computed by approximating the unresolved sub-grid fluctuation velocities. The model expresses the sub-grid velocity as an infinite Taylor series expansion. Further information on the model can be found in [57].

4. Sigma LES model (WALE):

The Sigma LES model is an eddy-viscosity based SGS model for LES. It is derived from the analysis of the singular values of the resolved velocity gradient tensor. This model is part of the zero equation models (standard Smagorinsky, dynamic Smagorinsky, and upwind LES). The proposed model has, by construction, the property to automatically vanish the strain rate of the resolved field in the near-wall region. In other applications, the model has been also shown to properly calculate low levels of SGS viscosity. Model details are presented in [72].

5. Scale-similarity model:

Backscatter was addressed in the similarity model of Bardina *et al*. (1980) [73]. In this model, the sub-grid scale stresses can be approximated from the resolved field; thus, the sub-grid stresses are similar to the smallest resolved stresses. Tests show that the model predicts reasonably well the local sub-grid scale stresses. However, it does not ensure that there is a net positive transfer of energy to the sub-grid scales (Bardina *et al.* (1983) [74]).

<u>One-equation sub-grid models:</u>

The accuracy of the LES sub-grid models can be improved by using an additional transport equation for the SGS kinetic energy. Moreover, the use of the transport equation should allow for coarser grids than in the case of zero-equation models. The reason for this is that sub-grid information and a budget for the associated kinetic energy are available for the formulation of SGS scale models, which should serve to improve the modeling of the effects of the SGS on the resolved scales. An one-equation viscosity-based SGS model was proposed by Menon *et al.* (1996) [75]. Results demonstrated that the scale-similarity model performed better than the one-equation model for relatively fine grids. In the case of a relatively coarse numerical mesh, the one-equation model showed its potential, and provided significantly better results than the scale-similarity model.

1. One-equation viscosity model:

Yoshizawa and Horiuti (1985) [76]) developed the one-equation viscosity model to overcome the deficiency of local balance assumption between the SGS energy production and dissipation adopted in the eddy viscosity models. The imbalance may occur in high Reynolds number flows and/or in the cases of coarse grid resolution. The one-equation model is similar to the zero-equation standard Smagorinsky model, with the difference that a transport equation for the sub-grid kinetic energy is used, instead of assuming local equilibrium. The turbulent viscosity is modeled in terms of the sub-grid kinetic energy. Details of the model formulation are presented in [76] and [75].

2. Dynamic structure model:

The one-equation dynamic model was proposed by Ghosal *et al*. (1995) [77]. It addresses the problem of negative model coefficients and the inverse energy cascade by enforcing a budget

on the sub-grid energy. The dynamic structure model uses the turbulent viscosity to close the momentum equation [78].

2.5.3 LES modeling for spray primary breakup

Different approaches can be found in the literature for simulating spray primary breakup with LES. Senecal *et al.* (2013) [79] simulated evaporating sprays ('Spray A' reference setup) under noncombusting conditions using n-dodecane as fuel. Here, the dynamic structure LES model was used, and the results have demonstrated a small overprediction of the liquid core length, in comparison to experiments. In the primary breakup zone, the predicted vapor penetration matched the experimental measurements very well. Habchi (2012) [80] investigated Diesel sprays experimentally and numerically, in order to advance the understanding of transient processes of short injection, used in multi-injection strategies of internal combustion engines. In his work, simulations have included both the standard and the dynamic-Smagorinsky LES models. It was concluded that both models can readily be used in engine applications; the standard Smagorinsky model was suggested for applications with coarser grids. The standard Smagorinsky model was used in the LES studies by Xiao *et al*. (2014) [81] to simulate a liquid jet in a coaxial airflow, by Befrui *et al*. (2016) [82] to compute a spray in a 'Spray G' reference setup, and in the work of Zheng (2019) [83] to simulate a reactive spray in a 'Spray A' reference setup. In [84], the general structure of primary atomization of Diesel sprays was successfully characterized using an one-equation viscosity LES model. It is underlined that all of the above LES spray studies refer to a problem setup corresponding to an axisymmetric mean flow. The work included in the present Thesis is the first to account for a non-axisymmetric mean flow, representative of large two-stroke marine Diesel engine sprays. To this end, LES simulations with the zero-equation dynamic-Smagorinsky model are deployed.

2.5.4 Grid requirements in LES

In general, LES provides more accurate results than RANS, provided that a sufficiently fine numerical grid is utilized. LES requires a very fine grid, in comparison to RANS. Turbulent mixing, spray formation, and combustion depend strongly on the intensity of turbulent fluctuations, and the convection of turbulence by the mean flow. Therefore, when using LES in engineering applications, it is crucial to generate numerical grids of high resolution and proper quality.

In wall-bounded flows, such as in-nozzle flows, the near-wall flow structures are very small compared to the overall geometry dimensions. These small near-wall structures play a very important part in the turbulent boundary-layer dynamics, and therefore need to be well resolved. The resolution requirements for LES are increasing with Reynolds number, which is therefore the main limitation for using LES in engineering applications [85-90].

The first complete analysis of grid-resolution requirements for LES of turbulent boundary layers was presented by Chapman (1979) [88], where the boundary-layer was divided into an inner layer, where the viscous effects are important, and an outer layer with negligible influence of the viscosity on the mean velocity. In this study, the resolution requirements for the inner and outer layers were analyzed separately. LES requirements, regarding grid density, are an increasing

function of the Reynolds number. For wall-bounded flows, Choi and Moin (2011) [89] revisited Chapman's estimate of these requirements ($N \sim Re^{9/5}$), proposing a modified dependence of $N \sim Re^{13/7}$. The latter considers the one-seventh power velocity distribution law, valid for $10^6 \leq Re \leq 10^9$. In all cases, grid requirements are substantial (Meyers *et al.* 2008 [90]).

With the one-seventh power velocity distribution law, the following correlations were obtained for the boundary layer thickness, δ, and the skin friction coefficient, c_f, as functions of the Reynolds number [89]:

Boundary layer thickness $$\frac{\delta}{x} = 0.16 \cdot \mathrm{Re_x}^{-1/7} \quad (28)$$

Wall skin friction coefficient $$c_f = 0.027 \cdot \mathrm{Re_x}^{-1/7} \quad (29)$$

These correlations are in accordance with other studies, for instance, Nagib *et al.* (2007) [91], Monkewicz *et al.* (2007) [92].

By utilizing the above-given correlations, the requirements for the number of cells for wall-resolved LES can be approximated [89-94].

Number of grid points $$N_{wr} \sim Re_x^{(-\frac{13}{7})} \quad (30)$$

Grid spacing estimation of nozzle bore boundary layer

The boundary layer can accurately be resolved in terms of a wall function, which leads to using the WALE-LES turbulence model [72], or to resolving the boundary-layer with a sufficiently high number of cells, requiring at least 8 cell layers, based on literature suggestions. This number has been clearly exceeded in the present LES studies of in-nozzle flow. Here, in-nozzle flows have been considered as turbulent pipe flows, and the boundary layer thickness was estimated based on the nozzle bore diameter (characteristic length in pipe flows), the fuel viscosity, and the mean flow velocity. The calculated Reynolds number was then used to calculate the skin friction coefficient, assuming a smooth wall, based on the Nikuradse correlation (Nikuradse (1950) [95]):

Pipe skin friction coefficient $$\lambda = 0{,}0032 + 0{,}221 \cdot \mathrm{Re_D}^{-0{,}237} \quad (31)$$

Further information on properly estimating skin friction coefficient in pipe flow can be found in [96-100].

For a known value of friction coefficient, the wall shear stress can be readily calculated:

Wall shear stress $$t_w = \frac{\rho \cdot \bar{v}^2 \cdot \lambda}{8} \quad (32)$$

The friction velocity can be now also calculated.

Friction velocity $$u_t = \sqrt{\frac{t_w}{\rho}} \quad (33)$$

The nondimensional wall distance Y^+ provides a guideline to the boundary layer thickness estimation. In the wall resolved case, meeting the condition $Y^+ \leq 1$ is recommended for placing the first cell layer in high-Reynolds number wall-bounded flows. Here, it is important to resolve the flow in the near wall (viscous sub-layer). To achieve accurate results, at least 2 cell layers are required in the viscous sub-layer, which is located typically at $Y^+ \leq 5$ [97,100,101]. This guideline was adopted, and exceeded, in the present study. To identify the viscous sub-layer width, the following formula was used [102]:

Width of viscous sublayer $$\delta_v = 5 \cdot \frac{\mu_{fuel}}{\sqrt{\rho_{fuel} \cdot t_w}} \quad (34)$$

Finally, the inner layer was estimated from the following formula [102], and literature suggestions were used to estimate a proper number of cell layers. Details on the grids used in the present LES studies of in-nozzle flow are presented in Chapter 3.

Width of inner layer $$\frac{\delta_{in}}{\delta} < 0.1 - 0.2 \quad (35)$$

3 CHAPTER: Diesel Sprays: Physics and Simulation

In two-phase flow CFD studies, the differential equations accounting for the conservation principles for mass, momentum and energy are solved, requiring proper boundary conditions at the domain boundaries [103-105]. Spray breakup modeling makes use of a wide range of models to account for primary and secondary spray breakup.

3.1 Two-phase flow modeling for fuel injection

In-nozzle flow and Diesel spray simulations require a proper modeling framework, which should include identifying the interface boundary between the liquid phase and the gas phase. The following methods are widely used:

1. The Volume of Fluid (VOF) method (Noh and Woodward (1976) [106]) is suitable to capture small to large-scale deformations and interfaces; it is an Eulerian-Eulerian method, and thus the liquid and vapor are treated as separate phases. The void fraction (fraction of volume occupied by the gas phase) is determined from the solution of a corresponding transport equation, taking values between 0 (liquid phase) and 1 (gas phase). A liquid-gas interface can thus be approximated (**Figure 28**).

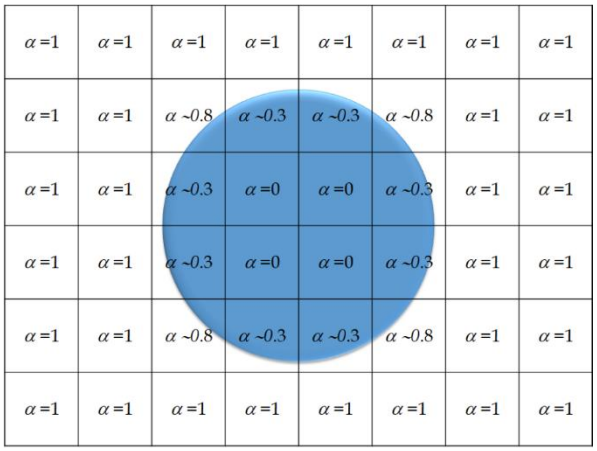

Figure 28 - VOF's void fraction representation with a droplet in gas flow [107].

Regarding in-nozzle flow in the presence of cavitation, when the local (cell) pressure drops below the vapor pressure, a cavitation bubble is formed. The VOF method can successfully predict the separation point, recirculation zone, and reattachment point of a cavitation bubble. Furthermore, the pressure distribution inside the compressible (gas) flow can also be accurately calculated. The solved transport equation of the vapor fraction also predicts the convection of bubble nuclei or cavitation micro-bubbles within the liquid. The basic drawback of this approach is the high numerical grid resolution required to sufficiently resolve the problem length and time scales [108].
The present study uses the VOF technique as a surface tracking method for URANS in-nozzle flow, and subsequently for spray primary breakup calculations resolved by LES.

2. The homogeneous Eulerian flow model considers the bulk (liquid or gas) flow as a continuous homogeneous mixture, and also solves a separate transport equation for the volume fraction of the dispersed phase. Thus, it can account for in-nozzle flow with cavitation; see [109] as a representative example. Commonly, a cavitation bubble is considered to form when the local pressure drops below the vapor pressure. Dabiri *et al.* (2007) [110] and Bode *et al.* [111] tested this criterion and found that the viscous stress contributes to the size of cavitating zones, resulting in earlier cavitation inception.

3. Multifluid Eulerian models [112-114] allow for a more detailed description of the flow, in comparison to the homogeneous model. The approach is characterized by different sets of conservation equations, one for each phase, with its own velocity, temperature, and pressure. A drawback of the present approach is that it cannot track the interface explicitly.

4. When the cavitation level is low and the generated bubbles sizes are smaller than the grid cells, it is possible to use an Eulerian-Lagrangian approach. In this approach, each generated cavitation bubble is tracked in a Lagrangian frame. Here, the liquid is the continuous phase, and the vapor is the dispersed phase. Examples of using this approach applied to nozzle flows were reported by Giannadakis *et al*. (2008) [115] and by Gavaises, *et al*. (2015) [116].

3.2 High-pressure sprays in Diesel engines

Spray development processes have been the subject of several research studies (see [117] and references therein]. In Diesel engines, the fuel is injected into the cylinder at high pressure, using nozzles with different number and size of orifices. Fuel spray is formed evolving from the orifice in a high-pressure surrounding gas. The Diesel spray has a high momentum and turbulence level, which results in a good fuel-air mixture formation inside the combustion chamber. The Diesel spray evaporates and ignites due to the increased temperature during the engine compression stroke. The spray structure has a complex boundary, mainly due to the turbulent motions of the surrounding medium. The spray also has a complex internal structure, affected by the mixing processes between the liquid-gas phase. Turbulence plays a key role in the dynamics of sprays. Spray characterization helps in relating its properties to engine performance. Important spray characteristics are the spray angle, the primary breakup length, the spray penetration length, as well as the distribution of droplet size (**Figure 29**).

In CFD, spray breakup mechanisms are accounted for by physical models. Two approaches most commonly used in spray CFD applications are the Eulerian-Lagrangian and the Eulerian-Eulerian. In both of these approaches, the gas phase is continuous, and modeled by the Navier-Stokes equations. In the Eulerian-Lagrangian approach, the Lagrangian discrete phase model is introduced to calculate the dispersed phase by tracking particles, droplets, or parcels [118].

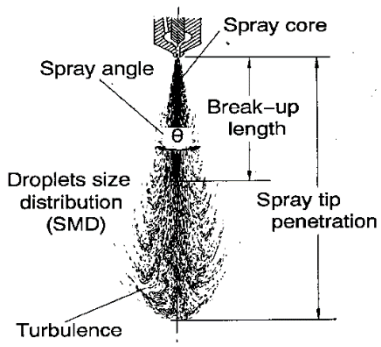

Figure 29 - Diesel spray characteristics [119].

3.3 Breakup of Diesel sprays

One of the most important elements of modeling diesel fuel injection is the accurate modeling of jet and droplet breakup. The fuel, injected at high pressure, enters, with a high velocity, the combustion chamber, which is filled with lower pressure air. The spray is subject to internal, as well as external forces, which result in its disintegration into blobs, ligaments, and droplets, of different sizes and shapes. The liquid fuel undergoes different atomization processes. Three different types of jet breakup mechanisms were distinguished by Arcoumanis *et al.* (1997) [120], namely, the aerodynamically-induced, the turbulence-induced, and the cavitation-induced atomization. In reality, jet breakup is the outcome of the combination of factors accounting for each of the three breakup mechanisms.

In the aerodynamically-induced atomization, the relative motion between the injected fuel and the surrounding gas initiates the generation of waves on the liquid jet surface, resulting in the jet breakup into large liquid entities [117].

The turbulence-induced atomization is initiated within the atomizer nozzle bore, where the highly-turbulent flow leads to velocity fluctuations in the jet, that disrupt its surface, followed by the disintegration of the liquid structure; see Desjardins and Pitsch (2010) [121].

Regarding in-nozzle cavitation, a main factor associated with its presence is the sudden geometrical change at the nozzle bore inlet. The collapse of the formed cavitation bubbles near the nozzle exit could lead to flow fluctuations, which substantially contribute to an intense jet breakup; see Arcoumanis *et al.* (2000) [122], Schmidt *et al.* (1999) [123], Schmidt and Corradini (2001) [124].

The large liquid entities that have been formed in the course of the liquid jet breakup (primary breakup), including blobs, ligaments, and droplets, break up into smaller droplets in the dispersed spray far field (secondary breakup). Details of the spray breakup mechanisms and pertinent modeling approaches are reported in [118-132]. A schematic of the jet breakup processes is shown in **Figure 30.**

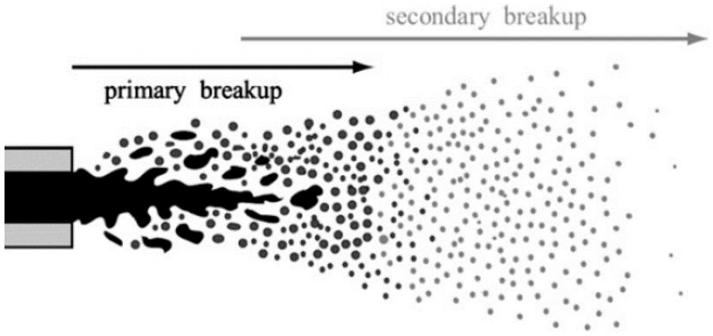

Figure 30 - Illustration of the Diesel spray atomization process.

3.3.1 Spray primary breakup

The fuel jet emanating from the nozzle orifice enters the combustion chamber. The internal and external forces competing on the surface of the liquid generate oscillations on the liquid surface. Consequently, the liquid jet surface undergoes the primary breakup mainly due to the work of the aerodynamic forces, supported by turbulence at inflow. At this stage, the spray structure consists of the liquid core, disintegrating into blobs, ligaments, and droplets. The spray primary breakup provides the initial conditions for the spray secondary breakup, which determines important characteristics as the size of droplets and the spray penetration length. The physics of spray primary breakup depends on the relevant non-dimensional parameters; these are the Reynolds number, the Ohnesorge number, and the Weber number [132].

1. Reynolds number:
   The Reynolds number (Re) is the ratio of the inertia and viscous forces acting on the fluid. If ρ_l is the liquid density, u_{inj} the injection (jet) velocity, D_n is the orifice diameter, and μ_l is the dynamic viscosity of the liquid, then the jet Reynolds number is defined as:

$$\mathrm{Re_l} = \frac{\mathrm{u_{inj}} \cdot \mathrm{D_n} \cdot \rho_\mathrm{l}}{\mu_\mathrm{l}} \tag{36}$$

2. Weber number:
   The Weber number represents the ratio of the aerodynamic forces to the surface tension forces (ρ_g: density of gas phase, σ: surface tension). The Weber number can also be defined for the liquid phase, using the liquid density. Thus:

   Weber number (liquid phase)
$$\mathrm{We_l} = \frac{\mathrm{u_d}^2 \cdot \rho_\mathrm{l} \cdot \mathrm{D_n}}{\sigma} \tag{37}$$

   Weber number (gas phase)
$$\mathrm{We_g} = \frac{\mathrm{u_{inj}}^2 \cdot \rho_\mathrm{g} \cdot \mathrm{D_n}}{\sigma} \tag{38}$$

3. Ohnesorge number

   The Ohnesorge number represents the ratio of liquid viscous forces to surface tension forces, and is defined as follows (Pilch and Erdman (1987) [133]):

Ohnesorge number $$Oh = \frac{\sqrt{We_l}}{Re} = \frac{\mu_l}{\sqrt{\sigma \cdot D_n \cdot \rho_l}} \quad (39)$$

Based on existing experimental evidence, four different regimes (modes) of spray primary breakup are identified, as shown in **Figure 31**. To demonstrate the influence of the surrounding gas on the spray primary breakup, Schneider [125], displaying the categorization of the breakup regimes; see **Figure 32**.

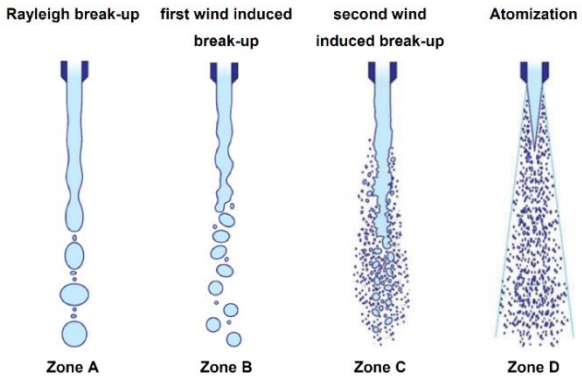

Figure 31 - Primary breakup zones [125].

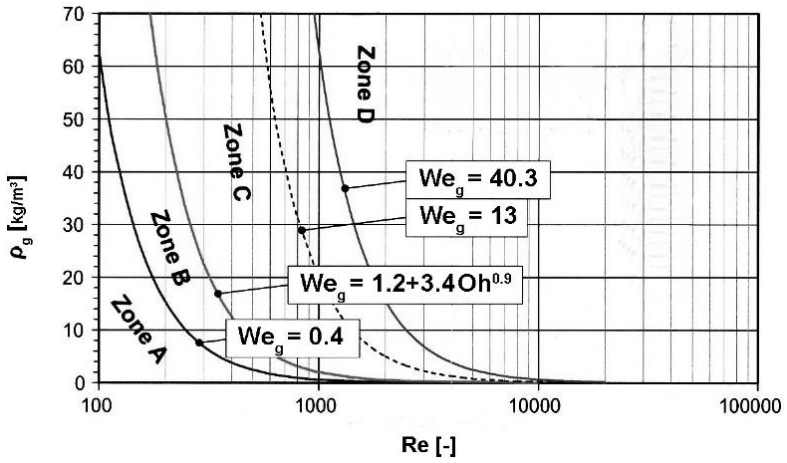

Figure 32 – Primary breakup regimes as function of the gas density and the jet Reynolds number. Zones are separated by lines defined in terms of the gas Weber number [125].

The primary breakup modes (zones) shown in **Figure 31** can be characterized as follows [135]

a) Rayleigh breakup, ZONE A:
In the case of laminar in-nozzle flow and low-velocity sprays, the surface tension forces determine the spray breakup characteristics. Small disturbances on the liquid surface lead to oscillations, and to the detachment of flow entities from the intact liquid. These entities have a size larger than the nozzle diameter. The spray velocity defines the spray penetration length.

b) First wind-induced regime, ZONE B:
With the increase of jet velocity, the Weber number increases, and the influence of aerodynamic forces becomes more significant than in the Rayleigh breakup zone. The perturbations appearing on the liquid surface result in the breakup of the liquid jet. The size of the disintegrated droplets is in the order of the nozzle orifice diameter. The jet penetration length is shorter compared to that in the Rayleigh breakup zone.

c) Second wind-induced regime, ZONE C:
With further increase in the jet velocity, the aerodynamic forces are dominant in the competition to surface tension forces, causing larger perturbations in the axial direction on the spray surface, which leads to oscillations in the transverse direction, manifesting a Kelvin-Helmholtz instability. As a consequence, smaller droplets are formed, characterized by a more frequent detachment.

d) Atomization breakup regime, ZONE D:
When the jet relative velocity is high enough, the liquid jet starts to breakup directly after emerging from the nozzle exit. The core penetration length decreases significantly, but a relatively short liquid core remains intact. This core is defined as a fuel column, and directly connected to the nozzle exit. The breakup in this zone is driven by aerodynamic stripping of smaller droplets from larger droplets through the Kelvin-Helmholtz instability, or by disintegration of larger droplets into smaller ones due to the effect of normal stresses (Rayleigh-Taylor instability).

Categorization of spray primary breakup into one of the above regimes can be based on the combination of values of the Reynolds and Ohnesorge numbers (see **Figure 33**).

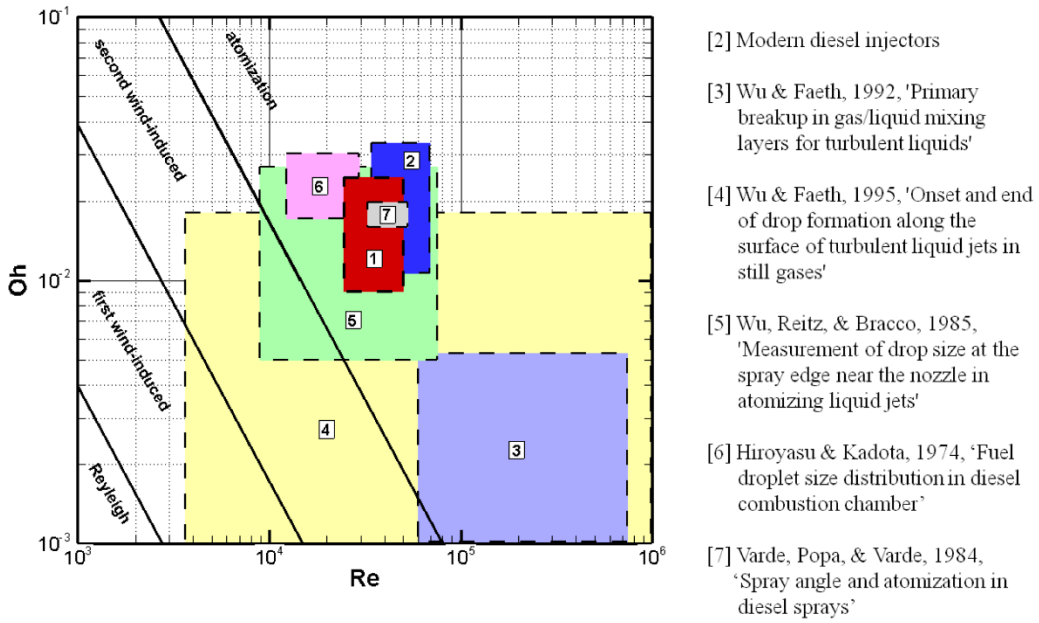

Figure 33 - Jet primary breakup regimes, based on the Ohnesorge and Reynolds numbers [127].

3.3.2 Spray secondary breakup

During the spray primary breakup, droplets, blobs, and liquid fragments are generated. Due to the aerodynamic forces, these disintegrated fluid entities interact with the surrounding air inside the combustion chamber, resulting in the spray secondary breakup. The secondary breakup is thus the generation of new child droplets from parent droplets. The secondary breakup depends on the droplet Weber and Ohnesorge numbers. The stability of droplets decreases at increasing Weber number. The different modes of secondary breakup, and the corresponding order of droplet gas Weber number, are shown in **Figure 34** [136].

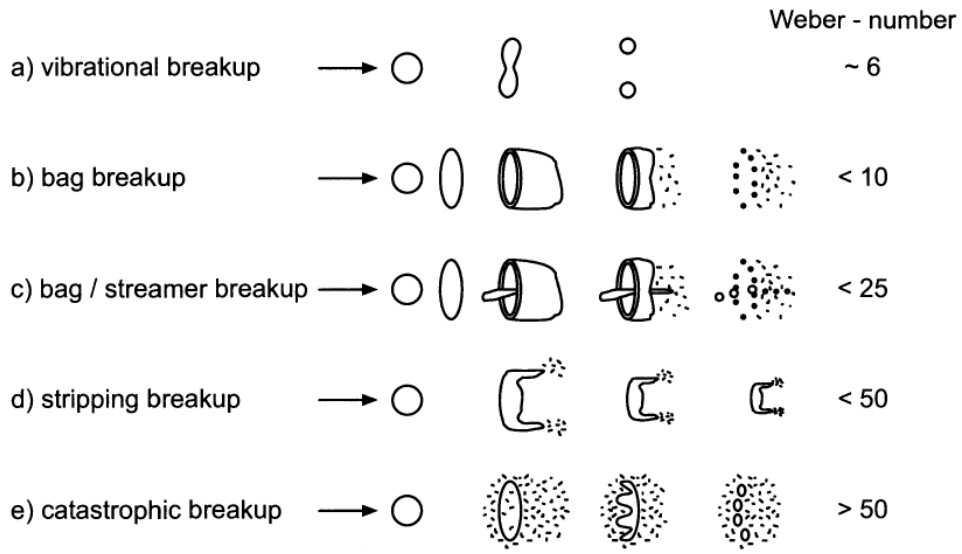

Figure 34 - Mechanisms of secondary breakup [136].

The spray secondary breakup starts with a droplet stretched towards a flat disk (**Figure 34**). During the bag breakup, the flat disk deforms into a thin membrane, and finally the membrane bursts into many fine droplets. During the stripping breakup, the membrane is stripped at the edges, and new small droplets are formed. When the relative velocity between the gas and liquid phase is high, droplets are elongated and then break up as the outcome of a Rayleigh instability (catastrophic breakup) [133,135,136]. In further detailed, the different modes of secondary breakup can be characterized as follows.

a) Vibrational breakup:
   If the Weber number is low, then the oscillation of a droplet will be amplified by the surrounding flow, resulting in slow disintegration of the droplet into new entities. In this case, the breakup time is large compared to all other breakup mechanisms.

b) Bag breakup:
   Here, the droplet is first deflected into a disc perpendicular to the flow direction, and then a balloon-like structure is created. In the next step, the mid area of this structure starts to disintegrate into smaller droplets, and the surrounding ring breaks up into a number of larger droplets.

c) Bag/streamer breakup:
By further increasing the Weber number, the bag/streamer breakup occurs. Here, the balloon-like and a cylindrical column structure coexist, oriented parallel to the flow direction, and break up at the same time as the surrounding ring-like structure.

d) Stripping breakup:
Stripping breakup can be observed at even higher relative velocities between the liquid and gas phase. In this process, a disc shape starts to disintegrate on the droplet periphery. The shear forces break off the disk boundary into smaller droplets, while a coherent residual droplet is present during the entire breakup process.

e) Catastrophic breakup:
The presence of very high relative velocity between the gas and liquid phase results in two different breakup mechanisms.

Kelvin-Helmholtz instability is created in the case of two parallel streams of different velocity. On the interface between the two phases, small disturbances appear, and result in local pressure differences. These pressure differences amplify the initial perturbation. When the growth of these waves reaches a critical level, breakup occurs, and the parent drop diameter decreases.

In the Rayleigh-Taylor instability, two streams of different density flow parallel to each other. In the case of droplet motion in air, surface waves with large-amplitude and short wavelength rapidly penetrate the droplet, causing the disintegration of the parent object into many new entities (drops). These new drops are subject to further breakup.

The catastrophic breakup is typical for Diesel injector applications.

3.3.3 Spray primary breakup models

Different physical models have been introduced to describe primary breakup of high-pressure sprays. One of the bottlenecks in model development is the scarcity of experimental data for primary breakup. The associated experimental challenges are related to the dense character of this spray regime, and its small dimensions. In conventional modeling approaches, the spray primary breakup cannot be calculated directly, i.e. in a DNS or LES frame. The nozzle flow could be simulated with an Eulerian approach, resulting in proper inflow conditions for spray simulations. Nonetheless, spray modeling commonly does not rely on such information, using different primary breakup models, accounting for different mechanisms (aerodynamically-induced, cavitation-induced, and turbulence-induced breakup). The simpler models require less input, and thus provide less accurate results. However, the relatively simple setup and implementation of these models make them popular in industrial CFD. The quality of spray simulations is directly affected by the assumptions regarding the nozzle bore exit (spray inflow) conditions [135]. With proper modeling of in-nozzle flow, and implementing the computed field at outflow in spray simulations, an accurate spray primary breakup modeling could be realized, thus also positively affecting the quality of spray secondary breakup simulations. This approach is undertaken in the present study.

1. Blob-Injection model (Reitz (1987) [137])

   In the blob-injection model, large drops (blobs) are continuously injected into the gas phase with a diameter in the order of the nozzle orifice. The fuel injection rate defines the injection frequency of the new blobs, assuming spherical shapes with constant density. After injection, Kelvin-Helmholtz instabilities appear on the liquid surface. In the next step, droplets start to disintegrate, as depicted in **Figure 35**. Further details on the model can be found in [135,136,137]. An improvement to the blob-injection model can be based on the phenomenological in-flow model developed by Kuensber *et al*. (1999) [138]. This model considers the in-nozzle flow, including flow losses and cavitation, injection pressure and combustion chamber pressure, and provides inflow conditions for primary spray breakup modeling. In particular, the model can provide dynamically the injector discharge coefficient, the effective injection velocity, and the size of blobs.

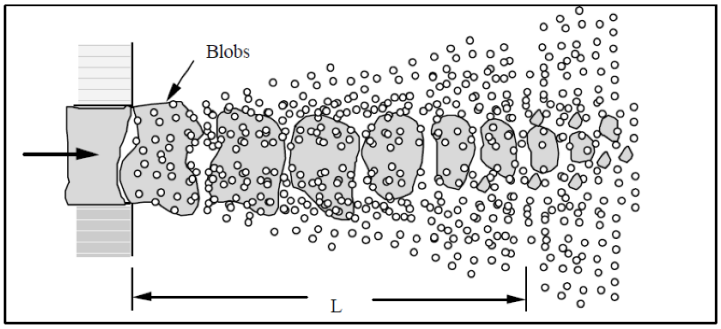

Figure 35 - Spray primary breakup: Blob-injection model [137].

2. Turbulence Induced Atomization (Huh-Gosman) model

   This atomization model was introduced by Huh and Gosman (1991) [139], and assumes the injection of large blobs, of the size of the orifice diameter. It accounts for turbulence-induced atomization, including prediction of the initial spray cone angle. The model assumes that initial surface perturbations on the liquid surface are generated by the turbulent forces at the nozzle exit. These perturbations grow exponentially due to the work of the aerodynamic forces, generating new droplets. In the model, the turbulent lengthscale is used to determine the wavelength of the most unstable surface wave. By using the mass, momentum, and energy balances, the turbulent kinetic energy at the nozzle bore exit can be estimated. The model assumes that unstable Kelvin-Helmholtz waves grow on the surface of injected blobs, which result in their breakup, associated with a characteristic length and timescale. The effects of turbulence are introduced by assuming that the atomization lengthscale is proportional to the turbulence lengthscale, and that the atomization time scale can be written as a linear combination of the turbulence time scale (from the nozzle flow) and the wave growth time scale (the latter associated with the external aerodynamic forces). The model relates the velocity of child droplets formed at blob breakup to the parent droplet's velocity. The model does not account for in-nozzle cavitation, but assumes that turbulence at the nozzle exit fully represents all in-nozzle flow features [135,139].

3. Linearized Instability Sheet Atomization (LISA) breakup model
   Pressure swirl atomizers are often used in order to establish hollow cone sprays, typically used in Gasoline Direct Injection (GDI) engines. The atomizer produces a rotating hollow-cone spray with a large angle, and with an air core at the centre. The liquid sheet emerges from the orifice, breaks up into ligaments, and then into droplets. The atomization process can be divided into three major steps: film formation, sheet breakup, and atomization. The Linearized Instability Sheet Atomization (LISA) model has been introduced in [140], to account for the primary breakup of hollow cone sprays. The model defines the liquid film thickness using a correlation for the injector exit velocity, and considers the primary breakup by means of a linearized instability analysis of a viscous liquid sheet. The model calculates important parameters of spray primary breakup, including breakup length, diameter of ligaments formed, and spray average angle. A detailed description of the LISA model can be found in [135,140], while the sheet breakup mechanism is sketched in **Figure 36**.

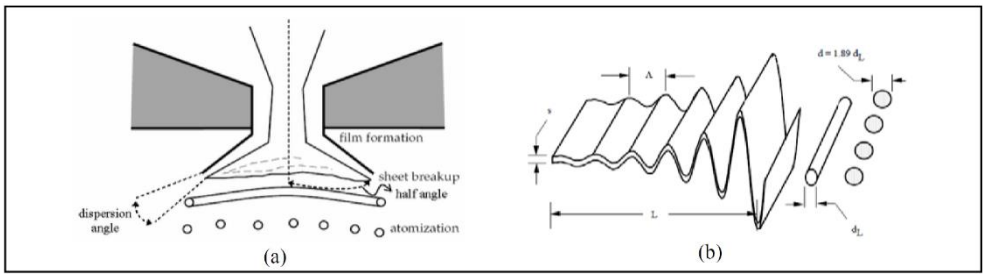

Figure 36 - Sheet breakup mechanism of the LISA model [141].

4. WAVE model
   The WAVE model, sketched in **Figure 37**, also referred to as Kelvin-Helmholtz primary breakup model [143,144], was used in the present study (in addition to LES modeling) to calculate spray atomization. The model considers that a round liquid jet, with radius $r_{l0} = D_{l0}/2$, where D_{l0} is the nozzle diameter, penetrates through the nozzle hole into a stationary incompressible gas environment. The model assumes that the liquid surface is subject to a number of infinitesimal perturbations, with an initial amplitude of η_0. The wavelength, λ, of such a perturbation corresponds to a wave number $k = 2 \cdot \pi / \lambda$. These perturbations may be initiated due to cavitation and turbulence of the in-nozzle flow. In the linear regime, the amplitudes of these perturbations increase exponentially (see Equation (*40*)) due to the liquid-gas interactions caused by aerodynamic forces. This increase can be associated with a complex growth rate, $\omega = \omega_r + i \cdot \omega_i$.

Perturbation $$\eta(t) = R(\eta_0 exp[ikx + \omega t]) \quad (40)$$

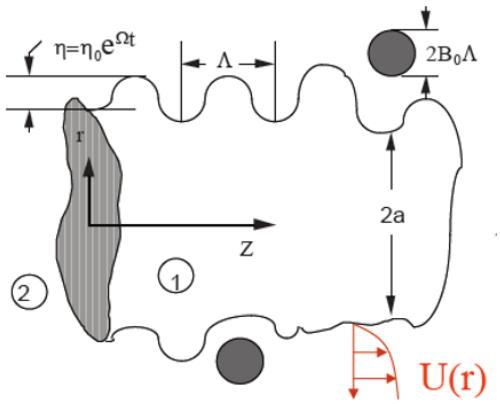

Figure 37 - Wave model [137].

Assuming an inviscid gas phase (free slip at the liquid-gas interface), and those perturbations have a wavelength much smaller than the jet radius, the dispersion relation, which relates the wavenumber, *k*, to the growth rate, ω, can be derived [143]). Assuming that only the fastest growing perturbation, corresponding to a growth rate Ω and a wavelength Λ, leads to the breakup, the values of Λ and Ω can be expressed as follows [137]:

Breakup relation Λ

$$\frac{\Lambda}{D_{l0}/2} = 9.02 \cdot \frac{(1 + 0.45 \cdot Z^{0.5}) \cdot (1 + 0.4 \cdot T^{0.7})}{(1 + 0.87 \cdot We_{gas}^{1.67})^{0.6}} \tag{41}$$

Breakup relation Ω

$$\Omega \cdot \left(\frac{\rho_{liquid} \cdot (D_{l0}/2)^3}{\sigma} \right)^{0.5} = \frac{0.34 + 0.38 \cdot We_{gas}^{1.5}}{(1 + Z) \cdot (1 + 1.4 \cdot T^{0.6})} \tag{42}$$

where $We_{liquid/gas} = \rho_{liquid\,/\,gas} \cdot U_m^2 \cdot D_{l0} \,/\, (2 \cdot \sigma)$, $Z = We_{liquid}^{0.5} / Re_{liquid}$ and $T = Z \cdot We_{gas}^{0.5}$ are Weber number (defined in terms of the liquid or gas density), Ohnesorge number, and Taylor number, respectively; and $Re_{liquid} = U_m \cdot D_{l0} \,/\, 2 \cdot \nu_{liquid}$ is jet Reynolds number. The resulting size (radius) of droplets formed is approximated by assuming a linear relation with Λ, with a proportionality constant of the order of 1. The length of the intact liquid core of the spray, L_{core}, can be approximated by considering the mass removed from the jet via atomization

Core length

$$L_{core} = \frac{c \cdot (D_{l0}/2)}{f(T)} \cdot \sqrt{\frac{\rho_{liquid}}{\rho_{gas}}} \tag{43}$$

where *c* is a constant which takes a value of 15-30, and accounts for details of the in-nozzle flow. The spray cone angle must be prescribed based on available experimental results. The estimation of the initial velocity for each droplet utilizes the assumption of equal probability of velocity direction within the spray cone (Huh and Gosman (1991) [139]).

A drawback of the model is the simple (top hat) velocity profile, which does not represent the continuous velocity variation between the two phases. This discontinuity can be seen in the sketch of **Figure 38**.

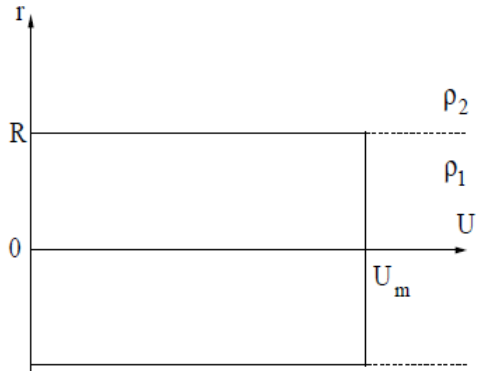

Figure 38 - Wave model velocity profile [131].

5. Modified WAVE model
   The WAVE model was modified by Sazhin *et al*. (2002,2005) [145,146], to account for the transient behavior of the Diesel jet during injection. Here, the rate of the spray disintegration was controlled by changing the WAVE model parameters. Additionally, a liquid core was also added to the model, which penetrates a certain distance into the spray before the core starts to disintegrate. Details of the modified WAVE model are provided in [145,146,131].

6. KH-ACT (Aerodynamics, Cavitation, Turbulence) model
   The standard WAVE model was modified in the frame of the KH-ACT model regarding the aerodynamically-induced breakup, thus also accounting for cavitation and turbulence effects generated in the nozzle bore. The influence of nozzle geometry on the spray formation and combustion processes are considered in order to calculate cavitation and turbulent intensity levels at the nozzle orifice, which are consequently applied as boundary and initial conditions in spray primary breakup simulations. Within KH-ACT, the *turbulence-induced breakup sub-model* includes calculation of a turbulent lengthscale and a turbulent timescale. The *cavitation-induced breakup sub-model* calculates cavitating bubble formation within the nozzle bore. Cavitation enhances the decay of the liquid core and decreases the characteristic breakup timescales. The model considers a breakup timescale which is the faster between the turbulence-induced breakup and the cavitation-induced breakup timescales. Moreover, the aerodynamically-induced spray breakup is calculated using the Kelvin-Helmholtz model. The model details are provided in [147-149].

3.3.4 Secondary breakup models

1. Taylor Analogy Breakup (TAB) model
   The TAB model (O'Rourke and Amsden (1987) [150]) describes the droplet breakup process in terms of a critical deformation of an oscillating droplet, which is approximated with a spring-mass system (see **Figure 39**). In the frame of the TAB model, a droplet is deformed and oscillates due to the action of aerodynamic forces (proportional to the gas density). The surface tension forces are associated with the restoring (spring) forces, while

the action of liquid viscosity is associated with damping. When the droplet deformation exceeds a certain threshold, child droplets are considered to form. The model details can be found in [150,136,135]. The model was improved by Tanner in the context of the ETAB model [151].

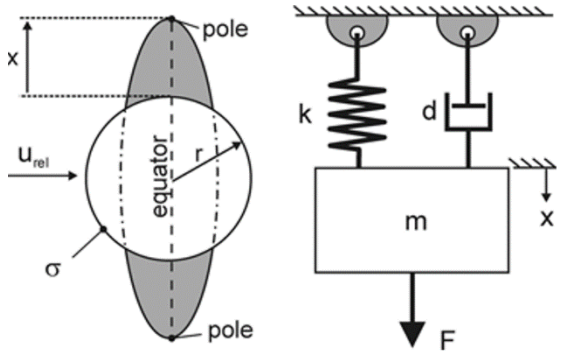

Figure 39 – TAB model: sketch of droplet deformation and of the corresponding damped spring-mass system [135].

2. Reitz-Diwakar model

The Reitz-Diwakar model (1987) [152] accounts for bag breakup and stripping droplet breakup, for low and high Weber number levels, respectively. Implementation of the model commonly considers a continuous (and not a discrete) reduction of parent droplets due to breakup, with the reduction rate expressed as:

Change of droplet radius over time

$$\frac{dr_d}{dt} = -\frac{r_d - r_s}{t_{bu}} \tag{44}$$

where r_d is the droplet radius, r_s a stable droplet radius, and τ_{bu} a characteristic breakup time [152].

The Weber number is defined as follows:

Gas Weber number

$$We_{gas} = \frac{\rho_{gas} \cdot {u_{rel}}^2 \cdot r_d}{\sigma} \tag{45}$$

The criterion for bag breakup is

Gas Weber number for bag breakup

$$We_{gas} \geq C_{b1} \tag{46}$$

where C_{b1} is a constant with a value in the range of 3.6 - 8.4.

The stripping breakup criterion is

Gas Weber number for stripping breakup

$$\frac{We_{gas}}{\sqrt{Re_{gas}}} \geq C_{s1} \tag{47}$$

where C_{s1} is a constant which commonly acquires a value of 0.5; and $Re_{gas} =$ the drop Reynolds number, based on the droplet diameter, D_d.

Gas Reynolds number

$$\mathrm{Re}_{\mathrm{gas}} = \frac{D_d \cdot u_{rel}}{\nu_{\mathrm{gas}}} \tag{48}$$

The corresponding lifetimes of unstable droplets are [137]

Bag breakup time

$$\tau_{\mathrm{bag}} = C_{b2} \cdot \frac{1}{4} \cdot \sqrt{\frac{\rho_{\mathrm{liquid}} \cdot {D_d}^3}{\sigma}} \tag{49}$$

Stripping breakup time

$$\tau_{\mathrm{stripping}} = C_{s2} \cdot \frac{1}{2} \cdot \frac{D_d}{u_{rel}} \cdot \sqrt{\frac{\rho_{\mathrm{liquid}}}{\rho_{\mathrm{gas}}}} \tag{50}$$

where $C_{b2} \approx \pi$ is a constant, and C_{s2} is a constant with values in the range 2-20. When one of the aforementioned breakup criteria is met, a drop is considered to break into smaller drops of equal size. The size (diameter) of new droplets is determined from the corresponding critical value of Weber number [Equations (*46*,*(47)*)], and their number is determined from mass conservation:

Droplet number

$$N_{d,child} \cdot {D_{d,child}}^3 = N_{d,parent} \cdot {D_{d,parent}}^3 \tag{51}$$

The values of the model constants used in the present study are given in **Table 1**.

Table 1: Values of the Reitz-Diwakar atomization model constants used in the present study.

Parameter	C_{b1}	C_{b2}	C_{s1}	C_{s2}
Value	6	π	0.5	20

3. Kelvin-Helmholtz Rayleigh-Taylor model

In the KH-RT hybrid model (sketched in **Figure 40**), the Kelvin-Helmholtz and the Rayleigh-Taylor instabilities are considered and calculated simultaneously; breakup is determined by the shortest characteristic breakup time. Concerning the liquid jet breakup, previous studies showed that the Rayleigh-Taylor instability is dominant farther downstream from the nozzle, whereas the Kelvin-Helmholtz instability has a stronger significance in the near-orifice regime (Beale and Reitz (1999) [153]; Baumgarten (2006) [135]).

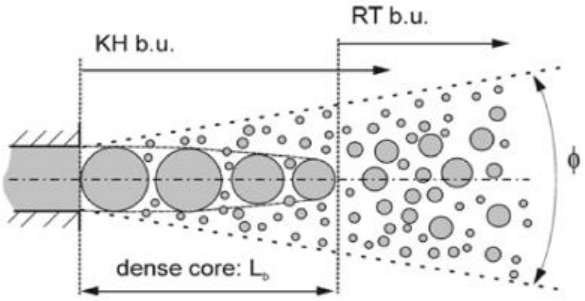

Figure 40 – Sketch of breakup regimes considered in the Kelvin-Helmholtz Rayleigh-Taylor breakup model [135].

In the frame of Kelvin-Helmholtz instability, aerodynamic forces act on the liquid surface, destabilizing the liquid (jet or drop) structure. The size of new droplets is proportional to the wavelength of the most unstable mode:

New droplet diameter $$D_{new} = 2 \cdot B_0 \cdot \Lambda_{\mathrm{KH}} \quad (52)$$

where D_{new} is the diameter of new droplets, Λ_{KH} is the wavelength of the most unstable surface wave, and B_0 is a model constant. As in the Reitz-Diwakar model, implementation of the model commonly considers a continuous (and not a discrete) reduction of parent droplets due to the breakup, with the reduction rate expressed as (Reitz and Diwakar (1987) [152])

Reduction rate $$\frac{dD_d}{dt} = -\frac{D_d - D_{new}}{\tau_{\mathrm{KH}}} \quad (53)$$

where τ_{KH} is a characteristic breakup time of the KH instability, expressed as [154,136, 137]:

KH breakup time $$\tau_{\mathrm{KH}} = \frac{3.726 \cdot B_1 \cdot D_d/2}{\Lambda_{\mathrm{KH}} \cdot \Omega_{\mathrm{KH}}} \quad (54)$$

where Ω_{KH} is the growth rate of the fastest-growing wave (Patterson and Reitz (1998) [155]), and B_1 is an adjustable model parameter. Relations between the wavelength Λ_{KH} and Ω_{KH} (dispersion relation) are reported in several sources (Patterson and Reitz (1998) [155]); Baumgarten (2006) [135].

The Rayleigh-Taylor (RT) model is based on the work of Taylor (1963) [156], who investigated the instability of the interface between two fluids of different density. In fuel injection, the liquid jet disintegrates into blobs, ligaments, and drops, which are decelerated due to the action of aerodynamic drag force:

Aerodynamic force $$F_{aero} = c_D \cdot \frac{{D_d}^2 \cdot \pi}{4} \cdot \frac{\rho_{\mathrm{gas}} \cdot {u_{rel}}^2}{2} \quad (55)$$

This generates unstable waves on the drop backside (Rayleigh-Taylor instability). Acceleration of the interface (aerodynamic force divided by drop mass) can be readily obtained as

Interface acceleration $$a = c_D \cdot \frac{3}{8} \cdot \frac{\rho_{\mathrm{gas}} \cdot {u_{rel}}^2}{\rho_{\mathrm{liquid}} \cdot \frac{D_d}{2}} \quad (56)$$

where c_D is the drag coefficient in flow past a spherical drop.

RT breakup occurs when the droplet diameter is larger than the wavelength of the fastest-growing wave; the number of new drops is calculated based on satisfying the mass conservation principle. Thus, if Λ_{RT} is the wavelength of the fastest-growing RT instability wave, the drop breakup criterion is:

Drop breakup criterion $$\mathrm{D_d} > \mathrm{C_3} \cdot \Lambda_{\mathrm{RT}} \quad (57)$$

where C_3 is an adjustable constant accounting for the unknown effects of initial conditions, as turbulence and cavitation inside the nozzle, on the secondary breakup (Baumgarten (2006) [135]). The wavelength of the most unstable mode, Λ_{RT}, can be determined based on the corresponding wavenumber, k_{RT}, which maximizes the growth rate, ω (Senecal *et al*. (2007) [154]; Baumgarten (2006) [135]):

Wave number $$k_{RT} = \frac{2 \cdot \pi}{\Lambda_{\mathrm{RT}}} \quad (58)$$

Growth rate $$\omega(\mathrm{k}) = -k^2 \cdot \left(\frac{\mu_{\mathrm{liquid}} + \mu_{\mathrm{gas}}}{\rho_{\mathrm{liquid}} + \rho_{\mathrm{gas}}}\right) + \sqrt{k \cdot \left(\frac{\rho_{\mathrm{liquid}} - \rho_{\mathrm{gas}}}{\rho_{\mathrm{liquid}} + \rho_{\mathrm{gas}}}\right) \cdot a - \frac{k^3 \cdot \sigma}{\rho_{\mathrm{liquid}} + \rho_{\mathrm{gas}}} + k^4 \cdot \left(\frac{\mu_{\mathrm{liquid}} + \mu_{\mathrm{gas}}}{\rho_{\mathrm{liquid}} + \rho_{\mathrm{gas}}}\right)^2} \quad (59)$$

where a is the interface acceleration.

The RT characteristic breakup time is determined as follows:

RT breakup time $$\tau_{\mathrm{RT}} = \frac{\mathrm{C_\tau}}{\omega_{\mathrm{RT}}} \quad (60)$$

where C_τ is constant.

The values of the KH-RT model constants in **Table 2** correspond to literature suggestions regarding high pressure Diesel sprays.

Table 2 - Suggested values of the KH-RT model constants for high-pressure Diesel sprays.

Parameter	B_0	B_1	C_3	C_τ
Value	0.61	40	0.1	1

The KH-RT model was proven to accurately account for spray secondary break in high-pressure Diesel sprays, in several literature studies. Thus, it is used as the main secondary breakup model of the present study.

3.4 Test facility

A large optically accessible test facility [spray combustion chamber (SCC)] was developed by Winterthur Gas & Diesel (ex. Wärtsilä Switzerland) and ETH Zürich for spray and combustion studies under conditions similar to those of large marine engines (Herrmann *et al.* (2007,2009, 2011) [46,47,48], Kyrtatos *et al.* (2013) [49]). The SCC facility enables nonreactive and reactive spray experiments representative of large marine engine applications (**Figure 41**). A pressure vessel equipped with fast-actuating valves provides the gas, which is heated in an electrically powered regenerator.

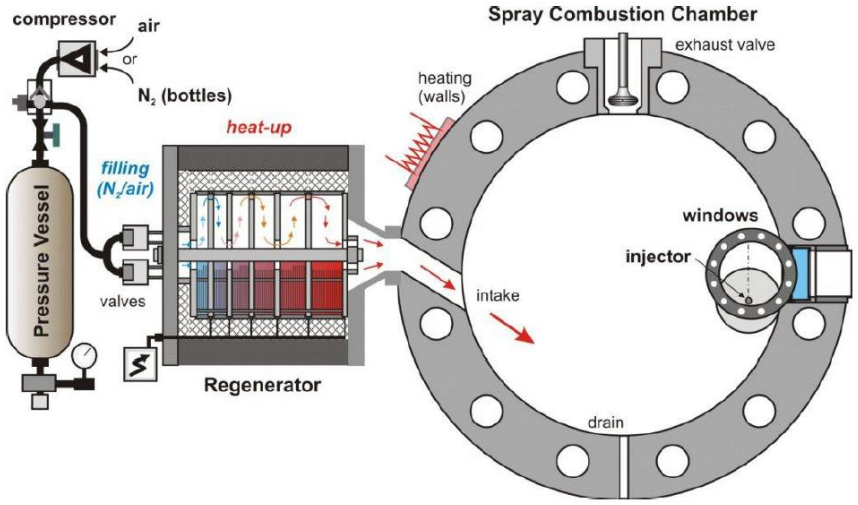

Figure 41 - Spray Combustion Chamber (SCC) [50].

The electrically powered heat exchange device grants a rapid temperature increase of the process gas. The tilted intake channel generates an engine-like swirling flow motion inside the chamber. The pressure and temperature levels, as well as the swirl, are adjustable by changing the accumulator pressure and/or duration of the blow-down process. The current setup allows the pressurization of the chamber directly via a compressor; thus, the accumulator is refilled by compressed air and the regenerator is reheated again to the desired values. The filling process is recorded with many pressure and fast-responding temperature indicators installed at different locations in the SCC. Injection in low swirl-level conditions can be attained by a proper delay of injection start, as well as by moving the injector closer to the chamber centre; visualization can be realized by a proper window position arrangement. Fuel admission is attained by engine-like injection systems (common rail, with pressure up to 1200 bar) through single-hole injectors located on the circumference of the chamber. The fuel injection system can operate with different types of marine fuel oil [such as light fuel oil (LFO), marine diesel oil (MDO), and heavy fuel oil (HFO)] and surrogates (von Rotz *et al.* (2015) [159]).

Reference experimental data were acquired involving the variation of key parameters such as gas pressure and temperature (up to 13 MPa, 930 K, before injection/ignition), the number of (single-hole) injectors (one or two), and the injection orientation with respect to the swirling gas flow

(Schmid *et al*. (2013,2014) [50,158]; von Rotz *et al*. (2011,2015) [157,159]). In the present thesis, the results of these experiments are used for validation purposes.

Figure 42 shows the optical setup applied in the study reported in [50], where the experiments mainly targeted the spray development in a direction parallel to the injector's axis. A Mie-scattering technique was applied, where a Nd: YLF-Laser was used for illuminating the liquid phase of the spray. Two high-speed cameras, the first one located in the front and the second one on the spray side, were used to ensure the simultaneous spray visualization, recording the scattered light.

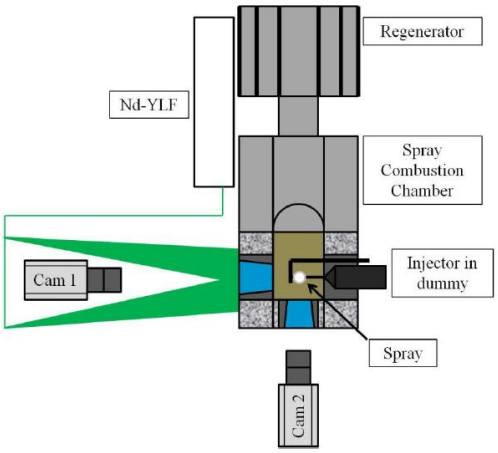

Figure 42 - Optical setup at SCC [50].

A special injector configuration was developed in order to investigate the impact of orifice eccentricity on the spray morphology, shown in **Figure 43**. The direction of the spray, originating from the single orifice and located at a certain eccentricity with respect to the axis of the injector, is indicated by the red arrow. To obtain the same flow conditions at the inlet of the injector as in a five-hole injector, a second orifice (bypass) with a correspondingly enlarged flow area is located at a sufficiently large distance downstream of the first orifice for avoiding any disturbance of the flow into the latter. Any potential impact of this second orifice on the processes inside the SCC is avoided by redirecting the fuel flowing into a plenum outside the SCC (black arrows) [50].

Figure 43 - Assembled injector (I) and view of injector arrangement including flow directions (II) (one-hole fuel injection (red arrow) and redirected bypass-flow (black arrows)) [50].

4 CHAPTER: In-nozzle Flow and Spray Primary Breakup Simulation

4.1 Introduction

Several studies investigated the formation of symmetric sprays and the effects of fuel injection processes on combustion (Arcoumanis *et al.* (1997) [120]; Baumgarten (2006) [135]; Heywood (1988) [161]; Hiroyasu and Arai (1990) [162]). However, in large marine diesel engines, it is typical for orifices to be arranged eccentrically with respect to the central bore axis of the injector (**Figure 44**), thus creating a highly asymmetric spray structure (Weisser *et al.* (2013) [163]; Schmid *et al.* (2013, 2014) [50,158]). In those engines, spray conditions and physical parameters are different from those of automotive engines, which were studied in detail by several research groups. For accurate computational fluid dynamics (CFD) calculations in large marine engines, precise physical models are essential. Although model validation studies of relevance to large marine engines are available (Takasaki *et al.* (2002) [164]; Pizza *et al.* (2007) [165]; Fink *et al.* (2008) [166]), they correspond to geometries and conditions closer to those of small or heavy-duty diesel engines.

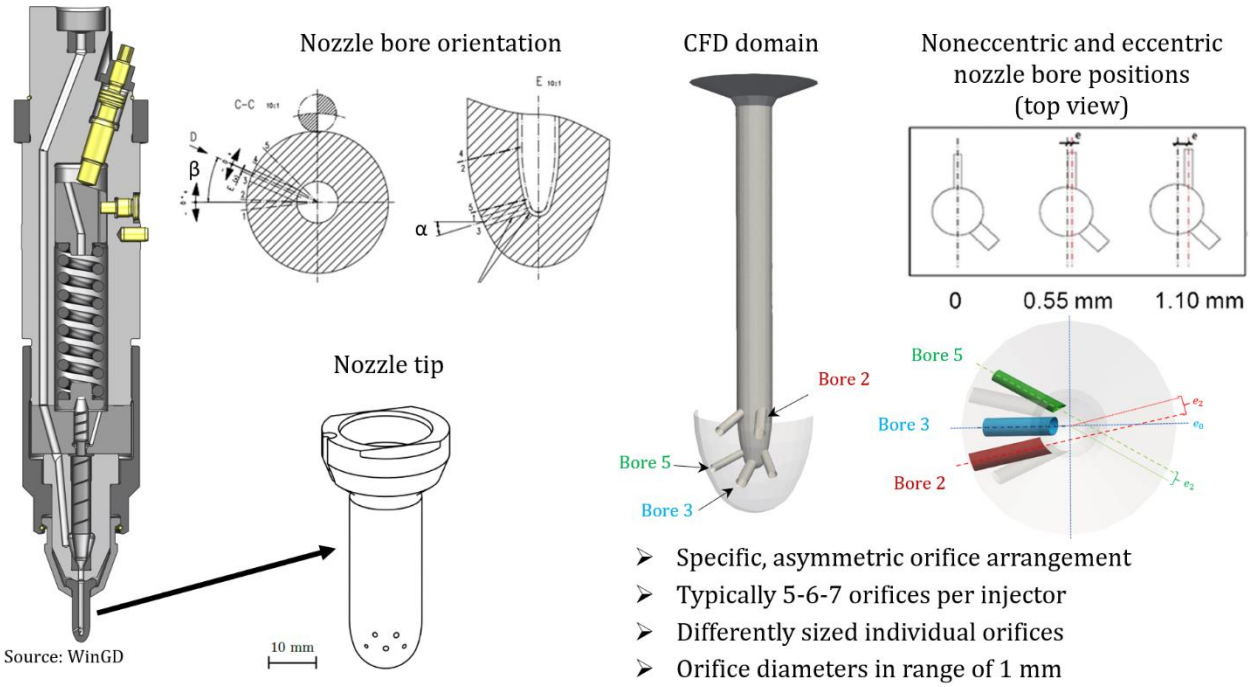

Figure 44 - Standard atomizer geometry (left) with a typical injector, CFD domain of a nozzle tip (middle), nozzle bore location in top view showing the eccentricity (bottom-right) and the simulated nozzle layouts (top-right).

Following extensive spray investigations in the SCC (3.4) contributed to the characterization and understanding of spray atomization and combustion, and enabled model validation for CFD studies. In this frame, Bolla *et al.* (2012) [167] investigated the performance of Lagrangian spray models by means of CFD simulations and compared their results against the SCC experiments. For orifice diameters representative of marine engines, Bolla *et al.* (2014) [168] analyzed the influence of diameter on the combustion of diesel sprays, both experimentally and computationally; their computations utilized Reynolds-Averaged Navier-Stokes (RANS) equations and validated spray breakup models. Li *et al.* (2019) [169] performed 2D simulations, where the blob injection model with the Kelvin-Helmholtz Rayleigh-Taylor (KH-RT) breakup

model was used and evaluated against experiments in a constant volume chamber (GUCCI) developed at Ghent University, representative of heavy-duty engines and medium-speed marine diesel engines. The study concluded that model modifications are necessary to account for the entire range of Reynolds (*Re*) and Weber (*We*) numbers characterizing marine engine sprays.

To account for the wide variation of thermophysical properties of different qualities of marine heavy fuel oil (HFO) used in large marine engines, Kontoulis *et al*. (2018) [170] developed an integrated model for calculating HFO thermophysical properties. The model was used in detailed CFD calculations of non-reactive and reactive spray flow in the SCC, utilizing the cascade atomization and drop breakup (CAB) model and a new ignition model accounting for HFO aromaticity. Results were presented in Kontoulis *et al.* (2019) [171] and included favourable comparisons with experiments in the SCC.

With respect to the effects of nozzle geometry on spray development, Hensel *et al*. (2012) [172] performed the first in-nozzle flow and primary breakup CFD simulations in large marine engine injectors. They showed that the spray structure and development are highly asymmetrical, with the asymmetry depending on the nozzle geometry, location of the orifice, and upstream flow conditions.

Following previous studies on marine diesel engine sprays, the present chapter aims at a detailed characterization of asymmetric nonevaporating sprays pertinent to large two-stroke marine diesel engine applications, using high-fidelity CFD simulations. The in-nozzle flow was calculated, and large eddy simulation (LES) approach was used to simulate spray primary breakup.

4.2 Computational approach

In studying the dynamics of marine diesel engine sprays, it is essential to account for the dynamics of flow within the injector, which causes the spray asymmetry. Thus, CFD simulations were employed as follows. Large eddy simulation was used to simulate the spray, using initial and inflow conditions derived from unsteady Reynolds-Averaged Navier-Stokes simulations of fuel flow inside the injector.

The atomizer geometries considered in this study corresponded to nozzles tested by Schmid (2013) [50], including a noneccentric and eccentric (0.55 and 1.10 mm) nozzle geometries. Eccentricity was quantified in terms of a normalized value, $e^* = e/(\frac{D-d}{2})$ where e is the distance from the orifice axis to the bore axis, '*D*' and '*d*' are the diameters of the bore and nozzle, respectively. To eliminate interference effects between the individual spray jets, injection from a single hole was considered. **Figure 45** presents information on the injector and geometry of the computational model and includes the injector arrangement used in experiments in the SCC (Schmid *et al*. (2013) [50]). **Figure 45** illustrates one noneccentric and two eccentric nozzle configurations.

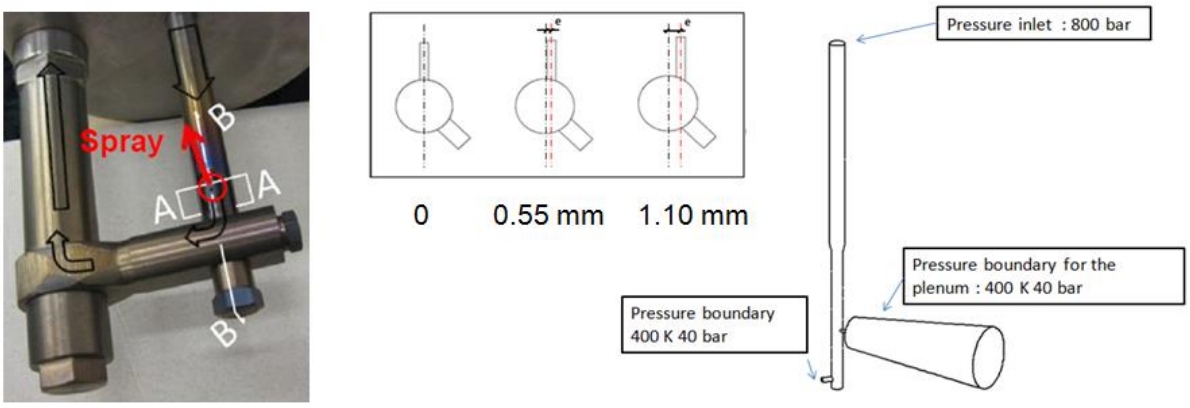

Figure 45 - Representations of injector, including the setup used in the SCC (left), nozzle layouts (middle), and the present computational model (right).

4.3 In-nozzle flow

The STAR-CD CFD code was used as the main platform for developing, performing and analyzing the simulations of the present study. The computational domain of the CFD simulations consisted of the atomizer tip needle; the nozzle bore, with a diameter of 0.75 mm and a length of 4-5 mm, and the plenum, with a length of 25 mm. The domain extended up to the bypass hole, with a diameter that accounted for the total area of the other four nozzle orifices of the actual injector (**Figure 45**). The determination of fuel properties was based on an n-dodecane fuel model; an entering fuel temperature of 333 K (60 °C) was considered, in accordance with experiments. The inlet boundary condition was 800 bar (8×10^7 Pa) at the needle inlet section. Calculation of spray development within the plenum considered a nonevaporating spray and a constant density of air, corresponding to a pressure of 40 bar (4×10^6 Pa) and a temperature of 400 K (127 °C); these values also were implemented as boundary conditions at the plenum and bypass hole boundaries. The Reynolds number at the nozzle bore outlet, based on mean velocity, and bore diameter, was estimated to be 1.35×10^5.

Structured grids were generated with the commercial software Ansys ICEM CFD v.16, containing approximately 1.2 million cells. These calculations were carried out with the volume of fluid (VOF) method [106] and a high-Reynolds number k-ε turbulence model (El Tahry (1983) [173]). Boundary conditions regarding turbulence parameters were determined after testing several values for turbulence intensity and lengthscale. The solution method utilized a velocity-pressure coupling based on the semi-implicit method for the pressure-linked equations (SIMPLE) method. The three-time-level implicit Euler central differencing scheme was applied. In URANS simulations, the time step was fixed to a value of 10^{-5} s, corresponding to values of the Courant [Courant-Friedrich-Lewy (CFL)] number in the range of 0-1. Each calculation was integrated in time until a converged solution was reached.

4.4 Spray primary breakup

Because the LES demands extensive computational resources, the nozzle geometry was simplified such that only a part of the nozzle bore was kept, and the plenum was shortened, extending up to 20 times the nozzle bore diameter (15 mm). The aforementioned URANS results were used to initialize the flow field for VOF-LES calculations. A cell layer of the URANS grid located in the

nozzle bore was attached to the LES grid, in which the flow properties of the cells were used as an inlet boundary condition for the LES. The primary breakup study used the Germano and Lilly dynamic-Smagorinsky subgrid-scale (SGS) turbulence model (Germano *et al*. (1996) [60]; Lilly (1992) [65]), in which, in addition to the low-pass filter (at the level of the numerical grid), a second spatial filter (the test filter), was applied (Scotti *et al*. (1997) [68]). The model coefficient was determined dynamically, and therefore it changed in time and space to account for the local state of turbulence.

In the present LES studies, the grid spacing in the order of the Taylor microscale, properly estimated, was utilized. The Taylor microscale characterizes scales in-between the Kolmogorov and the integral lengthscales see in **Figure 26**.

4.4.1 Grid spacing estimation inside the nozzle bore

Based on previously performed URANS calculation results, the turbulence kinetic energy and dissipation rate were calculated. In this study, the Taylor microscale (Equation (*14*)) was used to determine the numerical grid spacing suitable for LES. The nozzle bore characteristics of different layouts are summarized in **Table 3**. LES test grids were generated based on these values. The grid spacing for a LES based on the Taylor microscale would become over-resolved at high Reynolds number values; thus, a low limit on the filter scale (grid size) $\Delta = max(\lambda_{RM}, L_{RM}/10)$ is recommended. The calculated values of Taylor microscale (λ_{RM}), integral lengthscale, (L_{RM}) and the corresponding minimum grid spacing (Δ) are reported in **Table 3** for the different nozzles of the present study.

Table 3 - Estimates of turbulent scales, and grid spacing and time step values for LES.

Geometry	λ_{RM} [mm]	L_{RM} [mm]	Δ [mm]	ΔT Time step [s]
Ecc. 0.55 mm	1.87E-03	1.07E-02	1.87E-03	4.15E-09
Ecc. 1.10 mm	1.86E-03	1.17E-02	1.86E-03	3.83E-09
Noneccentric	2.01E-03	1.34E-02	2.01E-03	4.61E-09

Test grids using the 0.55 mm eccentric nozzle

Block-structures grids were generated using ICEM CFD with different grid spacings. An example of the geometry blocking, and the grid structure are presented in **Figure 46**. The cell quality exceeds the value of 0.4 for all test grids using the ICEM CFD mesh quality criteria (see **Table 4**).

Table 4 - Summary of the fine test grid quality for the 0.55 mm eccentric nozzle case

Range of quality	Ratio of max cell number [%]
0.95-1	48.14
0.9-0.95	24.63
0.85-0.9	11.19
0.8-0.85	6.76

0.7-0.8	7.85
0.6-0.7	1.3
0.5-0.6	0.1
0.4-0.5	0.003
0.4-0	0

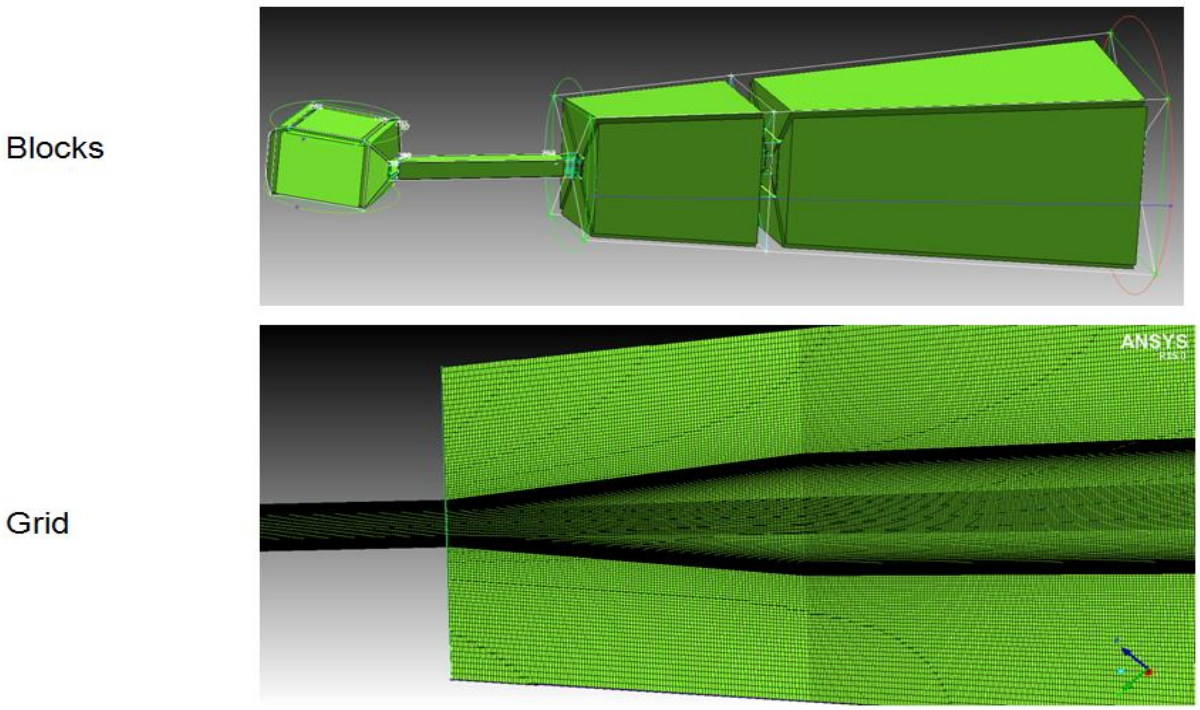

Figure 46 - Block structure and grid spacing inside the test volume.

The summary of the utilized test grids can be found in **Table 5**. The very fine grid consisted of approximately 14 million cells, the fine grid 10 million cells, the coarser grid 7.5 million cells, and the coarsest grid used 5.5 million cells, respectively.

Table 5 - Summary of the test grid sizes.

Test grid for 0.55 eccentric nozzle	Very fine grid	Fine grid	Coarser grid	Coarsest grid
Grid size	13.894.680	9.968.856	7.360.096	5.454.544
Grid refinement parameter [%]	1	≈ 0.71	≈ 0.53	≈ 0.39

4.5 Grid quality verification

In the LES, the discretization errors and the magnitude of SGS stresses increase with the size of computational cells; selecting a proper grid density is thus crucial for obtaining reliable results. In the LES, the mesh behaves like an implicit filter. In the case of the dynamic eddy viscosity model, a second filter is applied, contributing to the overall accuracy of simulations. Spatial resolution studies can be used to converge to a proper mesh for LES. According to Pope [52], a simple quality indicator, the turbulence resolution parameter (M), can be used to characterize grid quality:

Turbulence resolution parameter (M)

$$M = \frac{\langle k(x,t) \rangle}{\langle K(x,t) \rangle + \langle k(x,t) \rangle} \quad (61)$$

In the above relation, the turbulence resolution parameter *(M)* is the ratio of the averaged modeled SGS turbulent kinetic energy, $< k(x,t) >$, and the total averaged kinetic energy; $K(x,t)$ is the instantaneous resolved turbulent kinetic energy. Here, $M = 0$ corresponds to DNS, while $M = 1$ corresponds to RANS simulations, where all turbulent scales are modeled, and not resolved. For LES studies, Pope's recommended value for the turbulence resolution parameter is $M \leq 0.2$, which means that at least 80% of the turbulent kinetic energy must be effectively resolved.

4.6 Numerical results and discussion

4.6.1 URANS in-nozzle flow simulations

a. Definition of the inlet Turbulence Intensity (TI)

In a transient flow simulation, the initial and boundary conditions could have crucial effects on the development of the flow field. Therefore, a sensitivity analysis was performed to explore the influence of these simulation parameters. In these investigations, the middle eccentric nozzle geometry was included. As a first step, the main bore was assumed as a turbulent pipe flow, and the flow velocity was estimated. In the next step, the proper Reynolds number was calculated and used to determine the Turbulent Intensity value on the inlet.

Turbulence Intensity

$$TI = 0.16 \cdot Re_{hidr}^{-1/8} = 0.035 \quad (62)$$

The lengthscale of the inlet turbulence was estimated by using the hydraulic diameter.

Lengthscale

$$l = 0.07 \cdot D = 0.0014m \quad (63)$$

The influence of Turbulent Intensity on the inlet was analyzed by using 3.5%, 5%, and 10% as *TI* on the inlet, respectively. **Figure 47** shows the results of this analysis by depicting the velocity magnitude distributions in plane cuts at different locations inside the nozzle. Here, local maximum and minimum velocity magnitude values are also presented. Moreover, as an indicator of the velocity magnitude distribution, the nondimensional velocity uniformity index (Equation *(64)*) was calculated, based on the work of Weltens *et al*. (1993) [174].

Velocity Uniformity Index

$$U_i = \left[1 - \frac{1}{2n} \sum_{i=1}^{n} \frac{\sqrt{(u_z - \overline{U_z})^2}}{\overline{U_z}}\right] \cdot 100 \quad (64)$$

Based on these results, substantial influence of the inlet *TI* was not realized.

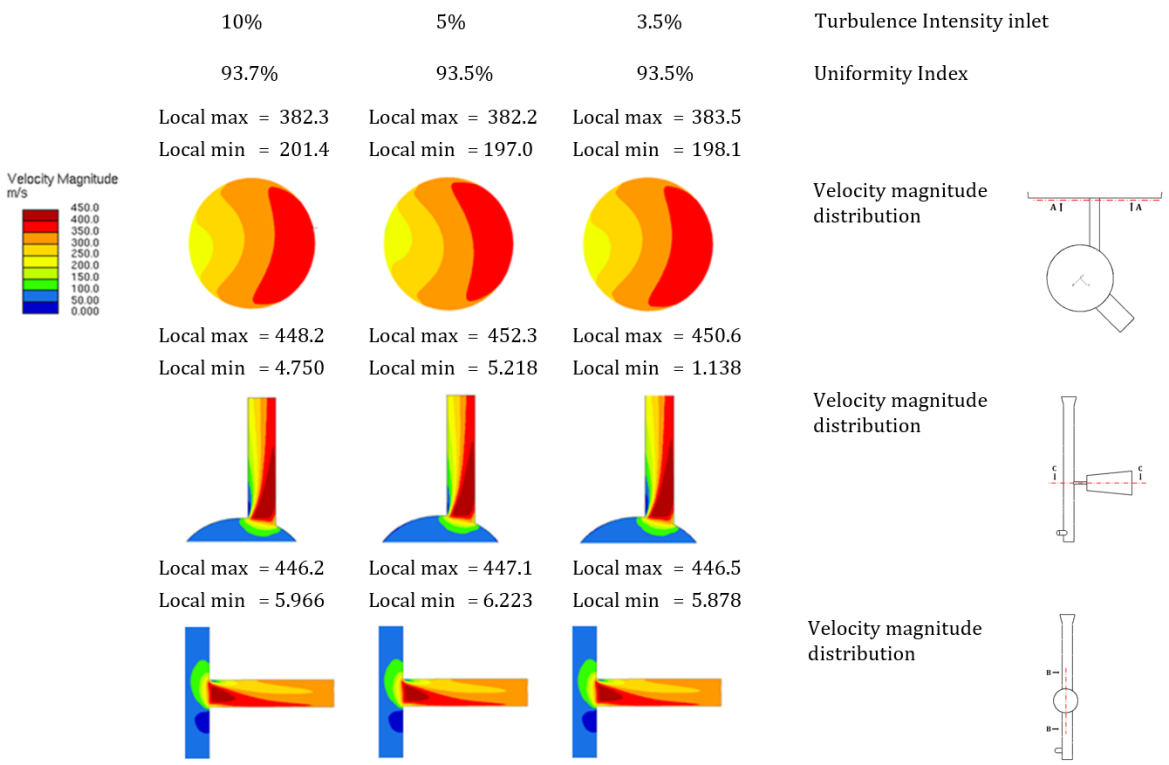

Figure 47- Influence of inlet TI on the velocity magnitude distribution in the nozzle bore for the 0.55 mm eccentric nozzle. Top row: cross-section at the nozzle bore exit; middle row: horizontal plane cut 'C-C' in the nozzle bore, and bottom row: vertical plane cut 'B-B' in the middle of the nozzle bore; t = 0.01s.

b. <u>Influence of equation of state</u>

In the next step, different models were used to calculate the equation of state in order to reveal their influence on the flow field. Here, the incompressible air model, the air ideal gas model, and the real gas model were considered. Results of the velocity magnitude distributions located in a plane cut located before the nozzle bore exit are shown in (**Figure 48**), suggesting a clear dependency of the flow field on the gas model used. The maximum velocity magnitude values decrease with the higher air density applied in the plenum.

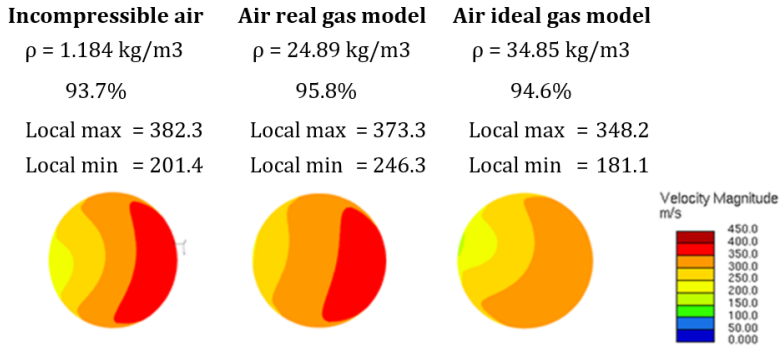

Figure 48 - Velocity magnitude distribution as function of the chamber air density, presented in cross-section before the nozzle bore exit ('A-A' in Figure 44) using the 0.55 mm eccentric nozzle; t = 0.01s.

c. Time discretization experiment

The influence of time discretization on the results was considered calculating three different cases, with either explicitly or implicitly defined time step. In the implicit case, the time step was varying while the CFD number was kept below 1. In the explicit cases, two different time steps were fixed. It was found, that in those cases, where the explicit time discretization scheme was used, the results differed significantly (**Figure 49**). The higher time step case resulted in a larger recirculation zone at the nozzle bore inlet with a lower velocity uniformity index at the nozzle bore outlet. Results of using the implicit time discretization and the explicit with lower time step show good agreement. Regarding computational costs, the implicit time discretization was the most expensive.

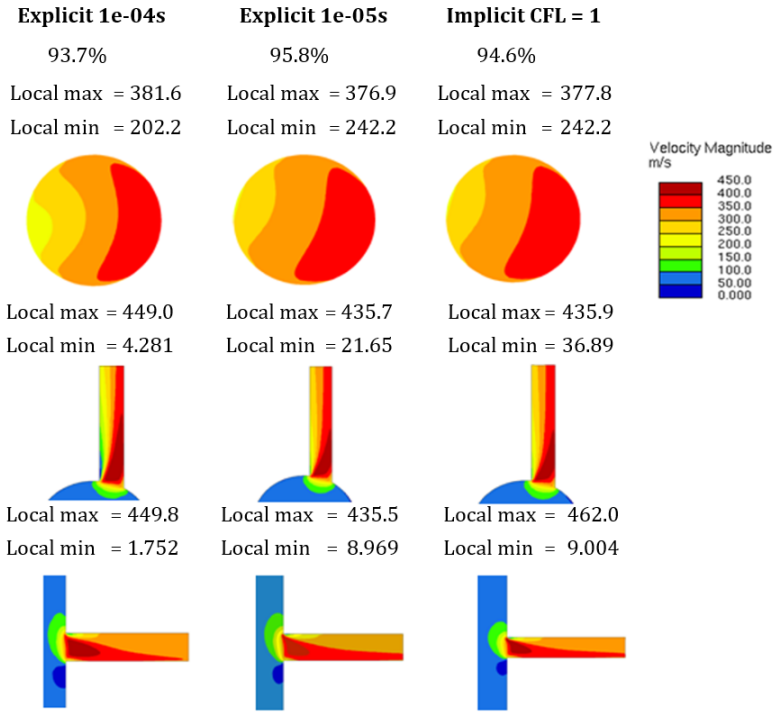

Figure 49 – Influence of time discretization on the velocity magnitude distributions inside the nozzle bore using the 0.55 mm eccentric nozzle. Top row: cross-section at the nozzle bore outlet ('A-A' in Figure 44); horizontal plane cut ('C-C' in Figure 44), and vertical plane cut ('B-B' in Figure 44) inside the nozzle bore; t = 0.01s.

d. Final numerical setup and predicted flow field of the nozzle layouts

Table 6 summarizes the numerical setup used to calculate the in-nozzle flow for all atomizer layouts. The high-Reynolds number k-ε turbulence model was chosen with the appropriate values defined based on the corresponding literature. This turbulence model is especially suitable for high-velocity injection applications. The real gas model was used as equation of state, the Turbulence Intensity on the inlet was set to 3.5%, and the Turbulence Lengthscale value was set according to Equation *(63)*. The time step was defined explicitly, keeping the CFL number around 1. The velocity-pressure field coupling was calculated by using the Semi-Implicit Method for Pressure Linked Equations (SIMPLE) [175].

Table 6 - RANS simulation setup.

Turbulence model	high-Reynolds k-ε
Turbulence Intensity inlet [%]	3.5
Turbulence lengthscale inlet [m]	0.0014
Air density in plenum [kg/m3]	24.89
Time step [s]	0.00001
Pressure-velocity coupling	SIMPLE
CFL number	≈ 0-1

Figure 50 depicts the obtained normalized velocity magnitude distributions in three different plane cuts for the three nozzle layouts. The influence of the eccentric geometry can be identified readily. The plane cut A-A is a cross-section at the position of the last cell layer of the nozzle bore, just upstream of the orifice exit. In the eccentric layouts, the velocity magnitude is higher on the right side of the nozzle than on the left side of the nozzle bore. The local maximum values of velocity magnitude were very close to each other, with the local minimum value highest in the noneccentric nozzle case, and significantly lower in the case of the most eccentric nozzle configuration. The same observations regarding the velocity distribution can be made for the horizontal plane cut B-B and the vertical plane cut C-C.

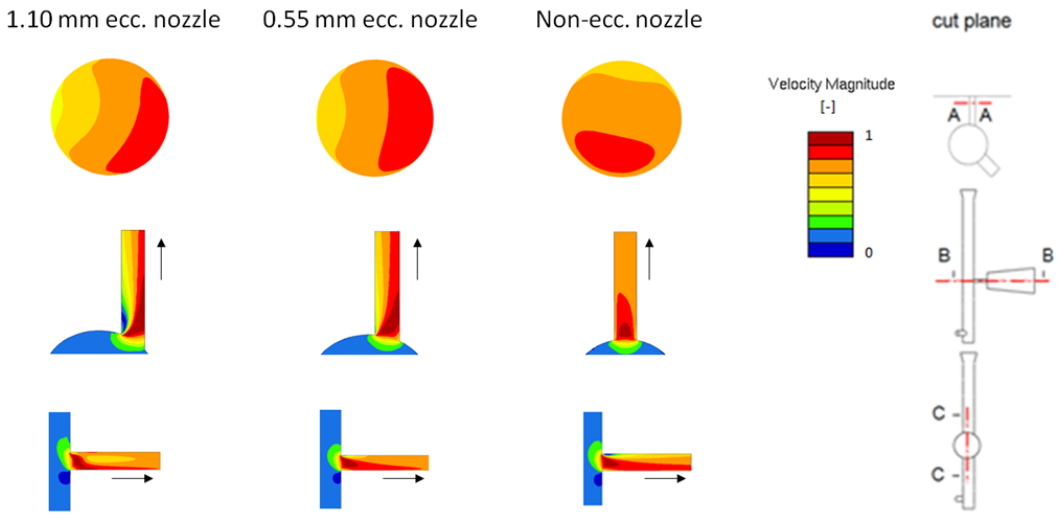

Figure 50 - Distributions of normalized velocity magnitude obtained from RANS simulations.

Although on the side of eccentricity the flow was characterized by the presence of remarkably high velocity values, on the left side of the nozzle bore, inlet velocities were lower. Thus, the sudden change in geometry caused a significant decrease in velocity on the left side of the nozzle bore inlet. The velocity distributions of **Figure 50** suggest the possibility of the existence of a cavitation zone, especially for the nozzle with 1.10 mm eccentricity. In summary, the URANS simulations showed that an eccentric nozzle bore results in an asymmetric velocity distribution at the nozzle outlet. The asymmetry, and its effects, can be analyzed further with LES.

With respect to computational cost, it is noted that typically an in-nozzle URANS simulation has required approximately 2.5 days using 36 cores of a parallel cluster.

4.6.2 LES results

The liquid fuel jet exiting the nozzle is characterized by the presence of disturbances on its free surface, initiated by turbulence in the flow within the orifice. Disturbances are amplified due to the action of aerodynamic forces from the surrounding air, which are resisted by surface tension forces. Consequently, the liquid jet undergoes the primary breakup, mainly disintegrating into large droplets.

Figure 51 presents isocontours of liquid fuel volume fraction at the horizontal plane cut (**Figure 50**, Plane cut B-B) of the plenum, corresponding to a midplane of the nozzle bore, for the nozzle with 0.4 eccentricity, for grids of different density (**Table 5**). These visualizations refer to a time t = 0.2 ms after the LES restart from a URANS simulation. For a large two-stroke engine operating at 100 RPM, this time corresponds to 0.12° of engine crank angle. A good agreement between the results of the different grids was found. For the very fine grid, a wider structure of the jet was identified, with finer structures, and a more intense breakup of the liquid core. The left side of the jet, corresponding to lower velocities at the nozzle exit, was characterized by a stronger disintegration, leading to an asymmetric spray structure. Although the fine and very fine grids resulted in a similar structure of spray, the details of this structure were not predicted by the lower-resolution grids, in particular the wrinkling in the left side of the flow domain. In all cases, the spray jet was deflected toward the left side of the plenum.

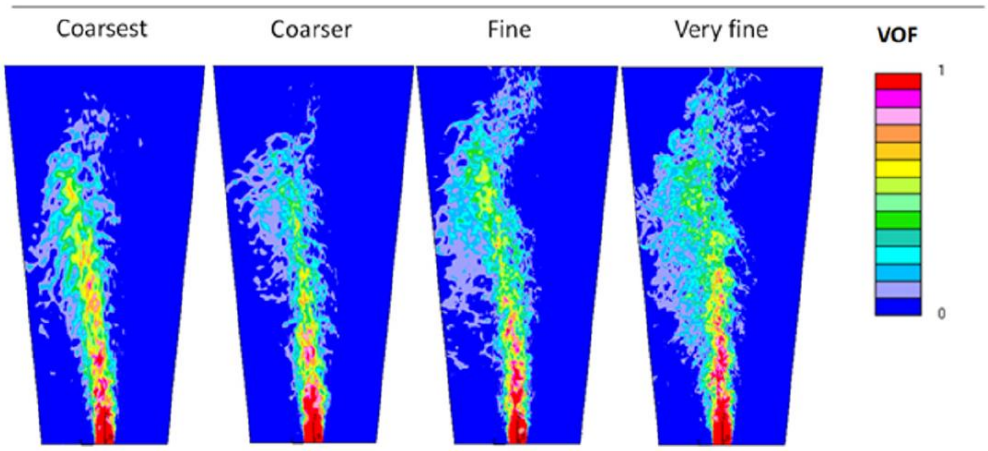

Figure 51 - Instantaneous distribution of liquid fuel volume fraction in the plenum (horizontal plane cut B-B of Figure 50) for the nozzle with an eccentricity of 0.55 mm, based on LES.

Figure 52 presents the spray structure in terms of the liquid volume fraction at a vertical cross-section (**Figure 50**, Plane cut C-C), for grids of different density, for the nozzle with an eccentricity of 0.55 mm. The time instant is the same as that of **Figure 51**. The low-resolution simulations predicted a more intense disintegration of the spray, and they did not capture the finer structures present, including smaller droplets. In all cases, the results showed a slight upward deflection of the spray structure.

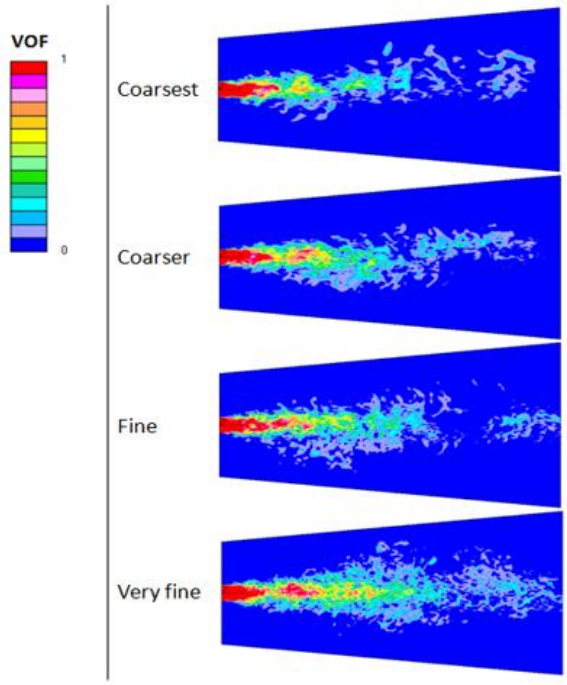

Figure 52 - Instantaneous distribution of liquid fuel volume fraction in the plenum (vertical plane cut C-C of Figure 50) for the nozzle with eccentricity of 0.55mm, based on LES.

The aforementioned tests illustrate the importance of having sufficient spatial resolution in LES of spray jets for resolving fine flow structures. Based on the results discussed, it was decided to use the very fine grid in the LES of all three atomizers.

4.6.3 Grid quality verification

For LES studies, Pope's recommended value for the turbulence resolution parameter is $M \leq 0.2$, which means that at least 80% of the turbulent kinetic energy should be resolved effectively. Information related to this criterion in the present simulation for the nozzle with an eccentricity of 0.55 mm is provided in **Table 7**. Time steps ranging from 10^{-08} to 10^{-07} s were tested and yielded comparable results.

Table 7 - Number of cells not satisfying the criterion $M \leq 0.2$ [29] in the present LES calculations for the 0.55 mm eccentric nozzle.

		Nozzle bore + plenum			
	CAD	**Very fine grid**	**Fine grid**	**Coarser grid**	**Coarsest grid**
cell number		13.540.884	6.701.760	4.708.352	3.144.960
cells	0.09	12	399	269	1465
cells	0.10	9	100	236	1012
cells	0.11	5	23	139	619
cells	0.12	3	8	118	404

4.6.4 Comparison of nozzle layouts

Figure 53 presents instantaneous distributions of normalized velocity inside the nozzle bore for the three different nozzle geometries calculated with LES. These velocity fields were compared with the results obtained from the URANS calculations (**Figure 50**). The comparison suggests that URANS simulations do predict the qualitative velocity distribution that LES does; all sections presented supported this. In the LES results, local absolute values can be higher than those of URANS simulation. The discrepancy can be attributed to the improved resolution of the boundary-layer in the case of LES, as well as the presence of instantaneous fluctuations in the resolved LES field.

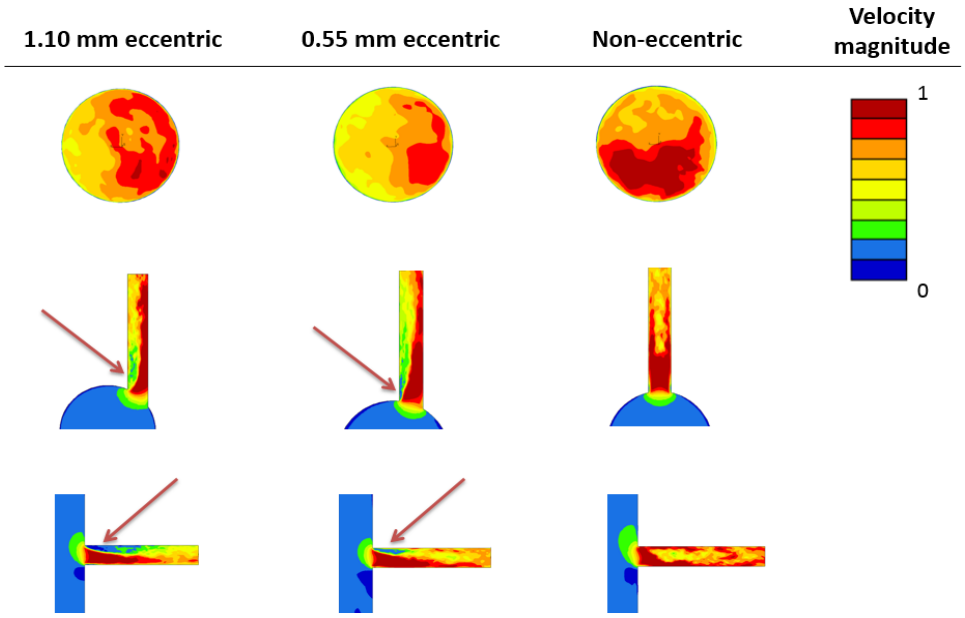

Figure 53 - Color-coded contours of normalized instantaneous velocity magnitude for different nozzle layouts, based on LES.

The LES results suggest that, for eccentric nozzles, the sudden change in the geometry at the nozzle bore inlet causes a significant decrease in velocity (**Figure 53**). Analysis of the pressure field indicated the possibility of the presence of a local cavitation zone in the areas marked by an arrow in **Figure 53**. The collapse of cavitation bubbles could lead to increased flow fluctuations, supporting a more intense jet breakup (Mitroglou *et al*. (20119 [176]).

Figure 54 illustrates the computed liquid fuel distributions (volume fractions) inside the plenum for a horizontal cross-section at the same time instant. Spray penetration length was higher for the noneccentric nozzle than for the eccentric nozzles. This also was associated with the decreased disintegration of the spray in the noneccentric nozzle. The spray deflection was maximal for the case of the highest geometric eccentricity (normalized value of 0.8); the spray of the noneccentric nozzle also was slightly deflected. For both eccentric nozzle layouts, a remarkably asymmetric and deflected spray was produced, with the deflection located on the side opposite to that of geometric eccentricity (i.e., on the left side). Asymmetry is associated with a wider spray structure, characterized by increased area and volume.

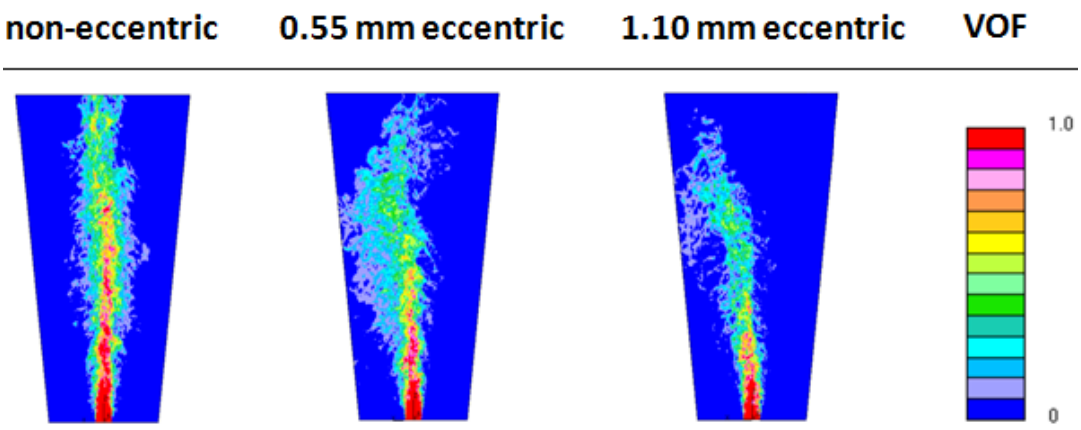

Figure 54 - Instantaneous distribution of liquid fuel volume fraction in the plenum (horizontal plane cut B-B of Figure 50) for the three nozzle configurations, based on LES.

The decay of the spray core started earlier for eccentric nozzles, possibly due to the increased turbulence at inflow, caused by the sudden change in geometry. As the injected fluid enters the plenum, surface waves are generated on the liquid core. Interestingly enough, it was found that spray wrinkling is asymmetric and faster on the lower-velocity side of the jet. Once ligaments and large drops are disintegrated from the liquid core, the aerodynamic forces have a more pronounced effect, with more drops, of smaller size, resulting from atomization.

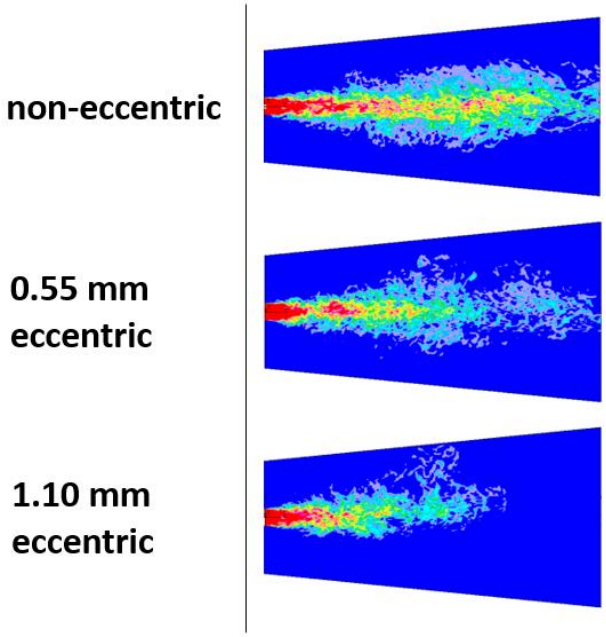

Figure 55 - Instantaneous distribution of liquid fuel volume fraction in the plenum (vertical plane cut C-C of Figure 50) for the three nozzle configurations, based on LES.

Figure 55 shows the visualization of the liquid phase in the vertical plane for the three nozzles considered, at the same time instant as that of **Figure 54**. For the noneccentric nozzle, the spray structure is that of a turbulent axisymmetric spray.

For the eccentric nozzles, as concluded from the visualization of the horizontal section, sprays were deflected onto the left side of the plenum, which corresponds to the lower velocities at the nozzle outlet. **Figure 55** illustrates the resulting asymmetry in terms of the upward deflection of the spray structure in the vertical plane.

Regarding computational cost, it is noted that an LES simulation using the very fine grid has required approximately 2.5 weeks using 36 cores of a parallel cluster.

4.7 Conclusions

A combination of URANS and LES simulations was performed for different large two-stroke marine Diesel engine atomizer geometries, including in-nozzle flow. The influence of initial and boundary conditions on the computed flow field was analyzed. A description of the generated grids and the importance of the proper resolution in LES were stated. Highly asymmetric spray behavior was experienced for the different nozzle layouts. The resulting spray structures were analyzed, and it was illustrated that the eccentric arrangement of the nozzle results in a deflection normal to the main spray direction. The deflection increased as a function of eccentricity. The present results showed that the spray is not just deflected in the spanwise direction, but it also deviates from its symmetry line upwards, in the radial direction.

5 CHAPTER: In-nozzle Flow Considering Cavitation

The present chapter includes results of experiments conducted by R. Balz in the SCC, which are reported in Balz *et al.* (2021) [177]. These experimental results were used to validate CFD simulations of in-nozzle cavitating flow, analyzed in the present chapter.

5.1 Introduction

Large two-stroke marine Diesel engines belong to the most efficient internal combustion engines existing and reach efficiencies over 55% [178]. To further decrease emissions and increase the overall efficiency, the understanding of the fuel injection plays a crucial role. Development strategies that can maintain highly efficient combustion while reducing pollutant formation require a more granular understanding of the mixture preparation which is the driving force of in-cylinder combustion.

Due to the large bore of two-stroke marine Diesel engines and a strong swirl motion of the charged air, multiple fuel injectors are used and arranged around the single exhaust valve. As a result, the typical three fuel injectors arranged by 120° have highly eccentrically and asymmetrically arranged nozzle bores. A typical nozzle tip that is mounted on the fuel injector is illustrated in **Figure 56**. Note the five-hole nozzle design which all face a similar direction. This particular atomizer layout and the large nozzle bore diameters limit the usability of research focused on small and medium-sized Diesel engines.

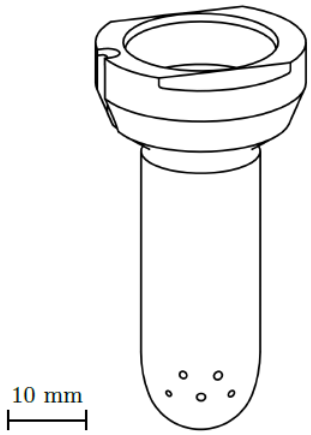

Figure 56 - Illustration of a standard nozzle tip for large two-stroke marine Diesel engine fuel injectors indicating the typically five-hole design of the nozzle bores. [Courtesy of WinGD]

Some of the specific issues that affect fuel injection in large marine Diesel engines were examined by experiments conducted in the constant-volume Spray and Combustion Chamber (SCC) at Winterthur Gas & Diesel Ltd. (WinGD) [179]. Investigations in the SCC have shown that the asymmetric and eccentric nozzle layout of large two-stroke marine Diesel engine fuel injectors have a considerable influence on spray formation [50,158]. Additionally, CFD simulations have shown that inhomogeneous fuel velocity profiles in the nozzle bore induced by geometric cavitation can lead to significant spray deflections, especially for eccentrically arranged nozzle bores [180,181].

5.2 Cavitation in marine Diesel engine injectors

As indicated in earlier chapters, in modern Diesel injectors, to enhance the aerodynamic breakup of the fuel spray and, to provide a sufficient level of fuel atomization, the injection is performed through nozzles of small diameters at high injection pressures. Under such flow conditions, cavitation becomes an essential feature of the flow. Therefore, control of the injection process requires understanding and reliable prediction of cavitation [182]. Thus, control of the injection process requires understanding and reliable prediction of cavitation.

Cavitation is the process of formation and consequent collapse of gaseous bubbles in a liquid under a local decrease in static pressure. Depending on the topology of the vapor structures in the flow, cavitation occurs in a form of traveling bubbles or vapor pockets, extending over a partial length of the nozzle bore (cloud cavitation and sheet cavitation), or supercavitation, when the vapor region extends over the entire length of the nozzle bore [183,184].

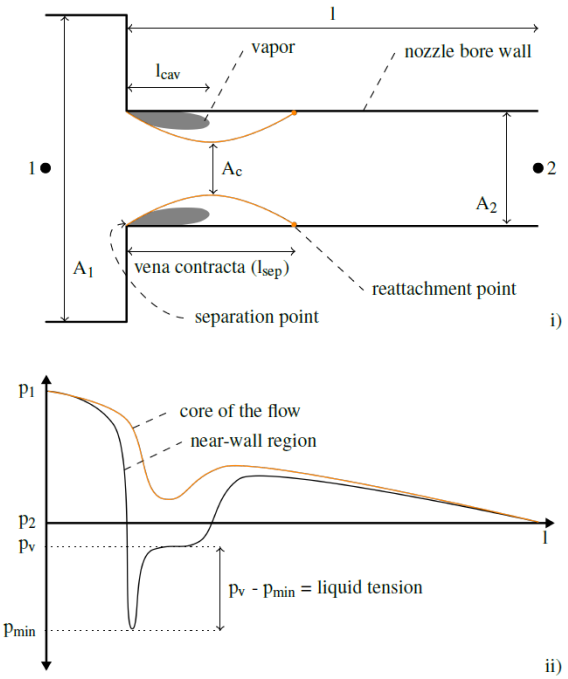

Figure 57 - Theoretical geometry induced cavitation i) and pressure variation ii) in an atomizer with the liquid flowing through the main bore (1) with diameter (A1) entering the nozzle bore with diameter (A2) and leaving at the nozzle bore exit, also called orifice (2) into the plenum. [Courtesy of R. Balz; R. Balz et al., 2020. Experimental and numerical investigation of cavitation in marine Diesel injectors, International Journal of Heat and Mass Transfer.]

In injectors, hydrodynamic cavitation occurs at high injection rates when the pressure drops below the critical level in the vena contracta region (**Figure 57**) inside the nozzle leading to vapor formation. If the pressure reduction is caused by a sudden change in the geometry of the stream, the flow tends to separate and form a vena contracta inside the nozzle bore; geometry-induced cavitation occurs. The contraction in the nozzle bore inlet reduces the cross-section area. This area reduction is accompanied by a velocity increase and a pressure depression in the throat of the nozzle. Furthermore, between the vena contracta and the nozzle bore inlet, a recirculation zone can be observed. In case the local pressure inside the nozzle throat drops below the vapor pressure of

the liquid, hydrodynamic cavitation happens. Pressure waves traveling through the fluid domain can cause pressure reduction leading to dynamically induced cavitation [182].

Cavitation is reported to improve the spray breakup processes [184-189], however other undesirable effects on the fuel injection performance may occur. Experiments have revealed that under certain conditions, cavitation can result in the formation of hydraulic flip flow which is not beneficial for atomization. Other undesirable effects of cavitation are associated with flow instabilities, excessive noise generation, and erosion, which can cause damage to injector nozzles [190].

The structure of cavitation flow in nozzles depends on the geometrical properties, fuel properties, and the pattern of the multiphase flow. The significant flow parameters are the Reynolds and cavitation numbers and geometrical resistance of the flow domain. In the case of nozzles with sharp entrances, without inlet radii, flow separation can occur which affects the flow field and the development of flow structures inside the nozzle bore. The presence and location of the recirculation zone at the sharp edges in high-Reynolds number flows (typical for fuel injection) determine the distribution of tensions and, therefore play a crucial role in the formation of hydrodynamic cavitation. Cavitation bubbles formed inside the nozzle can produce pressure fluctuations when collapsing in the high-pressure region downstream of the nozzle and as a result can enhance the spray disintegration. A cavitation number can be defined as an integral parameter of the flow, which relates the pressure drop (or dynamic head) to the local static pressures. The cavitation number (C_a) is defined as follows:

Cavitation number

$$Ca = \frac{p_1 - p_2}{p_2 - p_v} \cong \frac{\rho_f / 2 \cdot {v_m}^2}{p_2 - p_v} \tag{65}$$

where p_1 is the pressure upstream, p_2 is the pressure downstream at the outlet of the nozzle bore, p_v is the vapor pressure of the fuel and ρ_f is the fuel density. The velocity magnitude v_m is calculated at the nozzle bore exit (orifice) using ${v_m}^2 = {v_x}^2 + {v_y}^2 + {v_z}^2$ with the local velocity components v_x, v_y and v_z [193]. Studies revealed that the cavitation number implies the extent of certain vapor volumes generated inside the nozzle bore [194,193]. However, since (C_a) is relying merely on the pressure difference, it makes it an insufficient criterion to describe the development of cavitation as fuel injection can occur at completely different pressure levels and the geometrical properties of the nozzle are disregarded. Hence, to characterize the flow inside the nozzle, the dimensionless discharge coefficient providing the ratio between actual and theoretical discharge through the nozzle bore is used:

Discharge coefficient

$$C_d = \frac{\dot{m}_{real}}{\dot{m}_{ideal}} \tag{66}$$

where $\dot{m}_{ideal}$ is the theoretical mass flow based on Bernoulli's equation and $\dot{m}_{real}$ the actual, entropy bounded, mass flow through the atomizer.

5.3 Experimental methods

5.3.1 Optically transparent nozzles

Optically transparent nozzles were used to visualize the internal flow to improve the understanding of how the in-nozzle flow affects the primary breakup and the combustion process in the internal combustion engine. However, the research focus is limited to engines in the low and medium duty cycle. To deepen the understanding of the fuel injection process for large marine Diesel engines, a new transparent nozzle holder was designed that allows applying optical measurement techniques to real-size nozzles of large two-stroke marine Diesel engines.

Several different experimental methods were applied to study injector in-nozzle flow: Hydraulic characterization using flow rate and impingement measurements, investigations using optically transparent nozzles. While hydraulic characterization does not provide spatial cavitation information in the nozzle and usually disrupts the spray due to the impingement measurements, it is the standard for quality control in commercially manufactured nozzles [195]. Ionizing radiation investigations use nozzles made of materials with low photon or particle interaction and the fuel is usually enhanced with a supplement to enhance contrast. The photon flux of X-ray tubes is by far too low to acquire time-resolved images and hence synchrotron light sources fed by particle accelerators are used to investigate the in-nozzle flow [196-198].

Investigations using optically transparent nozzles with identical or scaled geometries allow us to visualize cavitation, spatially, and temporally using standard light sources and high-speed cameras. The optically transparent materials must have similar refractive indices as the fuel used to prevent optical distortion at the nozzle bore geometries. This leads to challenges as transparent materials with similar refractive indices as Diesel fuel are brittle and have low material strength. Falgout and Linne (2015) [199] compared past studies with transparent nozzles regarding injection pressure and materials used. While the thermoplastic polymethyl methacrylate (PMMA) and quartz glass (SiO_2) have similar refractive indices as Diesel fuel and therefore allow in-nozzle flow visualization, the much stronger sapphire is not feasible due to the previously mentioned optical distortions at the interface between Diesel and sapphire. Most previous work with transparent nozzles uses significantly lower fuel injection pressures to cope with the limited strength of the optically transparent materials. The work of Blessing *et al*. (2003) [200] showed very impressive results with non-scaled PMMA nozzles and injection pressures of up to 80 MPa, but the authors did not provide design specifications. Falgout and Linne (2015) [199,201] developed a transparent nozzle holder using PMMA and applying clamping forces on the material to decrease its failure probability at higher injection pressures. However, the design was scaled by 50% compared to large marine two-stroke Diesel engine injectors, as the available experimental facilities were limited in size for the relatively large spray emerging from the nozzle bore.

A transparent nozzle holder (TNH) to be mounted on fuel injectors proofed to cope with fuel pressures in the ranges of large marine two-stroke Diesel engines (50 to 80 MPa rail pressure) for a limited number of injections. The design uses transparent nozzles made from PMMA. The thermoplastic has a similar optical refractive index of Diesel (1.49 and 1.46 to 1.52 depending on the Diesel mixture, respectively) that allows visualization of the in-nozzle flow without optical distortions due to the round shape of the nozzle bore that otherwise would act as a cylindrical lens.

The transparent nozzle is mounted onto the TNH with rigid metallic clamps that apply an external force onto the nozzle to suppress the expansion of PMMA. For the optically interesting axis, polished sapphire bricks were used between the metal clamps and the PMMA nozzle to guarantee maximal optical access while still applying a clamping force on the plastic. Sapphire was used for its excellent optical and mechanical properties and as the contact surface between PMMA and sapphire is parallel, there are no significant optical distortions. Further details about the design of the TNH can be found in [199,201]. However, as the design was geometrically scaled (1:2), a new TNH was developed based on the existing design to fit the atomizers of fuel injectors used in the large marine two-stroke Diesel engines of WinGD.

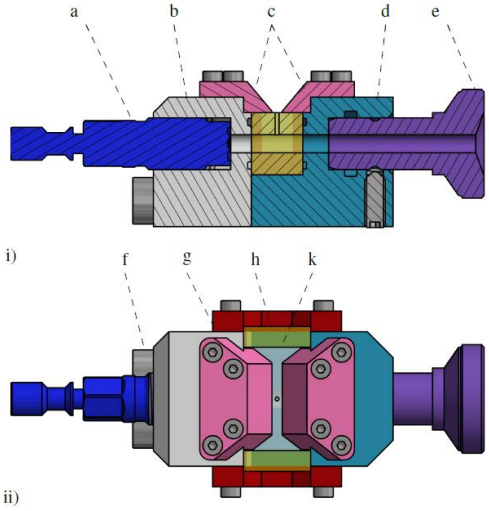

Figure 58- Sectional view (i) and top view (ii) illustration of the new transparent nozzle holder with pressure sensor (a), sensor-body (b), top-clamps (c), main-body (d), injector mount (e), fitting bolt (f) side-clamp (g), sapphire brick (h) and transparent nozzle (k). [Courtesy of R. Balz; R. Balz et al., 2020. Experimental and numerical investigation of cavitation in marine Diesel injectors, International Journal of Heat and Mass Transfer.]

Here, the transparent nozzles used are single-hole designs to simplify the measurements and CFD validation. The typical multi-hole nozzle design utilized in large marine Diesel engines would disturb a line-of-sight optical measurement technique, as the light would be scattered away from the area of interest due to the close distances of the individual nozzle bores and the fact that they are not on one single plane to be visualized. Additionally, single-hole geometries also allow better control of rounding the inlet of the nozzle bore by hydro-erosive grinding and reduce computational expenses for CFD cavitation simulations.

Figure 58 illustrates the newly developed TNH. The entire setup can be mounted on a typical WinGD injector by using the injector mount (e). The main bore leads the fuel to the PMMA nozzle (k) and the pressure sensor (a). The metallic top-clamps (c) apply force directly to the PMMA nozzle while the side-clamps (g) provide stability via two polished sapphire bricks (h) to maintain optical access. The PMMA nozzle is also fixed by using two fitting bolts (f) that connect the sensor-body (b) and the main-body (d). As a result, the newly developed design allows the utilization of forces on all surfaces of the cuboid body of the PMMA nozzle applying rail pressures up to 80 MPa with low failure probabilities. The application of manufacturing tolerances eliminates the difficulty of varying applied torques on the screws which can change with the

friction of threads in contact with Diesel fuel. The depicted transparent nozzle (k) is a single-hole, perpendicular design with a nozzle bore diameter of 0.75 mm. The PMMA nozzle design can be altered cost-efficiently, as manufacturing prices are low due to the material's simple machinability. The new TNH design also allows changes in the nozzle layout, thus providing the possibility of using multiple single-hole nozzle designs with various nozzle bore geometrical properties. O-rings made from NBR with a hardness of 90 Shore-A ensure the proper sealing while the corresponding grooves are designed according to ISO-3601.

The commercial finite element analysis (FEA) software Ansys Workbench 16.1 was used to develop the new TNH design, especially with regards to the applied forces on the PMMA nozzle. Multi-body, static-structural calculations were performed with bonded, no-separation, and friction contact models together with the different materials (stainless steel 1.4301, sapphire, and cast PMMA). The maximal occurring stress is at the sharp corner between the main bore and the nozzle bore. The rounding of these sharp edges by applying hydro-erosive grinding further reduces the maximal stresses in the nozzle by removing the stress concentration, and therefore decreases the failure probability significantly. The manufacturing tolerances of the TNH parts were evaluated using the von Mises equivalence stresses and deformation results of the FEA. The used piezo-resistive absolute pressure sensor from Kistler (type 4067C2000) has a natural frequency of over 200 kHz that allows dynamic acquisition of the fuel pressure in the main bore of the nozzles. In the new design, a pressure tap between the pressure sensor and the main bore of the nozzle was removed. This was done to eliminate acquisition frequency limitations due to Helmholtz-resonator effects within the long, thin tap that connects the main bore and the pressure sensor. The pressure sensor allows accurate data acquisition that is necessary to investigate cavitation behavior during the quasi-steady-state injection conditions. The pressure at the main bore must be known during the whole injection process to better understand cavitation fluctuations in the nozzle bore. The measured data has crucial importance as a boundary condition in CFD simulations since fuel injectors usually have significant pressure losses.

5.3.2 Optical imaging

The TNH is designed to visualize the in-nozzle flow using a line-of-sight optical measurement technique like Shadowgraph imaging, where a light source illuminates one side of the transparent nozzle and an imaging system is installed on the other side. A schematic of the optical setup is depicted in **Figure 59** where a schematic of the fuel injector (j) is shown with the mounted TNH (d). The dashed line indicates the optical axis. The setup used consisted of a Cavitar Cavilux Smart diode laser (i) emitting at a centre wavelength of 640~nm together with a Questar QM100 far-field microscope (b) and a Photron Fastcam SA5 CMOS high-speed camera (a). A diffuser plate (e) was installed in front of the TNH to guarantee a uniform background illumination. An additional 150~mm plano-convex spherical lens (f) was applied together with an optical fiber (h) and its matching collimator (g) to focus and concentrate the diode laser emission onto the diffuser plate in front of the TNH (d). A mirror (c) was used to protect the far-field microscope from possible debris in case of material failure. The use of a short-pulsed light source with short pulse lengths is necessary to acquire sharp in-nozzle flow images under realistic fuel pressure conditions. This is due to motion blur that would occur with a constant light source because of the relatively long

exposure times in the range of microseconds compared to the fuel velocities of a few 100 m/s in the nozzle bore.

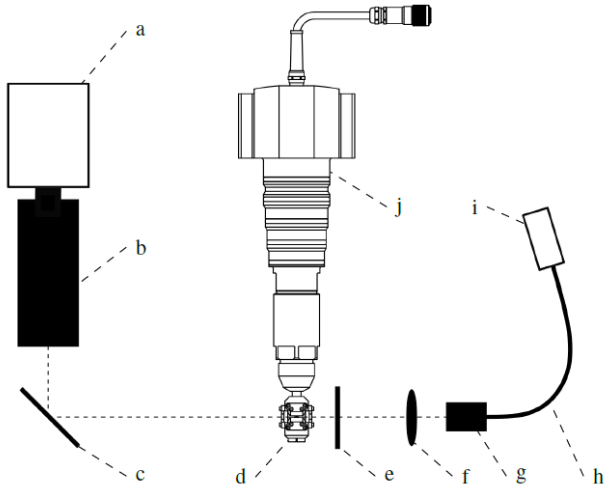

Figure 59 - Schematic of the optical setup used with high-speed camera (a), far-field microscope (b), mirror (c), transparent nozzle holder (TNH) (d), diffuser plate (e), focusing lens (f), collimator (g), optical fiber (h), diode laser (i) and injector (j). The dashed line represents the optical axis. Note that the spray chamber surrounding the TNH is not illustrated. [Courtesy of R. Balz; R. Balz et al., 2020. Experimental and numerical investigation of cavitation in marine Diesel injectors, International Journal of Heat and Mass Transfer].

5.3.3 Impingement measurements

To quantitatively characterize the different single-hole nozzle geometries, the spray momentum flux was measured using a calibrated piezo-electric force sensor from Kistler (type 9215a). The so-called impingement measurements are further described in [192] and use conservation of momentum based on the assumption that the spray impingement area is much smaller than that of the sensor. Hence, the momentum flux of the spray at the nozzle bore exit is identical to the force measured on the sensor.

To align the force sensor exactly on the nozzle bore axis, three different sensor holders were manufactured according to the different nozzle geometries and mounted directly on the two top clamps of the TNH to minimize the distance between the nozzle bore exit and the force sensor.

5.3.4 Test rig

The experiments were conducted in a constant-volume spray and combustion chamber at WinGD, where the geometry represents the combustion volume with the piston at the top dead centre of an RT-flex50 engine from WinGD's portfolio. The chamber operates under realistic engine loads regarding charge pressures, swirl motion, and temperatures. The chamber diameter is identical to the cylinder bore and measures 500mm. The fuel is pressurized using a standard common-rail system equipped with an injection control unit (ICU) as used on each cylinder of the RT-flex engines. The rail pressure was set to 50MPa, which represents a standard value at part load engine operation. Since only the in-nozzle flow was investigated for this work, the back pressure and gas temperature in the spray chamber were set to ambient conditions. Experiments have shown that the back pressure and fuel temperature play a less significant role for the in-nozzle flow cavitation

patterns when the pressure differences are large and the fuel temperatures less than 80°C [202-204]. The fuel used is a standard Diesel from Preem AB with the product code DMK1UA-SE, a density of 815.9kg/m3 (at 15°C), a viscosity of 2.112mm2/s (at 40°C) and a net heat of combustion of 43.16MJ/kg.

5.3.5 Nozzle geometries

Three different single-hole nozzle designs were chosen based on the realistic five-hole atomizer designs of large marine two-stroke Diesel engine injectors. **Figure 60** shows geometry projections of the three different nozzle types adapted for the TNH: isometric, side, and top views. The fuel flow enters the nozzle main bore from the top and the pressure sensor is mounted at the bottom side in the isometric projection (see **Figure 60** for reference).

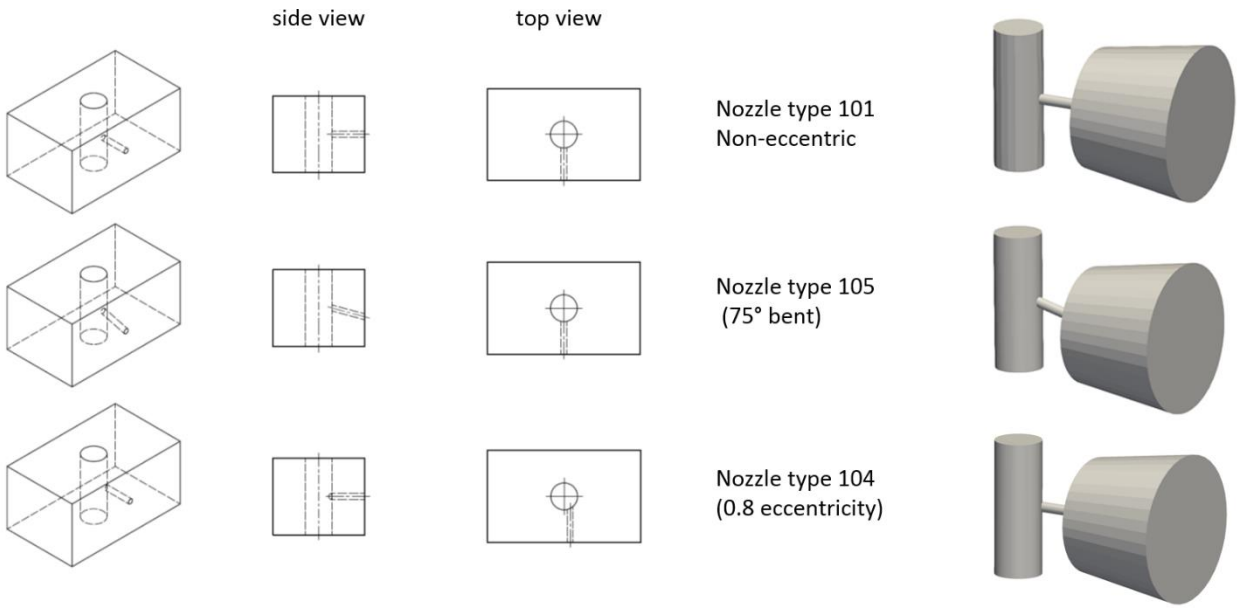

Figure 60 - Isometric, side, and top projection of the three different transparent nozzle types used. N101: centrically arranged 90° setup, N105: centrically arranged 75° setup and N104: eccentrically arranged 90° setup. The main bore diameter is 3.5mm and the nozzle bore diameter is 0.75mm. [Courtesy of R. Balz; R. Balz et al., 2020. Experimental and numerical investigation of cavitation in marine Diesel injectors, International Journal of Heat and Mass Transfer].

The nozzle N101 represents the simplest arrangement of the three designs, where the nozzle bore is located centrally with reference to the main bore and perpendicular to the main bore axis. The nozzle N105 has also a centrally arranged nozzle bore, but with an angle of 75° The nozzle N104 has a perpendicular angle as well, but the nozzle bore is 0.8mm and eccentrically arranged. The nozzle bore and main bore diameters are identical for all three nozzles and are 0.75mm and 3.5mm, respectively.

5.4 Numerical modeling

5.4.1 In-nozzle flow CFD simulations

Modeling turbulent cavitating flows is a challenging task because of the complexity of the phenomenon itself and the highly dynamic interaction between phases and non-equilibrium thermodynamic states. Recent numerical simulations have proven the applicability of CFD in

cavitating flow predictions, thus supporting experimental measurements and product development [205-208]. Most of the published numerical work is limited to small- and medium sized engine fuel injectors and due to large geometrical differences, only insufficiently useful for the validation and optimization of cavitation formation in large marine Diesel engine fuel injectors.

Several different models were developed for cavitation in nozzles. Giussani *et al*. (2020) [108] provide an extensive overview of numerical modeling approaches of cavitating flows in fuel injector nozzles. The available methodologies for simulating multiphase flows can be classified either according to the adaptation of the multiphase fluid modeling or according to the mass transfer mechanism assumed for cavitation. Concerning multiphase modeling, in Diesel fuel nozzles involving cavitation, the most common implementations are the homogeneous mixture models, the heterogeneous multi-fluid models, and the Lagrangian models.

In this study, the widely-applied sharp interface capturing method, Volume of Fluid (VOF) technique [108,116-210], was chosen to capture the liquid/gas interface. The model is similar to the homogeneous model, where a single momentum equation is calculated for all phases that interact using the VOF model. In this particular study, the VOF method was chosen to track the interface of different phases. High Resolution Interface Capturing (HRIC) [211] was applied in the VOF method to avoid artificial effects and, to minimize numerical diffusion and compressive character. VOF and HRIC governing equations can be found in [212].

5.4.2 Cavitation model

The numerical representation of cavitation and flash-boiling is an important area of research due to the difficulties of representing their physics by robust and accurate numerical methodologies. Schmidt *et al*. (2012) [109] and Giannadakis *et al.* (2008) [115] provide an extensive discussion on various models available. A widely utilized Eulerian approach to simulate cavitation is based on the Rayleigh-Plesset equation, which describes the growth and collapse of a bubble in a liquid assuming no slip between the two phases. In [213], Neroorkar *et al*. (2012) simulated the cavitation phenomenon based on the Homogeneous Relaxation Model (HRM), thus providing an alternative to the Rayleigh-Plesset equation. It was found that despite the differences between cavitation (driven by pressure) and flash boiling (driven by temperature as well), these models are sufficiently similar to suggest that the homogeneous relaxation model can also model cavitation [214,215]. The results were validated against geometries experimentally evaluated by Neroorkar *et al*. (2012) [213] and demonstrated that the model can correctly reproduce the cavitation in a nozzle. Battistoni *et al*. [216] in his study compared a mixture model in conjunction with the HRM phase change model with a multifluid model utilizing the Rayleigh bubble dynamics for phase change and validated against experimental data. It was concluded that from an engineering point of view, the two models showed good predictive capabilities.

The cavitation model implemented in the commercial software Converge was used for this study. The model is based on the flash-boiling hypothesis of Shields *et al*. in 2011 [217] with rapid heat transfer between vapor and liquid phase [109, 218,219]. The method represents a similar procedure to cavitation where the vapor formation happens through a pressure drop on a constant temperature level, except that the pressure drop is lower and there is a temperature elevation in the system. The mass exchange between phases is predicted by the HRM which describes the process of vapor

mass fraction approaching its equilibrium state. This mass fraction rate is calculated by the formula:

Mass fraction rate

$$\frac{D_x}{D_t} = \frac{\bar{x} - x}{\Theta} \tag{67}$$

where $\bar{x}$ represents the equilibrium mass of vapor phase, x is the instantaneous mass and Θ is the time scale over which x relaxes to $\bar{x}$. For evaporation, Θ_E is expressed in Equation (*68*). Furthermore, the condensation time scale is described by equation

Evaporation time scale

$$\Theta_E = \Theta_0 \cdot \alpha^{-0.54} \cdot \varphi^{-1.76} \tag{68}$$

Condensation time scale

$$\Theta_C = F \cdot \Theta_0 \cdot \alpha^{-0.54} \cdot \varphi^{-1.76} \tag{69}$$

where F is the condensation time scale factor with a typical value of $5e^{03}$, meaning that the condensation is $5e^{03}$ times faster than the evaporation under similar conditions. The Θ_0 coefficient is set to $3.84e^{-07}$ s based on validated work from [213,220,221]. The non-dimensional pressure ratio φ, is given by the formula:

Pressure ratio

$$\varphi = \frac{p_{sat} - p}{p_c - p_{sat}} \tag{70}$$

where p_c means the critical pressure. Further information of the cavitation model can be found in [107].

In the flow field, O_2 and N_2 representing the air inside the nozzle and the gas state of n-Dodecane as fuel surrogate were initialized. The equation of state was handled by the Redlich-Kwong cubic equation (shown in Equation (*71*)) while the real gas properties are calculated as function of temperature:

Pressure

$$p = \frac{R \cdot T}{v - b} - \frac{a}{v^2 + u \cdot v \cdot b + w \cdot b^2} \tag{71}$$

Further information of the coefficients can be found in [107]. Based on its very similar physical properties compared to the measured Diesel fuel, n-Dodecane was utilized as Diesel surrogate.

5.4.3 Simulation setup

The CFD domain with the applied boundary conditions can be seen in **Figure 61**. The main bore is modeled as a wall boundary. Static pressure derived from the measurements is applied at a fuel temperature of 323K at the main bore inlet. The mass fraction of the entering fuel is 99.9% of n-Dodecane and 0.1% of air. The turbulent intensity and lengthscale are approximated and set to 0.02 and 0.0001m, respectively.

Table 8 - Physical properties of n-Dodecane.

Physical Properties	n-Dodecane
Reference density [kg/m^3]	755.2
Critical Temperature [K]	691.9
Dynamic viscosity [N·s/m^2]	0.003284

Surface tension [N/m]	0.02743
Vapor Pressure (300-330K) [Pa]	1000
Density [kg/m^3]	787

The nozzle walls are treated as no-slip walls assuming smooth wall conditions. The plenum, which is a constant volume filled with air, has atmospheric conditions. Here, the outflow boundary condition is applied. The turbulent kinetic energy is specified at a value of 0.02 m^2/s^2 and the lengthscale is set to have a value of 0.0003 m. Together with the wall boundary conditions the law of the wall, for high-Reynolds number applications, is applied. In the absence of prism layers, the viscous sub-layer of the boundary-layer cannot be sufficiently resolved, therefore the application of the wall function is obligatory. The law of the wall approach is a logarithmic curve fit of the turbulent boundary-layer; thus, the tangential components of the stress tensor can be calculated. The simulation is set to reach a quasi-steady solution at 0.01 s.

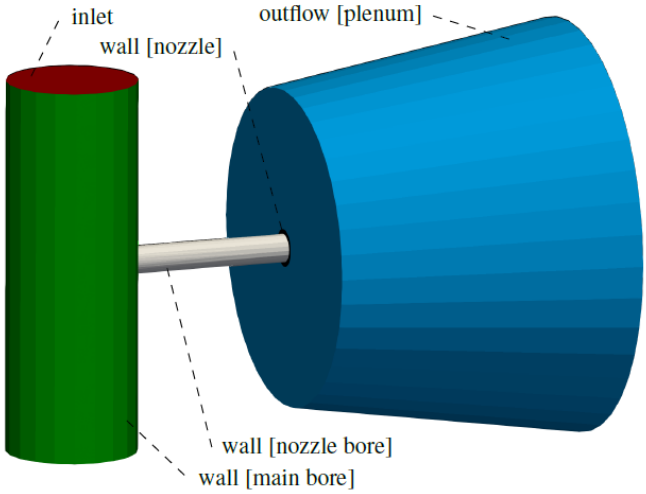

Figure 61 - Schematic figure of CFD domain with applied boundary conditions presented for nozzle type N101.

5.4.4 Grid generation

Three different grids were created for the noneccentric nozzle (type N101, see **Figure 49** for further information) to investigate the grid resolution influence on the computational results. Based on the nozzle bore diameter, 40, 35 and 30 cells were placed in the nozzle bore, respectively. With the aforementioned nozzle bore resolution, a base grid size was calculated for the entire geometry of the nozzle. The nozzle bore region was computed by the so-called fixed embedding, utilizing a scaling factor of 4 compared to the chosen base cell size, where a stationary zone was defined including the nozzle bore length, the vicinity of the nozzle bore inlet and the near nozzle bore region inside the plenum (**Figure 61**). The plenum region was computed by Adaptive Mesh Refinement (AMR), where the automated grid refinement cuts the cells by a scaling factor of 4, based on velocity and void fraction sub-grid criteria (**Figure 62**). The wall boundaries were computed by a permanent grid resolution by keeping the non-dimensional wall distance value Y^+ at 30, which is appropriate in case of high-Reynolds number turbulent flow applications.

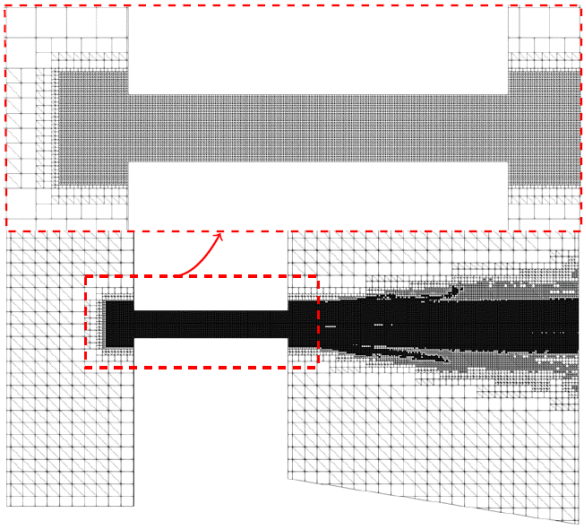

Figure 62 - Grid structure applied in the simulation in case of the nozzle N101 with detail view around the nozzle bore (top).

5.4.5 Solver settings

The transient solver with the full hydrodynamic simulation mode was chosen for this application. Both the gas and liquid flow solvers are fully compressible. The Pressure-Implicit with Splitting of Operators (PISO) algorithm with a tolerance of 0.001 was used for the pressure-velocity field coupling, while the momentum, pressure, density, and energy equations were taken care of the linear solver method, thus allowing a faster convergence. The time step was set to be varied between $1e^{-10}$ and $1e^{-06}$, while the maximum CFL (Courant–Friedrichs–Lewy condition) number and diffusive CFL number were chosen to be lower than 0.25 and 0.5, respectively. A representative summary of the applied numerical settings can be found in **Table 9**.

Table 9 - CFD solver settings.

Solver settings		
Min. time step	[s]	1e-10
Max. time step	[s]	1e-06
Max. convection CFL	[-]	0.25
Max. diffusion CFL	[-]	0.5
Max. Mach CFL	[-]	5.0
PISO iterations	[-]	20
PISO tolerance	[-]	1e-03
Momentum eq. Convergence tolerance	[-]	1e-05
Pressure eq. Convergence tolerance	[-]	1e-06
Density eq. Convergence tolerance	[-]	1e-05
Energy eq. Convergence tolerance	[-]	1e-05
Species eq. Convergence tolerance	[-]	1e-05
TKE Convergence tolerance	[-]	1e-05
EPS Convergence tolerance	[-]	1e-05

The global transport parameters influence the mixing properties and are suggested values by Convergent Science based on experience with cavitating diesel injector simulations. Here, the turbulent Prandtl number was set to 0.9 and the turbulent Schmidt number to 0.78. The Renormalization Group (RNG) k-ε turbulence model was applied. The model coefficients were taken from the literature and follow the instructions for cavitating flows in Diesel injectors suggested by Convergent Science. Further information on the turbulence kinetic energy and turbulence dissipation equations can be found in [107].

5.4.6 Turbulence modeling

RANS and URANS simulations have been popular within the industry due to time and cost constraints, predicting flows acceptably on a macroscopic level. LES, DES, and hybrid RANS/LES approaches among other turbulence models still have a high computational demand but resolve transient large-scale turbulent structures and provide more detail of the flow [224,225]. Koukouvinis *et al.* (2016) [225], in their extensive work, tested several turbulence models with different cavitation models at several pressure drops and compared those results to experimental data. They found that RANS produced less accurate results at low pressure drops. Edelbauer *et al.* (2014) [226] compared RANS and LES simulations of cavitating flows and concluded that RANS can predict cavitation with reasonably acceptable accuracy in an operating condition with high pressure difference.

Two-equation models

Different turbulence models have been used in previous studies for modeling cavitation in diesel nozzles. In their numerical study, Yuan *et al.* (2001) [227] simulated cavitation phenomena inside injector nozzles using the k-ω turbulence model [228], with VOF interface capturing. The nozzle consisted of a 2D rectangular-shaped channel; water at 20 C° with 80 bar injection pressure and 21 bar back-pressure was utilized. It was concluded that the numerical approach was able to reproduce complex cavitation phenomena as observed in injection nozzle experiments. In their numerical study, Giannadakis *et al.* (2008) [115] tested the standard k-ε model, the RNG k-ε model [229], and a non-equilibrium two-equation model by Shyy et al. (1997) [230]. The results of [115] revealed that a variation of up to 3% in the predicted nozzle discharge coefficient can be attributed to the turbulence model. They also show that the choice of the turbulence model does not significantly affect the details of computed flows. Furthermore, none of the above RANS turbulence model was found to predict cavitation better than the rest for all test cases considered. Martynov (2005) [231], in his study of cavitating injector flows, used the RNG k-ε turbulence model, for the geometry presented by Yuan *et al.* (2001) [227]. Rakshit (2012) [232] presented two-dimensional validations with the simulation of a Venturi nozzle, a sharp nozzle, and a throttle from Winklhofer *et al*. (2001) [233], using the standard k-ε turbulence model. In [232], results of three-dimensional simulations for the ‘spray A’ and ‘spray H’ injectors from the Engine Combustion Network [234] were also reported. The results showed that the mass flow rate and cavitation at incidence are low, while high-speed nozzle flows were successfully predicted. Matlok *et al.* (2016) [235] published their investigation of cavitation in injection nozzles of two-stroke Diesel engines. Here, both experimental and numerical development work was performed using several experimental rigs, to investigate different aspects of the flow and cavitation properties in

the fuel injector. CFD simulations utilized the RNG k-ε turbulence model. Computed time-averaged in-nozzle velocity fields, as well as the prediction of the location of cavitation, showed good agreement with the experiments. Furthermore, the predicted loss coefficients of the individual nozzle holes excellently matched the experimental results. Papadopoulos and Aleiferis (2015) [236] performed numerical simulations of in-nozzle flow of a Diesel injector with a moving needle during and after the end of a full injection event, for an injection pressure of 400 bar and a back-pressure of either 60 bar or 1 bar. They considered a sector model of the injector geometry with 0.12 mm orifice size, applied both the k-ε and k-ω SST models, and compared simulation results against experiments. The k-ω SST model was found to predict better the injector flow rate, with differences of the order of 3% against experiments. Overall, a main conclusion of these studies is that, in simulating in-nozzle flows, the results between the different two-equation models do not differ substantially.

5.4.7 Comparison of different turbulence models

In the present study, the performance of different two-equation turbulence models in predicting cavitating flow of two-stroke marine Diesel injectors was evaluated. Here, the geometry of the high eccentricity nozzle was considered. Transient simulations were performed for a total time of t = 0.001 s, and convergence to steady state was verified. The setup of these simulations, including values of CPU time required and the computed mass flow rate, is summarized in **Table 10**, indicating that an in-nozzle URANS simulation accounting for cavitation has required an average of 4.5 days using 48 cores of a parallel cluster.

Results of the computed flow fields are presented in **Figure 63**, **Figure 64**, and **Figure 65**, for the velocity magnitude, the density, and the turbulent kinetic energy, respectively. The present results demonstrate that, with the exception of the standard k-ε model, the choice of turbulence model has a minor effect on the computed flow. On this ground, the k-ε RNG model is used in all subsequent simulations of in-nozzle flow. The model coefficients were taken from the literature and are in accordance with the suggestions for in-nozzle flow provided in [107].

Table 10 – Parameters and resulting quantities of simulations testing the effects of different turbulence models.

	Unit	Standard k-ε	Realizable k-ε	RNG k-ε	k-ω SST
Cell number	[-]	2.5×10^6	2.5×10^6	2.5×10^6	2.5×10^6
CFL number	[-]	≤ 0.5	≤ 0.5	≤ 0.5	≤ 0.5
Nr. of CPU cores	[-]	48	48	48	48
Computational time	[h]	100	112	94	120
Aver. massflow rate	[kg/s]	0.0678	0.0674	0.0674	0.0664
Av. cell gas volume fraction at bore exit	[%]	19.3	24.8	21.9	23.1

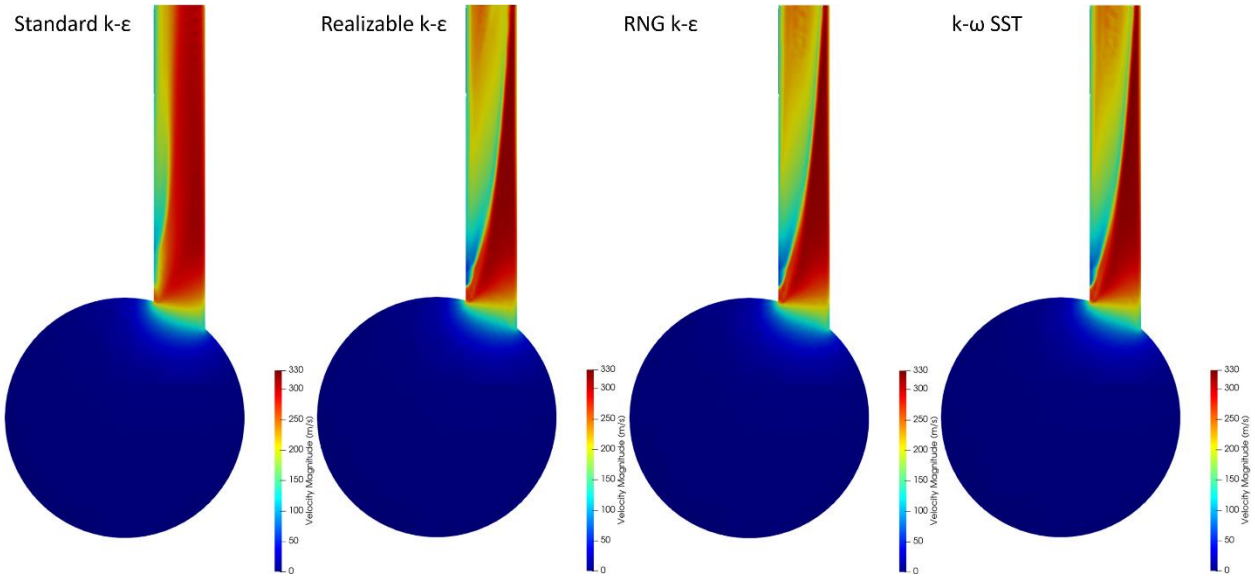

Figure 63 - Velocity Magnitude distribution [m/s] for the high eccentricity nozzle (e = 1.10 mm) using different turbulence models.

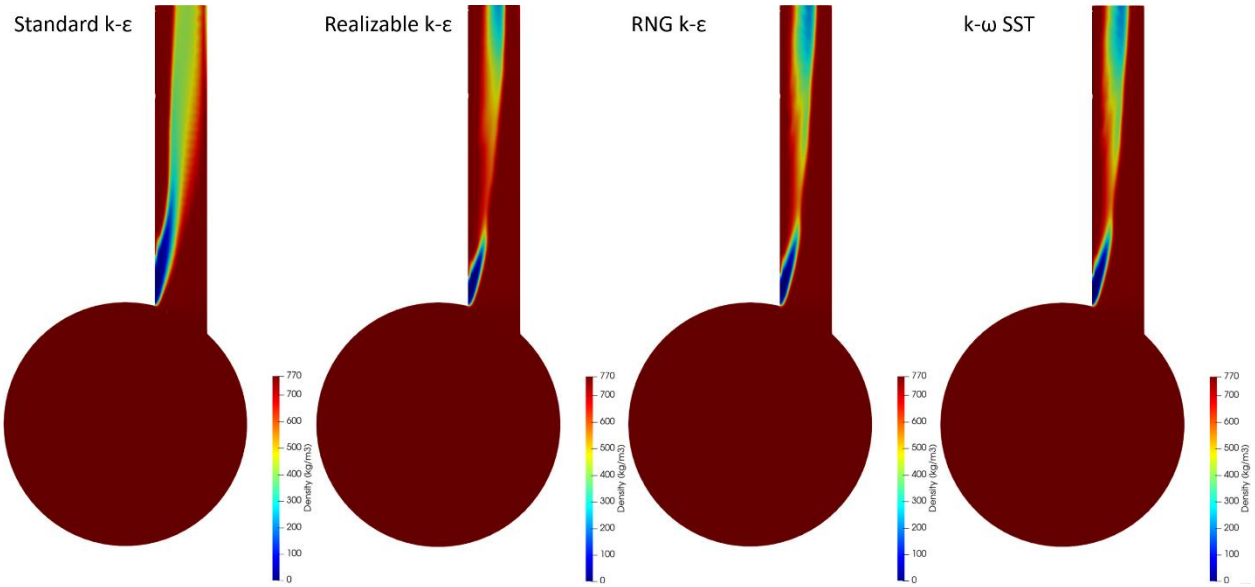

Figure 64 - Density distribution [kg/m^3] for the high eccentricity nozzle (e = 1.10 mm) using different turbulence models.

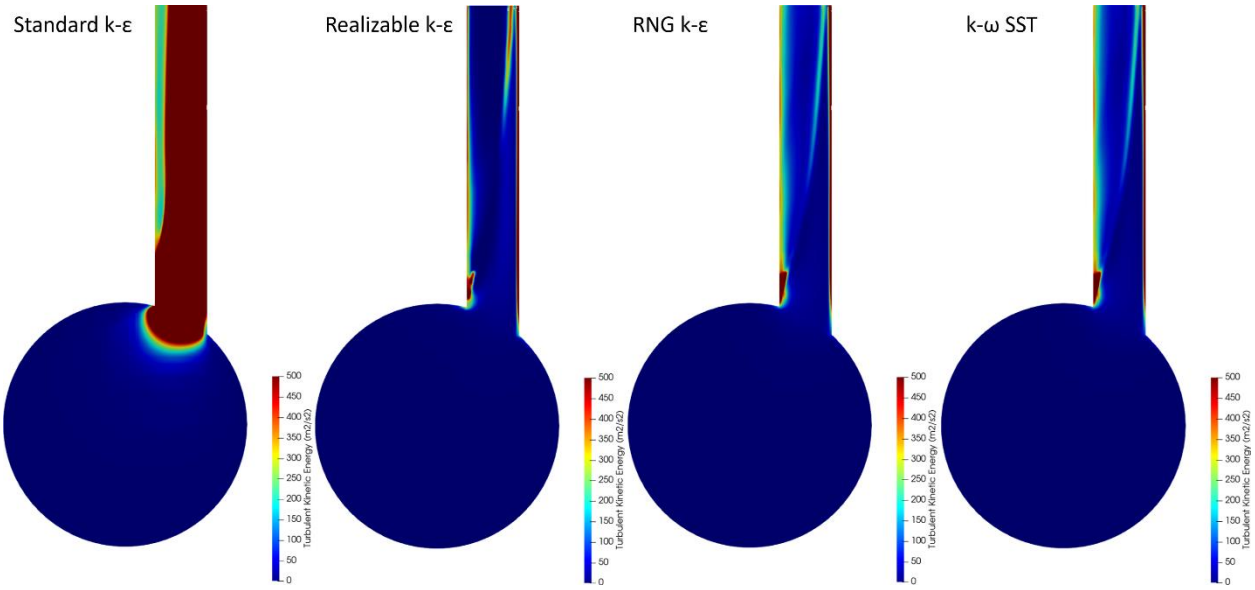

Figure 65 - Turbulence kinetic energy distribution [m^2/s^2] for the high eccentricity nozzle (e = 1.10 mm) using different turbulence models.

5.5 Results and analysis

5.5.1 Experimental results

The fuel pressure measured in the main bore of the nozzle mounted in the TNH and the corresponding normalized current signal of the injector solenoid are depicted in **Figure 66**. The signals shown are averaged over 20 injections. The time axis origin is the triggered start of injection (tSOI). The shift between current and pressure signal indicates the hydraulic delay due to the needle movement in the fuel injector. The quasi-steady-state injection period was defined between 5 and 13 ms after tSOI and was used to average the pressure, the momentum flux, and the in-nozzle flow images for comparison with the CFD results. The depicted pressure curve in **Figure 66** represents the data of the nozzle type N101.

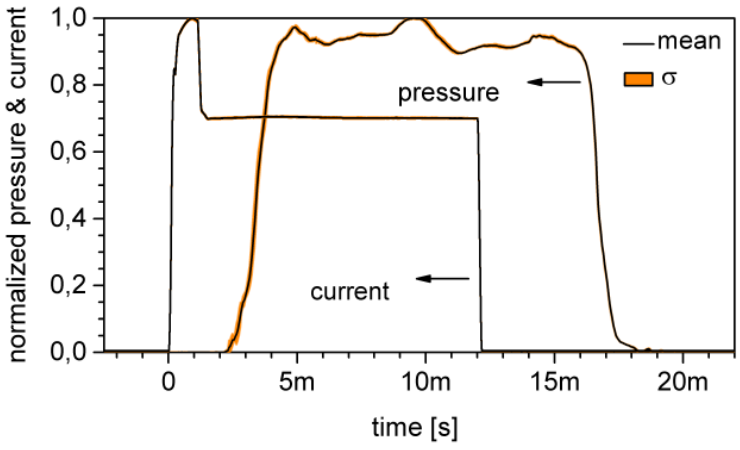

Figure 66- Averaged fuel pressure and injector solenoid current for injection duration of 12 ms. The time origin is the triggered start of injection (tSOI). [Courtesy of R. Balz; R. Balz et al., 2020. Experimental and numerical investigation of cavitation in marine Diesel injectors, International Journal of Heat and Mass Transfer.]

As there is no significant difference in the pressure signals of the three nozzle types, the pressure curves of the nozzles N104 and N105 are not depicted for visibility reasons.

The momentum flux data acquired for the three different nozzles used is depicted in **Figure 67**. Note the similar curve characteristics compared with the pressure curve shown in **Figure 66**. The pressure and momentum flux results were averaged over the quasi-steady-state period of the fuel injection process between 5 and 13 ms after tSOI. The averaged values and the corresponding standard deviations of the pressure measurements are depicted together with the momentum flux results from the impingement measurements in **Table 11**. The averaged pressure data was used for the CFD boundary conditions.

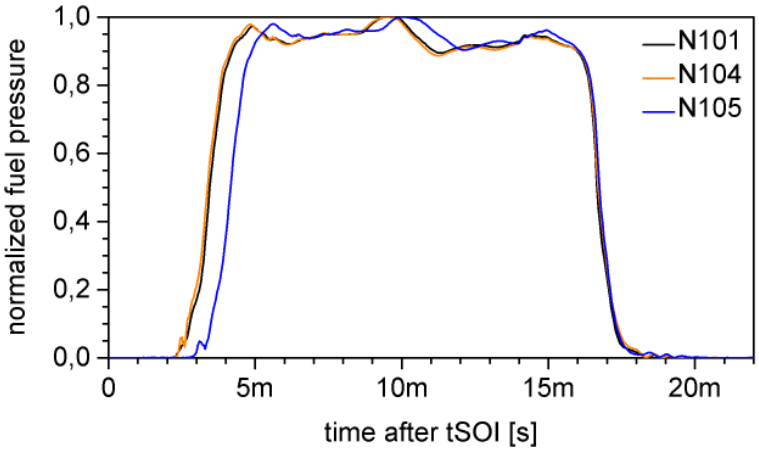

Figure 67 - Averaged fuel pressure curves for the standard nozzle N101, the eccentric nozzle N104 and the 75° angled nozzle N105, respectively. Note the time delay at the beginning of the pressure increase for the nozzle N105. [Courtesy of R. Balz; R. Balz et al., 2020. Experimental and numerical investigation of cavitation in marine Diesel injectors, International Journal of Heat and Mass Transfer.]

Although the quasi-steady-state period of the pressure and momentum flux curves show fluctuations, the signal is very stable as indicated by the small standard deviations as sown in **Table 11**. Those fluctuations originate from the hydraulic high-pressure system providing the injector with fuel and are fully reproducible.

Table 11 Measurement results; nozzle average Pressure and Momentum flux values with standard deviation.

avg. Pressure	N101	[MPa]	38.51 ± 1.08
avg. Pressure	N104	[MPa]	38.98 ± 1.04
avg. Pressure	N105	[MPa]	38.32 ± 1.00
avg. $\dot{M}_f$	N101	[N]	21.46 ± 0.09
avg. $\dot{M}_f$	N104	[N]	19.97 ± 0.07
avg. $\dot{M}_f$	N105	[N]	20.93 ± 0.11

The acquired images of the in-nozzle flow were only intensity adjusted, rotated, and cut, to remain the maximal image information. A series of selected in-nozzle flow images are shown in **Figure 68** where i) shows the with Diesel fuel-filled nozzle bore before the needle opening, ii) - vi) during needle opening, and vii) during the quasi-steady-state fuel injection at around 8 ms after tSOI. The

field of view used covers the entire nozzle bore (vertical) of the transparent nozzles and a small area of the nozzle main bore (horizontal, top of image). Since the refractive index of the PMMA material and the Diesel fuel used are not perfectly identical, the main bore and nozzle bore walls are always visible in the images acquired. Therefore, the image before needle opening as depicted in **Figure 68** (i) serves as a reference background. In the other images shown in **Figure 68**, the additional dark areas represent gaseous flow, i.e., cavitation. The light is refracted away from the optical axis due to the phase and consequent refractive index change and therefore does not arrive on the camera sensor. The bright areas within the walls of the nozzle bore indicate the liquid fuel flow as the light passes the transparent nozzle with only slight distortions and arrives on the camera sensor. For comparison with the CFD results, only the images during the quasi-steady-state injection period as depicted in **Figure 68** (vii) were used and averaged. However, the images acquired during needle opening (**Figure 68** (ii) - (vi)) are quite interesting as well. Image (ii) represents the in-nozzle flow at around 2.1 ms after tSOI (compare with pressure curve in **Figure 66**) and shows the first cavitation in the acquired measurement series. The pressure is still quite low compared to the maximal pressure achieved roughly 1 ms later. The following images (iii) to (vi) are the consecutive frames with 50 µs interval given by the 20 kHz frame rate of the high-speed camera. The cavitation development within these five sequential images is interesting since the cavitation pattern develops to supercavitation in image vi) and then forms back to film and cloud cavitation as shown in images (iii) and (vi) [183, 222]. This reduction in cavitation intensity can be traced back to the small pressure fluctuation at the beginning of the pressure curve as depicted in **Figure 66**. Another interesting fact is the very similar supercavitating pattern in image (v) and (vii) although the pressure difference with approximately 40 MPa is extensive (compare with pressure curve in **Figure 66**, image (v) acquired at around 2.25 ms and image (vii) at around 8 ms after tSOI).

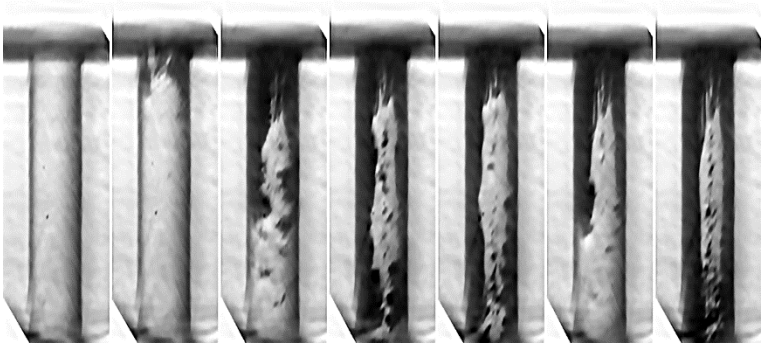

Figure 68 - In-nozzle images of nozzle N101. Note that dark areas within the nozzle bore indicate gaseous flow, i.e., cavitation. Nozzle bore filled with Diesel, but no cavitation flow (i), first sign of cavitation (ii) and following image frames with 50 µs time interval (iii - vi), and during quasi-steady-state fuel injection at around 8 ms after tSOI (vii). [Courtesy of R. Balz; R. Balz et al., 2020. Experimental and numerical investigation of cavitation in marine Diesel injectors, International Journal of Heat and Mass Transfer].

5.5.2 CFD in-nozzle flow investigations

Grid sensitivity analysis with nozzle type N101

A grid sensitivity analysis investigating three different numerical grids was executed by utilizing the standard nozzle N101 (**Table 12**). After reaching a converged quasi-steady solution, the spray Reynolds number of each mesh type based on the velocity magnitude values stored in a section 0.05 mm before the nozzle bore was defined. Here, the flow field was sampled along a straight line in the nozzle bore cross-section in 50 points (**Figure 69**). Then, the grid types were compared by means of averaged pressure, density, and velocity fields, as well as by taking the cell gas fractions at the nozzle bore exit. It can be stated that only minor deviations among the test grids could be found. The finest grid predicts the highest maximum velocity magnitude at the nozzle bore exit while the coarsest grid shows a loss in velocity magnitude by approximately 20 m/s. The average velocity magnitude analyzed at the same cross-section of the nozzle bore results in a very similar behaviour.

Table 12 - Test grid properties.

		N101		
		Grid1	Grid2	Grid3
Cell number across nozzle bore	[-]	40	35	30
Cell number ratio across nozzle bore	[%]	0	12.5	25
Base cell size	[mm]	0.3375	0.375	0.4125
Cell number in nozzle bore	[-]	213000	157000	120000
Max. cell number	[-]	1540000	1260000	955774

Furthermore, the test meshes were compared employing time-averaged Mach number and cell densities stored in the sampling points. The coarser grid resulted in very similar values in any investigated physical flow properties to the finest grid and still having remarkably less computational time (**Figure 69**). As a result, the grid spacing of the coarser grid was utilized for all three nozzle layouts for further numerical investigations.

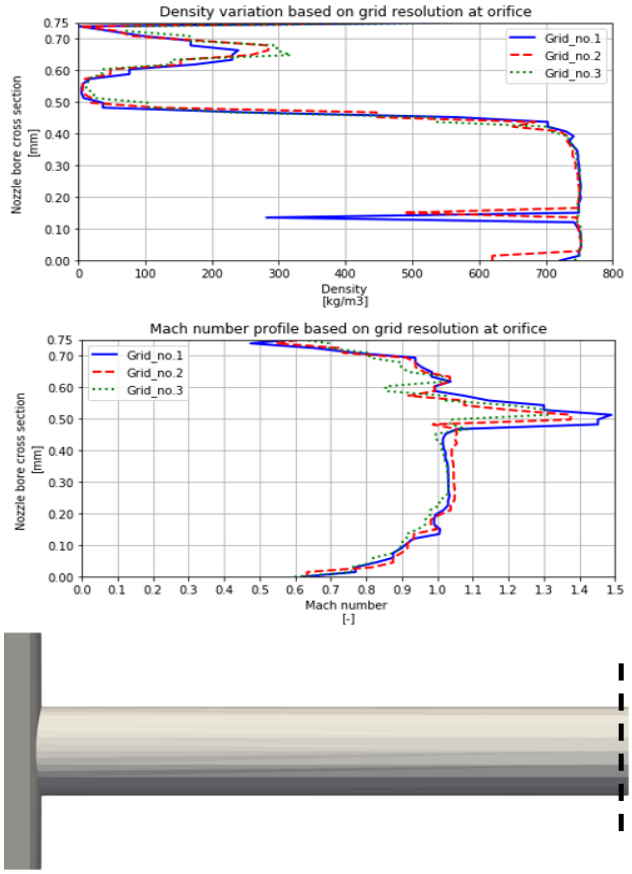

Figure 69 - Comparison of density variation (top) and Mach number profile (middle) for all grids in case of nozzle type N101 in a cross section taken before the nozzle bore exit (bottom).

A vertical cross-section cutting the nozzle bore exactly in the middle and visualizing the density distribution inside the nozzle is depicted in **Figure 70** (left). The density distribution shows not just a separation of flow at the sharp nozzle bore inlet, but also a flow detachment close to the nozzle bore exit can be seen, which has a pronounced effect on the spray formation. Regarding the pressure field **Figure 70** (right), one can state that the pressure reduces while entering the nozzle bore, where the fuel velocity increases according to Bernoulli's law. The local pressure at the nozzle bore inlet drops below the vapor pressure of the fuel at the given temperature level and additionally, the sudden geometrical change invokes immediate cavitation inception. Both density and pressure distributions show very similar results at the end of the converged simulation (0.001s).

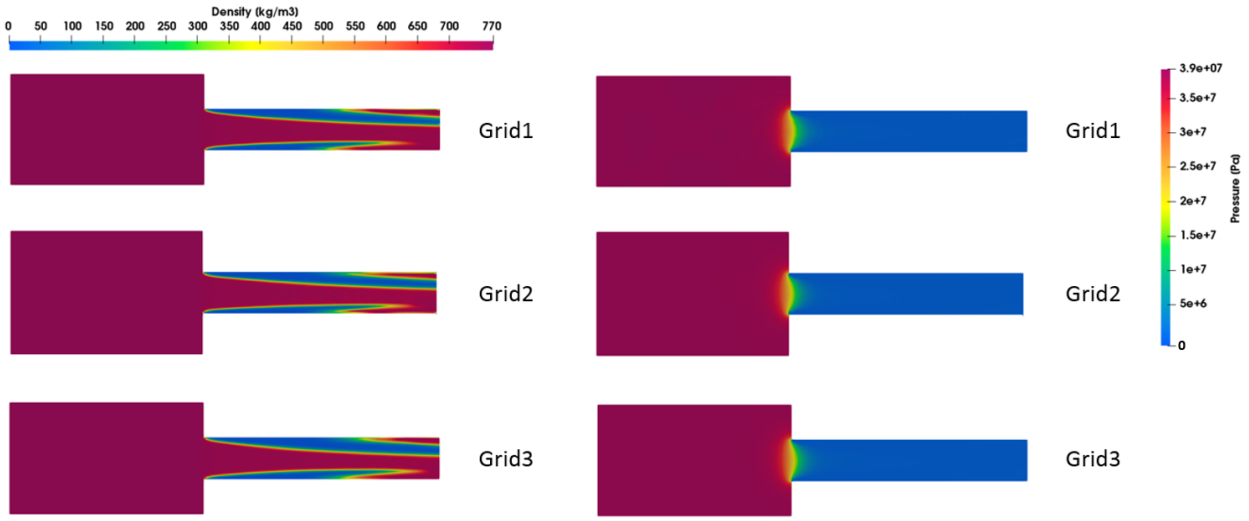

Figure 70 - Density (left side) and pressure distribution inside the nozzle bore computed based on different grid resolutions for a noneccentric nozzle. (Vertical section cut in the middle of the nozzle bore, side view).

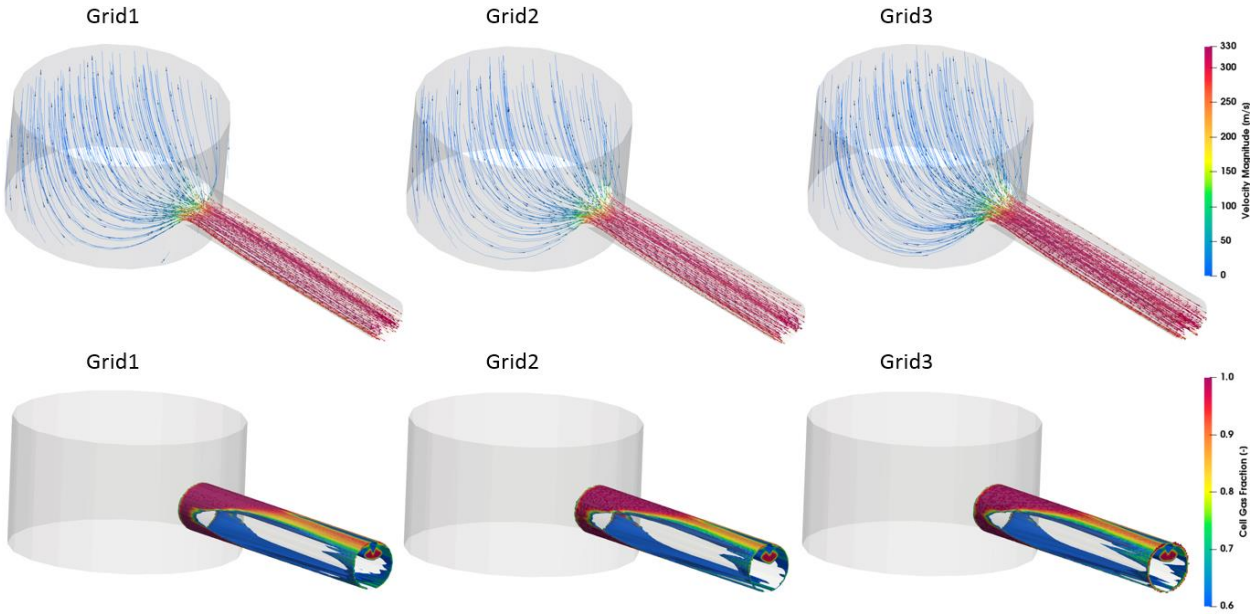

Figure 71 - Velocity magnitude streamlines inside the nozzle bore (isometric view, top) and gas fraction content of cells visualized by iso-volumes (isometric view, bottom) depending on grid resolution in case of Nozzle type 101.

All grids predict a significant cavitation zone appearing inside the nozzle bore, initiated from the bore inlet. The air at the orifice extends back into the vena contracta region of the nozzle. Such a phenomenon, according to the literature, is called a hydraulic flip. The hydraulic flip greatly reduces the disturbances of the spray, but increase the noise dramatically. A more pronounced separation can be realized on the upper side of the nozzle bore, which is expected since the fuel enters directly from the needle inlet direction, therefore suffering through a significant stream redirection caused by the geometrical properties of the nozzle.

Streamlines coloured by velocity magnitude in **Figure 71** (top) show the path of the fuel inside the nozzle, where the vena contracta is represented by the compressed streamlines after the fuel enters

the nozzle bore from the main bore. The fully developed cavitation in this section can be recognized, thus indicating the asymmetric nature of the cavitation inside the nozzle bore.

The gas fraction content of the cells inside the nozzle bore shows the actual vapor distribution (**Figure 71**). An obvious vapor film formation along the entire nozzle bore length reaching the orifice can be realized. The vapor formed tube inside the nozzle bore shows a fully developed cavitation, reducing the effective area of the cross-section.

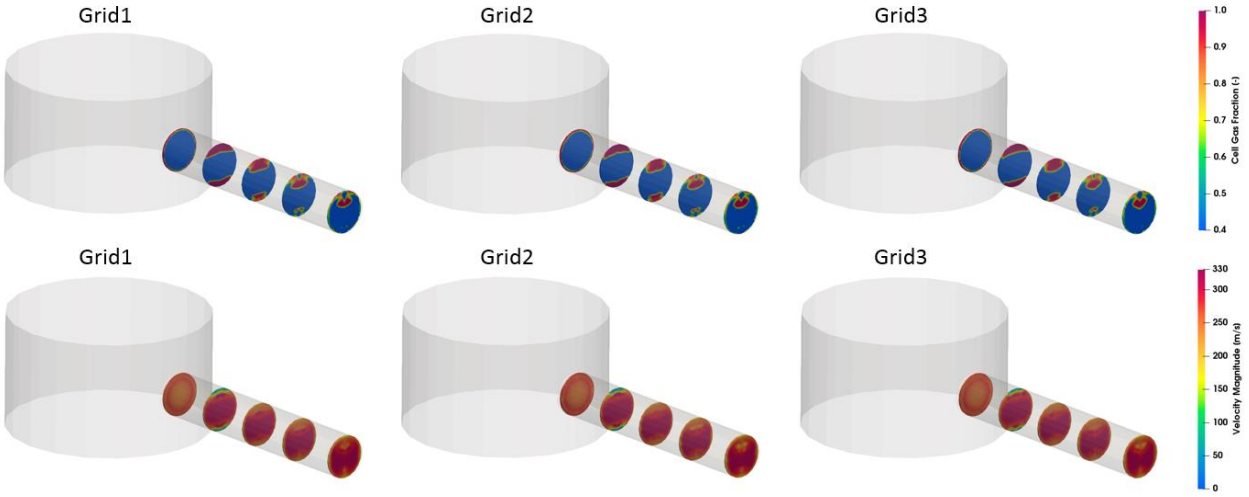

Figure 72 – Color-coded contours of gas fraction (top) and velocity magnitude (bottom) at representative nozzle cross-sections, for Nozzle type 101, using different grid resolutions.

The cross-sectional analysis of the flow in the nozzle bore can be seen in **Figure 72**. The cross-sections are placed evenly along the nozzle bore keeping a 1mm distance. The test grids predict very similar results, where the vapor formation on the top and bottom side of the bore is present with, at the same time the velocity decreases. The vapor tube on the upper side of the nozzle bore clearly can be seen at the orifice while at the bottom the vapor volume significantly reduces and reaching the orifice almost completely diminishes. The gas fraction at the orifice decreases the uniformity of the velocity magnitude distribution just right before the nozzle bore exit.

As an outcome of the grid resolution test, one can state that the finest and the coarser grids provide very similar results. The coarser grid results in values of the investigated physical flow properties identical to those predicted by the finest grid with remarkably less computational time. Hence, the grid spacing of the coarser grid was utilized for all three nozzle layouts for further numerical investigations.

Simulation results of nozzle type N104 (eccentric)

The following section introduces the cavitating flow simulation results in the case of a nozzle with 1.10 mm eccentricity. The cavitating flow simulation results of this nozzle type (N104) are depicted in **Figure 73** and **Figure 74**. **Figure 73** presents the flow field as the density distribution (top), pressure variation (middle), and velocity field (bottom) inside the nozzle. The flow enters the nozzle bore through a huge distortion caused by the sharp inlet of the nozzle bore inlet.

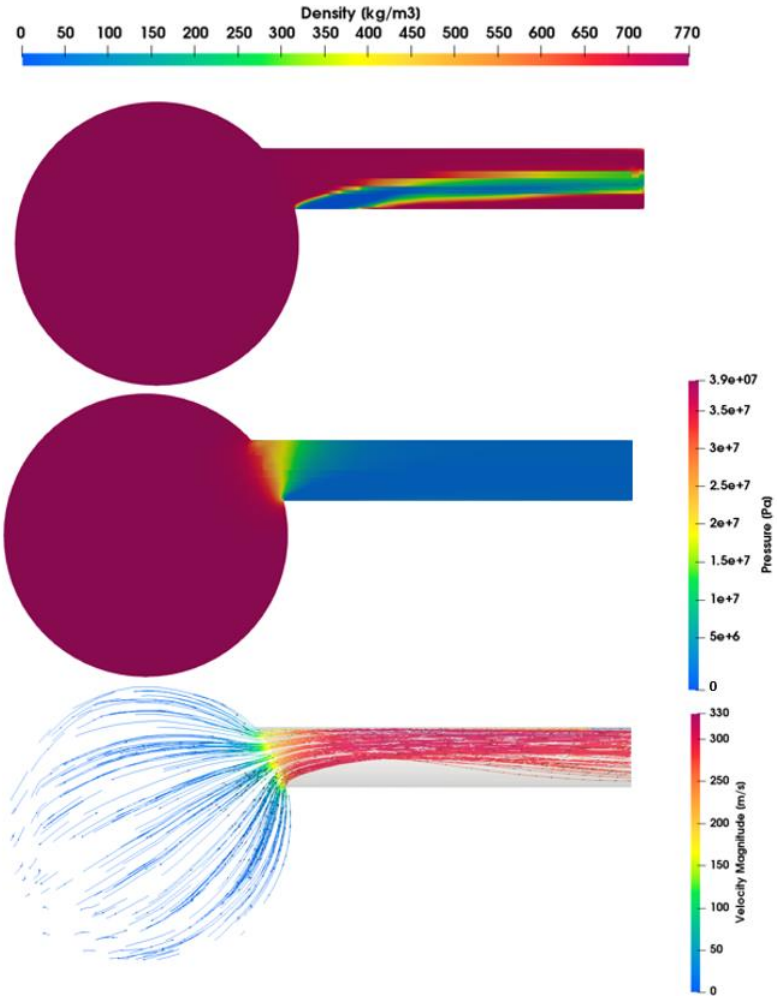

Figure 73 - Nozzle type 104: density (top) and pressure (middle) distribution inside the nozzle (horizontal section cut in the middle of the nozzle bore, top view), and streamlines coloured with velocity magnitude (bottom).

Flow separation inside the nozzle bore on the main bore symmetry side occurs, and as a result, a huge recirculation zone is created where this region is filled by fuel vapor. This region extends until the nozzle bore exit forming a massive vapor tube inside the nozzle bore and therefore significantly reducing the effective area of the nozzle bore. The eccentric side of the nozzle bore seems to be undisturbed by the geometry and, thus the presence of a remarkably high-velocity zone can be found. The highly non-uniform velocity magnitude distribution is an obvious outcome of the nozzle bore eccentricity and the geometrically induced cavitation which is suggested by the presented CFD results. **Figure 74** (left side) presents the generated vapor region inside the nozzle bore on the opposite side of the eccentricity. The cavitation zone at the nozzle bore inlet detaches after approximately a distance of the nozzle bore diameter and separates from the nozzle bore wall into the internal region of the nozzle bore. The extended and coherent vapor zone reaches the nozzle bore exit while vapor bubbles travel through the flow. This sort of vapor formation is a typical characteristic of string cavitation and supercavitating nozzles [185, 223]. Vapor formation can also be experienced at the nozzle bore exit which means flow detachment from the nozzle bore and therefore significantly influencing the spray formation and causing spray core deformation.

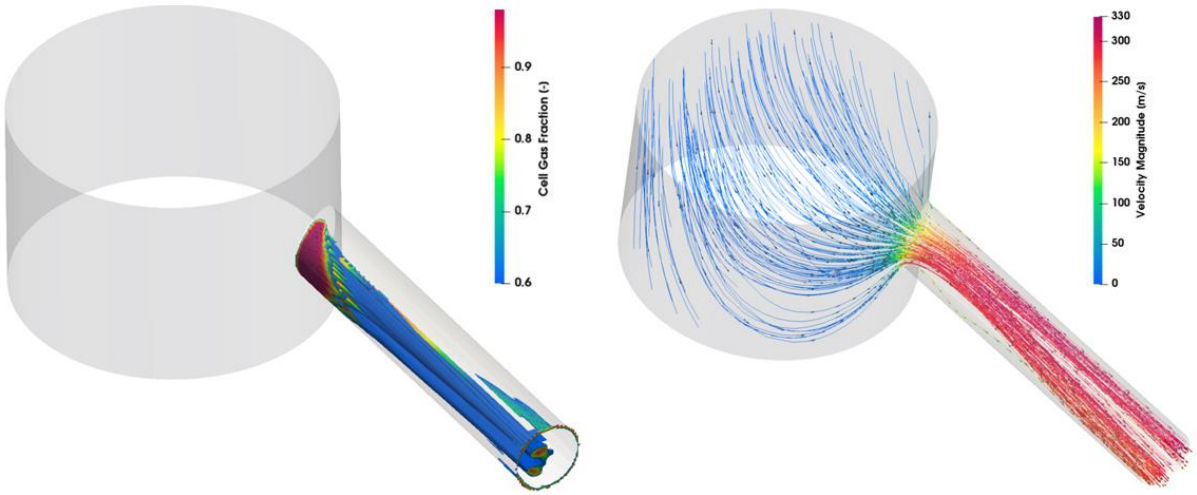

Figure 74 - Nozzle type 104: color-coded contours of gas fraction in the nozzle bore region (left), and streamlines coloured with velocity magnitude (right).

Simulation results of nozzle type N105 (inclined)

Nozzle type 105 is a noneccentric nozzle with a 75° bent nozzle bore. **Figure 75** helps to understand the flow behavior inside the nozzle. The density distribution (top) shows an extended separation zone on the bottom side of the nozzle bore, initiated by the sudden geometrical change at the nozzle bore inlet.

The separation zone is confirmed by the pressure contour plot (middle) where the depression is initiated at the nozzle inlet. Further on, this zone evolves into the fluid domain, compressing the streamlines to the upper side of the nozzle bore, therefore creating a high-velocity region. The upper edge of the nozzle bore inlet shows a small depression zone, which can be identified as cavitation inception at the nozzle bore inlet, although it has not a significant effect on the flow field.

A summary of the nozzle and flow field properties of the CFD simulation results can be found in **Table 13**. Taking the average velocity magnitude evaluated by the CFD simulations at the nozzle bore exit (orifice), the standard nozzle N101 has the highest velocity, and the eccentric nozzle N104 the lowest. Based on these velocities, the corresponding Reynolds numbers (Re) were defined for all three nozzle geometries, proving the presence of highly turbulent flow. The velocity magnitude distribution in the vicinity of the nozzle bore exit can be defined by the velocity uniformity index (U_i) introduced by Weltens *et al*. (1993) [174] described in Equation (*64*).

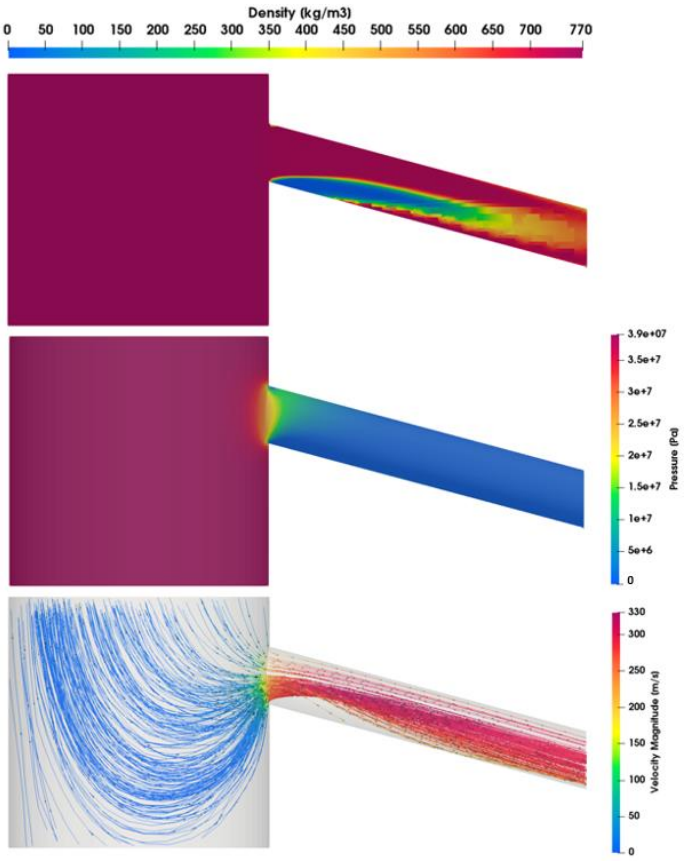

Figure 75 - Nozzle type 105: density (top) and pressure (middle) distribution inside the nozzle (vertical section cut in the middle of the nozzle bore, top view), and streamlines coloured with velocity magnitude (bottom).

The velocity uniformity index (U_i) shows uniform flow velocity distribution arriving at the nozzle bore exit for the standard and the inclined nozzles (N101 and N105, respectively) while the eccentric nozzle N104 stays by a few percentage points behind (see **Table 13** for further details). Another indicator of the flow uniformity is the void fraction of phases at the nozzle bore exit. Therefore, averaging of the gas fraction of cells was executed using the CFD simulation results. The standard N101 and the eccentric nozzle N104 have higher gas fraction while the inclined nozzle N105 results in less gas-phase content just right before entering the plenum.

The discharge coefficient, C_D, gives a good indication of nozzle efficiency where with the reduced effective nozzle bore area due to cavitation, the value decreases and therefore influences the injected fuel velocity. The eccentric nozzle N104 provides the lowest discharge coefficient, while the rest of the nozzles have slightly higher values (see **Table 2** for reference). The momentum flux, $\dot{M}_f$, also was evaluated from the CFD simulation results as it remains the only quantitative result to compare directly with the experimental results. The angled nozzle N105 has the highest momentum flux and the eccentric nozzle N104 with a significant deviation, the lowest.

Table 13 - Summary of the flow properties of the nozzle types.

		Nozzle types		
		N101	N104	N105
Ave. Velocity magnitude at orifice	[m/s]	296	278	285
Ave. Reynolds number at orifice	[-]	69.9k	65.6k	67.2k
Velocity Uniformity index U_i	[%]	94	89	96
Average cell gas fraction at orifice	[%]	31	30	23
Discharge coefficient C_D	[-]	0.65	0.62	0.69
Momentum flux $\dot{M}_f$	[N]	21.06	18.81	21.71

Another indicator of the flow uniformity is the void fraction of phases at the nozzle bore exit. Therefore, averaging of the gas fraction of cells was executed. Here, the eccentric nozzle type N105 has the lowest gas fraction among the nozzles by 23%; the rest of the nozzle geometries result in higher gas-phase content just right before entering the plenum.

5.5.3 Comparison of numerical and experimental results

Figure 76 depicts the measured and simulated momentum flux values as a function of the Reynolds number evaluated from the CFD results. The higher momentum flux increases the average velocity of the fuel in the nozzle bore and therefore results in a larger Reynolds number. The experimentally acquired momentum flux of the three different nozzle types show error bars with a span of 5% to illustrate the deviations between experiment and simulation.

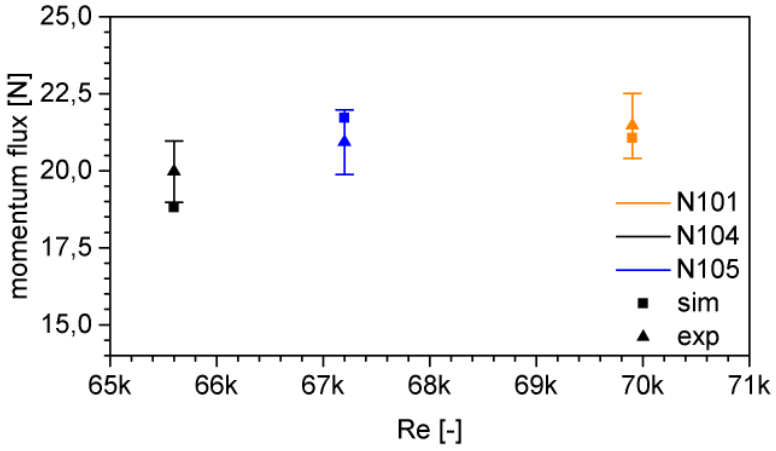

Figure 76 - Experimental and simulated momentum flux of analyzed atomizer geometries as function of Reynolds number. [Courtesy of R. Balz; R. Balz et al., 2020. Experimental and numerical investigation of cavitation in marine Diesel injectors, International Journal of Heat and Mass Transfer.]

Although the standard deviation of the measured and averaged force signals from the impingement experiments were evaluated (see **Table 11**, the errors are likely to be larger due to observational errors and hence, a fixed span of 5% was chosen instead of the standard deviation of approximately only 0.1 N. The simulation results fit to the experimental data well for nozzle type N101 while predicting a slightly lower value for the eccentric nozzle N104 and a slightly higher value for the

angled nozzle N105. The standard nozzle N101 has the smallest discrepancy with less than -2% compared to the experimentally measured value.

Figure 77, **Figure 78**, and **Figure 79** show the experimentally acquired in-nozzle flow images compared to CFD simulation results. To create CFD images that are qualitatively comparable to the experimental images, a time frame was defined for statistical examination after the simulation has reached a quasi-steady state. This allows a comparison to the outcome of the time-averaged experimental images. The Strouhal number, as non-dimensional shedding frequency of the emerging spray, was determined by utilizing the obtained velocity at the nozzle bore exit. Then as a next step, simulation time of six shedding periods was chosen as a time interval for a statistical examination for the simulation results.

These images (**Figure 77 - Figure 79**) depict the acquired in-nozzle flow of the nozzles N101, N104, and N105, respectively. The first image shows the background (i) which is the transparent nozzle filled with Diesel fuel but no mass flow. The second image (ii) shows a single acquisition of the in-nozzle flow during the quasi-steady-state fuel injection at approximately 8 ms after tSOI. And the last image (iii) is correspondent to the arithmetic mean, created by averaging the single frames over the quasi-steady-state injection period between 5 and 13 ms, which at the frame rate of 20 kHz are approximately 160 images.

As the flow in the nozzle bore is cavitating, the light from the laser pulse is scattered away from the line-of-sight optical axis and therefore the areas appear dark on the image. The Diesel fuel flow in the main bore is not cavitating and hence, no dark areas appear in the visible areas. Some small optical distortions occur due to not perfectly polished surfaces on the PMMA nozzles, the transition between the PMMA nozzles, and the sapphire bricks (see **Figure 58** for reference), and fuel deposits.

The standard nozzle design N101 with the centrically 90° arranged nozzle bore (**Figure 77**) is supercavitating as the gaseous phase reaches the nozzle bore exit [222].

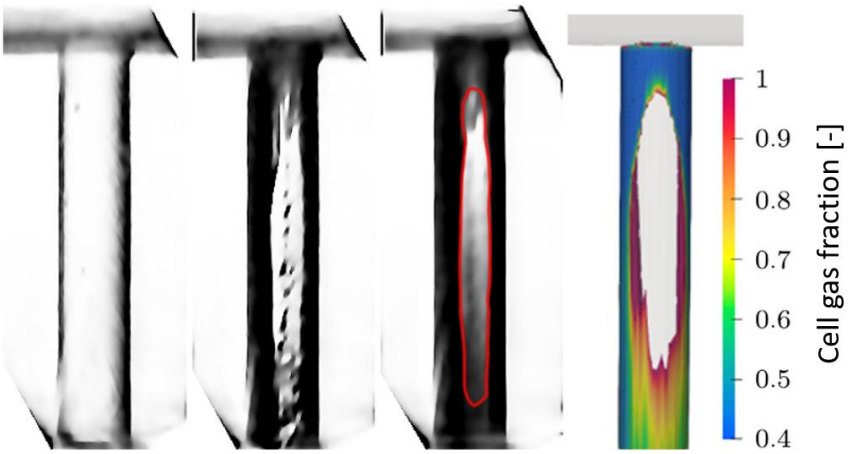

Figure 77 - Experimental in-nozzle flow images showing background (i), single-shot (ii) and average during injection (iii) together with the corresponding CFD result (iv) depicting isovolumes of cell fuel vapor pressure fraction in a non-dimensional range for the nozzle N101.

The fuel flow enters the main bore from the left side and hence the cavitation in the nozzle bore on the left side is more distinctive. At the nozzle bore inlet, the flow is fully cavitating around the nozzle bore inlet circumference. However, after approximately one times the diameter of the nozzle bore, the cavitation is limited to the two side walls. Transient cavitation phenomena in the middle of the nozzle bore, as visible in the single-shot image (ii), expand in cavitation volume towards the exit and result in darkening the averaged image (iii) towards the bottom.

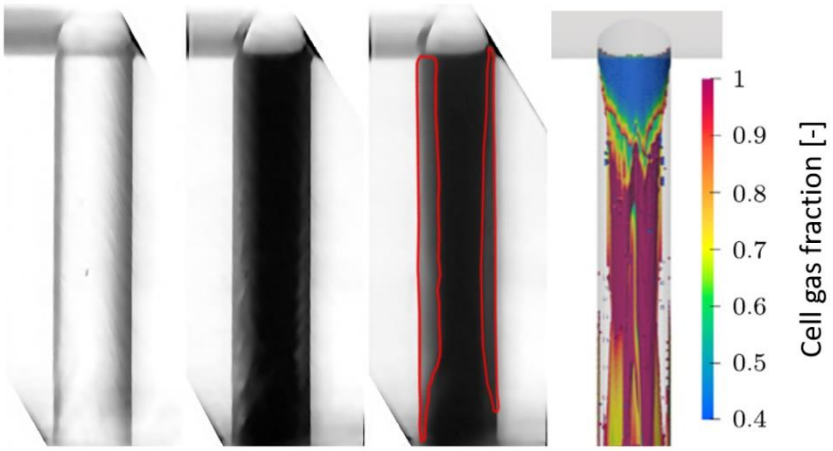

Figure 78 – Experimental in-nozzle flow images showing background (i), single-shot (ii), and average during injection (iii), together with the corresponding CFD results (iv), depicting isovolumes of cell fuel vapor pressure fraction in a non-dimensional range, for the nozzle N104.

The CFD result predicts a very similar phenomenon as the measurement; chosen isovolumes of cell gas fraction in a non-dimensional range of 0.4 to 1 visualize the vapor formation along the entire nozzle bore. As in the experimental images, the presence of a coherent vapor layer on the upper and lower walls of the bore extends to the nozzle bore exit and indicate a supercavitation cavitation pattern (**Figure 77** (iv)).

The eccentrically arranged nozzle N104 (**Figure 78**), where the nozzle bore has an angle of 90° and an eccentricity of 0.8 mm with respect to the axis of the main bore (see **Figure 60** for reference), shows a different cavitation pattern: due to the axis of the eccentricity, the cavitation pattern refracts most of the incoming light away, resulting in almost completely dark nozzle bores. The single-shot (ii) scarcely reveals non-cavitating zones on the left and right side of the nozzle bore indicating that the supercavitation zone is rotated into the optical axis. The fuel flow also enters the horizontal main bore from the left side although the cavitation patterns at the nozzle bore inlet indicate strong flow lines from the right side. This is due to the flow pattern in the nozzle main bore that diverts the flow as visible in the streamline CFD result for nozzle N105 in **Figure 74** (ii)). The simulation is in a very good agreement with the experiments (see **Figure 78** (iv)). The asymmetric vapor formation is well captured, while the locations of the cavitating zones are also corresponding to the results of the optical measurements.

The 75° angled, centrically arranged nozzle bore design N105 (**Figure 79**) shows the most moderate level of cavitation compared to the other two nozzle designs. The images are rotated so that the nozzle bore walls appear vertical. As a result, the nozzle main bore on the upper side of

the images is angled. The fuel enters the main bore from the left side and the nozzle is also supercavitating, although only on the right side where the angle between the main and nozzle bore remains the sharpest. There are some additional small cavitation patterns at the nozzle bore inlet, but they dissipate immediately leaving all geometrical cavitation to one side of the nozzle bore. This can also be realized by examining the results of the numerical simulation (**Figure 79** (iv)). The small dark area on the left side at the nozzle bore exit, is an optical distortion and not cavitating flow as clearly visible by comparing the background (i) with the single-shot (ii) and averaged (iii) images.

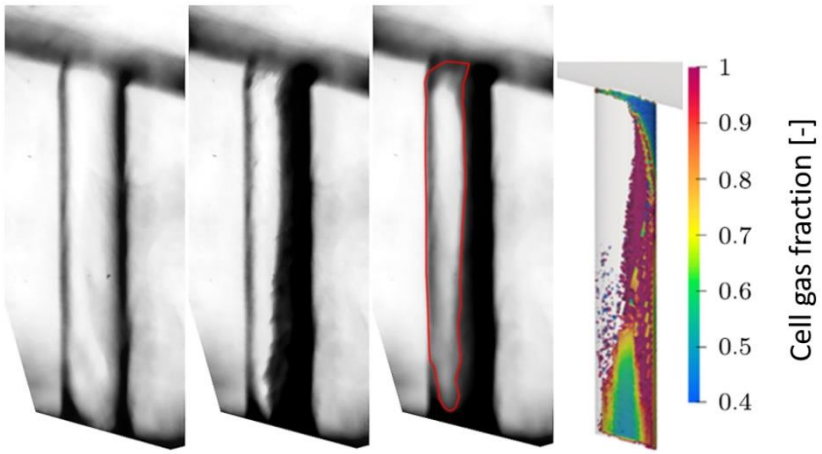

Figure 79 - Experimental in-nozzle flow images showing background (i), single-shot (ii), and average during injection (iii), together with the corresponding CFD results (iv) depicting isovolumes of cell fuel vapor pressure fraction in a non-dimensional range, for the nozzle N105.

5.6 Conclusions

The TNH together with the transparent PMMA nozzles was successfully used to acquire reliable in-nozzle flow images under large two-stroke marine Diesel engines like fuel pressure conditions and simplified (one-hole instead of five-hole setup), but realistic nozzle geometries [courtesy of R. Balz]. The experimental in-nozzle visualization reveals cavitation patterns in the nozzle bore with high contrast and high temporal resolution. Although experimental setup applied does not provide information on the third dimension, the in-nozzle flow images reveal interesting and useful details on the formation and stability of cavitation. This insight can be used to optimize the layout process for large two-stroke marine Diesel engine injector nozzles.

The present simulations have computed the cavitating in-nozzle flow of large two-stroke marine Diesel engine injectors accurately. A good agreement between simulation and experimental results was found for the qualitative comparison of the cavitation patterns, as well as for the quantitative validations using the momentum flux, showing differences of less than 6%. The simulations were able to capture the cavitation zone locations and vapor formation inside the nozzle bore for each of the three nozzle geometries accurately. The results deliver important insight into the flow properties that cannot be evaluated using the experimental data such as the strong redirection of the flow in the nozzle main bores and the three-dimensional information about the two-phase flow in the nozzle bores. By means of CFD, several complex cavitation phenomena, such as

supercavitation, geometry-induced cavitation and film-like cavitation were identified inside the nozzle bore for the different geometries.

The comparison of the three different nozzle setups with identical nozzle bore diameter indicates that the standard nozzle N101 has the highest velocities and most turbulent flow, while the eccentric nozzle has the lowest values in that regard. As a consequence, the standard nozzle N101 has the highest gas fraction at the end of the nozzle bore and hence the lowest discharge coefficient. The angled nozzle N105 has by far the lowest level of cavitation and therefore the highest discharge coefficient and momentum flux. As a consequence, this makes it the best, out of the three nozzles investigated, for large two-stroke marine Diesel engine injectors.

6 CHAPTER: Characterization of Spray Primary Breakup

6.1 Introduction

Following the LES spray primary breakup studies (Chapter 4), the present chapter focuses on the spray structures generated by the strongly nonuniform velocity distribution at the orifice outlet. Utilizing the LES results, for different atomizers, the resulting intact core, identified by a new method, and its breakup are investigated. Further, a new approach in characterizing droplet breakup is implemented, which is based on the Q-criterion introduced by Hunt *et al.* [286]. The droplet distribution is analyzed and compared between different atomizer layouts. Finally, the operational regime of the atomizer is characterized in terms of the non-dimensional numbers of the spray jet, which affect the spray dynamics.

Spray formation is already initiated in the nozzle bore. The injected liquid spray, emerging from the nozzle orifice into the combustion chamber, contains a coherent liquid core of high liquid percentage, which is directly connected to the orifice. The existence of the intact liquid core was proven by several spray experiments for conditions relevant to Diesel engines (Paciaroni *et al*. (2015) [237]; von Rotz (2015) [159]). In experimental studies of spray visualization, the outline of the illuminated spray is directly dependent on the minimum detectable droplet concentration and is identified according to a certain percentage of the maximum in the background grey-scale value. Von Rotz (2015) [159] identified the spray outline based on a cut-off value of 10% of the grey-scale maximum, while a limiting value of 90% was used for the spray core. While a similar approach can be followed in processing CFD results, care should be taken, as the volume fraction of liquid at a boundary depends on the local spatial resolution.

To identify the liquid core, a cut-off limit was set for the local liquid fuel volume fraction; cells with higher values than the cut-off were considered to be within the liquid core. As the results evidently depend on the cut-off value, three values were chosen, namely 0.9, 0.95, and 0.99, to investigate this dependence. Here, the concept was implemented by considering a seed cell at the nozzle orifice outlet, and proceeding to neighboring cells, thus categorizing all cells with respect to their inclusion to the intact core.

In turbulent flow to identify vortical structures, which dominate the momentum transfer between different flow regions (von Terzi *et al*. (2009) [238]), the validated method of Hunt *et al.* (1988) [239] referred to as the ‘Q criterion’, was chosen. The criterion defines a vortex as a "connected fluid region with a positive second invariant of velocity gradient tensor" i.e. $Q > 0$. This criterion also adds a secondary condition on the pressure, requiring it to be lower than ambient pressure in the vortex. In implementing the method, the parameter Q was computed for each computational cell, as follows:

Q-criterion

$$Q = \frac{1}{2} \cdot \left(\Omega_{ij} \cdot \Omega_{ij} - S_{ij} \cdot S_{ij} \right) \tag{72}$$

where S_{ij} and Ω_{ij} are exemplary elements of the strain rate and vorticity tensors, respectively.

Vorticity tensor

$$\Omega = \begin{pmatrix} 0 & \Omega_{12} & \Omega_{13} \\ -\Omega_{21} & 0 & \Omega_{23} \\ -\Omega_{31} & -\Omega_{32} & 0 \end{pmatrix} \quad (73)$$

Vorticity tensor element

$$\Omega_{ij} = \frac{1}{2} \cdot \left(\frac{\partial u_j}{\partial x_i} - \frac{\partial u_i}{\partial x_j} \right) \quad (74)$$

Rate of strain tensor

$$S = \begin{pmatrix} S_{11} & S_{12} & S_{13} \\ S_{21} & S_{22} & S_{23} \\ S_{31} & S_{32} & S_{33} \end{pmatrix} \quad (75)$$

Rate of strain tensor component

$$S_{ij} = \frac{1}{2} \cdot \left(\frac{\partial u_i}{\partial x_j} + \frac{\partial u_j}{\partial x_i} \right) \quad (76)$$

When $Q > 0$ the vorticity magnitude is more dominant than the strain rate in the flow field, thus fulfilling the definition of vortical structures, the asymmetric part of the tensor is predominant over the symmetric part. $Q > 0$ implies that the local pressure is smaller than the surrounding pressure.

Blobs, ligaments, and droplets are the outcomes of hydrodynamic instabilities developing at the intact core surface. To characterize the formation of new drops at each time step, the above existing entities were properly marked, and the corresponding cells are not further considered. The remaining cells were identified as a possible source of new drops if the local value of the volume of fluid exceeded a certain threshold. All such neighboring cells were merged into a larger (droplet containing) entity. The results of droplet identification were further processed to yield an actual spherical droplet size, of a proper value of velocity (determined from a momentum balance).

In the next step, the vicinity of the coherent liquid core was split in the streamwise and azimuthal directions, thus dividing the primary breakup zone into sectors (see **Figure 80**). For each segment, the droplet number and location, as well as statistics including the maximum, mean, and variance values of droplet diameter, and velocity were recorded.

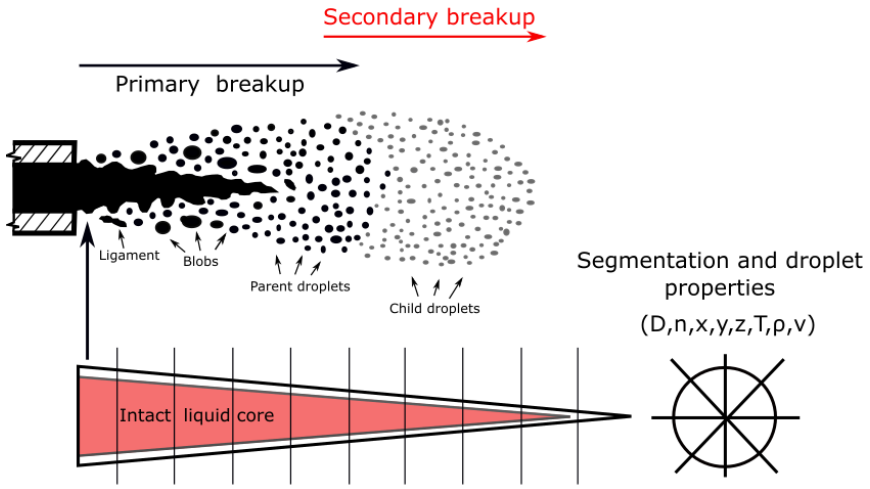

Figure 80 - Sketch of primary breakup and division of volume into segments used for statistical processing of included droplets.

Normalized mean values and variances of the aforementioned droplet properties were used to create distributions in terms of β-PDFs (Probability Density Functions) in all segments, thus

describing the spray primary breakup. The beta distribution is a continuous PDF function, defined in the interval [0,1], and parameterized with two positive shape parameters (α, β). These parameters are exponents of the independent variable (x), and control the shape of the distribution curve [240].

PDF of Beta distribution function

$$f(x;\alpha,\beta) = \frac{1}{B(\alpha,\beta)} \cdot x^{\alpha-1} \cdot (1-x)^{\beta-1} = \frac{\Gamma(\alpha+\beta)}{\Gamma(\alpha)\Gamma(\beta)} \cdot x^{\alpha-1} \cdot (1-x)^{\beta-1} \quad (77)$$

In Equation (*77*), $\alpha, \beta > 0$, $0 \leq x \leq 1$, B is a normalization parameter, ensuring that the cumulative probability is 1, and Γ() is the Gamma function [241-244]. The gamma function was calculated using the Lanczos approximation (1964) [241]. If $\alpha = \beta = 1$ and $x \in [0,1]$, the beta PDF is a normal distribution. For $\alpha, \beta > 1$, the most probable value (corresponding to the PDF maximum) can be calculated as follows:

Most probable value of Beta distributed x

$$M = \frac{\alpha - 1}{\alpha + \beta - 2} \quad (78)$$

When both parameters in Equation (*78*) are less than 1 ($\alpha, \beta < 1$), M becomes the least probable value.

The mean value (μ) can be calculated from the two parameters α, β: a

Mean value of Beta distributed x

$$\mu = \frac{\alpha}{\alpha + \beta} \quad (79)$$

The Beta distribution can thus be parameterized in terms of its mean value:

α

$$\alpha = \mu \cdot \nu, \text{where } \nu = (\alpha + \beta) > 0 \quad (80)$$

β

$$\beta = (1 - \mu) \cdot \nu, \text{where } \nu = (\alpha + \beta) > 0 \quad (81)$$

The variance of the distribution can be calculated from Equation (*82*):

Variance of Beta distributed x

$$\text{var}(x) = \frac{\alpha \cdot \beta}{(\alpha + \beta)^2 \cdot (\alpha + \beta + 1)} \quad (82)$$

The standard deviation is thus:

Standard dev. of Beta distributed x

$$\sigma(x) = \frac{1}{\alpha + \beta} \cdot \sqrt{\frac{\alpha \cdot \beta}{(\alpha + \beta + 1)}} \quad (83)$$

The applicability of beta distribution to spray applications was suggested by Pope in [52]. More information on the beta distribution and its properties can be found in [240].

6.2 Computational results

6.2.1 Primary breakup characterization

The liquid core is characterized by local high levels of liquid content. In the present CFD study, to identify the liquid core, a low cut-off limit was set for the local liquid fuel volume fraction; cells with higher values than the cut-off are considered to be within the liquid core. As the results evidently depend on the cut-off value, three values were chosen, namely 0.9, 0.95, and 0.99, to investigate this dependence. Here, the concept is implemented by considering a seed cell at the nozzle orifice outlet, and proceeding to neighboring cells, until cells not fulfilling the intact core condition are encountered.

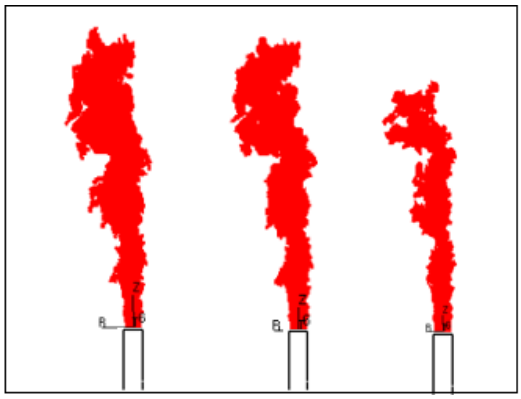

Figure 81 - Upper view of instantaneous intact liquid core, for different cut-off values of local liquid fuel volume fraction (VOF): VOF=0.9 (left), VOF=0.95 (centre), VOF=0.99 (right) in the spray primary breakup.

Results are presented in **Figure 81** for the case of a nozzle characterized by moderate eccentricity. The size of the intact liquid core decreases at higher threshold values.

Figure 82 presents computed time-averaged liquid core length generated by three different atomizer tips with the cut-off limit of VOF=0.99 applied on the intact liquid core. The higher eccentricity resulted in a shorter intact core length.

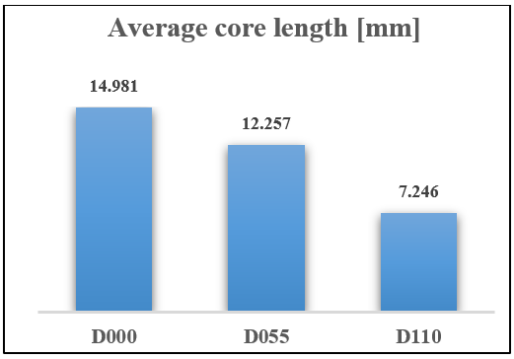

Figure 82 - Computed time-averaged liquid core length as function of nozzle eccentricity (VOF=0.99-1) in the spray primary breakup.

Figure 83 shows a comparison of the liquid core surfaces at an arbitrary time instance analyzed by Fast Fourier Transformation (FFT). The liquid core was segmented into 256 sectors in the

streamwise direction. The circumferential resolution was analyzed using slices with a size of 5°, where the core surface coordinates were averaged in each sector in order to assemble a general core surface presented by an intact line. In each case, many smaller amplitude wavelengths appear in the very near orifice $\lambda = 0 - 0.15$ mm, while further downstream the core length higher amplitude waves are observed. According to breakup models, the inspected waves on the core surface can correspond to the disintegrated droplet sizes, which fits well into the $0 - 1$mm droplet diameter range.

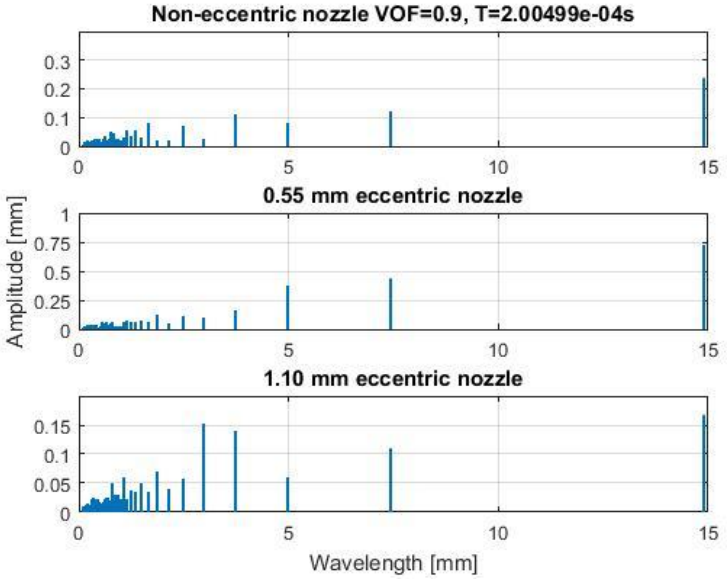

Figure 83 - Results of FFT analysis applied on the liquid core surface along the streamwise direction, in a circumferential segment 0-5° as function of nozzle eccentricity, at t=2.00499e-04s.

To fully characterize primary breakup, coherent structures at the liquid core boundaries need to be identified. As presented above, this is attained by implementing the Q-criterion analysis. The results are presented in **Figure 84**, for all three injector layouts of the present study, illustrating the spray structure at the liquid core border.

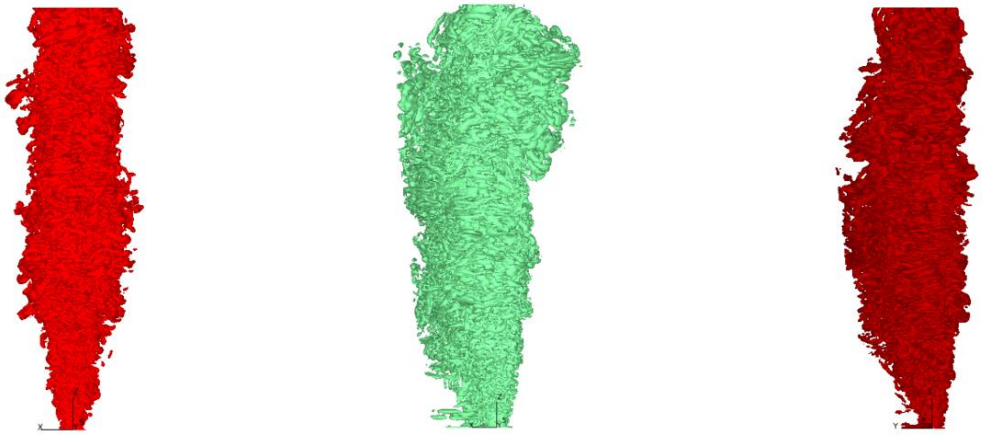

Figure 84 – Isosurfaces of the parameter Q, illustrating the spray structure, for a noneccentric nozzle (left), a nozzle with e = 0.55 mm (centre) and a nozzle with e = 1.10 mm (right).

Droplet identification, based on the procedure outlined above, resulted in a number of droplets ranging from about 6000 to about 20000, for the three nozzle layouts. **Figure 85** shows grid cells resulting from the identification of the droplet formation process. The cells presented in **Figure 85** (nozzle with eccentricity value of 0.55 mm) are coloured based on the volume of fluid value. Evidently, a denser spray structure is present close to the nozzle tip. Regarding droplet size, analysis of results indicates that the differences in Sauter Mean Diameter (SMD) for the three nozzle layouts are not significant; SMD values close to 0.04 mm were obtained.

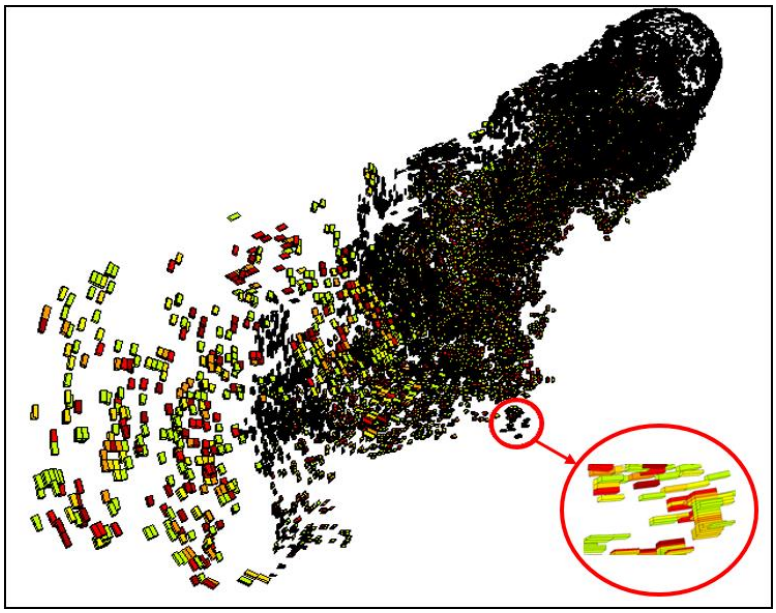

Figure 85 - Cells resulting from the droplet identification process, color-coded with volume of fluid value.

Figure 86 presents the computed number of droplets in the vicinity of the liquid core, for the mildly eccentric nozzle, using three different values as cut-off limit for the cell VOF content. The applied threshold on the core changes the surface wavelengths redound to a different breakup. It is verified that the higher threshold value results in a reduced number of droplets. Over time, a relatively steady number of droplets are identified. The differences in Sauter Mean Diameter (SMD) for the three cut-off values are not substantial; SMD values close to 0.04 mm are obtained.

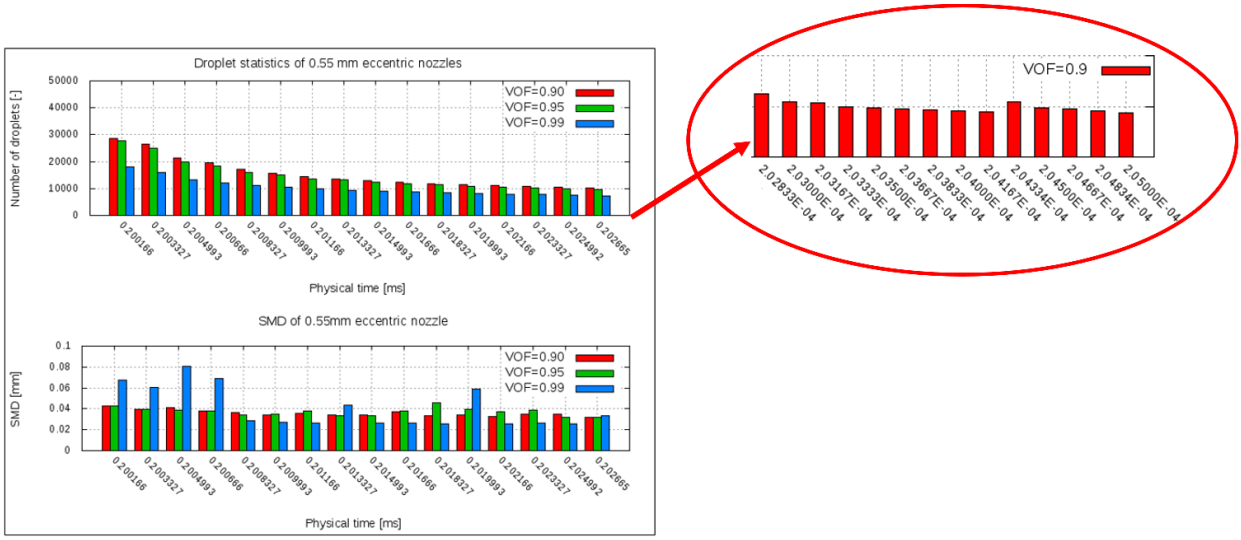

Figure 86 - Calculated number of droplets in the vicinity of the liquid core as function of time in the case of a moderate eccentric nozzle (e =0.55 mm), using three different cut-off limits for VOF content of cells.

During the core breakup, a detached droplet with a size of 0.5 mm was identified (see **Figure 87**). This liquid element is 20 times larger than the second most frequent droplet size during these time steps, and is in the range of the nozzle bore diameter. This droplet can be comprehended as a blob.

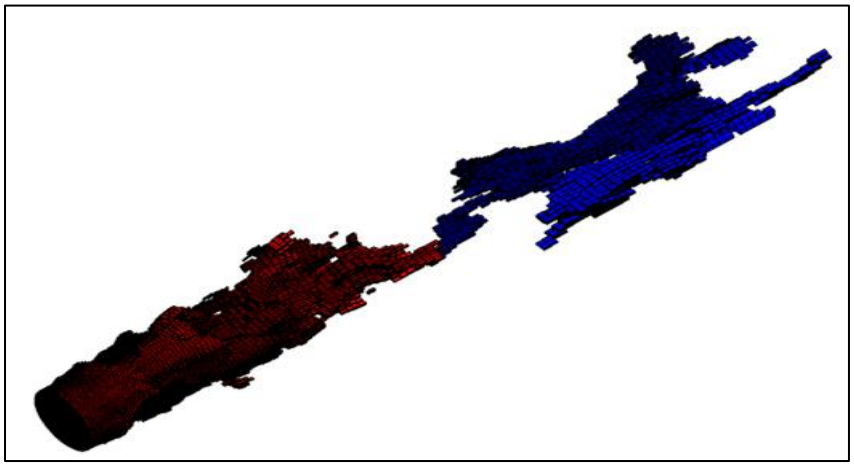

Figure 87 - Breakup of intact liquid core in the case of an eccentric nozzle (e =0.55 mm) with VOF=0.99 threshold on intact liquid core; "blob" disintegrating from the liquid core with a size of the nozzle bore diameter.

A comparison of three atomizer layouts is presented in **Figure 88,** using VOF=0.9 threshold on the coherent liquid core. It is found that the generated number of droplets is highest for the noneccentric nozzle. The middle eccentric nozzle generates droplets with the highest value of Sauter mean diameter (SMD), while using the noneccentric and the highest eccentric nozzles result in smaller droplets.

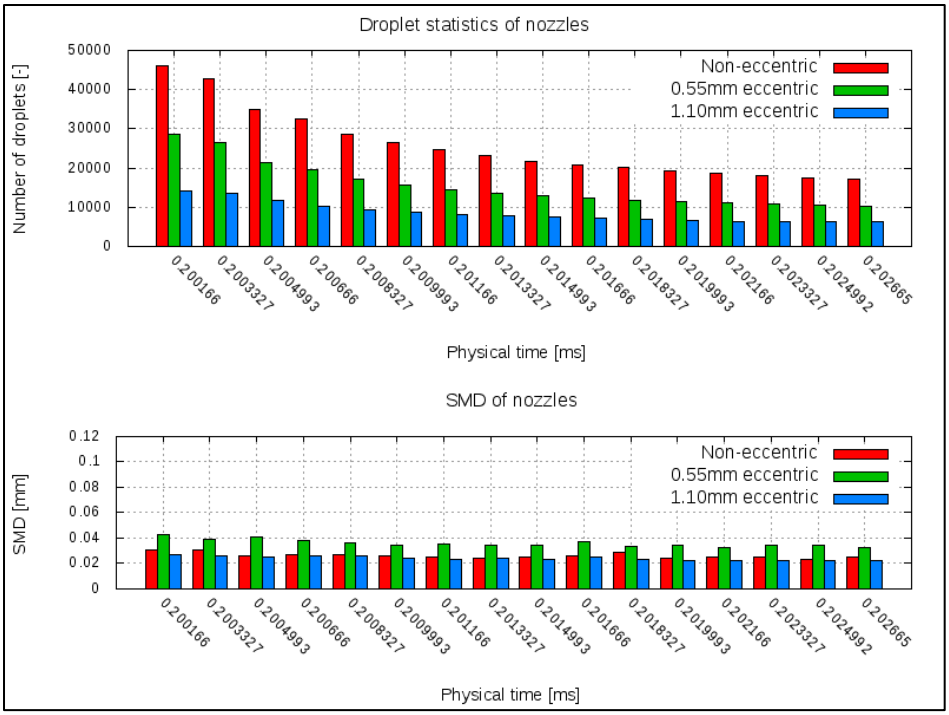

Figure 88 - Identified number of droplets (top) and calculated SMD for three atomizer layouts as function of time, using VOF=0.9 threshold on intact liquid core.

Figure 89 illustrates the atomizer categorization chart, where the atomizer types are defined by the relation of nondimensional Ohnesorge - Reynolds numbers. Based on calculation results, it can be stated that the investigated three atomizer geometries are in the same jet operation zones, namely in "the onset and end of drop formation along the surface of turbulent liquid jets in still gases". Moreover, the determined operation zone is located close to the "modern diesel injectors" and the "measurement of drop size at the spray edge near the nozzle in atomizing liquid jets" zones defined by Wu *et al*. (1995) [245]. These verify that the obtained results are in the regime relevant for engine applications.

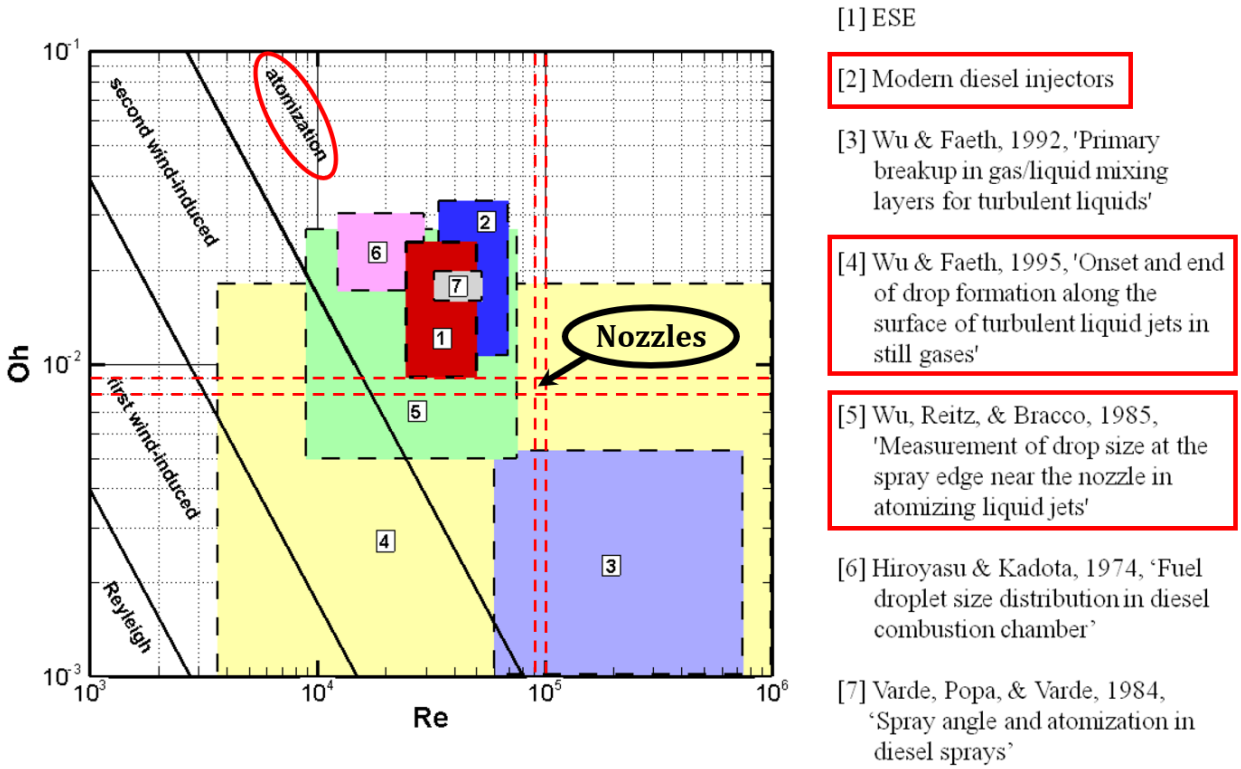

Figure 89 - Liquid jet operation regimes; location of the present nozzles is presented [246].

6.3 Conclusions

Spray structures, generated by the strongly nonuniform velocity distribution at the orifice outlet, were analyzed. Utilizing LES results of spray primary breakup for different atomizers, the resulting intact core, identified by a new method, and its breakup were investigated. Moreover, a new approach in characterizing droplet breakup, based on the Q-criterion, was implemented. To characterize the formation of new drops at each time step, a new droplet identification approach was implemented. The droplet number and location, as well as statistics including the maximum, mean, and variance values of droplet diameter, and velocity were analyzed and used to generate β-PDFs (Probability Density Functions) describing the spray primary breakup. The influence of nozzle eccentricity on the number of droplets generated in the spray primary breakup was investigated. Finally, the operational regime of the atomizers used in this study was characterized in terms of the nondimensional numbers of the spray jet. Computational results verify that the sprays investigated in the present Thesis are in the relevant atomization regime for engine applications.

7 CHAPTER: Proper Orthogonal Decomposition Analysis of Asymmetric Sprays

7.1 Introduction

This chapter presents results of Proper Orthogonal Decomposition (POD) analysis of asymmetric spray jets emanating from large two-stroke marine Diesel engine injectors. Low-dimensional modeling has proven its applicability in internal combustion engine research, in particular in the characterization of flow structure and dynamics. In the present thesis, spray primary breakup is simulated by means of (three-dimensional) Large Eddy Simulation (LES); these simulation results are further processed in terms of POD analysis, as presented in this chapter. First, proper tests are performed to verify the independence of results on the number of snapshots and shedding cycles. POD analysis identifies the dominant modes of the sprays studied here, and is used to reconstruct instantaneous fields. The time coefficients of POD modes are characterized using spectral analysis. Finally, the role of Kelvin-Helmholtz instabilities of the spray shear layer in disintegrating the spray liquid core is considered.

7.2 Proper Orthogonal Decomposition

The POD method was extensively used over the last two decades in several applications of thermo-fluids, ranging from incompressible flows to engine flows and sprays [247-256]. Qin *et al*. (2011) [257] has investigated the spatial and temporal evolution of in-cylinder spray characteristics by applying POD on Mie-scattered spray images. Here, it was found that the mean field contains more than 90% of the total intensity. In [258,259], the POD technique was applied on the scalar field (combustion images), suggesting that POD contributes useful information for combustion variation. POD analysis was used to the characterization of large and small structures of fuel spray data [260], while in [261] the method of snapshots was implemented to the POD analysis of a subsonic jet computed by LES. Chen H. and Xu M. (2013) [268] have conducted the POD analysis in order to distinguish spray structure variations from different engine conditions by using 50 snapshots to reach convergence.

In the present work, a 3-D non-mean subtracting POD approach is implemented, in the context of the method of snapshots, to analyze simulation results of asymmetric diesel sprays. These results, also reported in [180] and [181], are the outcome of a coupled Volume of Fluid (VOF) – LES approach, focusing on the primary spray breakup, and have demonstrated the significance of nozzle geometry on spray formation. Specifically, in the current study, POD analysis is applied to the velocity and scalar fields of a nonevaporating spray emanating from an eccentric atomizer, calculated by the VOF – LES approach. These findings are used to reveal the properties of coherent flow structures identified and distributed among the POD modes.

7.3 POD analysis

POD is a powerful approach for analyzing large computational and experimental datasets describing the response of dynamical systems, intending to identify low-order models that capture the dominant system dynamics. POD was introduced in the field of fluid mechanics by Lumley [263]. It has gained significant popularity in the last three decades, for the analysis of simulation

and experimental data. Using numerical or experimental data, the method identifies the basis functions (proper orthogonal modes), which optimally capture the system energy. As a result, the system dynamics can be accurately reproduced by using an appropriate (finite) number of these functions and proper time-dependent coefficients; the latter is calculated by projecting the data onto the computed modes. By projecting the governing equations onto these modes, it is possible to obtain low-dimensional ordinary differential equation models for a system such as a fluid flow. To minimize the cost of calculating the spatial modes (eigenfunctions), Sirovich introduced the 'method of snapshots' [264], also adopted in the present study.

In the present work, the tangential, radial, and axial velocity components of the spray jet (functions of space and time) are denoted by $\vec{v}\,(x,t) = \{u, v, w\}$. All velocity vectors are arranged in the following matrix (U), with k being the number of points in space and m the number of snapshots (points in time). It is noted that POD analysis can be performed both for the velocity vector and for each of the individual components. All velocity vectors are arranged in the following matrix (U):

Velocity fluctuation matrix

$$U = \left[\bar{V}^1\ \bar{V}^2 .. \bar{V}^k\right] = \begin{bmatrix} \begin{pmatrix} u_1^1 & u_1^2 & u_1^3 & \cdots & \cdots & u_1^k \\ \vdots & \vdots & \vdots & \vdots & \vdots & \vdots \\ u_m^1 & u_m^2 & u_m^3 & \cdots & \cdots & u_m^k \\ \vdots & \vdots & \vdots & \vdots & \vdots & \vdots \\ v_1^1 & v_1^2 & v_1^3 & \cdots & \cdots & v_1^k \\ \vdots & \vdots & \vdots & \vdots & \vdots & \vdots \\ v_m^1 & v_m^2 & v_m^3 & \cdots & \cdots & v_m^k \\ \vdots & \vdots & \vdots & \vdots & \vdots & \vdots \\ w_1^1 & w_1^2 & w_1^3 & \cdots & \cdots & w_1^k \\ \vdots & \vdots & \vdots & \vdots & \vdots & \vdots \\ w_m^1 & w_m^2 & w_m^3 & \cdots & \cdots & w_m^k \end{pmatrix} \end{bmatrix} \quad (84)$$

In the next step the auto-covariance square matrix (M x M) is created:

Auto-covariance matrix

$$\theta = U^T \cdot U \quad (85)$$

And the corresponding eigenvalue problem becomes:

Eigenvalue problem

$$\theta\varphi_i(t) = \lambda_i\varphi_i(t) \quad (86)$$

where $\varphi_i = \varphi_1 \ldots \varphi_m$ are the eigenvectors and λ_i are the eigenvalues. The magnitude of each eigenvalue is representative of the energy of the corresponding eigenmode (eigenvector); eigenvectors are commonly arranged in a decreasing order, i.e., from the most energetic to the least energetic modes ($\lambda_1 > \lambda_2 > \lambda_3 > \lambda_m$) [265].

The eigenvectors of the aforementioned eigenvalue problem make up a basis for reconstructing the original flow vector $\bar{V}\,(x,t)$:

Original flow vector

$$\bar{V}\,(x,t) = \sum_{i=1}^{m} \alpha_i(t)\lambda_i\varphi_i\,(x) \quad (87)$$

The low-order modes are usually associated with large-scale flow structures. If a flow contains such structures, these can be realized in the first few high-energy POD modes. Therefore, the flow

field can be sufficiently approximated by taking into account a proper number, p, of high-energy POD modes ($p < m$):

Flow vector with high-energy modes

$$\overline{V}(x,t) = \sum_{i=1}^{p} \alpha_i(t)\lambda_i\varphi_i(x) \quad (88)$$

According to Chatterjee [266], performing the POD analysis with or without subtracting the average does not affect the calculation, but only the interpretation of the results. It is commonly stated that the first mode of the POD analysis is equivalent to the mean of the ensemble. Siegel *et al*. (2007) [284] have performed POD without subtracting the mean flow on a generic wake flow developing a von Karman vortex street behind a D-shaped cylinder. Here, it was stated that the first POD mode will typically be the mean flow, which is followed by large scale fluctuating modes, in this particular case, representing the von Karman vortex street. H. Chen in [268] has aimed to reveal the extent of the importance of subtracting or not subtracting the ensemble average prior to performing the POD analysis. In this particular investigation, measured in-cylinder engine flows by POD analysis using 200 velocity field snapshots proved that POD mode 1 was an excellent estimate with respect to the kinetic energy. It was shown that the energy content of POD mode 1 was approximately equal but slightly larger than, that of the ensemble-averaged value. M. El-Adaway in [269], has applied POD on velocity vector field images taken by utilizing Stereo-PIV technique inside an engine cylinder. This study has concluded, similarly to [262], that the resulted in flow pattern of the ensemble average was identical to POD mode 1 without subtracting the mean prior performing the POD analysis. In terms of energy content, it was found that POD mode 1 had slightly higher than that of the ensemble average value. The analysis has led to the conclusion that the first POD mode was an excellent estimate of, but not completely identical to, the ensemble average. In [268], argumentations for not subtracting the mean before executing a POD analysis were discussed. It was demonstrated that keeping the ensemble average coefficients of POD mode 1 can reveal the extent to which the mean flow is present and its cycle-to-cycle variability. Further information on POD methodology and, the interpretation and application of subtracting and non-subtracting POD can be found in [247-268].

In the present study, a non-mean subtracting POD implemented in Star-CD v.4.28, is applied on the scalar-velocity fields.

7.4 Problem setup and numerical approach

As part of the CFD studies of the present thesis, also reported in [180,181], combined URANS - LES simulations were performed for different large two-stroke marine Diesel engine atomizer geometries, including in-nozzle flow under nonevaporating conditions (40 bar, 400 K). The spatial domain of the CFD simulations has consisted of the atomizer tip needle, the nozzle bore, with a diameter of 0.75 mm and a length of 4-5 mm, and the plenum, with a length of 25 mm. The domain has extended up to the bypass hole, of a diameter which accounted for the total area of the other four nozzle orifices of the actual injector (**Figure 45**). The spray primary breakup was computed based on the approach of coupled Volume of Fluid (VOF) - Large Eddy Simulation (LES). To assess the spatial resolution requirements of the LES calculations, prior transient in-nozzle flow simulations were carried out with RANS turbulence modeling. Each URANS calculation was

integrated in time up to 0.015s (for a large two-stroke engine operating at 100 RPM, this time corresponds to 3.25° of engine crank angle) until reaching a converged steady-state solution; the results were then used as initial conditions for LES calculations of different grid densities. For the URANS simulations, structured grids were generated with the commercial software ICEM CFD, containing approximately 1 million cells. These calculations were carried out with the Volume of Fluid (VOF) method and the High-Reynolds-number k-ε turbulence model. Turbulence parameters were initialized after testing several values for turbulence intensity and lengthscale. The solution method utilized a velocity-pressure coupling based on the implicit SIMPLE method. The three-time level implicit Euler central differencing scheme was applied. The time step was fixed to a value of 10^{-05} s, corresponding to values of the Courant (CFL) number in the range of 0.2-1. Since LES demands extensive computational resources, the nozzle geometry was simplified in that only a part of the nozzle bore was kept, whereas the plenum was shortened, extending up to 20 times the nozzle bore diameter (15mm). The aforementioned URANS results were taken to initialize the flow field for VOF-LES calculations. A cell layer of the URANS grid located in the nozzle bore was attached to the LES grid, where the flow properties of the cells were used as an inlet boundary condition for the LES. In the present primary breakup study, the Germano and Lilly dynamic-Smagorinsky subgrid-scale turbulence model was utilized (Germano *et al.* (1996) [60]; Lilly (1992) [65]), where, in addition to the low pass filter (at the level of the numerical grid), a second spatial filter (the test filter), was applied (Scotti *et al*. (1997) [68]). The model coefficient was determined dynamically, thus changing in time and space to account for the local state of turbulence.

The computational time of the LES investigations was correspondent to approximately 10 shedding periods of the emerging spray. The results demonstrated that the eccentric nozzle geometry significantly affects the injected fuel, already within the nozzle bore. Surface disturbances were initiated on the surface of the liquid right after entering the plenum. Here, the liquid surface went through a primary breakup process in the vicinity of the liquid core, mainly due to aerodynamic forces and turbulence-induced atomization, resisted by the surface tension forces. Highly asymmetric spray behavior was experienced for the different nozzle layouts. The resulting spray structures were analyzed, and it was illustrated that the eccentric arrangement of the nozzle results in a deflection normal to the main spray direction. The deflection increased as a function of eccentricity. The results showed that the spray was not just deflected in the spanwise direction, but it also deviated from its symmetry line upwards, in the radial direction. Further information regarding the numerical setup, grid sensitivity analysis and CFD modeling can be found in 4.6.

Nozzle eccentricity can substantially affect the resulting structure of spray flow, as illustrated in **Figure 54** and **Figure 55**, which show the computed instantaneous fuel concentration (void fraction) in the horizontal and vertical plane crossing the plenum in the middle of the nozzle bore, for three values of nozzle eccentricity, respectively. These CFD results were calculated using the VOF – LES approach with the Star-CD code; the fuel thermophysical properties are those of n-Dodecane. In the present study, the nozzle characterized by an eccentricity of 0.55 mm was chosen as the flow geometry of the POD analysis.

The LES results show that a statistical steady state is reached at a time of 0.2 ms (0.12° engine crank angle degree), at which the spray Reynolds number at the nozzle bore outlet is calculated. Here, a time-averaged velocity is considered, based on the velocity magnitude values in the last cell layer of the orifice.

Reynolds number
$$\mathrm{Re_D} = \frac{\mathrm{U_D} \cdot \mathrm{D}}{\nu} = \frac{330 \cdot 0.00075}{1.8446 \cdot 10^{-6}} = 1.35 \cdot 10^{5} \tag{89}$$

Using the calculated Reynolds number of the turbulent flow, a typical Strouhal number (non-dimensional shedding frequency) can be defined for the spray jet, using a validated literature correlation. Typical values of Strouhal number for turbulent jet flows are in the range of $0.1 - 0.5$ [278-282]:

Strouhal number
$$\mathrm{St_D} = 0.198 \cdot \left(1 - \frac{19.7}{\mathrm{Re_D}}\right) \approx 0.198 \tag{90}$$

The value is consistent with values obtained by means of FFT analysis of the present LES results. The approximated vortex shedding frequency and period are calculated based on the spray Strouhal number.

Shedding frequency
$$\mathrm{f_D} = \frac{\mathrm{St_D} \cdot \mathrm{U_D}}{\mathrm{D}} = 88\ \mathrm{kHz} \tag{91}$$

Shedding period
$$\mathrm{T_D} = \frac{1}{\mathrm{f_D}} = 1.136 \cdot 10^{-5} \approx 1.14 \cdot 10^{-05}\ \mathrm{s} \tag{92}$$

Siegel *et al*. (2015) [267] have shown for time-periodic flow modes identical to those calculated from snapshot-based ensembles containing a large number of shedding cycles can be obtained by using snapshot ensembles of a small integer number of cycles, down to a minimum of one shedding cycle. An account of the validity of physical POD modes through transient flow situations, the POD analysis needs to be performed on a data set of relatively short length so that the POD modes represent the spatial flow features.

To characterize the turbulent spray jet flow, four full shedding periods were calculated for the spatial POD modes starting from the previously obtained URANS-LES results (approximately 1300 and 10 vortex-shedding periods, respectively). A small constant time step of $\Delta t = 1\mathrm{e}^{-09}\ \mathrm{s}$ was chosen, maintaining the CFL number below 0.2.

Simulation time
$$\mathrm{T_{sim}} = \sum_{4\ \mathrm{periods}} 4 \cdot \mathrm{T_D} = 4 \cdot 1.14 \cdot 10^{-5} = 4.6 \cdot 10^{-05}\ \mathrm{s} \tag{93}$$

The complete data set utilized in the POD analysis consists of 150 snapshots, where the sampling interval was correspondent to 0.67% of a shedding period.

With respect to computational cost, it is noted that the present calculation of four shedding periods by means of LES has required approximately 7 days using 36 cores of a parallel cluster.

7.5 Results and discussion

Applying POD on the flow field provides an appropriate orthonormal basis to represent the flow. POD modes are sorted in an order of decreasing energy; thus, the first mode contains the maximum energy, and higher modes are characterized by decreasing energy content. POD analysis reveals the dominant flow patterns, identifies large scale structures, and determines the number of modes necessary to reconstruct the flow fields, thus providing a reduced-order representation of the flow. Large coherent structures are associated with the most energetic modes, while small structures are associated with the higher modes. In the present flow problem, the large structures are induced by Kelvin-Helmholtz instabilities in the shear layer of the spray, disintegrating further into ligaments and drops. To ensure the overall accuracy of POD analysis, different tests were performed, varying (i) the number of snapshots for a constant time frame, and (ii) the number of shedding periods, for a given number of snapshots within one period. The results are presented next.

7.5.1 Variation of number of snapshots

In varying the number of snapshots, the sampling time was kept constant, equal to four shedding periods. Three tests were performed, corresponding to a total of 50, 100, and 150 snapshots. **Figure 90** shows the fractions of relative energy (multiplied by 100) captured by the first 15 POD modes for all three velocity components to determine the contribution of each mode to the original field. Different sample numbers of ensembles for four shedding cycles are considered.

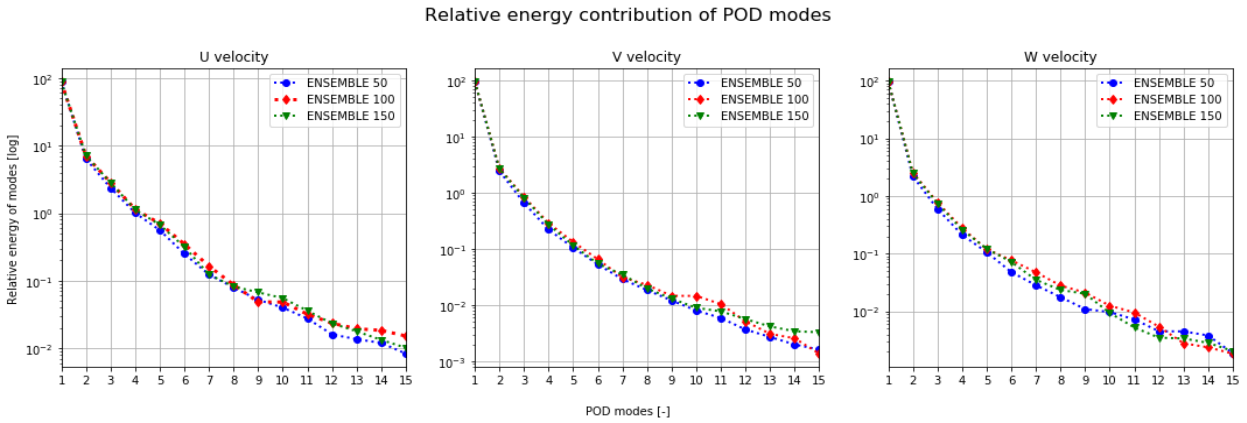

Figure 90 - Mode relative energy of the circumferential (U), the radial (V) and the axial (W) velocity component, for the 15 most energetic POD modes, computed for different numbers of snapshots. The sampling time is equal in all cases to four shedding cycles.

The corresponding cumulative energy content versus the number of modes is presented in **Figure 91**. The present results show a good agreement for all three numbers of snapshots, while the results for 100 and 150 snapshots nearly coincide. Similar observations also were made regarding the concentration field (**Figure 92**). These findings are consistent with the observations in [260] for

the POD analysis of experimental spray data. In summary, the analysis verifies that the number of snapshots used here is appropriate.

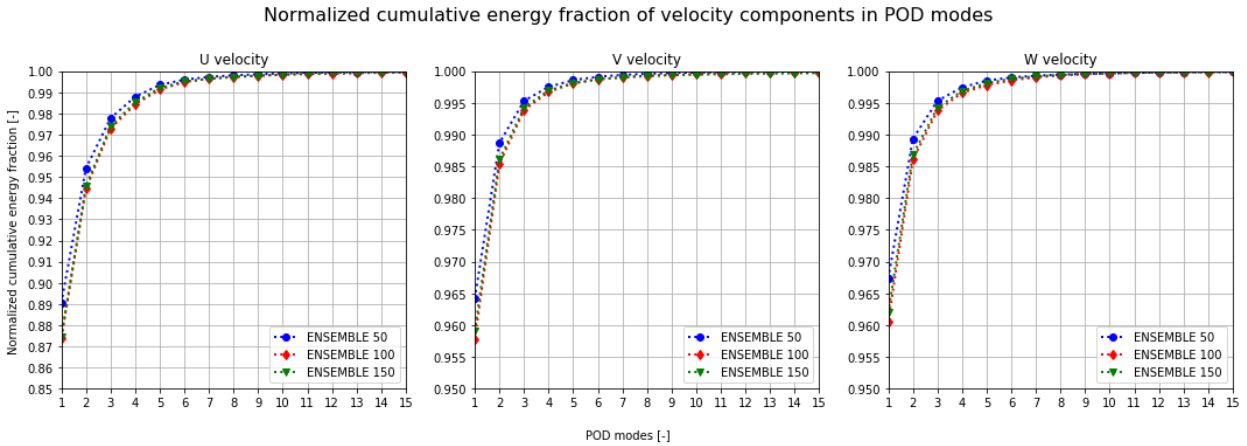

Figure 91 - Cumulative energy versus number of modes, of the circumferential (U), the radial (V) and the axial (W) velocity component, up to the 15th most energetic POD mode, computed for different numbers of snapshots. The sampling time is equal in all cases to four shedding cycles.

Further, the present POD analysis of the velocity field shows that about 98% of the total energy is contained in the first four modes and that practically all the energy is captured with few modes (**Figure 91**). **Figure 92** presents the cumulative energy content of the concentration field (void fraction). Here, POD mode 1 has approximately 80% of the energy, while the lower modes demonstrate relatively high energy contents (Mode 2 5%, Mode 3 2.5% and, Mode 4 1.7%) compared to the velocity field modes.

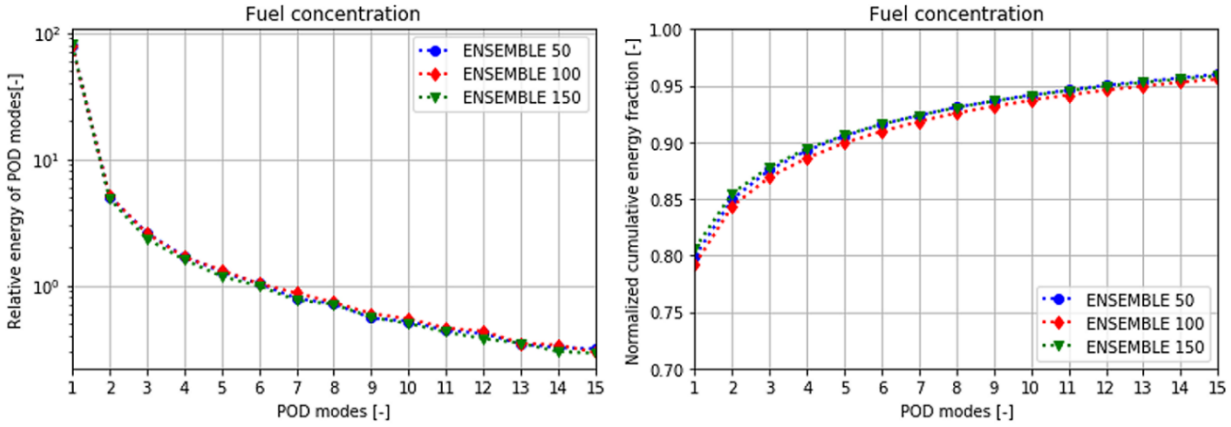

Figure 92 - POD analysis of concentration (void fraction) field: mode relative energy, multiplied by 100 (left), and cumulative energy versus number of modes (right), up to the 15th most energetic mode, computed for different numbers of snapshots. The sampling time is equal in all cases to four shedding cycles.

The results also reveal that POD mode 1 can be of the greatest contribution to the original flow field reconstruction. Furthermore, the presence of higher modes of the concentration field indicates the occurrence of small flow structures, which are still significant for turbulent mixing in the present spray jet problem. **Figure 93** summarizes these findings.

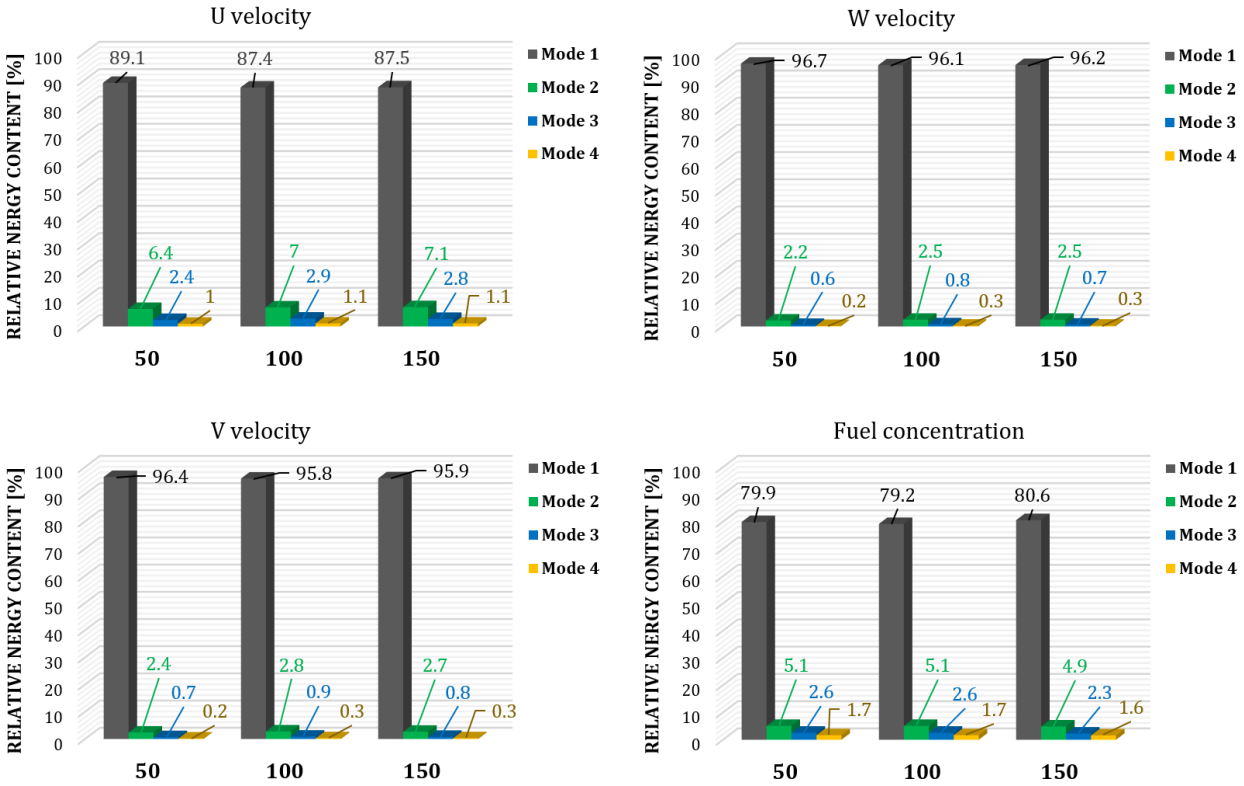

Figure 93 Values of relative energy content of the four most energetic modes, multiplied by 100, of the circumferential (U), the radial (V) and the axial (W) velocity component, and for fuel concentration (void fraction), computed for different numbers of snapshots.

7.5.2 Variation of spray shedding periods

Next, the effect of varying the number of shedding periods on the results of POD analysis is checked, for a number of periods ranging from one to four. Using the outcome of the previous subsection (effects of varying the number of snapshots) the number of snapshots on the current variation is kept constant, equal to 150.

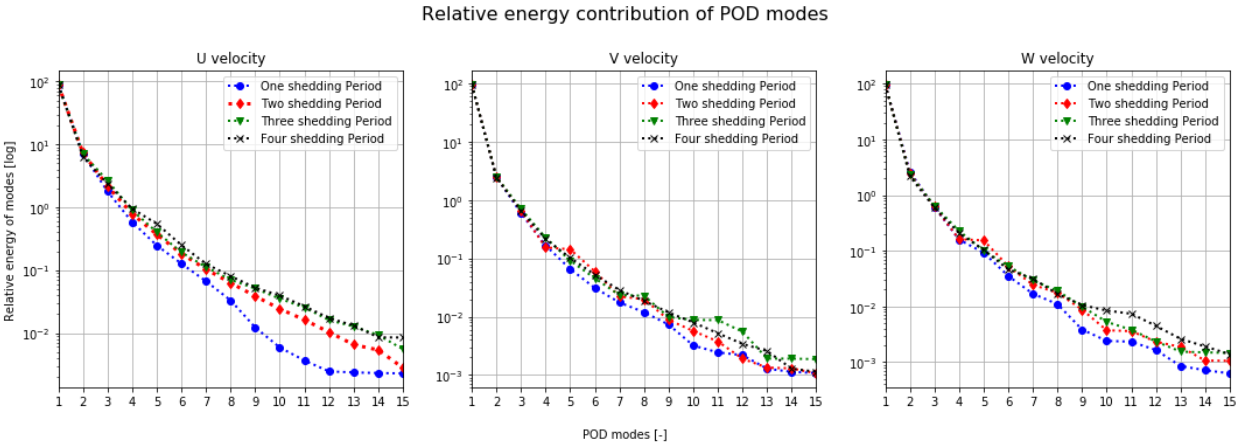

Figure 94 - Mode relative energy of the circumferential (U), the radial (V) and the axial (W) velocity component, for the 15 most energetic POD modes, computed for different numbers of shedding periods. A number of 150 snapshots is used in all cases.

Figure 94 presents the relative energies for the first 15 POD modes for all three velocity components, for different numbers of shedding periods. The corresponding cumulative energy versus the number of modes is presented in **Figure 95**. The current outcome shows that the discrepancies in energy content are rather small and practically non-existing between the analyses for 3 and 4 periods. This is also valid for the results regarding the liquid concentration (void fraction) field (**Figure 96**).

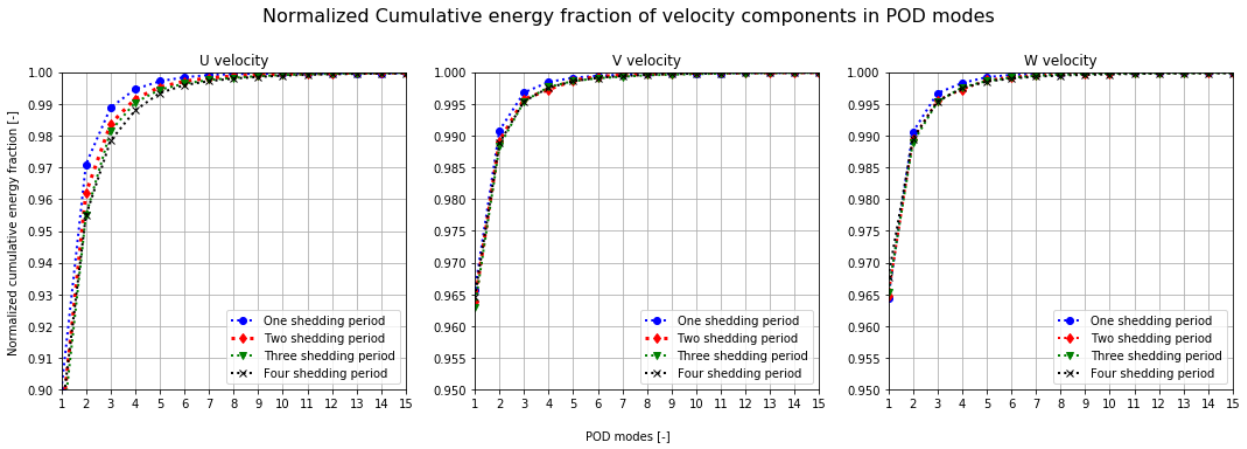

Figure 95 - Cumulative energy versus number of modes, of the circumferential (U), the radial (V) and the axial (W) velocity component, up to the 15th most energetic POD mode, computed for different numbers of shedding periods. A number of 150 snapshots is used in all cases.

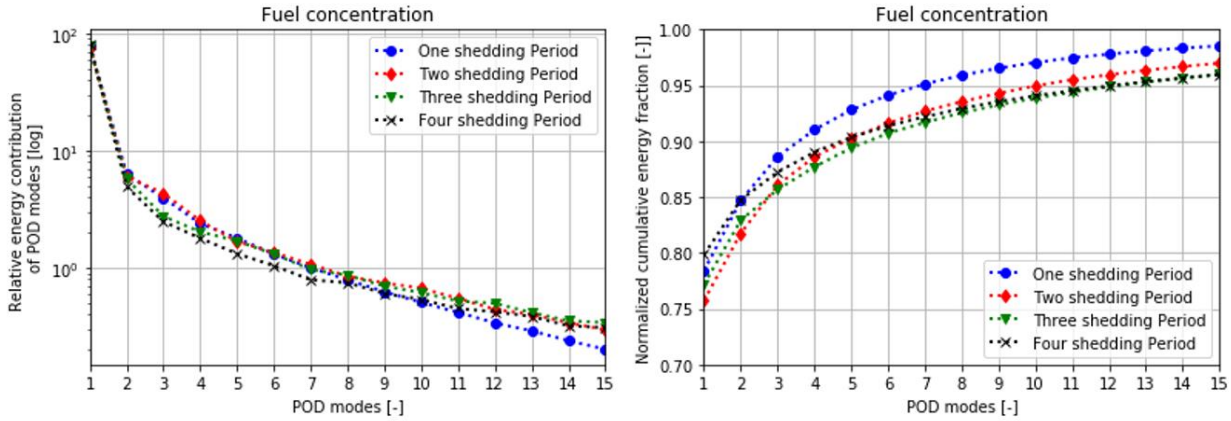

Figure 96. POD analysis of concentration (void fraction) field: mode relative energy, multiplied by 100 (left), and cumulative energy versus number of modes (right), up to the 15th most energetic mode, computed for different numbers of shedding periods. A number of 150 snapshots is used in all cases.

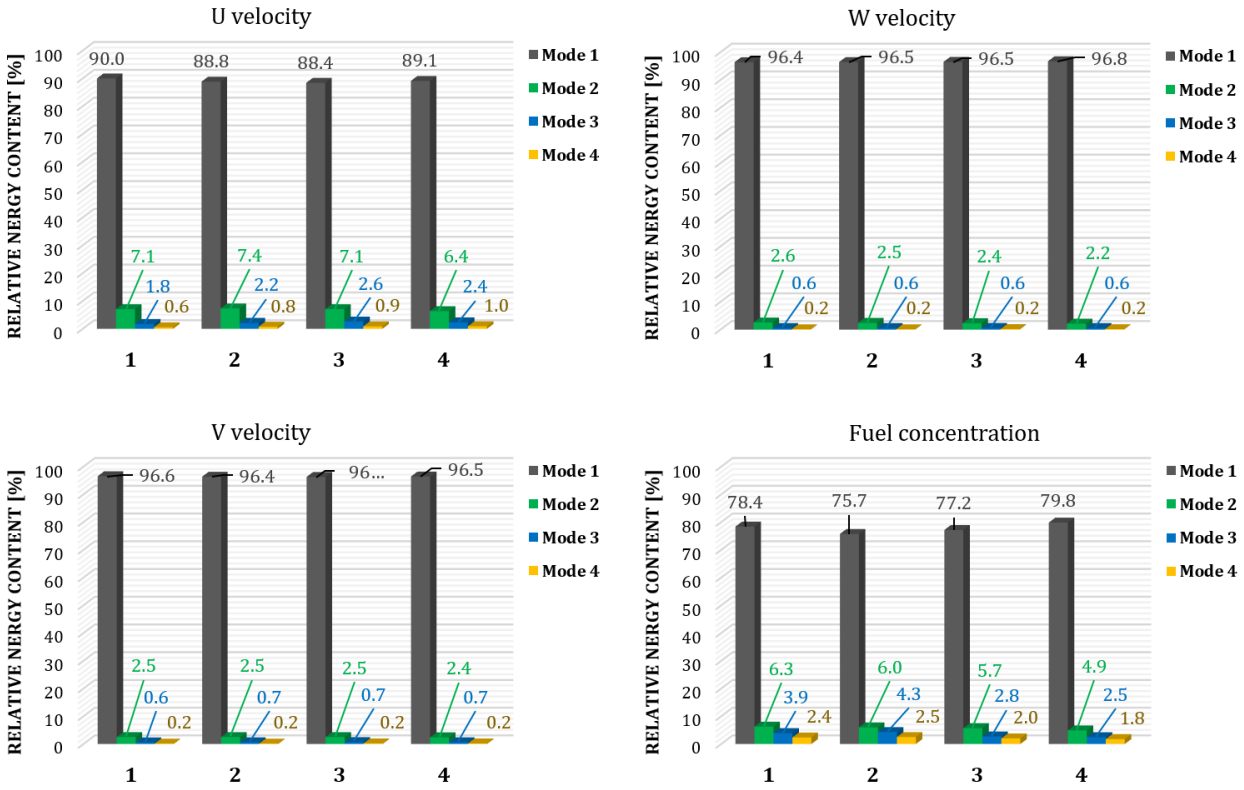

Figure 97 POD analysis of relative energy content of modes depending on the number of shedding periods considered.

Figure 98 depicts a comparison of POD modes 2 and 3 of the three velocity components, for the different shedding periods, verifying that the same mode structure is calculated for all values of flow sampling time considered. Focusing on spray primary breakup, the disintegration of liquid blobs, ligaments, and droplets from the liquid core at the air-liquid interface is expected. The analysis of POD modes can provide an insight into the mixing and explanation of spray fluctuation by extracting quantitative information on the characteristics of the spray atomization.

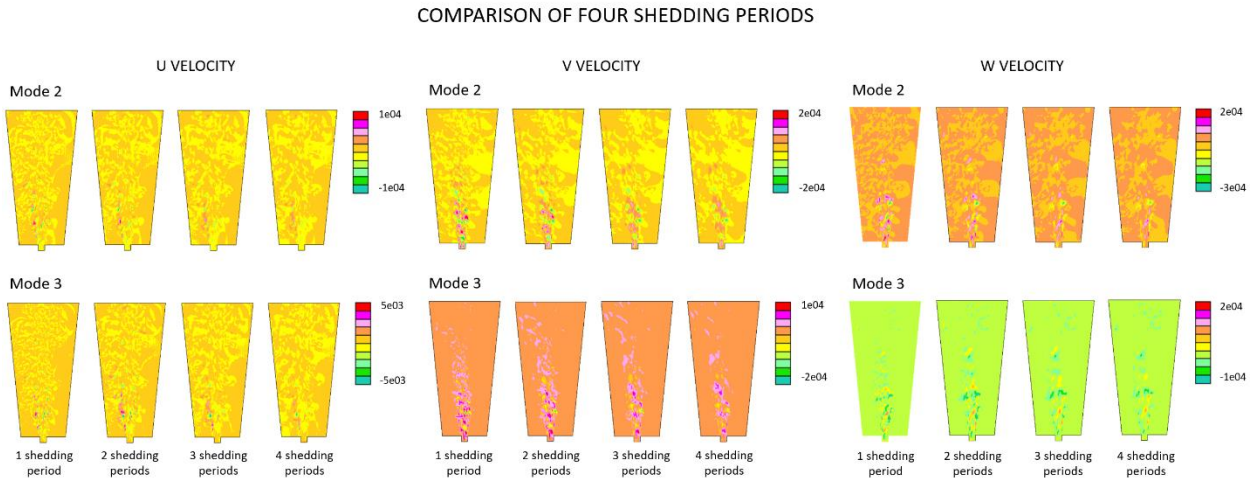

Figure 98 - Spatial structure of the 2nd and 3rd most energetic eigenmodes of the velocity components fields (horizontal plane cut).

POD modes are characterised by positive and negative regions. Visualizations of a scale from green to red colours are presented here. The change of sign and colour can be interpreted as a negative correlation of intensity fluctuation between these regions. Therefore, in the case of an individual snapshot, when the intensity is higher than average in a red region, the image intensity is lower than average in a green region and vice versa. In physical terms, this signifies an alternation in the presence of liquid in the corresponding regions, which causes the intensity of the image to change [285].

7.5.3 POD modes and flow reconstruction

Results of POD analysis are presented next for a sampling time of four shedding periods. According to Holmes *et al.* (2012) [271], the suggested criteria for reconstructing a low order system by summing up just the most dominant modes are, at least 90% of the total energy should be included, and the mode with energy fraction larger than 1% should be considered. By utilizing the criteria, in this specific study, the first 6 modes are required for the reconstruction of the ensemble-averaged flow field. G. Charalampous *et al*. (2019) [285] has described in his study the morphology of cluster formation and their evolution by analyzing spray primary breakup of a co-axial airblast atomizer. Following his findings, this section attempts to describe the spray primary breakup by examining the spatial distribution of the six most energetic modes of the fuel concentration (void fraction) field presented in **Figure 99**.

The spatial flow structures in the full spray region are identified by the different POD modes. These structures are the spray liquid core, disintegrating blobs, ligaments, and large drops in the spray primary breakup zone. Moreover, spray morphology in terms of the spray breakup length, spray deflection and cone angles, are well recognised through physical processes. These large-scale flow structures are the most energetic POD modes in the entire primary breakup regime. The characteristic dimensions of the flow structures contributing to both the liquid core and the full spray decrease with the POD mode number. The relationship between the dimension of the flow structure and POD mode provides an estimate of the required spatial scale to resolve these structures.

Mode 1, containing approximately 80% of the total energy, is characterized by the bulk spray structure and should be thus associated with the intact spray core emerging from the orifice and large structures forming in the shear layer region. The redistribution of mass from the continuous liquid are the large-scale flow structures induced by the Kelvin-Helmholtz instability due to the interaction of the liquid jet with the surrounding air. The change in colour highlights the negative relation between the intact liquid core and the detached liquid elements. For the liquid core, the POD mode 1 describes the liquid jet injection and its deflection on the opposite side of eccentricity in the plenum. Disintegrating large-scale structures from the liquid core are also well represented by this POD mode. The deflected distribution of fuel mass and the more identified large-scale structures on the left side of the liquid core suggests a clearly asymmetric spray development.

Mode 2 and 3, with an energy content of 5% and 2.5%, should be associated with the ligaments and blobs forming out of the disintegrating large structures. The atomization process presented by these modes is mild; droplet clusters formed out of the liquid core. Mode 3 shows longer nodes emerging from the nozzle than mode 2 and their presence of liquid suggests an inverse relationship.

The width of the identified structures increases with the distance from the orifice. The deflected spray formation is clearly presented in these Modes.

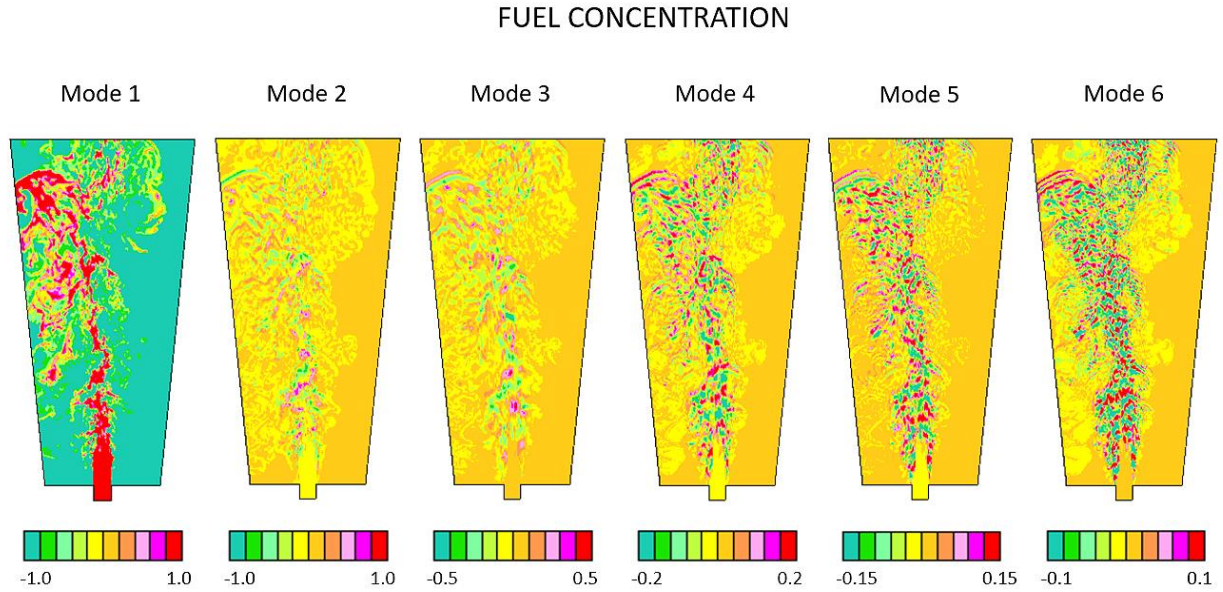

Figure 99 - Spatial structure of the six most energetic eigenmodes of fuel concentration (void fraction) field (horizontal plane cut).

Higher modes, characterized by finer scales, correspond to the smaller structures and droplets forming out of the disintegration of larger entities. In contrast, these modes represent the fine local details surrounding the edge of the spray and, a more chaotic behavior than the high-energy fraction containing lower modes. Mode 4-6 show the presence of more symmetric structures and capture well the highly asymmetric spray formation. Atomization is more distinct on the low-velocity side of the nozzle bore. These higher modes follow the droplet formation from their creation at the liquid jet surface and their transfer downstream. The spatial locations of the different modes do not coincide since the airflow accelerates the disintegrated liquid particles. When a new breakup happens, the previously formed liquid structures are still adjacent (see POD mode 6). It is noted that the first four modes capture 90% of total energy, thus successfully depict the spray characteristics and in all cases taken, the mode structure reflects the spray asymmetry induced by the eccentric nozzle geometry.

A reconstruction of the instantaneous field, using the computed four spatial modes and corresponding time coefficients, is expected to provide a rather good representation of the instantaneous field. Indeed, the results presented in **Figure 100** verify a very good comparison between the actual void fraction field, computed via LES, and the reconstructed field, at a time instant corresponding to the end of the sampling time. The ensemble average has a similar, but not identical structure compared to POD mode 1, which suggests that the identified bulk spray structure can represent the spray characteristics and the higher modes have less significant roles. The reconstructed field is in good agreement with the instantaneous field at each investigated cross-section of the flow domain, proving that in this particular case, the first four most dominant modes are enough to represent the original flow field.

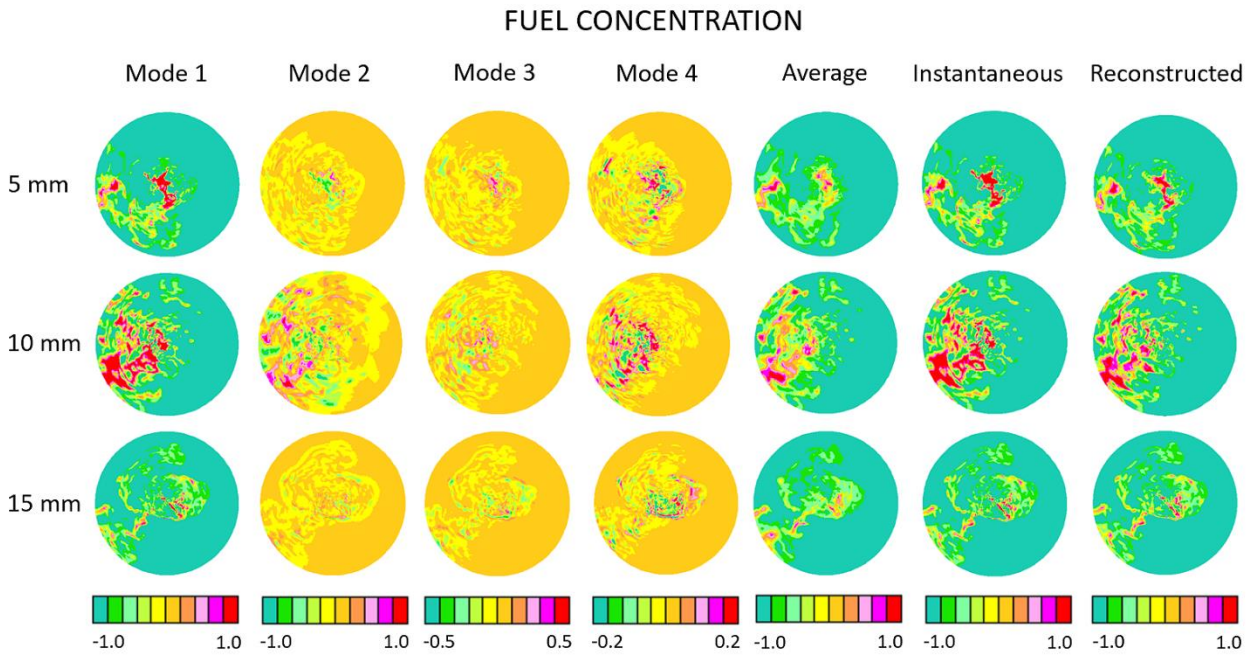

Figure 100 - Spatial structure of fuel concentration (void fraction) at three representative cross-sections of the plenum: spatial structure of the four most energetic eigenmodes, computed time-averaged and instantaneous fields, and corresponding reconstructed field.

A similar outcome can be found in [252], where the temporal and spatial evolution of an in-cylinder fuel spray was studied and in [262,269], in the case of POD applied in in-cylinder flow analysis. A possible even better comparison can evidently be attained by adding higher modes in reconstructing the instantaneous field.

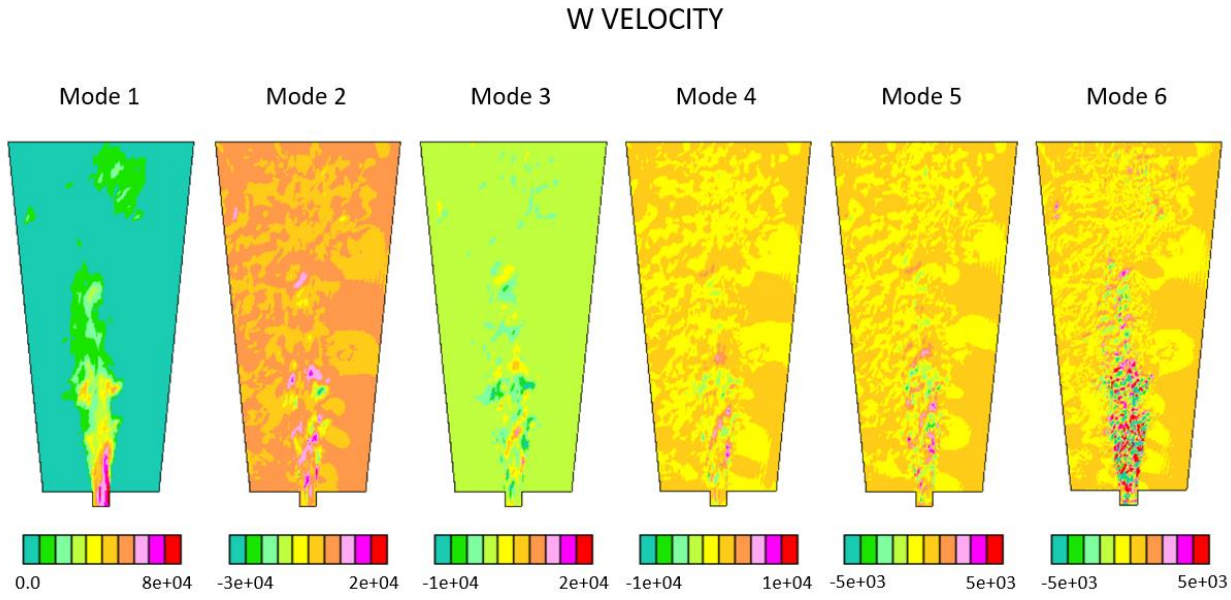

Figure 101 - POD modes 1-6 of axial velocity.

To characterize the spatial structure of velocity modes, the computed six most energetic modes of the W (axial) velocity component are presented in **Figure 101**. The spatial structure of the 1st mode is suggestive of the axisymmetric type of shedding and showing a clear outline of the injected spray. High intensity of velocity fluctuations in the orifice near field can be realized by analyzing the 2nd and 3rd POD modes. Some of the higher modes are indicative of an azimuthal instability, while mode 6 is characteristic of the presence of small scales in a highly turbulent and chaotic flow.

7.5.4 Temporal analysis of flow structures

The analysis of time coefficients may provide insight into the periodicity of features captured by the POD analysis and, the relation between different modes and the flow nature. Time coefficients are calculated by projecting the mean-centred snapshot matrix onto the POD modes and are represent the fraction of the POD mode that contributes to the snapshot. Negative or positive values of the time coefficient depict the corresponding contribution of the analyzed POD mode to the particular snapshot.

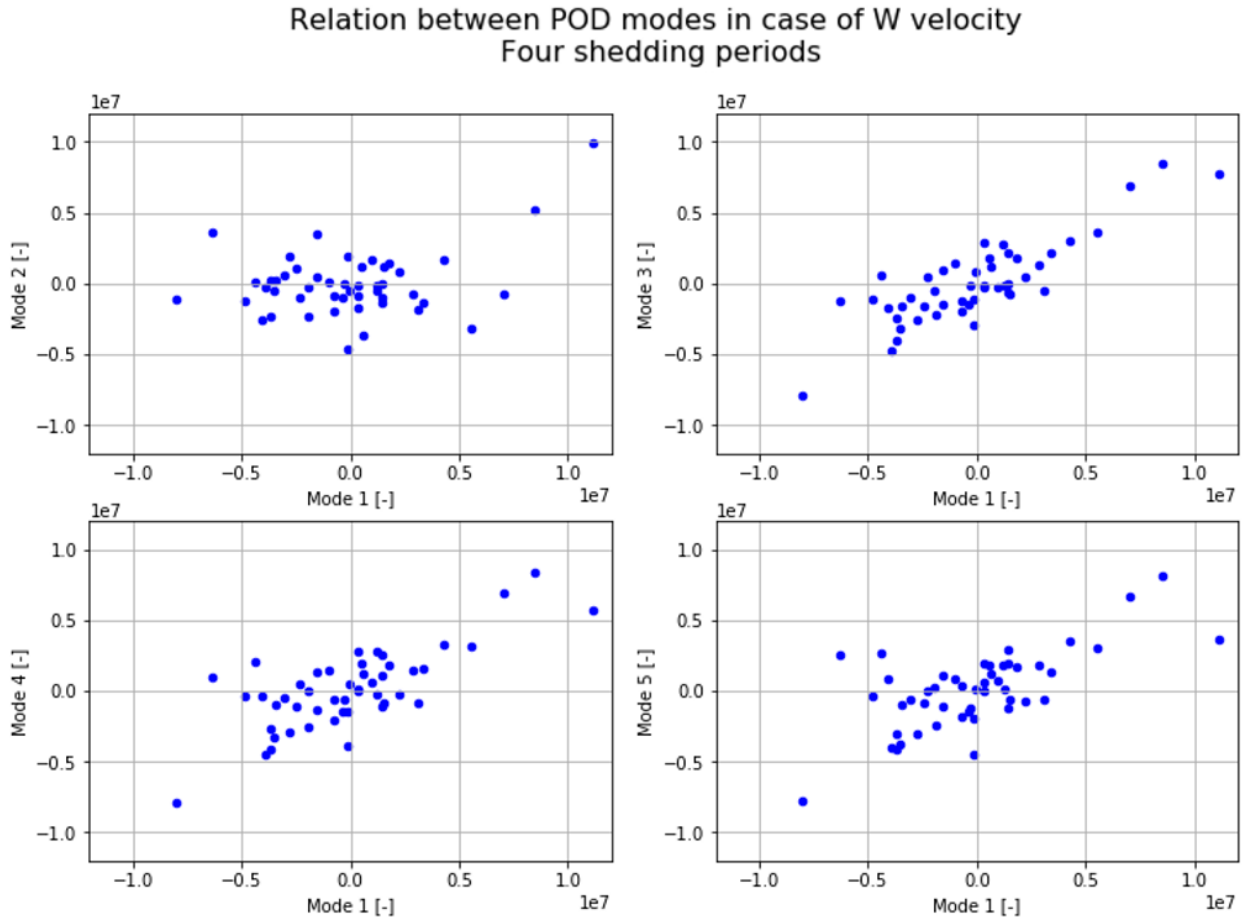

Figure 102 - Streamwise velocity component: scatter plots of time coefficients of POD Modes 2-5 versus Mode 1 coefficient.

Figure 102 presents phase-space plots of mode coefficients 2-5 versus the coefficient of mode 1 of the axial velocity component (analysis of 150 snapshots). The presence of a symmetric distribution for mode 2 suggests symmetric shedding structures, while the skewed distributions for

modes 3-5 suggest a correspondence with helical vortex structures in the shear layer regions. The POD mode magnitude coefficients can be used for the analysis of spectral characteristics of the individual modes. The frequency content of POD modes can be identified by means of Fast Fourier Transformation (FFT) analysis (see also [249], [286-289]). In the current study, the Power Spectral Density (PSD) is used to execute the frequency spectral analysis. PSD describes how the power of a signal or time series is distributed over frequency. In this example, PSD simply represents the square of the real part of the frequency obtained from the FFT on the original signal. A similar approach was utilized in the work of Khan *et al*. (2016) [286] in order to identify and characterize coherent structures inside a gasoline injector nozzle.

Results are presented in **Figure 103** for the axial velocity component mode coefficients. The modes demonstrate fairly identical temporal characteristics and a clear periodicity for each mode can be realized. The outcome of the FFT analysis verifies the presence of a non-dimensional frequency Strouhal number close to 0.2 and, in accordance with the value computed above by means of an established correlation, as well as the presence of a subharmonic and higher harmonics.

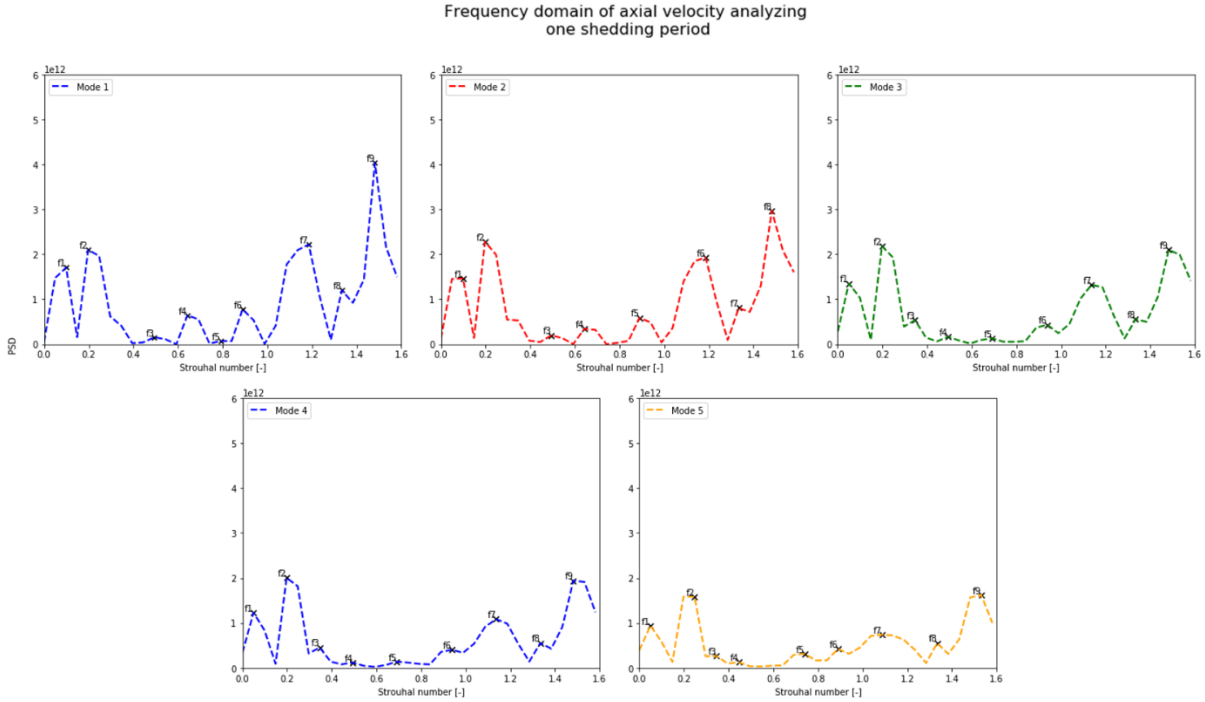

Figure 103 - Calculated frequency spectra of time coefficients of axial velocity component POD modes 1-5.

7.6 Conclusions

In the present study, an asymmetric diesel spray generated by an eccentric nozzle of a large two-stroke marine Diesel engine was computed by means of LES. A 3D POD analysis was implemented to characterize the spray morphology in terms of the calculated velocity and fuel concentration fields. For the full spray, the POD modes successfully represented the fuel injection, deflection, disintegration, and droplet cluster formation.

The POD analysis successfully identified small-large characteristic scales; the calculated modes were correlated to disintegrating flow structures from the intact liquid core and interpreted as a liquid atomization process. Simulation results enlightened the role of Kelvin-Helmholtz instabilities in disintegrating the spray liquid core, generating ligaments, and large droplets during the primary breakup. The characteristic dimensions of the flow structures contributing to both the liquid core and the full spray decrease with the POD mode number. The relationship between the dimension of the flow structure and POD mode provides an estimate of the required spatial scale to resolve these structures.

The first POD mode qualitatively provided a very good estimate of the flow pattern of the ensemble average. Higher POD modes (Mode 4-6) show the presence of more symmetric structures and capture well the highly asymmetric spray formation. Atomization is more distinct on the low-velocity side of the nozzle bore, suggesting that the asymmetric spray formation is originated from the highly nonuniform and nonsymmetric velocity field inside the nozzle bore. The results demonstrated that the flow dynamics can be represented by a few dominant modes; thus, the flow field can be reconstructed by including the 4-5 most energetic modes. Analysis of time coefficients of the POD modes presented that they were characterized by dominant frequencies representative of turbulent axisymmetric jets. Overall, the present POD analysis clearly represented the spray morphology and successfully accounted for the asymmetric spray formation in the primary breakup regime.

8 CHAPTER: Spray Secondary Breakup Simulations

8.1 Introduction

This chapter presents simulations of spray secondary breakup by means of Reynolds-Averaged Navier-Stokes (URANS) equations in conjunction with validated spray models. Spray simulations were performed in a Lagrangian framework, and accounted for the further breakup of large droplets identified in the LES spray primary breakup studies. β-PDFs, statistically describing the spray primary breakup (Chapter 6) were used as inflow conditions in the secondary breakup simulations. Spray morphology parameters were quantified, and were found to be in good agreement with those of recent experiments. The present approach was also shown to yield superior results for spray breakup, compared with the conventional, URANS-only, approach.

8.2 Computational method

Numerical simulations were carried out by using commercial CFD software Star-CD version 4.26 in nonevaporating conditions (40 bar, 400 K). The computational volume corresponds to the simplified geometry of the SCC with a diameter of 500 mm and a deepness of 150 mm. The injection location was comparable to the engine like arrangement. Block-structured numerical grids were generated with the overall cell size of approximated 1 million hexahedral cells. Grid test was performed under nonevaporating conditions, where inside the relevant spray zone the cell size was varied in the range of 1.2-3 mm. Here, the spray tip penetration length was used as a validation criterion. The initial conditions of the domain were adapted to experimental conditions inside the combustion chamber. Important simulation parameters are presented in **Table 14**.

Table 14 - Summary of nozzle layouts, fuel properties and boundary conditions.

Properties	Specifications
Injected droplets (velocity, location, number, diameter)	From LES of primary breakup
Chamber conditions	40 bar, 400 K (non -evaporating) 90 bar, 900 K (evaporating)
Surrogate fuel	n-Dodecane
Fuel temperature	333 K
Turbulence model	URANS-High Re number k-Ɛ
Nozzle eccentricity	0.0, 0.55, 1.10 mm
Grid size	≈ 1 million

Based on earlier investigations, (CHAPTER: 4) the high-Reynolds k-ε turbulence model was used with model constants found in the literature. The pressure-velocity field was coupled by a first order predictor-corrector (PISO) algorithm, whilst the spatial discretization was solved by a second-order MARS scheme. The temporal discretization was performed with the value of 10^{-5} s. The walls were modeled as no-slip boundaries with the adiabatic condition. The injected fuel was n-Dodecane has comparable physical parameters to the Light Fuel Oil (LFO) used in the experiments. The initial temperature of the fluid was set to 333 K. The fuel mass was defined based on measured injection duration and calculated mass flow at the orifice. The injected number of

droplet parcels in each time step was defined as the ratio of the injected fuel mass and the sum mass of the droplets taken from each segment of the primary breakup zone.

8.3 Initialization of secondary breakup

The total injected fuel mass (m_{fuel}) and injection duration (Δt_{inj}) were calculated from the in-nozzle flow simulation results. The simulated injection massflow rate very closely matched the measured value. In the secondary breakup calculations, the time step (t_{step}) was explicitly defined with a constant value of 10^{-05} s. Injected droplets were derived from LES spray primary breakup simulations. In the secondary breakup simulation, it was ensured that the mass and momentum flux calculated in the nozzle bore were preserved in the identified droplets of the spray primary breakup. The number of parcels and their masses were calculated iteratively, considering (1) a momentum balance between the jet momentum flux (based on nozzle flow), and the momentum flux of the new parcels introduced, and (2) a mass balance between the injected mass flow rate (based on nozzle flow) and the one of the new parcels. Driving equations of this iterative calculation are the followings:

Nozzle area

$$A_{nozzle} = \frac{{D_{nozzle}}^2 \cdot \pi}{4} \tag{94}$$

Mass flux of nozzle flow

$$\dot{m}_{nozzle} = \bar{v}_{nozzle} \cdot A_{nozzle} \cdot \rho_{fuel} \tag{95}$$

Mass of injected fuel

$$m_{fuel} = \dot{m}_{nozzle} \cdot \Delta t_{inj} \approx m_{fuel\_exp} \tag{96}$$

Where D_{nozzle} is the nozzle orifice diameter, $\bar{v}_{nozzle}$ is the time-averaged velocity magnitude of liquid calculated before the orifice by LES in-nozzle flow simulation. The mass flux was closed by using a droplet velocity correction. This was performed by using the ratio of the mean values of injection velocity ($\bar{v}_{nozzle}$) and the droplet velocity ($\bar{w}_{drop}$) based on the primary breakup droplet identification results.

Adapted droplet streamwise velocity

$$w_{drop_{new}} = \frac{\bar{v}_{nozzle}}{\bar{w}_{drop}} \cdot w_{drop} \tag{97}$$

The mass and sum injected mass of droplets can be calculated as follows:

Mass of droplet

$$m_{drop} = \frac{\pi}{6} \cdot D_{drop}(i,j)^3 \cdot \rho_{fuel} \tag{98}$$

Sum mass of injected droplets

$$\sum_{i,j=1}^{i=nseg,j=ncirc} m_{drop} = (\frac{\pi}{6} \cdot D_{drop}(i,j)^3) \cdot n_{drop}(i,j) \cdot \rho_{fuel} \quad (99)$$

The injected number of parcels in each time step is calculated as follows:

Number of injected parcels

$$n_{parc} = \frac{m_{fuel}}{\sum m_{drop} \cdot \frac{\Delta t_{inj}}{t_{step}}} \quad (100)$$

After closing the mass flux of the disperse phase with the streamwise velocity component, the momentum flux was closed as well. Momentum closure in the streamwise direction was done by adjusting the number of droplets, as well as the droplet diameter in each sector and segment in the specified time step. It was assumed that 99% of the momentum generated in the nozzle bore was conserved around the intact liquid core.

Momentum of injected fuel

$$P_{nozzle} = 0.99 \cdot m_{fuel} \cdot \bar{v}_{nozzle} \cdot \frac{\Delta t_{inj}}{t_{step}} \quad (101)$$

The generated momentum of injected droplets in each segment and sector can be calculated using the sum mass of injected droplets and the new adapted droplet velocity ($w_{drop_{new}}$):

Sum momentum of injected drops

$$P_{drops} = \sum_{i,j=1}^{i=nseg,j=ncirc} m_{drop} \cdot w_{drop_{new}} \cdot n_{drops} \quad (102)$$

The momentum flux of the injected droplets (I_{drops}) was assumed to satisfy the following criterion:

Momentum flux criterion

$$0.999 \cdot I_{nozzle} \leq I_{drops} \leq 1.001 \cdot I_{nozzle} \quad (103)$$

Here, the droplet diameters were changed to balance the momentum fluxes.

Diameter of new droplet

$$D_{drop\_new}(i,j) = \sqrt[3]{\frac{I_{nozzle}}{I_{drops}}} \cdot D_{drop}(i,j) \quad (104)$$

The adaptation of droplet diameter influences the mass of droplets and thus the number of parcels injected. Therefore, the droplet diameter and the number of droplets in each segment were iteratively calculated according to Equation (*98*) and (*100*), until the momentum flux criterion was not satisfied (Equation (*103*)).

8.4 Simulation setup

In the secondary breakup calculations, the previously presented spray primary breakup results were used as inflow conditions with the Kelvin–Helmholtz Rayleigh–Taylor (KH-RT) breakup model [155]. Further results were obtained using the Reitz (Reitz and Bracco (1982) [143], (1986) [144]) and Reitz–Diwakar models (Reitz and Diwakar (1987) [152]) for the primary and secondary breakup models in a URANS-only framework. The numerical setup of the Reitz-Reitz/Diwakar spray breakup case is summarized in **Table 15.** Based on experiments, a spray cone angle of 20° was implemented. Details of the nozzle geometry and associated parameters, as well as parameters pertinent to the actual SSC experiment, are reported in **Table 15**.

Table 15 - Geometry and physical parameters pertinent to the injector and injection characteristics.

Properties	Specifications
Orifice diameter	0.75 [mm]
Nozzle L/D	5.7
Discharge coefficient	0.85
Contraction coefficient	0.7
Injected fuel	n-Dodecane
Fuel temperature	333 [K]
Mass flow rate	0.11 [kg/s]
Injection duration	11 [ms]

8.5 Characterization of spray structure

Characteristic and important spray features are the tip penetration length, spray angle, as well as deviations from a symmetric structure pertinent to the present injectors. Results of the reference experiments are reported in Schmid *et al.* (2013) [50], where a detailed description of the image analysis process used also was given. In these experiments, spray visualization could be realized only in areas farther than 10 mm from the nozzle tip. In the present simulations of the secondary breakup, droplets were identified, and the droplet with the highest coordinate in the streamwise direction was used to define the penetration length. Care was taken to avoid presenting non-physical results based on the sole identification of an isolated droplet. In the experimental study of Schmid *et al*. (2013) [50], the spray angle was determined based on visualizing data at a distance $40 \cdot D_0$ from the orifice (see **Figure 104**). For consistency, this also was followed in processing results of the present simulations to determine the spray angle. Finally, it is noted that, for the asymmetric sprays of the present study, spray deflection was characterized with respect to two planes passing from the nozzle tip, in particular a horizontal and a vertical one. This was done by calculating the mass centre of gravity of the segments considered, and based on the outcome, the spray centreline.

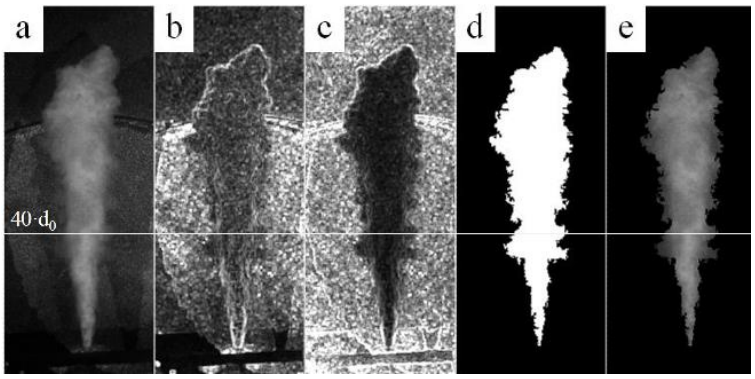

Figure 104 - Image processing steps [158].

8.6 Spray simulation in the SCC

Spray development in the SCC was simulated using a URANS modeling framework and spray models accounting for the breakup of large drops introduced at the nozzle tip and for the subsequent breakup of smaller droplets. Droplet β-PDFs, based on the LES results of the primary breakup, containing the most important droplet information, were used as initial conditions to calculate droplet breakup, in a Lagrangian framework. As indicated above, the SCC calculations of the present study are mainly based on the Kelvin-Helmholtz Rayleigh-Taylor (KH-RT) model and checked against results using the Reitz and Reitz-Diwakar models for the primary and secondary breakup, respectively, as well as against experiments.

The simulation setup accounts for droplet breakup, droplet drag calculation, turbulent dispersion, and droplet-wall interaction. The droplet surface tension and viscosity were set for the measured value of temperature at the injector inlet.

8.6.1 Grid sensitivity analysis

Grid sensitivity analysis is a commonly used procedure applied in spray simulation with the Euler-Lagrangian framework. Results of spray modeling depend critically on the spatial resolution [154,291,292]. In our case, the droplet diameters and the injected mass are originated from the LES simulation of the primary breakup. These droplets of each segment along the liquid core composed of droplet parcels being injected at each time step. The initial droplet diameters restrict the minimum cell size, as it was pointed out in [135] that the fundamental hypothesis of a void fraction close to one cannot be respected regarding the mesh size, especially close to the nozzle exit. Thus, cell sizes above 1.3 mm were chosen to complete the grid sensitivity analysis, respecting the Lagrangian theory and reaching convergence.

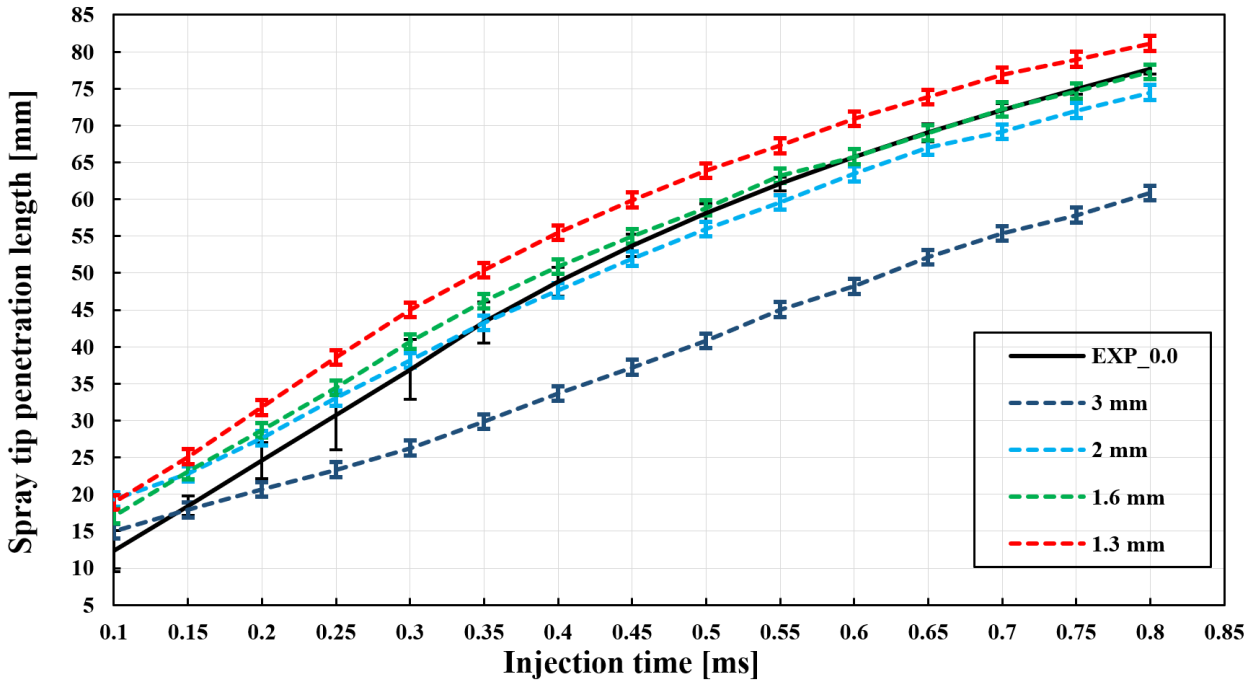

Figure 105 - Grid sensitivity analysis of noneccentric nozzle based on spray tip penetration length as function of injection time.

Figure 105 presents the temporal evolution of spray tip penetration length for the case of the noneccentric nozzle, for different spatial resolutions. **Figure 105** indicates that, for the present injector, a grid spacing finer than 3 mm is required to adequately capture spray development. In particular, grid spacing of 1.6 mm and 2.0 mm accurately reproduces the experimental penetration length of Schmid *et al*. (2013) [50]. Finally, for even finer resolution, computational results over-predict the spray penetration encountered in the experiment. Based on these results, a grid with a spacing of 1.6 mm was selected; all results reported subsequently correspond to this grid.

8.6.2 Influence of model constants

The influence of the KH-RT model constants on the spray characteristics was investigated by using a 3^k factorial Design of Experiment (DOE) method. Here, all three nozzle geometries with 1000 bar rail pressure were calculated. In spray secondary breakup modeling, it is usual practice to maintain standard values for B_0 and C_τ coefficients of the KH-RT model; thus, in the present study B_1 and C_3 model constants were considered. In the factorial design each factor is evaluated at "low", "intermediate" and "high" levels. Hereby, a 3^k factorial design with $\mathrm{k} = 2$ factors ($B_1(\mathrm{KH}); C_3(\mathrm{RT})$) and 3 levels was used. Firstly, a design table was generated, and 9 runs were performed for all three nozzles. In the second step, a regression model was used to generate response surfaces [293].

	Model variables					Yates notation	
No of Runs	KHB0	KHB1	RTC3	RTCt		KHB1	RTC3
1	0.61	40	0.1	1		0	0
2	0.61	20	0.1	1		-1	0
3	0.61	60	0.1	1		1	0
4	0.61	60	1	1		1	-1
5	0.61	60	0.01	1		1	1
6	0.61	20	1	1		-1	-1
7	0.61	20	0.01	1		-1	1
8	0.61	40	0.01	1		0	-1
9	0.61	40	1	1		0	1

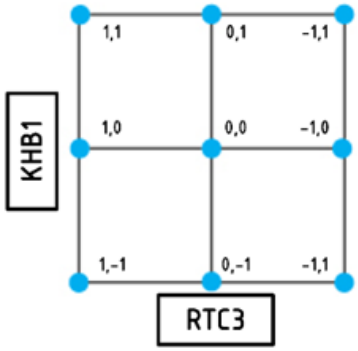

Figure 106 - 3^2 factorial experiment geometry view (left) and parameter table (right) [293].

Figure 106 shows the geometric view and the parameter table for a 3^k factorial design with k = 3 levels on 2 factors. A detailed description of the factorial experiment is provided in [293,294]. **Figure 107** presents the spray tip penetration length as a function of the B_1 and C_3 model constants. The spray tip penetration increases at higher C_3 and B_1 values, as it was expected since the increasing values of C_3 and B_1 result in larger stable droplet diameters, thus slowing down the associated momentum loss (Equations (*52*) and (*57*). As a result, the penetration increases. The influence of B_1 on the spray tip penetration is more dominant, which suggests that the Kelvin-Helmholtz breakup mechanism is more pronounced than the Rayleigh-Taylor in this phase of the spray. The simulation is in a good agreement with the measured spray tip penetration length, especially when the C_3 is at its lowest value in the validity range of the breakup model. At this C_3 level, the influence of B_1 model constant on the spray tip penetration length is rather low.

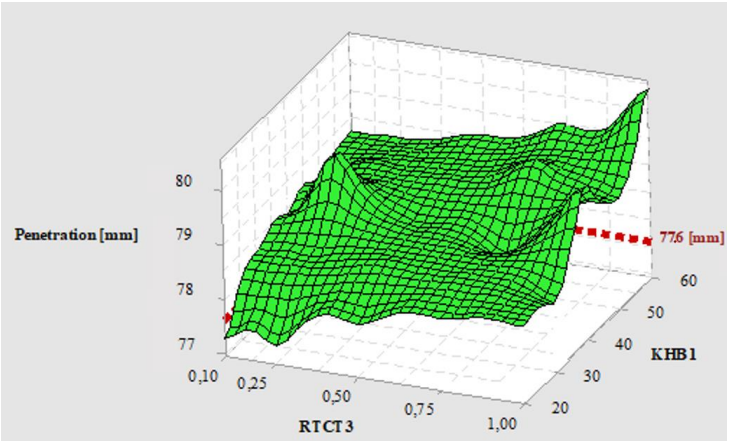

Figure 107 Spray tip penetration length as function of B_1 ("KHB1") and C_3 ("RTCT3") model constants in the KH-RT breakup model. Red dotted line shows the measured values.

Figure 108 shows the spray cone angle and deflection dependencies in the horizontal and vertical direction on varying B_1 and C_3 model constants in the KH-RT spray secondary breakup model. Obtained values are compared to measured ones, denoted by the red dotted lines. The Rayleigh-Taylor breakup mechanism (C_3) shows in both directions stronger influence on the spray cone angle, while an increase in the value of C_3 results in larger spray cone angles.

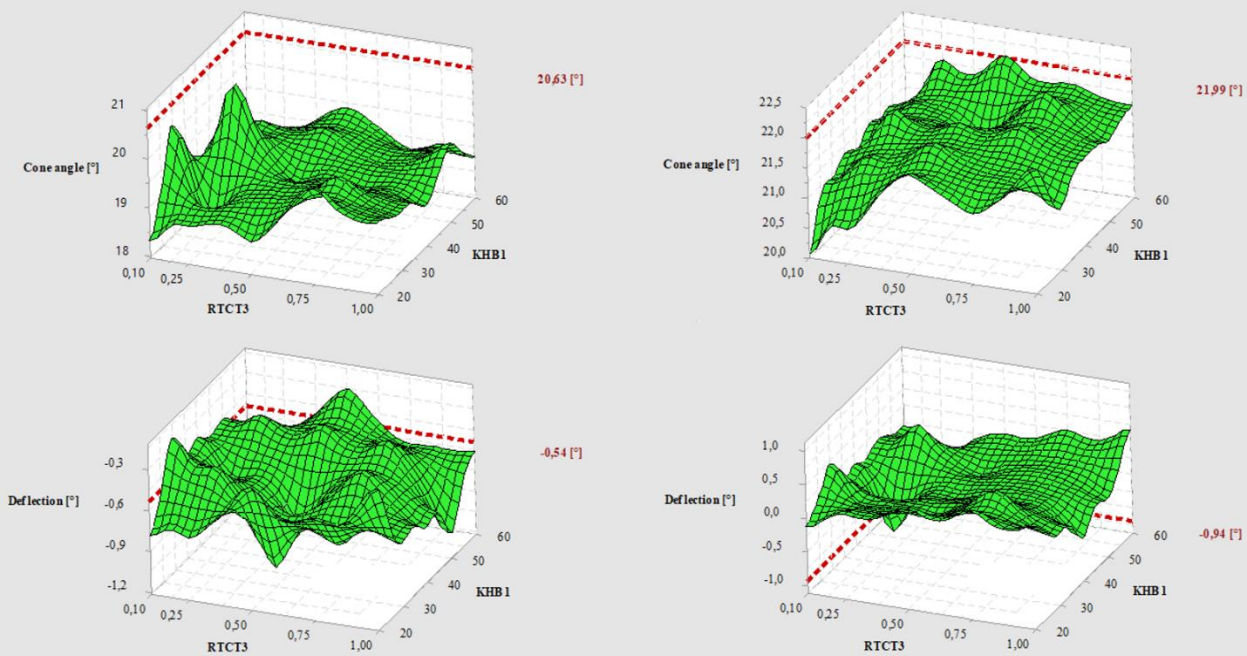

Figure 108 - Spray characteristics of the noneccentric nozzle depending on the B_1 ("KHB1") and C_3 ("RTCT3") model variables. (Horizontal spray cone angle (Top left); Vertical spray cone angle (Top right); Horizontal spray deflection (Bottom left); Vertical spray deflection (Bottom right). Red dotted line shows the measured values.

Changing the B_1 model parameter slightly affects the spray cone angles. Regarding the spray deflection, a clear trend is not found, and the variation of the deflection angles are less significant. **Table 16** summarizes the best fit found for the three atomizer geometries compared to the experimental results. These model parameters were further utilized in spray secondary breakup calculations in the KH-RT model.

Table 16 - Values of constants of the KH-RT breakup model used in the present study.

Model constants \ Normalized eccentricity	B_0	B_1	C_τ	C_3
0.0	0.61	40	1	0.25
0.4	0.61	20	1	0.1
0.8	0.61	60	1	0.1

8.6.3 Spray tip penetration

Figure 109 presents the computed history of spray penetration length, for the nozzles used in the present study. Results using the Reitz and Reitz-Diwakar models for the primary and secondary breakup, respectively, are also included (the approach is referred to as 'conventional' in **Figure 109**), as well as the experimental results of Schmid *et al*. (2013) [50]. **Figure 109** indicates that, for the noneccentric and moderately eccentric nozzle, the present computational approach predicts a slightly faster penetration in the early development of the spray, in comparison to experiments. Particularly good agreement is obtained for times larger than about 0.4 ms. The lower values of experimental spray penetration length during the early spray development observed in a number

of the experiments may be attributed to the low values of jet velocity due to remaining fuel in the nozzle (from a previous injection shot). Finally, it is noted that, in all cases, the results of the present approach outperform those corresponding to the use of Reitz and Reitz-Diwakar models for spray breakup.

Interestingly, the nozzle with e^*= 0.4 normalized eccentricity (**Figure 109**, middle) is associated with a higher penetration length in the first stage of the spray tip penetration than the noneccentric spray. At later instants in time, the two penetration lengths are comparable, which indicates a faster disintegration of the spray emanating from the eccentric nozzle. The spray produced by an atomizer with e^*=0.8 (**Figure 109**, bottom) is characterized by lower spray tip penetration, in comparison to the other two nozzle geometries, for all times. It appears that a highly asymmetric spray structure, associated with a higher effective area, is subject to more intense atomization, and thus a slower penetration.

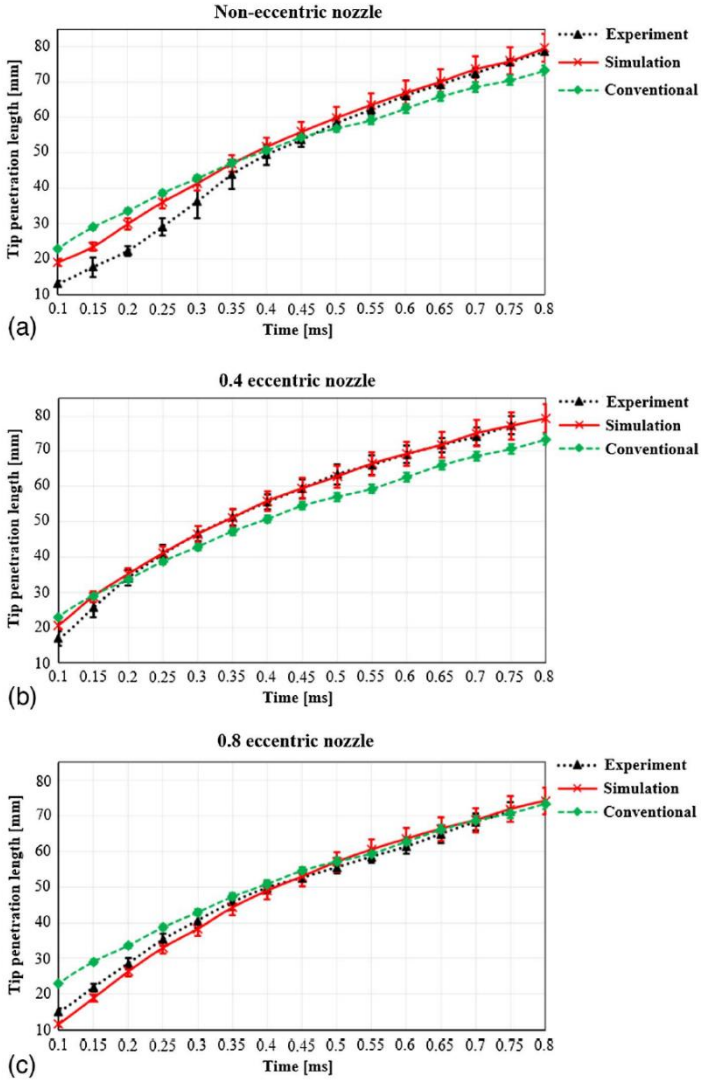

Figure 109 - Computed time history of spray penetration length, for the three injectors of the present study. The corresponding experimental curves of Schmid et al. (2013) are also included, as well as computational results based

on the Reitz and Reitz-Diwakar models for the primary and secondary breakup, respectively ("conventional" approach").

Figure 110 presents the spray parcel diameter distribution for the three nozzles of the present study, at *t*=0.15 ms after SOI. The penetration lengths displayed are in accordance with the values of **Figure 109**. **Figure 110** verifies the presence of larger droplets for the sprays characterized by stronger penetration. A deviation from a symmetric structure is evident for the two eccentric nozzles. A downward deflection of the case of noneccentric nozzle is also realized and is associated with the asymmetric velocity distribution within the orifice.

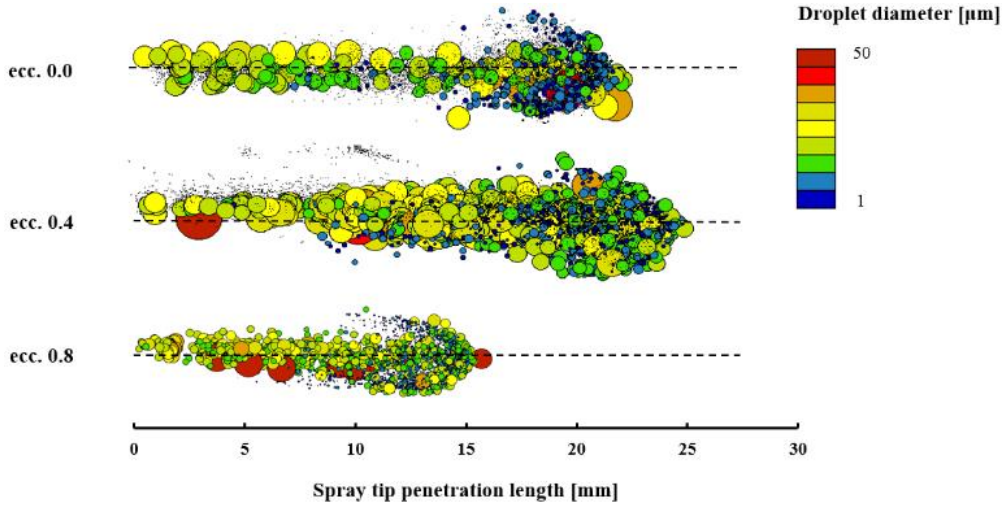

Figure 110 - Computed parcel diameter distribution, for the three injectors of the present study, at 0.15 ms after the simulation start.

8.6.4 Spray cone angles

a. Horizontal spray cone angle

Figure 111 presents computational and experimental results of the spray cone angle, the latter from Schmid *et al*. (2013) [50], calculated at a horizontal plane, at a location 40 nozzle diameters downstream of the nozzle tip.

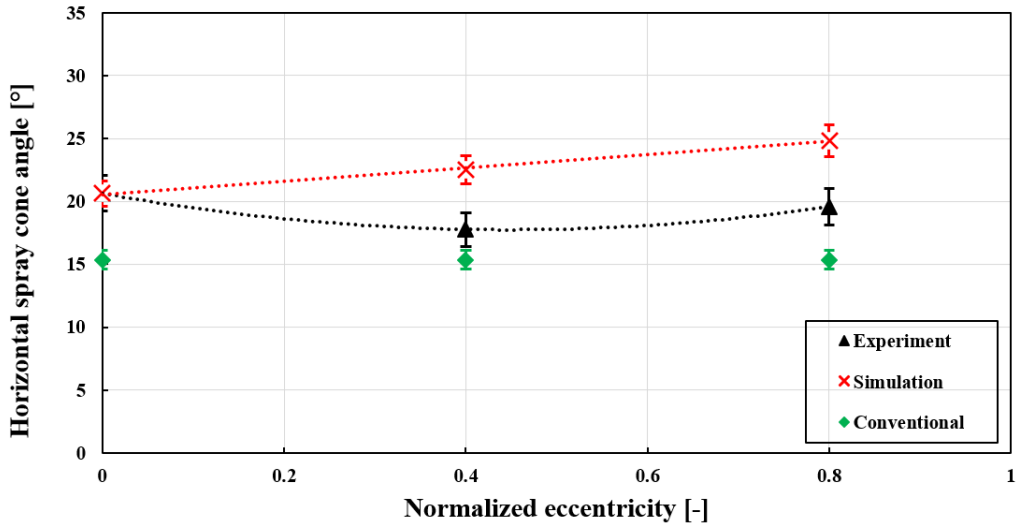

Figure 111 - Measured (black) and computed (red and green) values of spray cone angle in a horizontal plane, at a distance of 40 nozzle diameters from the nozzle tip, versus nozzle normalized eccentricity.

The present computational results verify an increase of spray angle with nozzle eccentricity, which is associated with an increase of effective spray area, and is consistent with the corresponding decreasing trends of penetration length (**Figure 110**).

Agreement with experiments is very good for the noneccentric nozzle, and moderate for the eccentric nozzles. Regarding the computational results of the 'conventional' approach (which only accounts for an axisymmetric flow at the nozzle tip), discrepancies with the experiment should be associated with deviations from axisymmetry (present even in the case of the noneccentric nozzle) due to the nozzle geometry. Finally, for the eccentric nozzles, discrepancies between the computational results of the present approach and experiments should be associated with the uncertainties in both simulations and experiments, which may also include small deviations of the actual injector geometry from the ideal one considered in simulations.

b. Vertical spray cone angle

Results regarding spray angle values in a vertical plane, at the same distance of 40 nozzle diameters from the orifice, are presented in **Figure 112**. A very good agreement between the results of the present computational approach and experiments is realized, with the results of the 'conventional' approach under-predicting the experimental values.

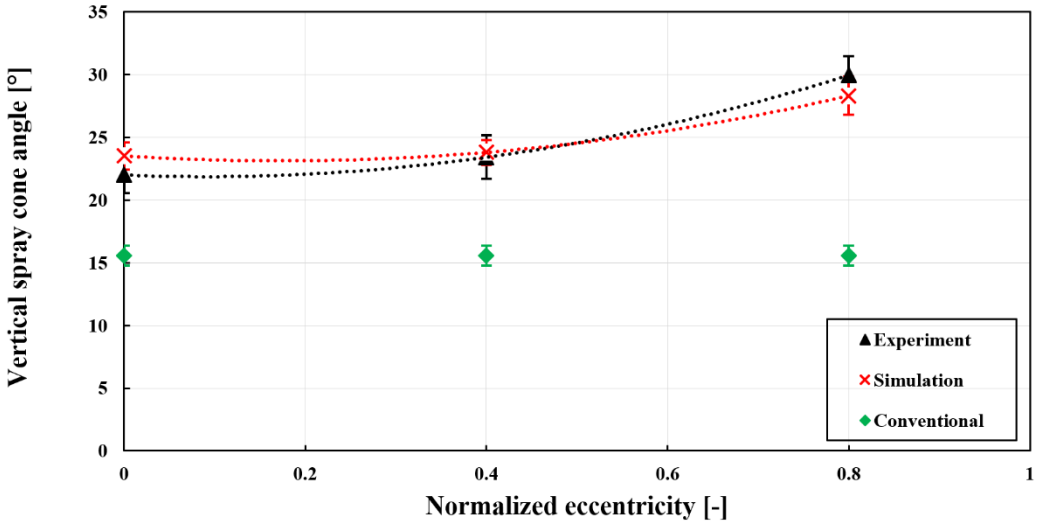

Figure 112 - Measured (black) and computed (red and green) values of spray cone angle in a vertical plane, at a distance of 40 nozzle diameters from the nozzle tip, versus nozzle normalized eccentricity.

An increasing trend of spray cone angle with nozzle eccentricity is verified for the cone angle in the vertical plane. The significant differences between horizontal and vertical cone angles highlight the asymmetric structure of marine Diesel sprays generated by eccentricity.

8.6.5 Spray deflections

a. Horizontal spray deflections

Figure 113 presents computational and experimental results of spray deflection angle at a horizontal plane, at a distance of 40 nozzle diameters downstream of the nozzle tip. A good agreement between the results of the present computational approach and experiments is found for the noneccentric and moderately eccentric nozzles. (A near-zero value is verified in the results of the 'conventional' approach.) The noneccentric nozzle has a very slight deflection from the symmetry axis with a value close to zero, which is well represented by the simulations. The deflection generated by the middle eccentric nozzle is successfully modeled by the new method, while the conventional approach does not follow the changing spray behavior. Deviation in the horizontal deflection shows about 50% error in the case of the highest eccentric nozzle geometry. Results illustrate the increase of spray deflection with nozzle eccentricity.

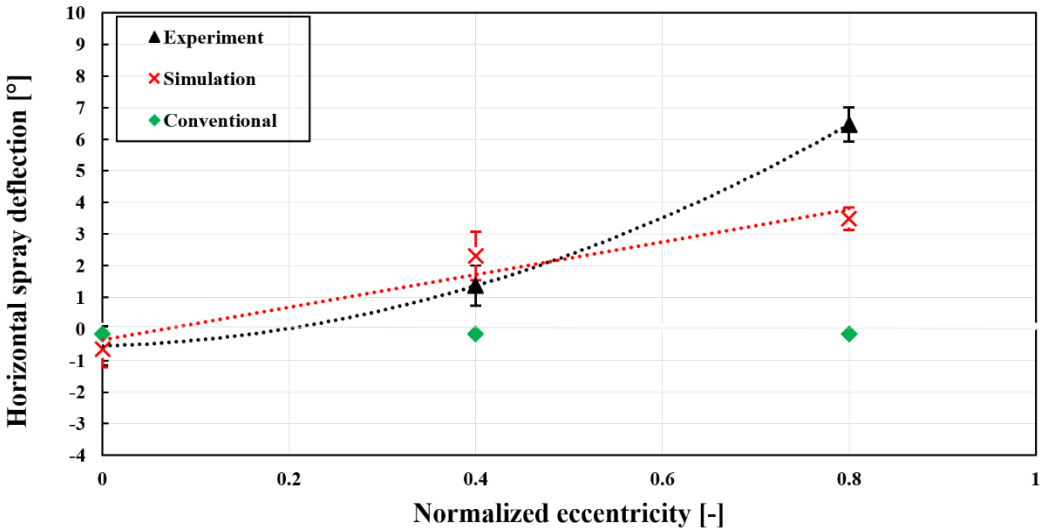

Figure 113 - Measured (black) and computed (red and green) values of spray deflection angle in a horizontal plane, at a distance of 40 nozzle diameters from the nozzle tip, versus nozzle normalized eccentricity.

b. Vertical spray deflections

Figure 114 presents spray deflection angles in a vertical plane, at the same distance from the orifice. Again, a good agreement is obtained between the computational results of the present approach and the experimental ones. Interestingly, the spray in noneccentric and middle eccentric cases deviates from its symmetry line downwards, whilst the highest eccentricity redirects the spray upwards in the vertical direction. The slight deflections in low eccentricity are successfully captured by the new method, however, the positive deflection resulted from high eccentricity is not reproduced by the simulations.

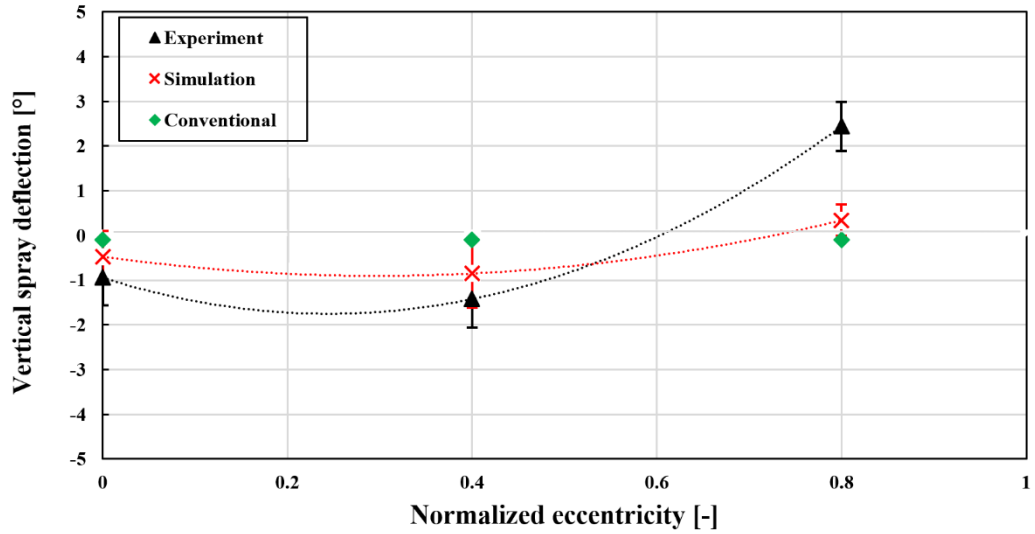

Figure 114 - Measured (black) and computed (red and green) values of spray deflection angles in a vertical plane, at a distance of 40 nozzle diameters from the nozzle tip, versus nozzle normalized eccentricity.

8.7 Adaptation of primary breakup results to different injection pressures

This section introduces a model adaptation to increase the applicability of the new approach presented in this thesis, considering other relevant conditions in large 2-stroke marine Diesel

engines. The primary breakup simulations of the present study have considered an injection pressure of 1000 bar. Here, lower injection pressure levels are considered, namely 600 and 800 bar, with the goal of properly adapting the results corresponding to 1000 bar, without repeating the LES simulations. The approach is applied for all three nozzle geometries of the present study.

The injection pressure affects the nozzle flow, and consequently droplet velocities, diameters, and their spatial distribution. Therefore, a proper injection velocity has to be defined for the different injection pressure levels. To this end, URANS in-nozzle flow simulations were performed with 600 and 800 bar injection pressures using all three nozzle geometries. Droplet velocity in the streamwise direction, droplet diameter, and droplet locations were adapted, using the LES resolved reference droplet dataset of the 1000 bar injection pressure case.

8.7.1 Adaptation of droplet velocities

Time-averaged injection velocity was calculated for each case at the nozzle bore exit. These values were then normalized by using the time-averaged injection velocity of the 1000 bar reference case, yielding velocity magnitude ratios (**Table 17**). Finally, the streamwise velocity component of the identified droplets in LES spray primary breakup reference case were adapted based on the velocity magnitude ratios.

Table 17 - Time averaged mean velocity magnitude values, and calculated velocity magnitude ratios at the nozzle bore exit as function of nozzle geometry and injection pressure.

Ecc. [mm] / P_inj[bar]	1.10	0.55	0.0
	Velocity magnitude [m/s]		
1000	314	334	334
800	292	292	292
600	262	252	250
	Velocity magnitude ratio [-]		
1000	1.00	1.00	1.0
800	0.93	0.88	0.87
600	0.84	0.76	0.75

8.7.2 Scaling of droplet diameters

Next, the droplet diameters in the reference dataset were adapted. The mean droplet diameter of fuel sprays depends on a large number of variables, such as fuel properties, operating conditions, and geometrical dimensions of the fuel nozzle. M. Elkotb *et al*. (1982) [295] introduced an empirical model, based on experimental data, expressing the droplet SMD dependence on the injection pressure:

SMD
$$SMD = 3.08 \cdot 10^{6} \cdot \Delta p_{nozzle}^{-0.54} \cdot (\sigma_L \cdot \rho_L)^{0.737} \cdot \rho_g{}^{0.06} \cdot \mu_L{}^{0.385} \quad (105)$$

where $\Delta p_{nozzle} = P_{inj} - P_{chamber}$, σ_L is the liquid surface tension, ρ_L and μ_L are the liquid density and dynamic viscosity, respectively. In the model adaptation, the influence of injection pressure

on the droplet diameter was determined using Equation (*105*). Similar correlations for the SMD of droplets in Diesel sprays can be found in [296].

First, time-averaged SMD values were calculated using the reference dataset, then the size of droplets was modified based on Equation (*105*) for each case considered. The calculated SMD values are summarized in **Table 18**, alongside the calculated SMD ratios for all injection pressures accounted for.

Table 18 - Time averaged SMD values of droplets, and the calculated SMD ratios as function of injection pressure and nozzle geometry.

Ecc. [mm] / P_inj[bar]	1.10	0.55	0.0
	SMD [mm]		
1000	0.024	0.026	0.023
800	0.028	0.030	0.025
600	0.033	0.035	0.028
	SMD ratio [-]		
1000	1	1	1
800	1.16	1.15	1.08
600	1.35	1.34	1.19

8.7.3 Scaling of initial droplet locations

Droplet coordinates of the reference dataset were adapted, using the measured spray tip penetration length and spray cone angles published in [50]. Droplet coordinates in the streamwise direction were modified based on measured spray tip penetration length. In the radial direction, the droplet coordinates were adapted according to measured horizontal spray angles, considering the upper and lower spray cone angles, respectively. In the radial direction, the droplet coordinates were adapted using the vertical spray upper and lower angles. **Table 19** summarizes the scaling ratios of the initial droplet coordinates as function of the nozzle geometry and injection pressure.

Table 19 - Scaling of droplet coordinates as function of injection pressure and atomizer geometry.

Eccentricity 0.0 mm			
Injection pressure [bar]	1000	800	600
Tip penetration [mm]	14.89	12.81	10.3
Scale Streamwise [-]	1	0.85	0.69
Scale Circumferential [-]	1	1.01	0.92
Scale Radial [-]	1	1.00	0.94

Eccentricity 0.55 mm			
Injection pressure [bar]	1000	800	600
Tip penetration [mm]	12.28	8.17	5.92
Scale Streamwise [-]	1	0.67	0.48
Scale Circumferential [-]	1	1.03	0.99
Scale Radial [-]	1	0.98	1.00

Eccentricity 1.10 mm			
Injection pressure [bar]	1000	800	600
Tip penetration [mm]	6.22	5.58	3.43
Scale Streamwise [-]	1	0.90	0.55
Scale Circumferential [-]	1	1.04	1.01
Scale Radial [-]	1	1.01	0.97

8.7.4 Mass and momentum conservation

Mass and momentum were conserved using the procedure outlined in section 8.3 for all cases.

8.7.5 Adaptation of KH-RT model constants

In the KH-RT secondary breakup model, model constant C_3 is related to the droplet velocity and stable diameter [135] (Equation (*106*)), influencing the spray penetration length. It was shown in 8.6.2 that the influence of model constant B_1 on the spray penetration length was not significant.

Therefore, in the present approach, only the C_3 constant of the KH-RT secondary breakup model was adapted at lower injection pressures.

$$C_3 \qquad C_3 \propto \frac{U_r}{D_{d,stable,RT}^{1.5}} \propto \frac{\sqrt{P_{inj} - P_{chamber}}}{D_{d,stable,RT}^{1.5}} \tag{106}$$

Table 20 summarizes the adapted values of model constant C_3, for all nozzles investigated, at the three values of injection pressure considered.

Table 20 – Adapted values of model constant C_3 of the KH-RT secondary breakup model, for the injector geometries and injection pressures of the present study.

Ecc. [mm] / P_inj[bar]	1.10	0.55	0.0
	RTC3 [-]		
1000	0.25	0.1	0.1
800	0.19	0.08	0.09
600	0.14	0.06	0.07

8.8 Simulation results at different injection pressures

8.8.1 Spray tip penetration

Figure 115 presents the comparison of measured and simulated (with the new scaling approach) spray trip penetration curves of a noneccentric nozzle for 600, 800, and 1000 bar injection pressures, respectively. The simulation results were sampled every 5 ms. The calculation method is the one outlined in section 8.6.3. The computed values of spray tip penetration presented in **Figure 115** are initially slightly higher than the experimental ones. After a time instant of about 0.55 s after the injection start, a very good agreement is reached for all injection pressure cases.

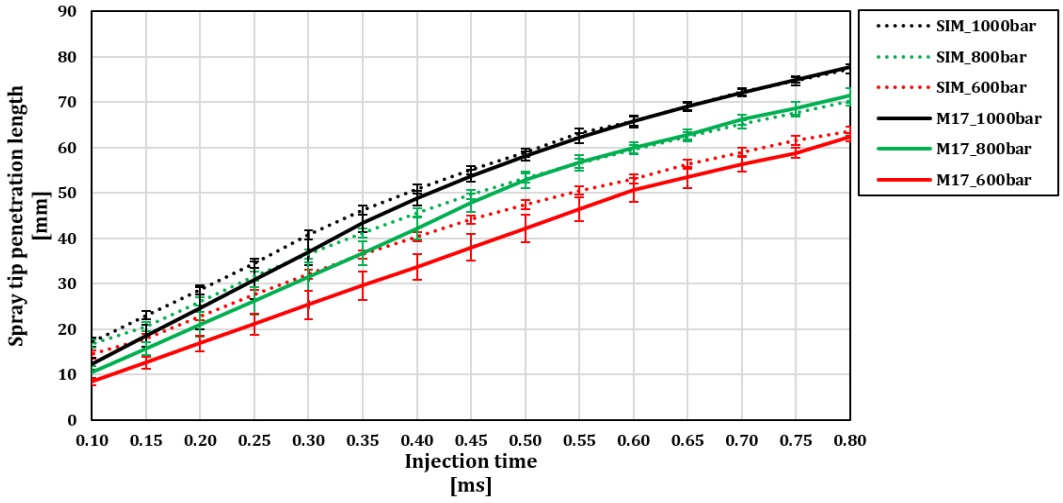

Figure 115 - Comparison of computed and simulated (new scaling approach) spray tip penetration length versus time, for different values of injection pressure, for the noneccentric nozzle.

In **Figure 116**, a similar comparison is presented for the case of the nozzle with medium eccentricity (0.55 mm). Similarly to the case of noneccentric nozzle, the computed values of spray penetration length are higher in the early stages of injection, and are closer to the experimental values at larger times.

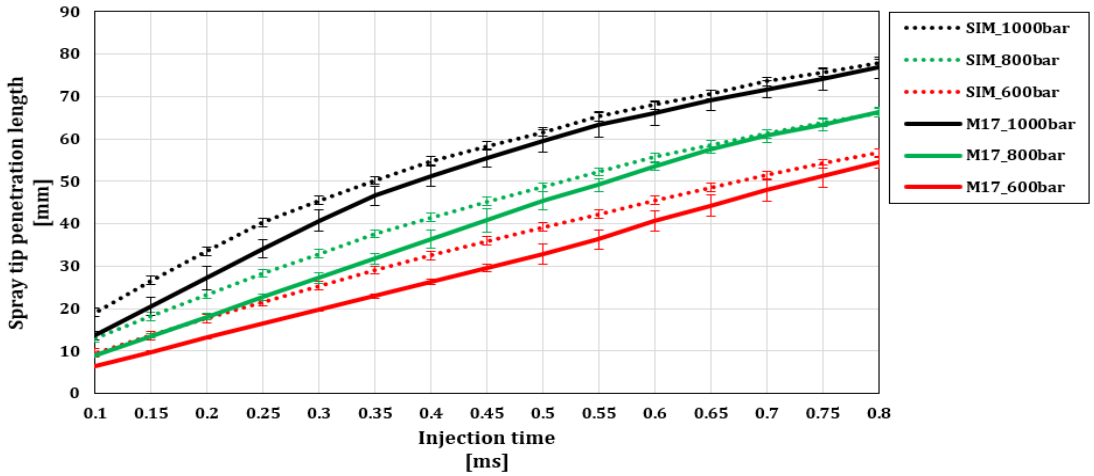

Figure 116 - Comparison of measured and computed (new scaling approach) spray tip penetration length versus time, for different values of injection pressure, for the nozzle of medium eccentricity (e=0.55 mm).

Computed and measured values of spray penetration length for the nozzle of highest eccentricity (1.10 mm) are presented in **Figure 117**. It is observed that, in the early stages of injection, the discrepancies between experiment and simulation are the smallest among all three nozzles. The comparison is very good for times close to t=0.8 ms.

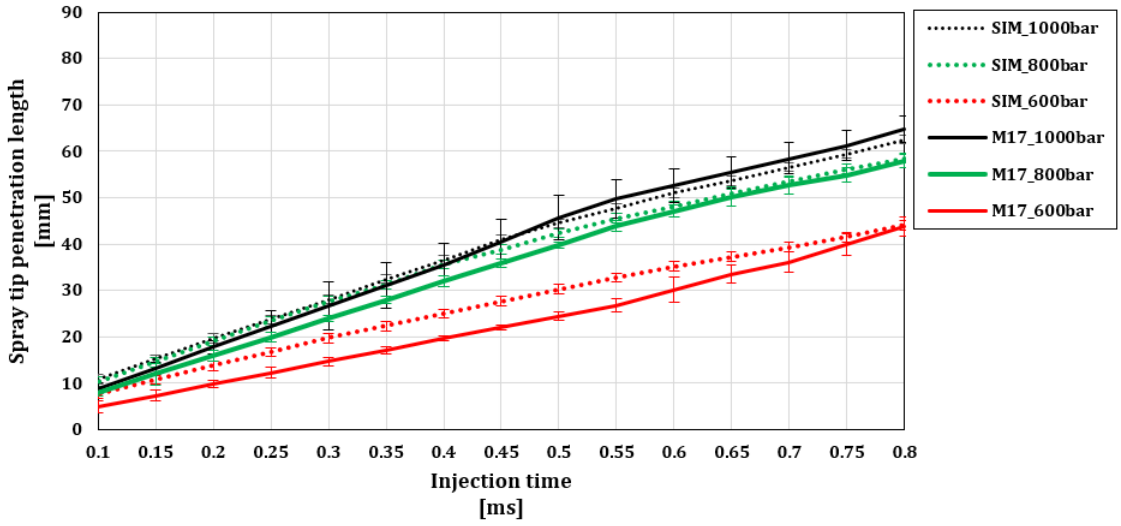

Figure 117 - Comparison of measured and computed (new scaling approach) spray tip penetration length versus time, for different values of injection pressure, for the nozzle of highest eccentricity (e=1.10 mm).

8.8.2 Horizontal spray cone angle

Figure 118 presents the horizontal spray cone angles computed using both the new approaches and the conventional approach, for the noneccentric nozzle. Simulation results are compared to

available experimental data at the three injection pressures considered, namely 600, 800 and 1000 bar. Simulation results for the injection pressures of 600 and 800 bar are based on the new scaling approach. As a first remark, the horizontal spray angles are shown to be rather insensitive to the change in injection pressure. **Figure 118** demonstrates a very good agreement between experiment and simulation with the new approaches introduced in the present thesis, for all three injection pressures, especially for the cases of 1000 bar and 800 bar. The results using the conventional (RANS-only) approach are shown to be inferior.

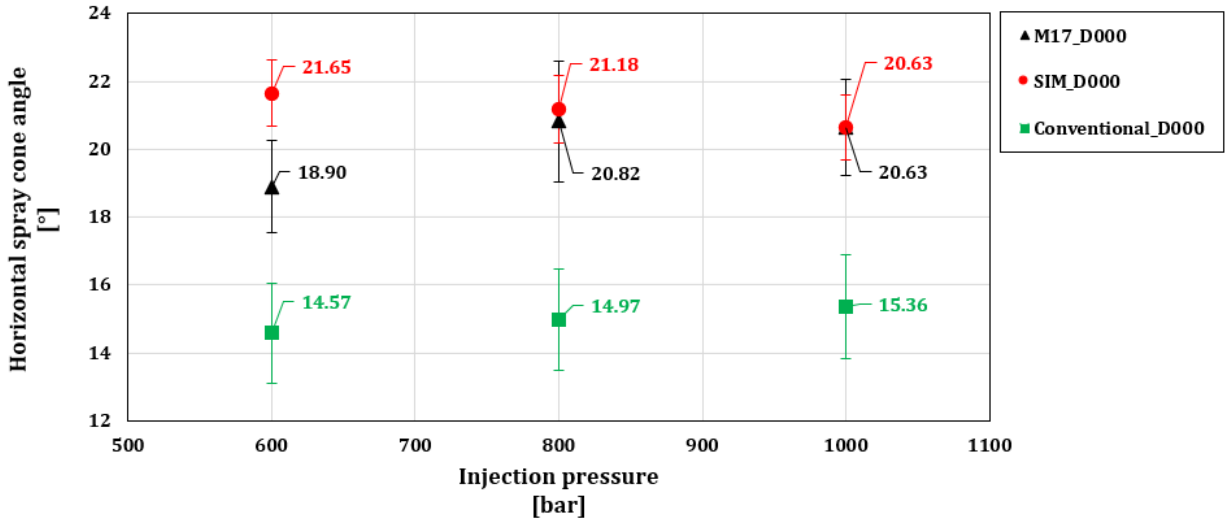

Figure 118 - Measured and computed horizontal spray cone angles as function of the injection pressure, for the noneccentric atomizer. Black: experiments, red: new approaches, green: conventional approach.

Figure 119 and **Figure 120** present the horizontal spray cone angles for the nozzles of medium and high eccentricity, respectively. In all cases, the new approaches introduced in the present thesis overpredict the measured values, while use of the conventional approach results in underprediction.

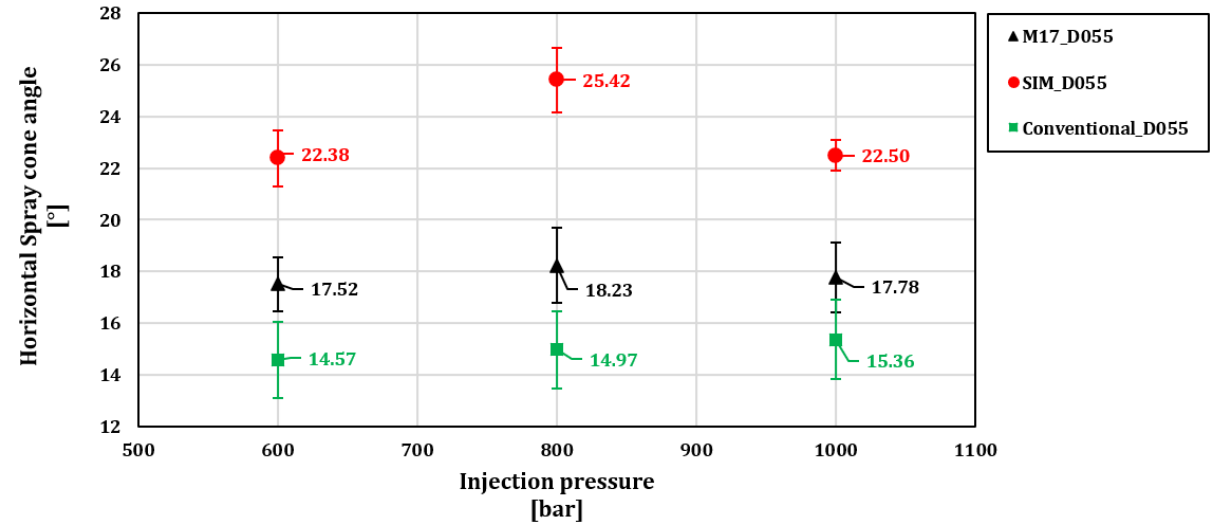

Figure 119 - Measured and computed horizontal spray cone angles as function of the injection pressure, for the nozzle of medium eccentricity (e=0.55 mm). Black: experiments, red: new approaches, green: conventional approach.

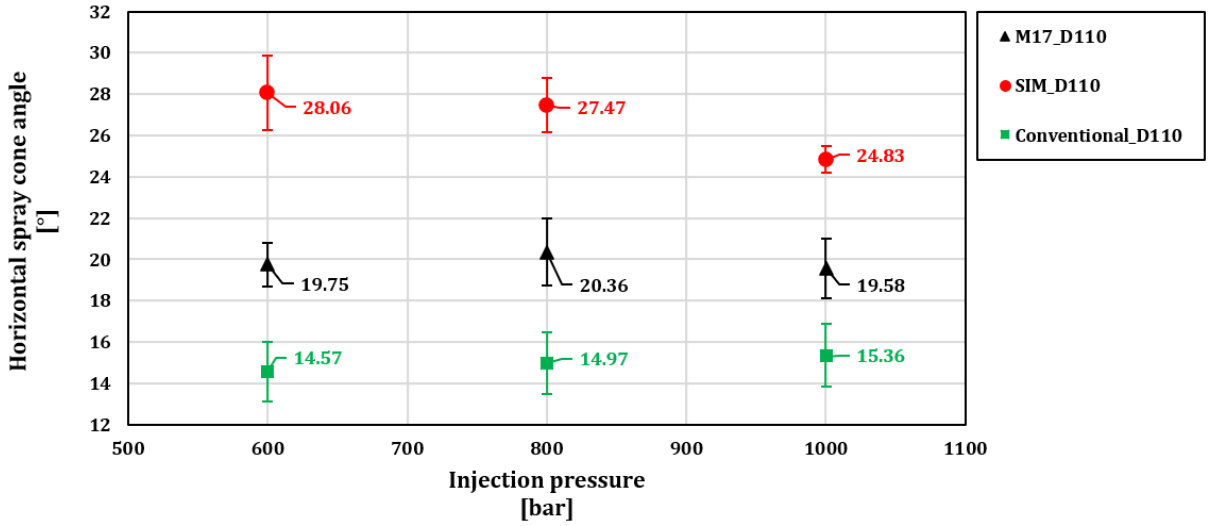

Figure 120 - Measured and computed horizontal spray cone angles as function of the injection pressure, for the nozzle of highest eccentricity (e=1.10 mm). Black: experiments, red: new approaches, green: conventional approach.

8.8.3 Vertical spray cone angle

Figure 121 presents the vertical spray cone angles based on experiments and the present simulations with the approaches introduced here, for the noneccentric nozzle, for the three values of injection pressure considered (600, 800 and 1000 bar). The new scaling approach is used for the injection pressures of 600 and 800 bar. **Figure 121** shows that the values of vertical spray cone angle remain rather flat with the variation of injection pressure. Furthermore, the results of the new approaches are rather close to experiments, which is, on the other hand, not the case for the results of the conventional (RANS-only) approach. Similar observations hold for the results of the middle eccentricity nozzle (**Figure 122**) and the one of highest eccentricity (**Figure 123**).

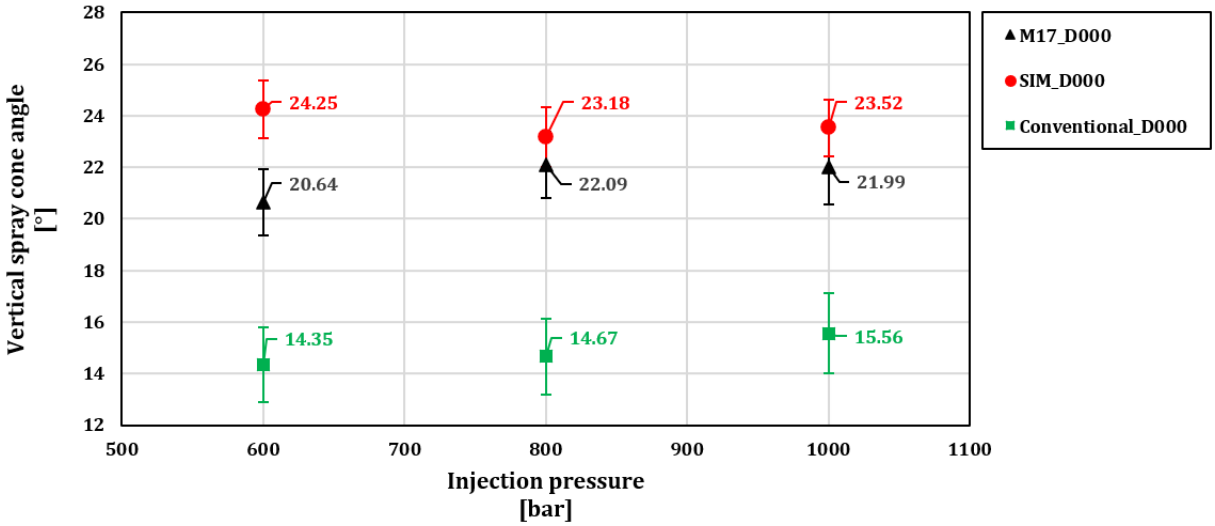

Figure 121 - Measured and computed vertical spray cone angles as function of the injection pressure, for the noneccentric atomizer. Black: experiments, red: new approaches, green: conventional approach.

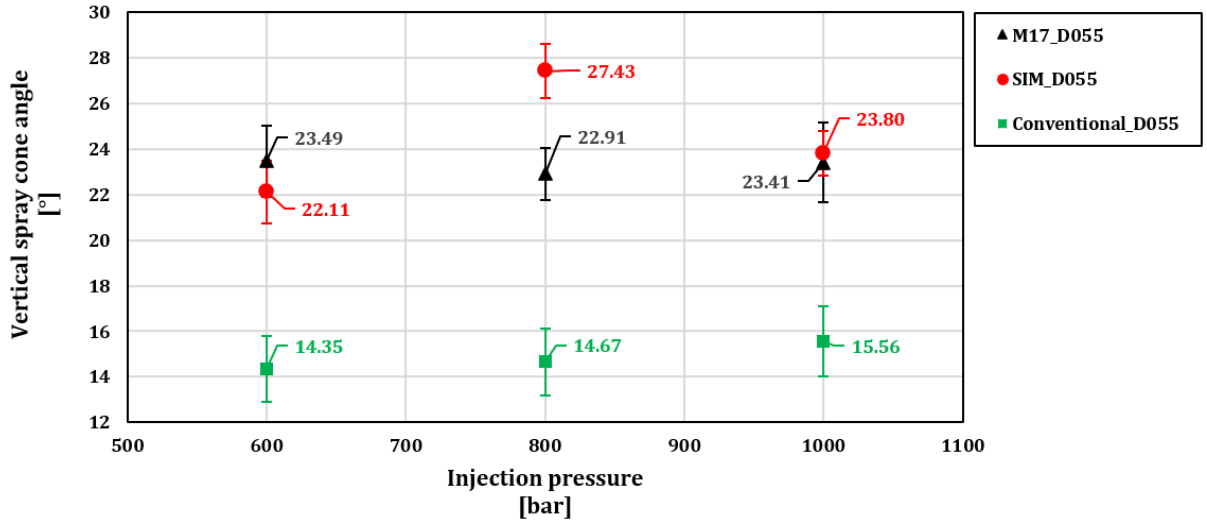

Figure 122 - Measured and computed vertical spray cone angles as function of the injection pressure, for the nozzle of medium eccentricity (e=0.55 mm). Black: experiments, red: new approaches, green: conventional approach.

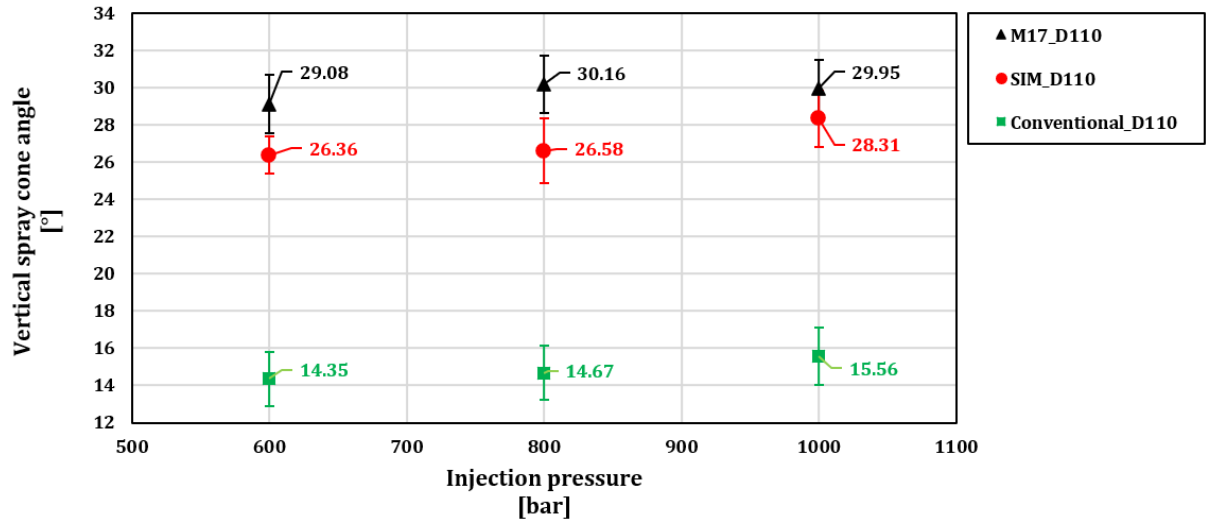

Figure 123 - Measured and computed vertical spray cone angles as function of the injection pressure, for the nozzle of highest eccentricity (e=1.10 mm). Black: experiments, red: new approaches, green: conventional approach.

8.8.4 Horizontal spray deflection

Figure 124 presents spray deflections in the horizontal direction, including measured values and computed ones with the present new approaches, for the noneccentric nozzle, for all values of injection pressure (600, 800 (scaling approach) and 1000 bar). **Figure 124** shows that the average deflection is rather low, nonetheless associated with a high uncertainty. Overall, the new approaches demonstrate a slightly better comparison against experiments, in comparison to the conventional approach.

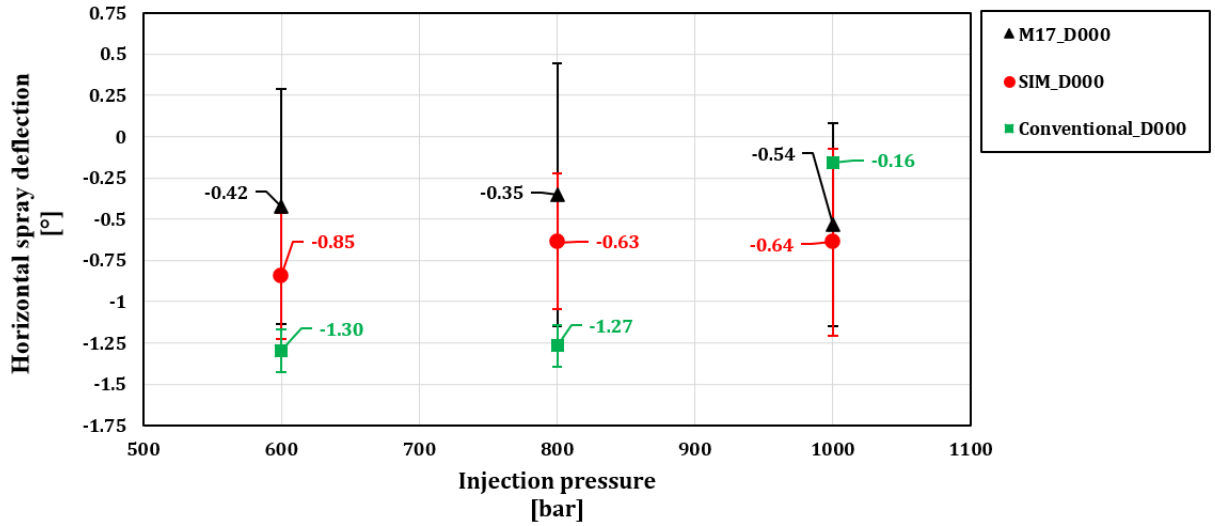

Figure 124 - Measured and computed horizontal spray deflection angles as function of the injection pressure, for the noneccentric atomizer. Black: experiments, red: new approaches, green: conventional approach.

Figure 125 presents results of horizontal spray deflection for experiment and the present simulations, for the nozzle of medium eccentricity (0.55 mm). Experiments indicate a rather flat dependence on injection pressure, characterized by low deflection angles. The results of the present simulations consistently overpredict the experimental values, while the opposite (underprediction) holds for the conventional approach.

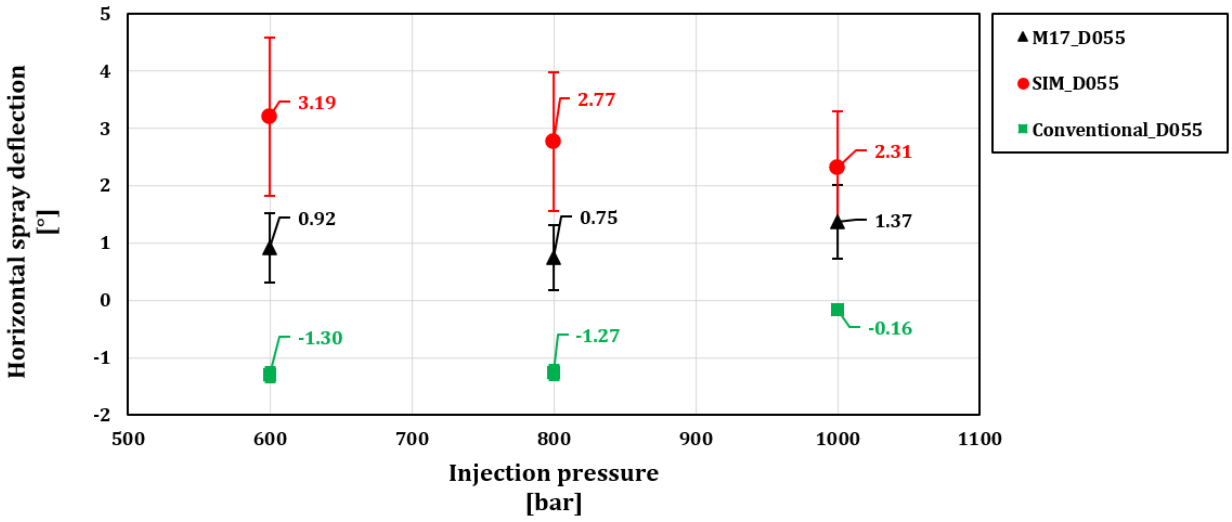

Figure 125 - Measured and computed horizontal spray deflection angles as function of the injection pressure, for the nozzle of medium eccentricity (e=0.55 mm). Black: experiments, red: new approaches, green: conventional approach.

Finally, **Figure 126** presents the results regarding the horizontal spray deflection for the nozzle of highest eccentricity (1.10 mm). Experiments verify a flat dependence on injection pressure, however, in the case of the present nozzle the deflection is substantial. The simulation results with the present approaches consistently underpredict the experimental values. For the cases of the conventional approach, the direction of deflection is not properly predicted, and the discrepancies with the experiments are high.

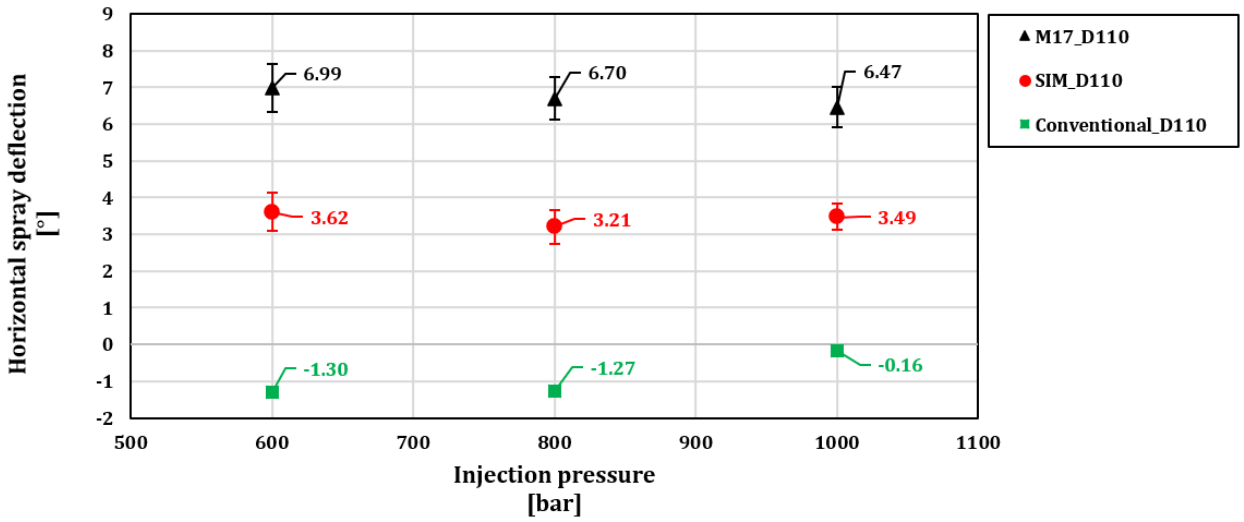

Figure 126 - Measured and computed horizontal spray deflection angles as function of the injection pressure, for the nozzle of highest eccentricity (e=1.10 mm). Black: experiments, red: new approaches, green: conventional approach.

8.8.5 Vertical spray deflection

Figure 127 presents spray deflections in the vertical direction, for experiment and the present simulations. The experimental results indicate a reflection downwards at an injection pressure of 600 bar, an upward one at 800 bar, and a downward one at 1000 bar; in all cases the deflection angles are rather low. In all cases the simulation results are close to experiments, with the comparison being best for the present approaches. The results of the conventional approach are also rather good, and this is to be expected for the present case of a noneccentric nozzle.

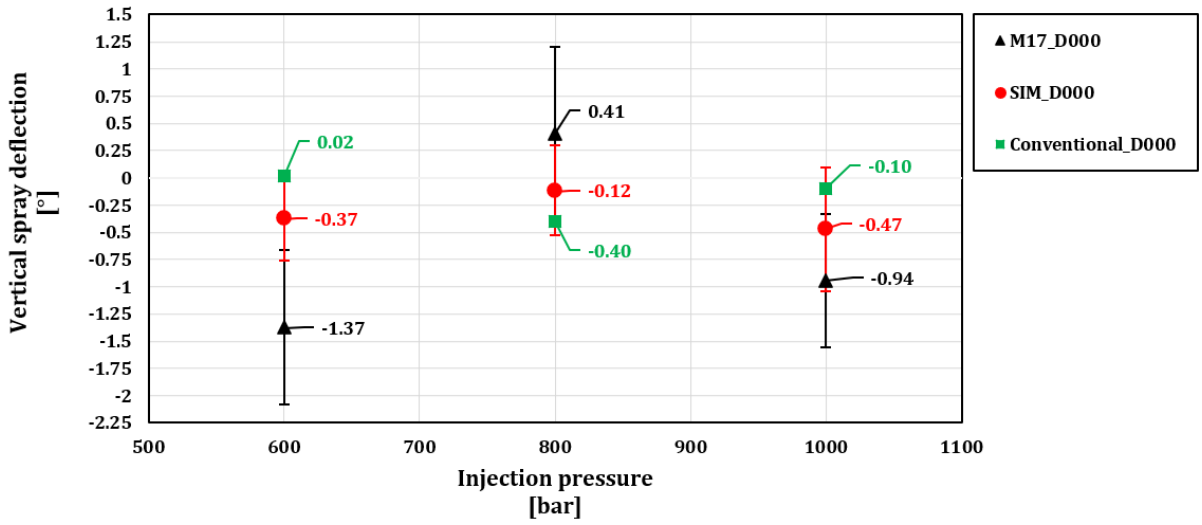

Figure 127 - Measured and computed vertical spray deflection angles as function of the injection pressure, for the noneccentric atomizer. Black: experiments, red: new approaches, green: conventional approach.

Figure 128 presents results of vertical spray deflection for experiment and the present simulations, for the medium eccentricity nozzle (eccentricity of 0.55 mm). Experiments indicate in general a mild deflection downwards, which becomes slightly stronger for the case of highest injection

pressure. The results of the present approaches match the experimental values quite well. The conventional approach also compares favourably to experiments.

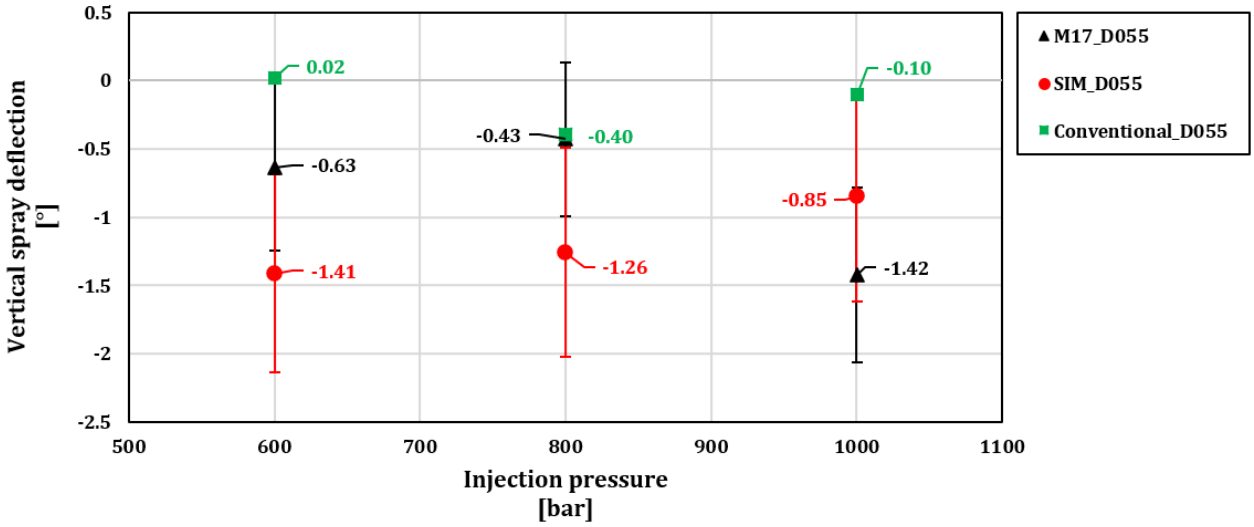

Figure 128 - Measured and computed vertical spray deflection angles as function of the injection pressure, for the nozzle of medium eccentricity (e=0.55 mm). Black: experiments, red: new approaches, green: conventional approach.

Figure 129 presents the results regarding vertical spray deflection for the nozzle of highest eccentricity (1.10 mm). Experiments indicate an upward deflection of the spray, in the range 2-4°. The computational results predict very mild deflections, i.e., deviations are non-negligible in comparison to experiments.

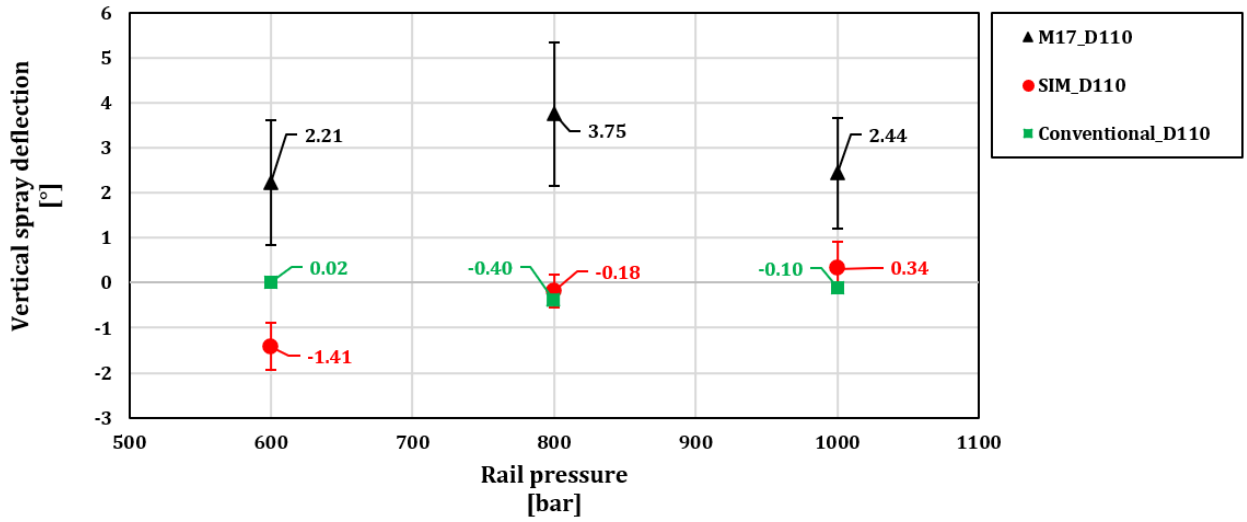

Figure 129 - Measured and computed vertical spray deflection angles as function of the injection pressure, for the nozzle of highest eccentricity (e=1.10 mm). Black: experiments, red: new approaches, green: conventional approach.

With respect to computational cost, it is noted that typically a URANS simulation of spray secondary breakup has required approximately 3 days using 36 cores of a parallel cluster.

8.9 Comparison of different atomizer layouts

This section summarizes the spray simulation results in terms of global morphological characteristics, in particular their dependence on nozzle eccentricity and injection pressure. Computational results using the new approaches of this thesis, namely, spray tip penetration, cone angles, and deflections, are presented and discussed.

Figure 130 presents the computed spray penetration length at t=0.8 ms after injection start, versus nozzle eccentricity and injection pressure. The expected increase with injection pressure is verified, as well as the decrease with nozzle eccentricity.

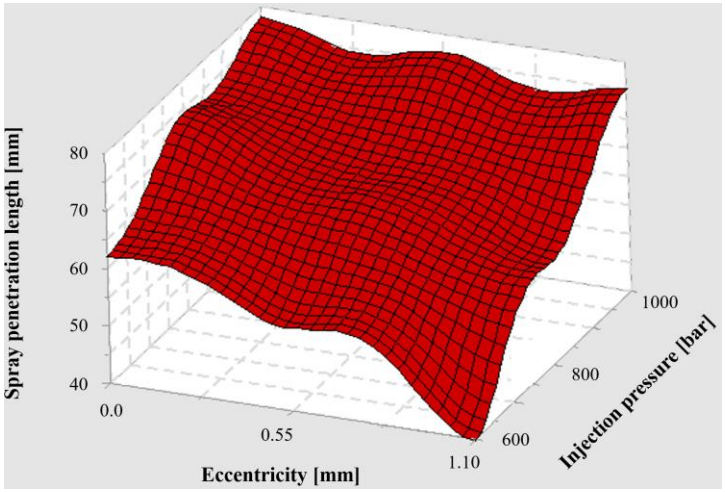

Figure 130 – Simulation results using the new approaches of the present thesis: spray penetration length at t=0.8 ms after start of injection versus nozzle eccentricity and injection pressure.

Figure 131 presents the computed average horizontal cone angle versus nozzle eccentricity and injection pressure. It is shown that the nozzle of moderate eccentricity is associated with the lowest values of spray cone angle, in comparison to the other two nozzles. Highest values are attained for the noneccentric nozzle. The effect of injection pressure is not substantial.

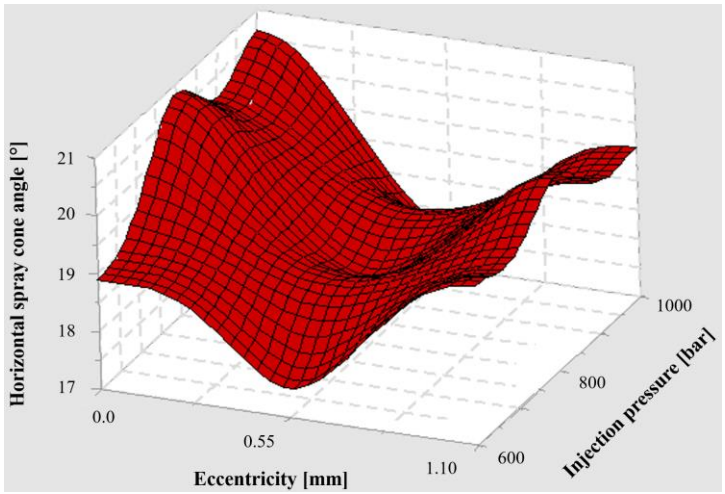

Figure 131 - Simulation results using the new approaches of the present thesis: spray average horizontal cone angle versus nozzle eccentricity and injection pressure.

Figure 132 presents the computed average vertical cone angle versus nozzle eccentricity and injection pressure. The vertical cone angle is found to increase with nozzle eccentricity, while the effect of injection pressure is not significant.

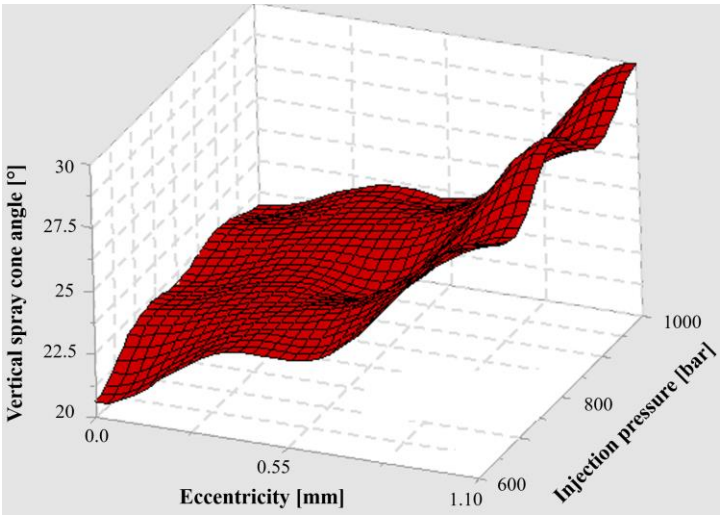

Figure 132 - Simulation results using the new approaches of the present thesis: spray average vertical cone angle versus nozzle eccentricity and injection pressure.

Figure 133 presents the computed average deflection angle in the horizonal direction versus nozzle eccentricity and injection pressure. The vertical cone angle is found to increase with nozzle eccentricity, and to mildly depend on injection pressure.

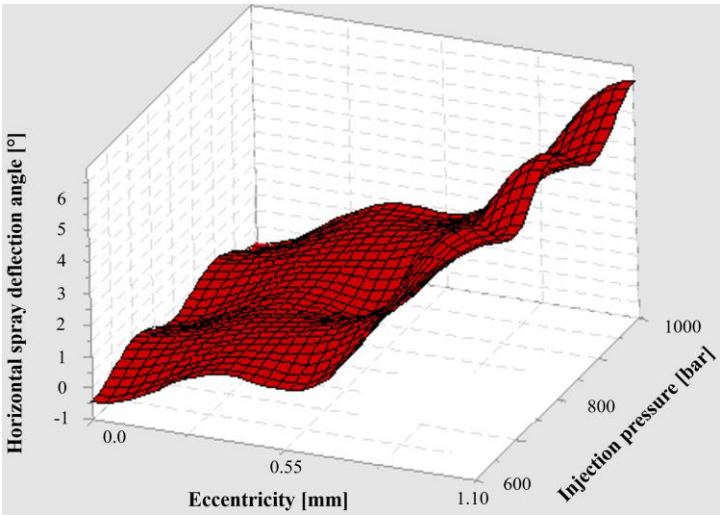

Figure 133 - Simulation results using the new approaches of the present thesis: spray average horizontal deflection angle versus nozzle eccentricity and injection pressure.

Finally, **Figure 134** presents the computed average deflection angle in the vertical direction versus nozzle eccentricity and injection pressure. A pronounced increase is observed for the nozzle of highest eccentricity. The effect of injection pressure is not substantial.

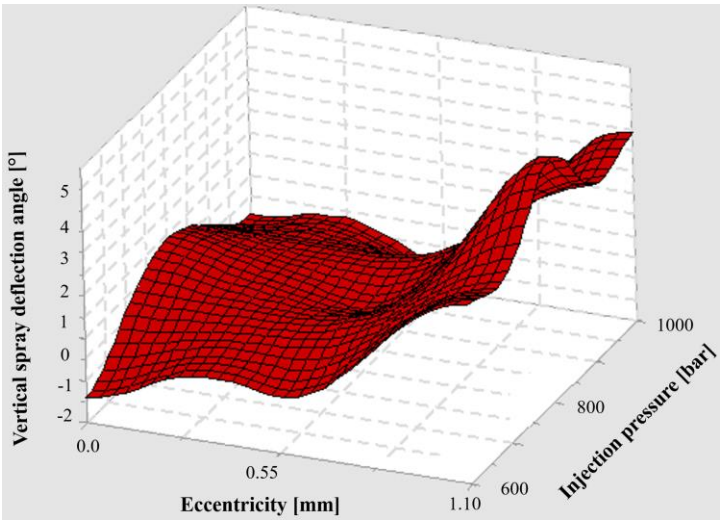

Figure 134 - Simulation results using the new approaches of the present thesis: spray average vertical deflection angle versus nozzle eccentricity and injection pressure

8.10 Conclusions

Spray secondary breakup simulations were presented and analyzed in the present chapter. To this end, inflow conditions were used from the β-PDF functions derived from processing the LES primary breakup results. The present simulations have relied on the Kelvin-Helmholtz Rayleigh-Taylor secondary breakup model, and were compared against results of conventional simulations, which utilize URANS for both primary and secondary breakup. Computational results were compared against experiments in terms of global characteristics, as spray cone and deflection angles, and penetration length; the present new approach was shown to perform better than the conventional one.

An adaptation of the new approach was introduced, using LES results at one injection pressure to approximate the primary breakup field at another level of injection pressure. The approach was validated using results at a reference pressure of 1000 bar to generate primary breakup results at injection pressures of 800 bar and 600 bar; a good comparison against experiments was demonstrated.

9 CHAPTER: Analysis of Reactive Sprays

9.1 Introduction

This chapter initially describes the experimental setup and measurement techniques applied in the present study to analyze sprays in reactive conditions. The primary goal of this part of the Thesis is to demonstrate that the computational approach developed here is applicable to reactive sprays. Preliminary combustion simulations were performed (courtesy of A. Matrisciano, results reported in [181]), using the new computational approach coupled to a combustion solver (LOGEapi), with a flamelet based combustion model. Comparison between computational and experimental results is mainly in terms of ignition delay times.

9.2 Experiment

9.2.1 Experimental setup

Experimental tests were performed in the SCC in order to test the applicability of the present spray modeling approach in reactive conditions (90 bar, 900 K). The principle, layout and operation of the test facility have been analyzed in section 3.4. **Figure 135** depicts the test facility during one of the present experimental campaigns.

Figure 135 – View of the experimental test facility.

Elongated nozzles were tested (see **Figure 22**). A modified chamber cover was designed, to account more closely to the combustion chamber of a large two-stroke marine Diesel engine. Further, a new injector holder was designed, to fit the modified chamber cover. In the present experiments, the window position was carefully chosen, thus allowing a direct view of the spray formation (**Figure 136**).

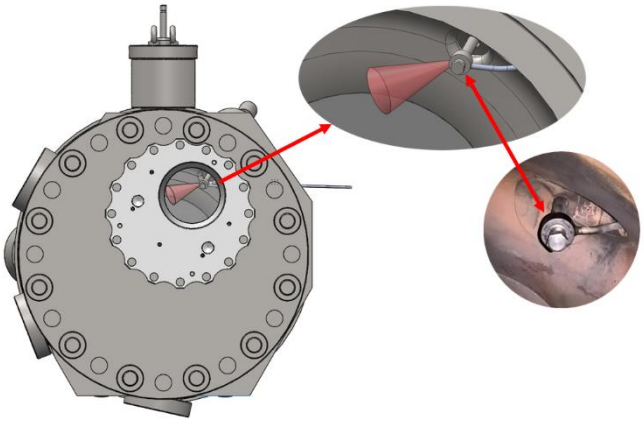

Figure 136 - CAD model of SCC showing the new design of the fuel bypass, with the spray structure also indicated.

A proper injected amount (fuel mass) is ensured by using the bypass, where the fuel first enters the bush around the nozzle tip, and then flows through the bypass piping. The piping transfers the uninjected fuel into a vessel, outside the combustion chamber (see sketch of **Figure 137**).

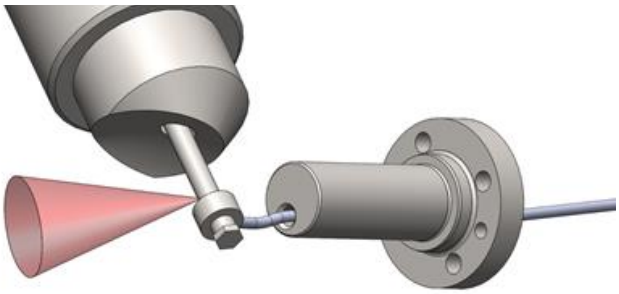

Figure 137 – Sketch of injection assembly, including the injector holder, the elongated nozzle, the bush, and the fuel bypass piping.

9.2.2 Operating conditions

In the present experiments under reactive conditions (90 bar, 900 K), injection was triggered in a low-intensity swirling air flow. The fuel rail pressure was set to 1000 bar (injection pressure).

9.2.3 Fuel and injection timing

To check for the repeatability of experiments, ten injections were realized and recorded for each of the three nozzles considered in the present study (as shown in **Figure 22**). All experiments were performed with n-dodecane as fuel. The injection temperature of the fuel was 333 K. Some important thermophysical properties of the fuel are presented in **Table 21**.

Table 21 Fundamental thermo-physical properties of n-dodecane.

	n-dodecane
Boiling Point [°C]	214-218
Auto-Ignition Point [°C]	210
Density [kg/m3] at 25 C°	750

9.2.4 Applied measurement equipment

Standard instrumentation

Sensors for pressure (piezoelectric pressure sensor) and temperature (type K thermocouple) were installed in the SCC. Hydraulic pressure transducers were also implemented into the rail, at the Injection Control Unit (ICU), mounted on the top of the injector. The data acquisition rate of these sensors was set to 125 kHz. The position of the pressure and temperature sensors is presented in **Figure 138**.

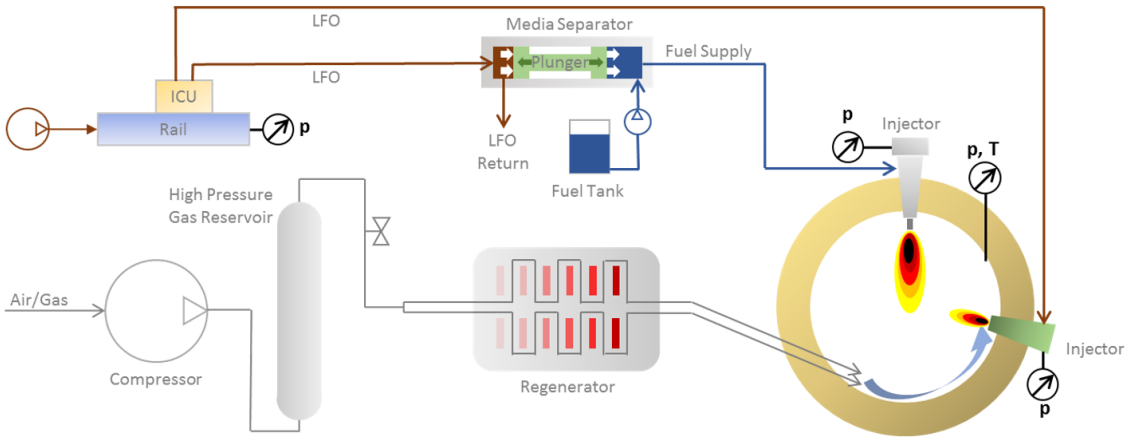

Figure 138 – Sketch of the experimental setup, in which pressure and temperature sensors have been included [Courtesy of N. Yamada, WinGD].

9.2.5 Optical setup

Optical measurements, as well as pressure and temperature measurements in time, were performed in the SCC. The target of optical measurements was the visualization of spray combustion, at high frequency (up to 20 kHz). A LaVision optical imaging system was used, with one laser and two cameras.

a. Sending optics

A schematic image of the sending optics is shown in **Figure 139**. The spray injected in the chamber is illuminated by an Nd:YAG laser (Edgewave, 20 kHz rep. rate, 532 nm) to perform spray imaging, detecting the entire spray development. Moreover, a UV diode laser (Edgewave, 10 kHz rep. rate, 355 nm) is applied to illuminate the flow field. The aim of the UV laser is to detect formaldehyde in the reacting flow in order to determine the detailed reaction zone and flame front.

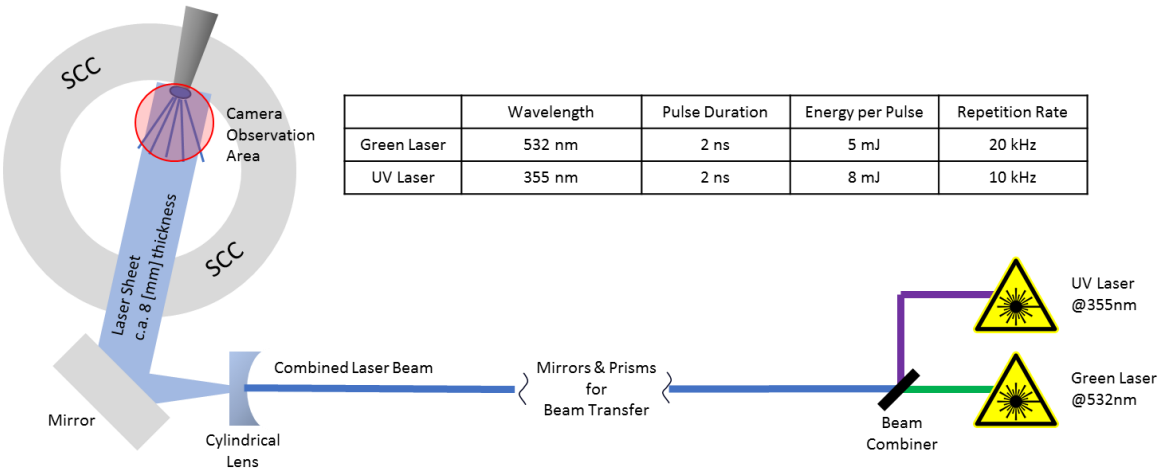

	Wavelength	Pulse Duration	Energy per Pulse	Repetition Rate
Green Laser	532 nm	2 ns	5 mJ	20 kHz
UV Laser	355 nm	2 ns	8 mJ	10 kHz

Figure 139 - Schematic image of optics, and specifications of laser used in the reactive spray experiments [Courtesy of N. Yamada, WinGD].

b. <u>Receiving optics</u>

The arrangement of the receiving optics and a summary of the targeted signals are depicted in **Figure 140**. The spray droplets before ignition are illuminated by the Nd:YAG laser, and the resulting images are recorded by Camera 1. The reacting flow is excited by the UV laser; formaldehyde, which is only present during combustion, is detected, and recorded by Camera 2. The OH radical, which is typically formed under combustion conditions, could be recorded by another camera (Camera 3), with an image intensifier; this camera was not used in the present investigation. Furthermore, two lasers, three cameras, and one image intensifier are synchronized. Appropriate dichroic mirrors and optical filters are placed between the reacting flow field and the camera, to filter out the unwanted optical noise. The synchronization of this optical system is provided by the Davis system, which is synchronized to the SCC system, and triggered by the SCC synchronization signal itself.

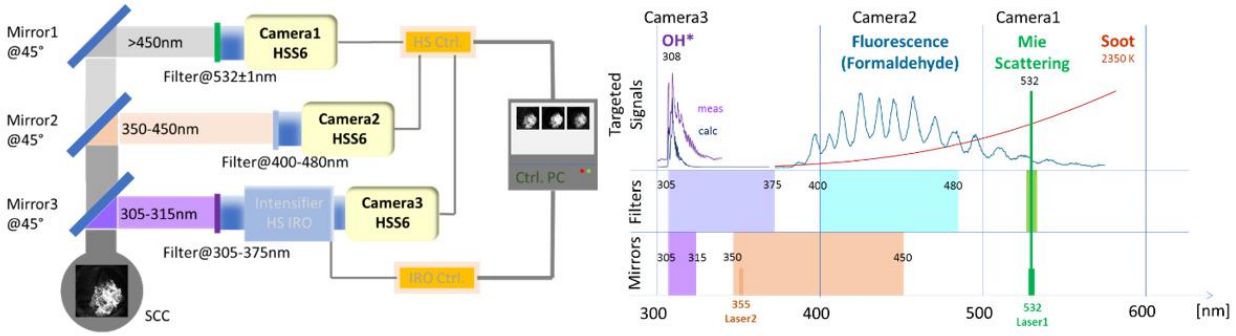

Figure 140 - Sketch of receiving optics and targeted signals applied [Courtesy of N. Yamada, WinGD].

c. Targeted optical signals

The optical setup described above provides both quantitative and qualitative data to study fundamental combustion characteristics at each injection condition. A summary of the targeted optical signals is presented in Table 22.

Table 22 Summary of targeted optical signals. Camera 3 was not used in the present study.

	Targeted Optical Signals	Physics to be characterized
Camera 1	Shadowgraphy	Start of injection End of injection Spray tip penetration Spray spatial distribution Flame development and shape (qualitative)
Camera 2	Formaldehyde	Precise combustion flame front (qualitative)
Camera 3	OH* radical	Auto-ignition timing Auto-ignition location Soot spatial distribution (qualitative)

d. Processing and interpretation of control signals

To operate the injector in the SCC system, a commercially available CCM-20 system was integrated. **Figure 141** presents an overview of the triggering schedule and acquired hydraulic readings with the received pressure signals. Important parameters of the experimental setup are presented in Table 23.

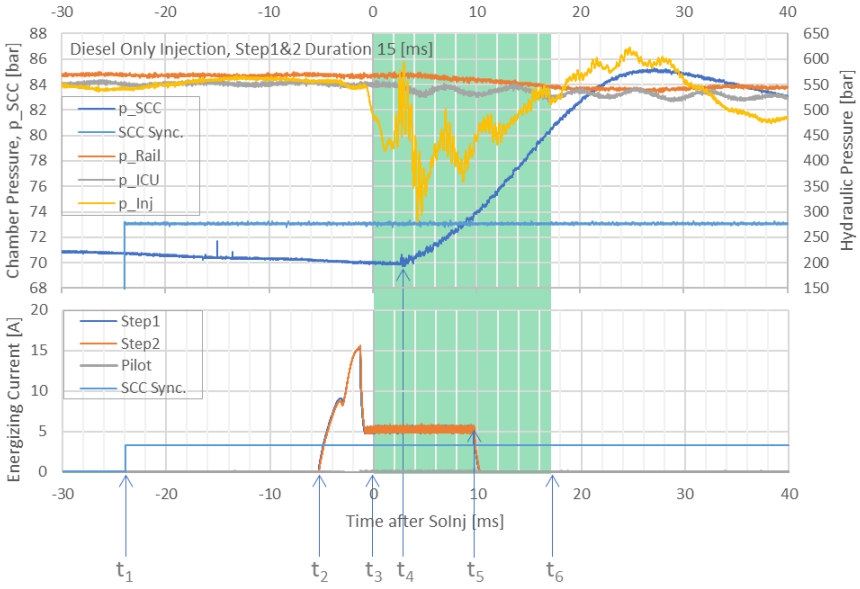

Figure 141 - Example of triggering and pressure signals. [Courtesy of N. Yamada, WinGD.]

Table 23 Notation of triggering and pressure signals of Figure 142.

Notation	Description	Remark
t_1	Start of sync. signal	Produced and sent by SCC transient system
t_2	Start of energizing	Start of pulling current to steps 1 & 2 coils
t_3	Actual start of injection	Determined by sequential camera1 (Mie) images
t_4	Start of ignition	Determined with sequential Camera 3 (OH*) images
t_5	End of energizing	End of holding the current to steps 1 & 2 coils
t_6	Actual end of injection	Determined by sequential camera1 (Mie) images
t_1 to t_2	Signal delay	Main contributor is the mechanical relay to convert 5 [V] signal from SCC to 24 [V] signal (to CCM-20)
t_2 to t_3	Hydraulic delay for opening	Depends on nozzle inner geometry, needle activity, supply pipe length, etc.
t_2 to t_5	Energizing duration	Sum of the pulling current and holding current durations
t_3 to t_4	Ignition delay	Subtraction (t_4-t_3)
t_3 to t_6	Actual injection duration	Subtraction (t_6-t_3)
t_5 to t_6	Hydraulic delay for closing	Depends on nozzle inner geometry, needle activity, supply pipe length, etc.

e. <u>Data filtering</u>

The acquired raw data contain strong fluctuations, in comparison to conventional Diesel combustion with standard injectors; these fluctuations affect computed quantities, as shown in **Figure 143** (right), on the example of heat release rate, computed from the pressure signal. In the present experiments, the signals of the piezoelectric sensors recording hot gas pressure naturally contain a certain level of high-frequency noise. To eliminate high-frequency fluctuations, the standard moving average filter was applied. In **Figure 143** (left), an example of the entire heat release rate curve, as derived from the measured pressure is shown (blue); the filtered curve is plotted in orange.

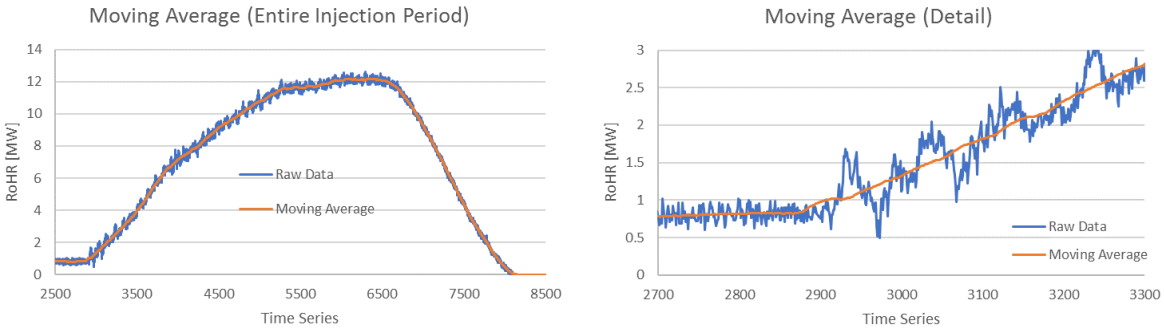

Figure 143 - Example of raw and filtered curves of HRR measured in the SCC.

9.3 Simulation setup

For the reactive case (90 bar, 900 K), the flow solver was coupled with the LOGEapi combustion solver [297]; the results of reactive flow have been presented [181]. Combustion is modeled using a flamelet based combustion model. This family of models, analyzed extensively by Peters in [298], assumes that a turbulent flame can be described by an ensemble of laminar one-dimensional flame structures, referred to flamelets. The model allows the de-coupling of the turbulent flow field and the combustion chemistry. After a coordinate transformation from physical space to flamelet space, it may be observed that the reactive scalars can be expressed as functions of the mixture fraction, *Z*, and the scalar dissipation rate, χ. For turbulent non-premixed combustion, the flamelet method provides the possibility to consider sub-grid-scale effects and the effect of turbulence on the evolution of chemistry. Mixture fraction is defined based on the mass flow rates of the fuel ($\dot{m}_F$) and oxidizer stream ($\dot{m}_{ox}$) [181].

Mixture fraction
$$Z = \frac{\dot{m}_F}{\dot{m}_F + \dot{m}_{Ox}} \tag{107}$$

The scalar dissipation rate is defined as [303]:

Scalar dissipation rate
$$\chi = 2D(\nabla Z)^2 \tag{108}$$

where,
D is the diffusion coefficient
Z is the mixture fraction.

Assuming unity Lewis numbers, performing the coordinate transformation, and neglecting the coordinate directions tangential to the stoichiometric mixture fraction isosurface, the equation solved for species conservation in flamelet space reads [303]:

Species conservation
$$\rho \frac{\partial Y_i}{\partial \tau} = \rho \frac{\chi}{2} \frac{\partial^2 Y_i}{\partial Z^2} + \omega_i \tag{109}$$

where,
Y_i is the mass fraction of species i
ρ is the density
τ is the flamelet time (equal to the physical time t)
Z is the mixture fraction
ω_i is the chemical source term of species i.

In Equation (*110*), the term including the scalar dissipation rate acts as a diffusion term in the mixture fraction space. Implementation of the TIF solver and its coupling with the flow solver are discussed in detail in [299]; a brief summary is presented below.

Transport equations for the mean mixture fraction can be expressed as [303]:

Transport equation
$$\rho \frac{\partial \tilde{Z}}{\partial t} + \rho \tilde{v} \cdot \nabla \tilde{Z} - \nabla \cdot \left(\bar{\rho} D_t \nabla \tilde{Z} \right) = \overline{\omega_i} \quad (111)$$

where,
t is the time
ρ is the density
$\tilde{Z}$ is the mean mixture fraction
$\tilde{v}$ is the mean velocity
D_t is the turbulent diffusivity
$\overline{\omega_i}$ is the source term

Equation (*111*) contains the spray evaporation source term on the right-hand side. Recently, Olguin and Gutheil [300] presented a derivation of the flamelet equations, where the influence of the spray source term on the flamelet structure was considered. However, in the present study, which employs a multiple flamelet strategy, the influence of the evaporation source term on the flamelet structure is neglected. Borghesi *et al.* [301] investigated the influence of the spray source terms in the Conditional Moment Closure (CMC) equation when studying the spray H flames and found that there was a small effect on the ignition delay time, but hardly any influence on the flame structure and the flame stabilization mechanism. Therefore, they assumed that the inclusion of the spray source term in the flamelet equation would not significantly impact the results obtained with the transient interactive flamelet method.

The mean scalar dissipation rate is modelled according to [303]:

Mean scalar dissipation rate
$$\tilde{\chi} = c_\chi \frac{\tilde{\varepsilon}}{\tilde{k}} \widetilde{Z''^2} \quad (112)$$

where
c_χ is the constant of proportionality, with a value of 1.5-3 (in this study $c_\chi = 2$)
$\tilde{\varepsilon}$ is the Favre averaged rate of dissipation
$\tilde{k}$ is the Favre averaged turbulent kinetic energy
$\widetilde{Z''^2}$ is the Favre averaged mixture fraction fluctuation.

In the TIF approach, multiple interactive flamelets are solved following a fuel-based splitting strategy. The implementation allows for using any number of flamelets. For each flamelet, a flamelet marker transport equation is solved, similar to the mixture fraction equation. In the present work, a single flamelet was used. The scalar dissipation rate is modeled in mixture fraction space using the inverse complementary error function [303], and the magnitude of the scalar dissipation rate profile is given by the conditional scalar dissipation rate. The scalar dissipation rate treatment for the individual interactive flamelets is described in [299]. An overview over different multiple flamelet strategies is presented in the same reference.

Since no species transport is solved in the physical space, the thermodynamic state in the flow field is updated using the mixture fraction, mixture fraction variance, and the flamelet markers. To

obtain density, specific heat, and enthalpy, the appropriate quantities present in the solution of the interactive flamelets are integrated by the mixture fraction PDF (assumed to be a beta-pdf determined by the mixture fraction and its variance), and weighted by the flamelet probabilities. Chemical species are retrieved in a similar manner for post-processing purposes.

In the present study, a single interactive flamelet was used. The mixture fraction grid utilized in the interactive flamelet calculations contained 101 grid points, which were non-uniformly distributed.

9.4 Experimental results

The spray was homogeneously illuminated by an Nd:YLF laser from below, where the laser sheet was placed in the centre of the spray plume. Experiments were carried out by using a fast-speed camera with a sampling frequency of 20 kH, capturing the scattered light. The exposure time was set to $1e-07s$. Three nozzle layouts were tested, namely the noneccentric, and the two eccentric nozzles, characterized by an eccentricity of 0.55 mm and 1.10 mm (normalized values of 0.4 and 0.8, respectively).

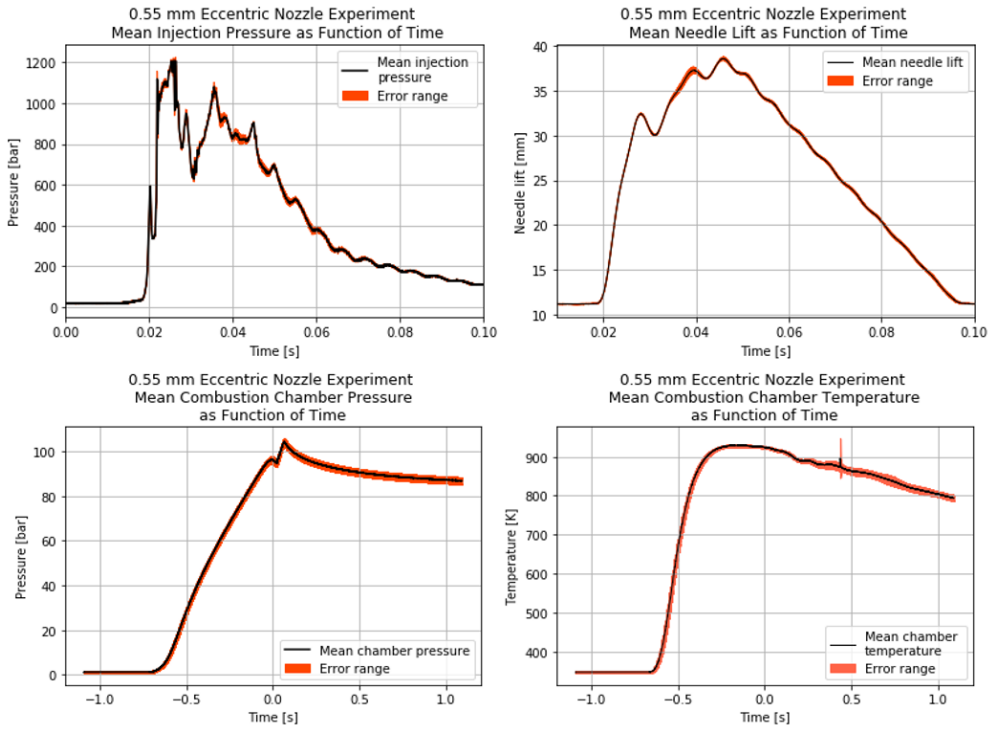

Figure 144 - Measured injection pressure, needle lift, chamber pressure and temperature versus time, for injection from the nozzle with an eccentricity of 0.55 mm (normalized value of 0.4).

The injection duration was set in accordance with the earlier experiments of Schmid *et al.* [50]. **Figure 144** presents the signals of injection pressure, needle lift, as well as the signals of average chamber pressure and temperature. Each nozzle tip was tested in a series containing 10 consecutive shots, averaged measured quantities were then calculated. An exemplary series of images, visualizing the temporal evolution of spray, and the subsequent propagation of flame is presented in **Figure 145**, for the case of noneccentric nozzle tip.

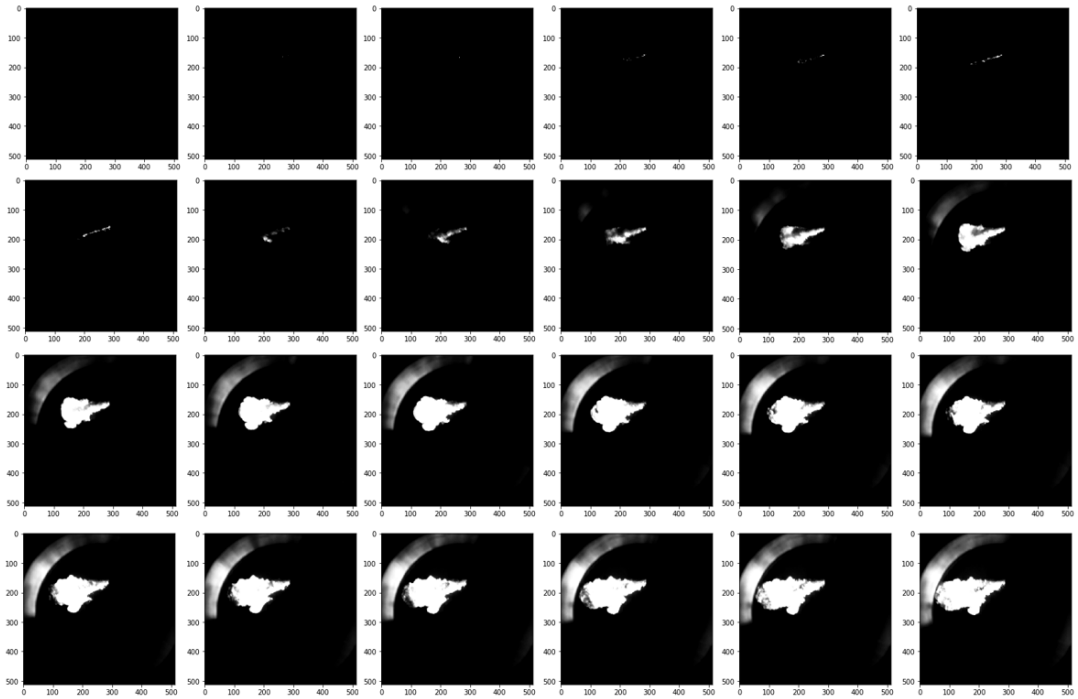

Figure 145 – Images of spray development and combustion, for injection from a noneccentric nozzle type in the SCC.

9.4.1 Ignition delay analysis

As an outcome of the image analysis, intensity matrices were created for each image, consisting of 512 x 512 pixels. To identify the ignition point, the time instant corresponding to the maximum intensity of each pixel was recorded, and the chronological development of the neighboring zone was analyzed. Furthermore, the measured pressure trace of the chamber was used to provide an initial guess for a realistic estimation of ignition time. A correction was introduced to account for the propagation of the pressure wave initiated by ignition to the point of the pressure sensor [157].

Firstly, images of the 10 consecutive shots were averaged, and a mean image was created for each time step analyzed. An example of the averaged images, corresponding t=0.00115 s, can be seen in **Figure 146**, where the bright colours represent the high-intensity pixels, indicating the reactive area. The maximum intensity was determined at each time instant and used for normalizing the intensity values.

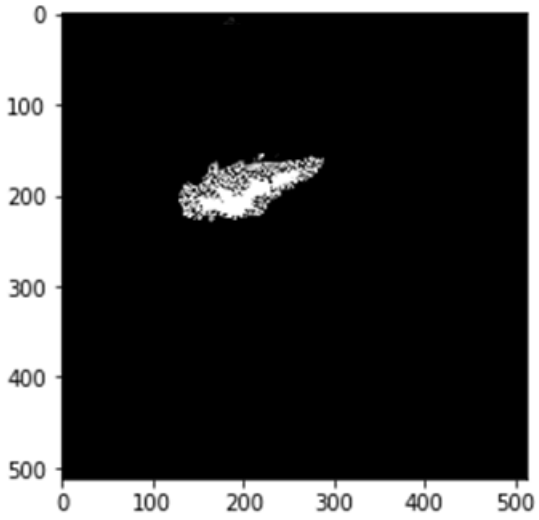

Figure 146 - Time averaged image of a spray corresponding to the eccentric nozzle with 0.55 mm eccentricity (normalized value of 0.4), at the t=0.00115 s.

9.5 Results of reactive flow simulations

To characterize reactive spray flow for the three nozzles of different eccentricity considered here (initial temperature and pressure of 900 K and 90 bar), reactive flow simulations were performed using the approach outlined above. **Figure 147** and **Figure 148** report the computed histories of maximum chamber temperature and rate of heat release, respectively, for all three nozzle geometries.

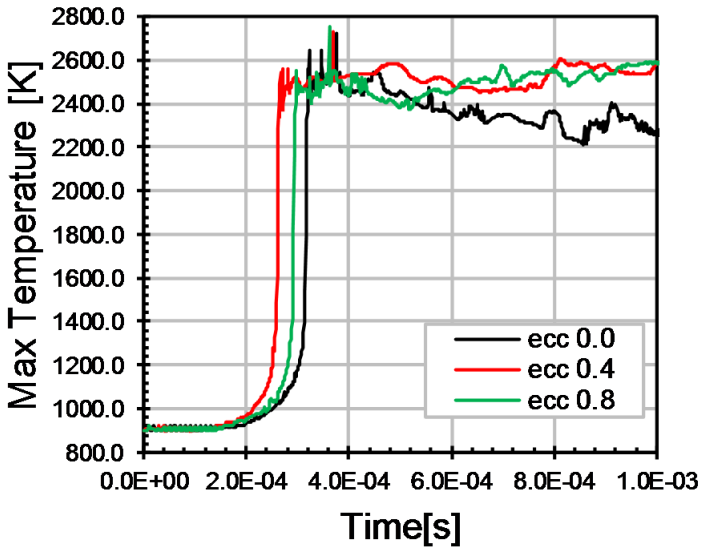

Figure 147 - Maximum temperature comparisons for all three investigated nozzle geometries (normalized eccentricity values of 0.0, 0.4 and 0.8). (Courtesy of A. Matrisciano. Reported in [181].)

In accordance with the trends identified for nonevaporating conditions, the nozzle of medium eccentricity exhibits the highest difference compared to the noneccentric one. The discrepancy

mainly refers to ignition delay (earlier ignition for eccentric nozzles), nonetheless it also characterizes the entire heat release event. Further increase in the nozzle eccentricity (from a normalized value of 0.4 to one of 0.8) results in an ignition event which is more similar to that of the noneccentric nozzle.

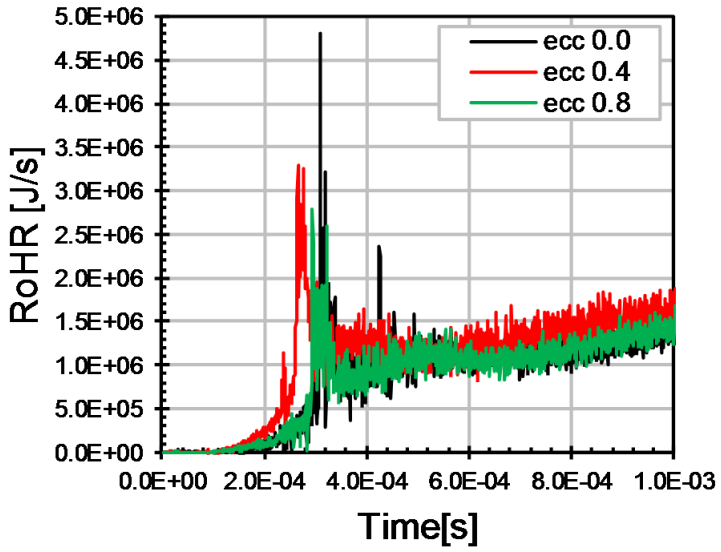

Figure 148 - Rate of heat release comparisons for all three investigated nozzle geometries (normalized eccentricity values of 0.0, 0.4 and 0.8). (Courtesy of A. Matrisciano. Reported in [181].)

The flame morphology of the three nozzles considered is presented in **Figure 149** in terms of temperature isocontours, at t=0.35 ms. Despite the similarities in the heat release curves (**Figure 148**), the flame structure is quite different in the three cases shown. The nozzle of highest eccentricity is associated with the strongest deflection of the flame with respect to the nozzle centreline, in accordance with the observations of the present study regarding the corresponding non-reactive sprays.

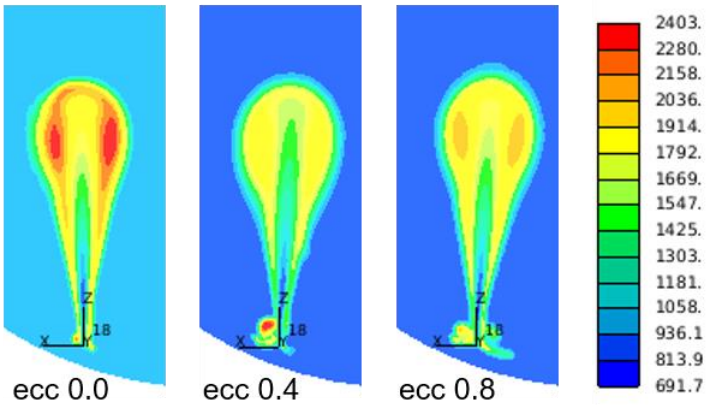

Figure 149 – Color-coded temperature contours [in K] for all three investigated nozzle geometries at t=0.35 ms (normalized eccentricity values of 0.0, 0.4 and 0.8) at $t=3.5 \cdot 10^{-4}$ s. (Courtesy of A. Matrisciano. Reported in [181].)

9.6 Comparison between experiments and simulation

In this section, a quantitative comparison between computed and measured ignition delay times is presented. In the simulations, ignition time is identified from the temporal history of maximum temperature, in particular, as the point of maximum temporal derivative. The experimental ignition delay was identified from the analysis outlined above, which combines the pixel intensity and the measured pressure signals. Results are presented in **Figure 150**. In the experiments, the normalized pixel intensity is also reported for each of the individual shots (triangles), as well as the resulting mean values (circles) and the associated standard deviation (half of the range of presented bars). A reasonably good agreement between the computational and experimental value of ignition delay is demonstrated, for all three nozzles considered.

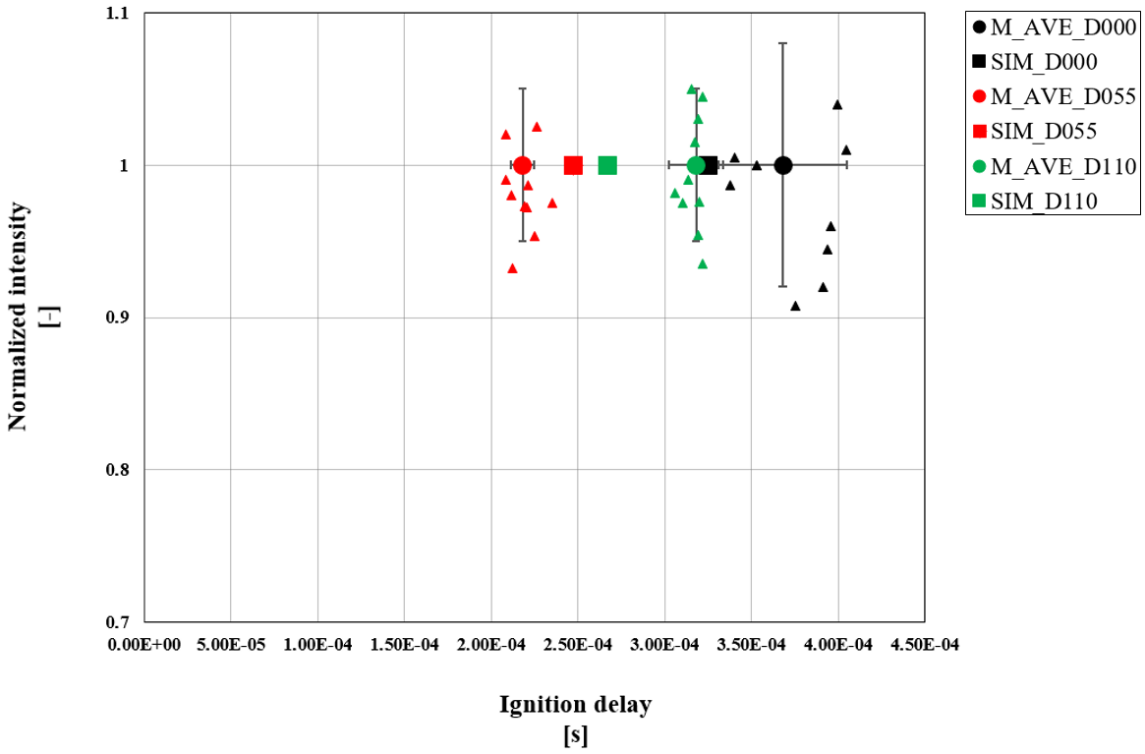

Figure 150 - Ignition delay times for all three investigated nozzle geometries, based on CFD simulations (squares) and the present experiments (triangles correspond to individual shots, circles to average values). The normalized pixel intensity is also reported for experiments. Normalized eccentricity values are: e^*=0.0 (black), e^*=0.4 (red), e^*=0.8 (green). (Simulations: courtesy of A. Matrisciano, reported in [181].)

9.7 Conclusions

In the course of the work presented in this chapter, the new approach of the present thesis was extended to study reactive spray flow in the SCC. Computational results were compared against new experiments. To realize the present experiments, a modified chamber cover, as well as a new injection setup, were designed and implemented. The first CFD results presented here were compared against experiments in terms of ignition delay time, demonstrating an overall good agreement, for all three injectors of different eccentricity considered. Both experiments and simulations have shown that ignition delay is shortest for the nozzle of medium eccentricity.

Visualization of the computed reactive flow fields has shown that the flame deflection increases with nozzle eccentricity, in accordance with the observations for non-reactive spray flow.

10 CHAPTER: Novelty of the Present Work and Contribution to Scientific Research

10.1 Proposed methodology

A new simulation approach for the accurate computation of asymmetric (and axisymmetric) sprays of large two-stroke marine Diesel engine injectors has been developed and validated against experiments. The new approach provides an integrated framework for the simulation of those spray flows at an increased accuracy in comparison to today's practice, while maintaining an affordable computational cost.

In particular, the following methodology has been proposed and tested here in the context of modeling the in-nozzle flow and spray development of large marine engine injectors:

- Simulation of the in-nozzle cavitating flow in a URANS framework.
- Simulation of spray primary breakup with LES, utilizing inflow conditions derived from the simulation of in-nozzle flow.
- Characterization of spray primary breakup applying, among others, a new droplet identification technique. Statistical analysis of results for deriving proper inflow conditions for secondary breakup simulations. Characterization of flow structure and dynamics by means of Proper Orthogonal Decomposition (POD) analysis.
- Modeling of spray secondary breakup in a URANS framework. Characterization of spray structure in terms of global parameters as penetration length, spray angles and deflection angles.
- Adaptation of LES results at a given injection pressure to another injection pressure, for setting up secondary breakup simulations at the new pressure.
- Application of the present approach to the simulation of reactive spray flow.

10.2 New findings of the present thesis

The method developed has been applied in CFD studies of spray simulations in nonevaporating and reactive conditions in the context of large two-stroke marine Diesel engine operation. The main findings can be summarized as follows:

(1) In-nozzle flow substantially affects the flow field at nozzle bore exit, resulting in a strong deviation from axisymmetry, and giving rise to a strongly asymmetric spray structure. In-nozzle flow cavitation patterns, and the resulting discharge coefficient values, vary substantially with nozzle eccentricity.

(2) The spray jet is deflected in a direction corresponding to the low velocity regime of the nozzle exit.

(3) POD results demonstrate that the flow dynamics is adequately represented by few dominant modes.

(4) The spray cone angle increases with nozzle eccentricity. Accompanied by the stronger deflection, this gives a higher effective spray area, resulting in increased intensity of spray breakup, and thus a decreased penetration length.

(5) First results show that the present modeling approach is applicable to reactive spray flow.

(6) Overall, the proposed approach yields results which are superior to those using the standard, URANS-only, approach implemented in commercial CFD codes.

10.3 Journal publications

The main core of present work has been presented in the following journal publications:

[1] Nagy, I. G., Papadopoulos C. and Kaiktsis L. 2020. *Proper Orthogonal Decomposition Analysis of Asymmetric Sprays of Large Two-Stroke Marine Diesel Engines*. International Journal of Latest Technology in Engineering, Management and Applied Sciences 9(2), 55-67.

[2] Nagy, I. G., Hensel S., Schmid A. and Kaiktsis L. 2021. *Computational Analysis of Spray Formation in Large Two-Stroke Marine Diesel Engine Atomizers*. Journal of Energy Engineering 147(2), 04020092 1-16.

[3] Balz, R., Nagy I. G., Weisser G. and Sedarsky D. 2021. *Experimental and Numerical Investigation of Cavitation in Marine Diesel Injectors.* International Journal of Heat and Mass Transfer 169, 120933 1-12.

10.4 Refereed conference publications

Two referred conference papers and two posters have resulted from the work presented in this thesis:

[1] Nagy, I. G., Schmid, A., Hensel, S., Dahnz, C. 2015. *Computational analysis of spray primary breakup in 2-stroke marine diesel engines with different nozzle layouts*. In Proc., 13th Triennial International Conference on Liquid Atomization and Spray Systems (ICLASS), Tainan, Taiwan.

[2] Nagy, I. G., Matrisciano, A., Lehtiniemi, H. and Mauss, F. 2017. *Influence of Nozzle Eccentricity on Spray Structures in Marine Diesel Sprays*. SAE International, SAE Technical paper 2017-24-0031, Capri, Italy.

[3] Nagy, I. G., Hensel, S. and Kaiktsis, L. 2016. *Characterization of Asymmetric Structure of Large Marine Diesel Engine Sprays.* Advanced Engine Modelling Workshop, International Combustion Institute (ICISS), Chania, Greece.

[4] Nagy, I. G., Hensel, S., Schmid, A. and Kaiktsis, L. 2017. *Influence of Nozzle Eccentricity on Spray Structures in Marine Diesel Sprays.* Experimental and Computational Tools for Combustion Optimization in Marine and Automotive Engines (ECCO-MATE) final meeting, Athens, Greece.

This page is intentionally left blank.

11 CHAPTER: Concluding Remarks

In this thesis, a new simulation approach, accounting for the asymmetric and axisymmetric spray formation in large two-stroke marine Diesel engines, was developed, and mainly applied for nonevaporating sprays.

Firstly, URANS in-nozzle flow simulations were performed for different large two-stroke marine Diesel engine atomizer geometries. Highly asymmetric velocity distribution was experienced inside the nozzle bore. Velocities were higher on the eccentricity side of the bore, while significantly lower velocities characterized the flow on the opposite side of eccentricity. In non-cavitating flow simulations, flow recirculation regions, especially in the case of high nozzle eccentricity, were computed, suggesting a cavitating flow behavior.

Next, URANS in-nozzle flow simulations were analyzed, considering cavitation inside the nozzles. These results provided new insight into the three-dimensional flow characteristics, that are hard to realize with common experiments. Good agreement between simulation and experimental results was found for the qualitative comparison of the cavitation patterns, as well as for the quantitative validation, using the computed and measured momentum flux values. Simulations accurately predicted the cavitation zone locations and vapor formation inside the nozzle bore for each nozzle. Several complex cavitation phenomena, such as supercavitation, geometry-induced cavitation and film-like cavitation were identified within the nozzle bore, for the different geometries considered. Furthermore, the comparison of the investigated different nozzle layouts indicated that the standard (noneccentric) nozzle had the highest velocities and strongest turbulence, while the eccentric nozzle the lowest levels in that regard. The standard nozzle was characterized by the highest average volume gas fraction at the orifice, and hence the lowest discharge coefficient. The inclined nozzle had by far the lowest level of cavitation, and therefore the highest discharge coefficient and momentum flux.

The spray primary breakup was simulated using LES. Here, the dynamic-Smagorinsky turbulence model was applied. Inlet boundary conditions were derived from the URANS in-nozzle flow simulations. Grid sensitivity tests ensured the proper resolution in LES. The resulting spray structures were analyzed, and it was illustrated that the eccentric arrangement of the nozzle results in a deflection normal to the main spray direction, giving a strongly asymmetric mean structure. The deflection increased as a function of nozzle eccentricity. The present results show that the spray is not just deflected in the radial direction, but it also deviates from its symmetry line upwards. Higher nozzle eccentricity is associated with a wider spray structure and a larger effective area. Consequently, a more intense atomization is experienced.

A new droplet identification method was introduced. LES results of spray primary breakup were post-processed, the disintegrating droplets were identified and used to develop β-PDFs, statistically describing the primary breakup. These distributions were used as input for the spray secondary breakup calculations.

A 3D POD analysis was implemented to the computed velocity and fuel concentration fields in the primary breakup regime. The calculated modes were correlated to disintegrating flow structures from the intact liquid core and interpreted as a liquid atomization process. The results

demonstrated that representation of the flow dynamics and flow reconstruction is feasible in terms of a small number of dominant modes. The computed POD modes are representative of the asymmetric spray structure in the primary breakup regime.

As indicated, the β-PDFs developed from the analysis of primary breakup LES simulations were used to generate inflow conditions for spray secondary breakup simulations, in which the Kelvin-Helmholtz Rayleigh-Taylor secondary breakup model was used. A conventional URANS-only approach, consisting in modeling primary breakup with the Reitz model and secondary breakup with the Reitz-Diwakar model was also implemented, to generate reference simulation results. All computational results were compared against experiments in terms of spray deflection, spray angles, and spray penetration length. It was demonstrated that the present approach, consisting in a combination of LES and URANS simulations for the primary and secondary breakup, respectively, predicts the strong flow asymmetry, and is superior to the conventional approach, in terms of predicting global spray characteristics as spray angles and penetration length. The present computational study has shown that spray deflection and the spray cone angles increase at increased nozzle eccentricity. Results can be associated with a higher effective spray area, yielding an increased intensity of spray breakup, and thus a decreased penetration length.

An adaptation for the new approach introduced in the present study was utilized to estimate the primary breakup field at different injection pressures, using the LES results of the spray primary breakup at an injection pressure of 1000 bar as a reference dataset. This has utilized the outcome of in-nozzle flow URANS simulations at reduced injection pressures (800 bar, 600 bar), in particular the nozzle exit velocity, as well as literature recommendations arising from dimensional analysis, and yielded an approximation of the flow field in the primary breakup regime, in particular mean droplet diameter and velocity, and the associated β-PDFs. Thus, a proper setup of secondary breakup simulations was enabled by means of the KH-RT secondary breakup model, also including a proper adaptation of model constants. The comparison of the new CFD results against experiments has demonstrated a good agreement regarding the spray tip penetration for all three nozzle layouts investigated, at the two reduced injection pressures. Computational results regarding spray cone angles were also in a general good agreement with experiments. Spray deflections were accurately modeled for the noneccentric nozzle cases, while a moderately good agreement was found for the eccentric nozzles. At each pressure level, the new method outperformed the conventional (URANS-only) simulation approach.

Finally, preliminary spray simulations were carried out under reactive conditions using the new approach in conjunction with a combustion solver and compared against new experiments in the SCC. The comparison was in terms of ignition delay times, for all nozzle layouts; a reasonably good agreement was demonstrated.

Overall, the present study has verified the strongly asymmetric structure of sprays emanating from large marine engine injectors, and presented a detailed characterization of flow physics, with emphasis on nonevaporating sprays. Thus, the present new approach, shown to accurately calculate these sprays, while maintaining the computational cost at an affordable level, can be adopted for accurate CFD studies of flow and combustion in large marine engine applications.

This page is intentionally left blank.

12 CHAPTER: Future Work

Suggestions for future work, following the present study, should aim at a further development and simplification of the present approach. Based on the experience gained during the present study, the following suggestions for future work are provided.

1. Detailed models:
   - A more accurate representation of the in-nozzle flow can be attained by simulating the real multi-hole nozzle geometry with all nozzle bores, including a moving needle. This should be accompanied by applying realistic time-dependent pressure and temperature functions at the inlet and outlet boundaries, derived from hydraulic and thermodynamic combustion simulations.

   - Diverse fuels, with properly prescribed thermophysical properties, should be accounted for.

   - Time-dependent inflow boundary conditions can be implemented in the LES simulations of primary breakup, either derived from in-nozzle LES or by means of synthetic turbulent boundary conditions.

2. Spray characterization:
   - Validation of computed quantities as droplet diameter distribution and velocity by means of experiments using laser techniques (PIV, LDA/PDA).

3. Engine applications:
   - A more detailed investigation of in-cylinder flow, including reactive conditions, should be undertaken.

This page is intentionally left blank.

REFERENCES

1. Eyring, V., et al. 2007. *Multi-model simulations of the impact of international shipping on atmospheric chemistry and climate in 2000 and 2030*. Atmos. Chem. Phys. 7 (3): 757–780.

2. ABS (American Bureau of Shipping). 2018. *Setting the course to low carbon shipping*. Houston, TX: ABS.

3. United Nations. 2019. *Review of maritime transport*. Geneva, Switzerland: United Nations.

4. Det Norske Veritas (DNV GL). 2018. *Assessment of Selected Alternative Fuels and Technologies*. Chapter 1-3, Hamburg, Germany.

5. Wik, C. and Niemi, S. 2016. *Low emission engine technologies for future Tier III legislations – options and case studies*. Journal of Shipping and Trade (2016) 1:3

6. Miola, A. and Ciuffo, B. 2011. *Estimating air emissions from ships: Meta-analysis of modelling approaches and available data sources*. Atmospheric environment. 45 2242-51.

7. Buhaug, Ø., Corbett, J., Endresen, Ø., Eyring, V., Faber, J. and S. Hanayama. 2009. *Second IMO GHG study 2009*. International Maritime Organization, London, UK.

8. Hoffmann, J. and Kumar, S. 2010. *Globalisation–the maritime nexus. in: C.T.H. Grammenos*. (Ed.). The Handbook of Maritime Economics and Business. Lloyd's List, London, UK.

9. Lister, J., Poulsen, R.T. and Ponte, S. 2015. *Orchestrating transnational environmental governance in maritime shipping*. Global Environmental Change. 34 185-95.

10. Balcombe, P., Brierley, J., Chester, L., Line, S., Jamie, S., Hawkes, A. and Staffell, I. 2019. *How to decarbonise international shipping: Options for fuels, technologies, and policies*. Energy Conversion and Management 182(02), pp. 72-88.

11. Det Norske Veritas (DNV GL). 2018. *Maritime Forecast to 2050, Energy transition outlook 2018*. Chapter 4, pp.55, Hamburg, Germany.

12. Future Ship Powering Options. 2013. *Exploring alternative methods of ship propulsion*. Royal Academy of Engineering (Great Britain) and Royal Academy of Engineering (Great Britain) Staff, ISBN 9781909327016, Chapter 1.

13. Exxonmobil. 2018. *The impact of regulation on cylinder oil lubricant selection*. Fathom Maritime Intelligence, Windsor, United Kingdom.

14. Azzarra, A., Rutherford, D., Wang, H. 2014. *Feasibility of IMO Annex VI TIER III implementation using Selective Catalytic Reduction*. The International Council on Clean Transportation.

15. Briggs, J. 2014. *The impact of Tier III NOx regulation on the shipping industry*. Bulletin 2014, 109(5).

16. American Bureau of Shipping (ABS). 2018. *Guide for Exhaust Emission Abatement*. Houston, Texas, USA.

17. Wuersig, G. 2018. *Status and Outlook for Alternatives to Conventional Oil Based Ship Fuels*. DNV GL Forum at SMM International Maritime Trade Fair, Hamburg, Germany.

18. Fenhann, J. V. 2017. *CO2 Emissions from International Shipping*. UNEP DTU Partnership Working Paper Series 2017 (4), Technical University of Denmark, Lyngby, Denmark.

19. Olmer, N., Comer, B., Roy, B., Mao, X. and Rutherford, D. 2017. *Greenhouse Gas Emissions from Global Shipping*. 2013–2015. Washington DC., USA.

20. Nyhus, E. 2018. *DNV GL Environmental regulations – what's hot?* DNV GL Forum at SMM International Maritime Trade Fair, Hamburg, Germany.

21. Det Norske Veritas (DNV GL). 2017. *DNV GL NOx TIER III Update, Choices and challenges for on-time compliance*. Germany, Hamburg.

22. Kackur, J. 2018. Wärtsilä Marine Solutions Business White Paper, *Shipping in the 2020 era – selection of fuel and propulsion machinery*. Vaasa, Finland.

23. Wärtsilä Services Business White Paper. 2018. *A clean environment, Towards zero-emission shipping*. Vaasa, Finland.

24. https://www.dnv.com/maritime/insights/topics/decarbonization-in-shipping/index.html

25. Det Norske Veritas (DNV GL). 2020. *Webinar: Decarbonization in shipping - status and outlook*. www.dnv.com.

26. Det Norske Veritas (DNV GL). 2015. *Uncovering the Potential*. Maritime Impact, Technology and Innovation, pp.19, Hamburg, Germany.

27. Det Norske Veritas (DNV GL). 2019. *Comparison of Alternative Marine Fuels*. Environment Advisory, Hovik, Norway.

28. Shell. 2020. *Decarbonizing shipping: Setting Shell's course*. www.shell.com/energy-and-innovation/the-energy-future/decarbonizing-shipping.html.

29. Det Norske Veritas (DNV). *Alternative Fuel Insights*. https://afi.dnvgl.com.

30. Clarkson Research Services Ltd ("Clarksons Research"), Commodity Quay, St Katharine Docks, London, United Kingdom, E1w 1bf. https://www.clarksons.com/services/research/.

31. Lloyd's Register Marine. 2014. *Global Marine Fuel Trends 2030*. London, UK.

32. Leclerq, X. 2021. *CMA SHIPS LNG Program - Achievements and Challenges*. IMO Symposium on alternative low carbon and zero carbon fuels for shipping.

33. Kyrtatos, A., Spahni, M., Hensel, S., Züger, R. and Sudvoj G. 2016. *The development of the modern low-speed two-stroke marine diesel engine*. In *Proc.*, CIMAC Congress Frankfurt, Germany: International Council on Combustion Engines.

34. Frigge, P., Affolter, S., Bachmann, D. and de Jong, R. 2011. *New two-stroke marine diesel engines from Wärtsilä*. MTZ Worldwide, Springer Professional.

35. WinGD 2018. *Environmental Technologies*. Winterthur Gas and Diesel Ltd., Regulations, Chapter 1.

36. Jääskelainen, H. 2014. *Fuel Injection for Clean Diesel Engines*. DieselNet Technology Guide, Engine Design for Low Emissions.

37. Andreadis, P., Chryssakis, C. and Kaiktsis, L. 2009. *Optimization of Injection characteristics in a Large Marine Diesel Engine Using Evolutionary Algorithms*. SAE Technical Paper 2009-01-1448, Detroit, MI, USA.

38. Stratsianis, V., P. Kontoulis, and L. Kaiktsis. 2016. *Effects of fuel post-injection on the performance and pollutant emissions of a large marine engine*. J. Energy Eng. 142 (2): E4016001. https://doi.org/10.1061/(ASCE)EY.1943-7897.0000337.

39. Minamino, R., Kawabe, T., Omote, H. and Okada, S. 2013. *Fuel Injection Concept for the Future Clean Diesel Engines*. In *Proc.*, CIMAC Congress Frankfurt, Germany: International Council on Combustion Engines. SAE International, SAE Technical paper

40. Gao, Z., Yin, B., Liu, S., Zhu, J., Ju, Y. and Hang, Y. 2013. *Development Trend and Optimization Matching of Fuel Injection System of Diesel Engine*. In *Proc.*, CIMAC Congress Frankfurt, Germany: International Council on Combustion Engines.

41. Wärtsilä, *The Sulzer RT-flex Common-Rail System Described*. Wartsila Corporation, Aug 2014.

42. Aeberli, K. and McMillan, J. 2002. *Common Rail at Sea, The Sulzer RT-flex Engine.* The Motor Ship Marine Propulsion Conference, Copenhagen.

43. Lamas, M. I., Rodriguez, C. G. 2013. *Numerical Model to Study the Combustion process and emissions in the Wärtsilä 6L46 4-stroke Marine Engine*. Polish Maritime Research 2(78) 20; pp. 61-66.

44. Luo, Q., Si, X. and Yin, H. 2016. *Application of CFD Technology in the Development and Research of Internal Combustion Engine*. In *Proc.*, International Conference on Computer and Information Technology Application, Atlantis Press.

45. Boulouchos, K. 2012. *Large vs. Small IC Engines - similarities and differences across scales*. 3rd MARINLIVE Workshop, Athens, Greece.

46. Herrmann, K., Schulz, R. and Weisser, G. 2007. *Development of a reference experiment for large diesel engine combustion system optimization*. In *Proc*., CIMAC Congress. Frankfurt, Germany: International Council on Combustion Engines.

47. Herrmann, K., Kyrtatos, A., Schulz, R., Weisser, G., von Rotz, B., Schneider, B. and Boulouchos, K. 2009. *Validation and initial application of a novel spray combustion chamber representative of large two-stroke diesel engine combustion systems*. In *Proc*., ICLASS 11th Triennial Int. Annual Conf. on Liquid Atomization and Spray Systems.

48. Herrmann, K., von Rotz, B., Schulz, R., Weisser, G., Schneider B. and Boulouchos, K. 2011. *A 'spray combustion chamber' facility for investigations in relation to large 2-stroke marine diesel engine combustion system optimization*. In *Proc*., Int. Symp. on Marine Engineering (ISME). Kobe, Japan: Japan Institute of Marine Engineering.

49. Kyrtatos, N. P., Hellberg, L. and Poensgen, C. 2013. *Ten years after: Results from the major programme HERCULES A-B-C on marine engine R&D*. In *Proc*., CIMAC Congress. Frankfurt, Germany: International Council on Combustion Engines.

50. Schmid, A., von Rotz, B., Schulz, R., Herrmann, K., Weisser, G. and Bombach, R. 2013. *Influence of nozzle hole eccentricity on spray morphology*. ILASS 2013, Chania, Greece, 1-4 September.

51. Tennekes, H. and Lumley, J. L. 1972. *A first course in turbulence*. MIT Press.

52. Pope, S. B. 2000. *Turbulent flows*. Cambridge University Press.

53. Gaitonde, U. 2008. *Quality Criteria for Large Eddy Simulation*. First year transfer report, University of Manchester.

54. Dodoulas, I. 2015. *Application of LES-PDF Methods on Turbulent Reactive Flows*. PhD Thesis, Department of Mechanical Engineering, Imperial College of Science, Technology and Medicine.

55. Naitoh, K., Teruyuki, I., Yasuo, T. and Kunio, K. 1992. *Large Eddy Simulation of Premixed-Flame in Engine based on the Multi-Level Formulation and the Renormalization Group Theory*. SAE International, SAE Technical Paper 920590.

56. Fukuda, K. 2012. *Numerical Simulation of Fuel Sprays in Diesel Engines*. Master Thesis, Faculty of Graduates Studies through Mechanical, Automotive and Material Engineering, University of Windsor, Ontario, Canada.

57. Bedford, K.W. and Yeo, W.K. 1993. *Conjunctive Filtering Procedures in Surface Water Flow and Transport*. Large Eddy Simulation of Complex Engineering and Geophysical Flows, eds. Galperin, B., and Orszag, S., Cambridge University Press.

58. Lund, T. S. 1997. *On the use of discrete filters for large eddy simulation*. Center for Turbulence Research, Annual Research Briefs, Stanford University, California, USA.

59. Germano, M. 1992. *Turbulence: The filtering approach*. J. Fluid Mech., 238:325- 336.

60. Germano, M., Piomelli, U., Moin, P. and Cabot., W. 1991. *A Dynamic Subgrid-scale Eddy Viscosity Model*. Phys. of Fluids 3(7), pp. 1760–1765.

61. Stein, O. 2009. *Large Eddy Simulation of Combustion in Swirling and Opposed Jet Flows*. PhD thesis, Department of Mechanical Engineering, Imperial College London, London, United Kingdom.

62. You, D. and Moin, P. 2007. *A dynamic global-coefficient subgrid-scale eddy-viscosity model for large-eddy simulation in complex geometries*. Physics of Fluids 19(6), pp. 065110.

63. Haworth, D. C. 1999. *Large-Eddy Simulation of in-cylinder flows*. Oil & Gas Science and Technology, Rev. IFP 54(2), pp. 175-185.

64. Stoll, R. 2011. *LES of turbulent flows. Lecture:8.* Department of Mechanical Engineering, University of Utah, USA.

65. Lilly, D. K. 1992. *A proposed modification of the Germano subgrid-scale closure method*. Phys. Fluids A 4(3), pp. 633–35, https://doi.org/10.1063/1.858280.

66. Jansen, K. E. 1994. *Unstructured-grid large-eddy simulation of flow over an airfoil*. Center for Turbulence Research, Annual Research Briefs, Stanford University, California, USA.

67. Tejada-Martinez, A. E. and Jansen, K. E. 2004. *A dynamic-Smagorinsky model with dynamic determination of the filter width ratio*. Physics of Fluids 16, 2514.

68. Scotti, A., Meneveau, C. and Fatica, M. 1997. *Dynamic Smagorinsky model on anisotropic grids*. Physics of Fluids 9, 1856, https://doi.org/10.1063/1.869306.

69. Tucker, P. G. and Lardeau, S. 2009. *Applied large eddy simulation*. Philosophical Transactions of the Royal Society, *A* 2009 367, doi: 10.1098/rsta.2009.0065, 15.06.2009.

70. Keskinen, J. 2010. *The use of Large Eddy Simulation in Modelling of Gas Engines*. Ene-34.4551 Postgraduate Seminar on Heat and Fluid Flow.

71. Bodart, J. and Larsson, J. 2011. *Wall-modeled large eddy simulation in complex geometries with application to high-lift devices*. Center for Turbulence Research, Annual Research Briefs, Stanford University, California, USA.

72. Nicoud, F., Toda, H.B., Cabrit, O., Bose, S. and Lee, J. 2011. *Using singular values to build a subgrid-scale model for large eddy simulations*. Physics of Fluids 23.

73. Bardina, J., Ferziger, J. H. and Reynolds, W. C. 1980. *Improved Subgrid Model for Large-Eddy Simulation*. AIAA Paper 80-1357.

74. Bardina, J., Ferziger, J. H. and Reynolds, W. C. 1983. *Improved Turbulence Models Based on Large Eddy Simulation of Homogeneous Incompressible. Turbulent Flows*. Report TF-19, Thermosciences Division, Department of Mechanical Engineering, Stanford University, Stanford, California, USA.

75. Menon, S., Yeung, P. K. and Kim, W. W. 1996. *Effect of Subgrid Models on the Computed Interscale Energy Transfer in Isotropic Turbulence*. Computer and Fluids 25(2), pp. 165-180.

76. Yoshizawa, A. and Horiuti, K. 1985. *A Statistically-Derived Subgrid-Scale Kinetic Energy Model for the Large-Eddy Simulation of Turbulent Flows*. Journal of the Physical Society of Japan 54(8), pp. 2834-2839.

77. Ghosal, S., Lund, T. S., Moin, P. and Akselvoll, K., 1995. *A Dynamic Localization Model for Large-Eddy Simulation of Turbulent Flows*. Journal of Fluid Mechanics Vol. 286, pp. 229-255.

78. Pomraning, E. 2000. *Development of Large Eddy Simulation Turbulence models*. PhD Thesis, Department of Mechanical Engineering, University of Wisconsin-Madison, USA.

79. Senecal, P. K., Pomraning, E., Xue, Q., Som, S., Banerjee, S., Hu, B., Liu, K., and Deur, J. M. 2013. *Large Eddy Simulation of Vaporizing Sprays Considering Multi-Injection Averaging and Grid-Convergent Mesh Resolution*. Journal of Engineering for Gas Turbines and Power 136(11).

80. Habchi, C. 2012. *LES and Experimental investigation of Diesel sprays.* ICLASS 2012, 12th Triennial International Conference on Liquid Atomization and Spray Systems, Heidelberg, Germany.

81. Xiao, F., Dianat, M. and Mcguirk, J. J. 2014. *Large eddy simulation of single droplet and liquid jet primary breakup using a coupled level set/volume of fluid method*. Atomization and Sprays 24(4):281-302.

82. Befrui, B., Aye, A., Bossi, A., Markle, B. E. and Varble, D. L. 2016. *ECN GDI Spray G: Coupled LES Jet Primary Breakup - Lagrangian Spray Simulation and Comparison with Data*. ILASS Americas 28th Annual Conference on Liquid Atomization and Spray Systems, Dearborn, MI, USA.

83. Zheng, C. 2019. *Modeling and Simulation of High-Density Spray Combustion*. PhD Thesis, Mechanical and Aerospace Engineering, Syracuse University, New York, New York, USA.

84. Ghiji, M., Goldsworthy, L., Garaniya, V., Brandner, P. A. and Hield, P. 2014. *CFD Modelling of Primary Atomisation of Diesel Spray*. 19th Australasian Fluid Mechanics Conference, Melbourne, Australia.

85. Larsson, J. and Kawai, S. 2010. *Wall-modeling in large eddy simulation: lengthscales, grid resolution and accuracy*. Center for Turbulence Research, Annual Research Briefs, Stanford University, California, USA.

86. Baggett, J. S., Jimenez, J. and Kravchenko, A. G. 1997. *Resolution requirements in large-eddy simulations of shear flows*. Center for Turbulence Research, Annual Research Briefs, Stanford University, California, USA.

87. Rezaieravesh, S., Liefvendahl, M. and Fureby, C. 2016. *On grid resolution requirements for LES of wall-bounded flows*. ECCOMAS Congress 2016 - 7th European Congress on Computational Methods in Applied Sciences and Engineering, Crete, Greece.

88. Chapman, D. R. 1979. *Computational aerodynamics development and outlook*. AIAA J. 17, 1293.

89. Choi, H. and Moin, P. 2011. *Grid-point requirements for large eddy simulation: Chapman's estimates revisited*. Center for Turbulence Research, Annual Research Briefs, Stanford University, California, USA.

90. Meyers, J., Geurts, B. J. and Sagaut, P. 2008. *Quality and Reliability of Large Eddy Simulations*. Springer Science & Business Media B.V.

91. Nagib, H. M., Chauhan, K. A. & Monkewitz, P. A. 2007. *Approach to an asymptotic state for zero pressure gradient turbulent boundary layers*. Phil. Trans. R. Soc. A 365 (1852), 755–770.

92. Monkewitz, P. A., Chauhan, K. A. & Nagib, H. M. 2007. *Self-consistent high Reynolds-number asymptotics for zero-pressure-gradient turbulent boundary layers*. Phys. Fluids 19, 115101.

93. White, F. M. *Viscous Fluid Flow*. 3rd edition. McGraw-Hill, 2005.

94. Cabot, W. and Moin, P. 1999. *Approximate wall boundary conditions in the large-eddy simulation of high Reynolds number flow*. Flow, Turbul. Combust. 63, 269.

95. Nikuradse, J. 1950. *Laws of flow in rough pipes.* National Advisory Committee for Aeronautics, Technical Memorandum 1292, Washington, USA.

96. Zanoun, E.-S., Durst, F., Bayoumy, O. and Al-Salaymeh, A. 2007. *Wall skin friction and mean velocity profiles of fully developed turbulent pipe flow*. Experimental Thermal and Fluid Science 32(1), pp.249-261. DOI: 10.1016/j.expthermflusci.2007.04.002.

97. McGovern, J. 2011. *Technical Note: Friction Factor Diagrams for Pipe Flow*. School of Mechanical and Transport Engineering, Dublin Institute of Technology, Dublin, Ireland.

98. McKeon, B. J., Swanson, C. J., Zagarola, M. V., Donnelly, R. J. and Smits, A. J. 2004. *Friction factors for smooth pipe flow*. J. Fluid Mech. 511, pp. 41–44.

99. Rao, AR and Kumar, B. 2007. *Friction factor for turbulent pipe flow*. In: Div. Mech. Sci., Civ. Eng. Indian Institute of Science, Bangalore, India.

100. Brkic, D. 2011. *Review of explicit approximations to the Colebrook relation for flow friction*. J. Pet. Sci. Eng. 77, 34–48, https://doi.org/10.1016/J.PETROL.2011.02.006.

101. Kline, S. J., Reynolds, W. C., Schraub, F. A. and Rundstadler, P. W. 1967. *The structure of turbulent boundary layers*. Journal of Fluid Mechanics 30, pp. 741-773.

102. Schlicting, H. and Gersten, K. 2017. *Boundary-Layer Theory*. Springer, Berlin, Heidelberg. https://doi.org/10.1007/978-3-662-52919-5.

103. Gómez-Aldaraví, P. M. 2014. *Development of a computational model for a simultaneous simulation of internal flow and spray break-up of the Diesel injection process*. Ph.D. Thesis, Department of Machines and Thermal Engines, Universitat Politecnica de Valencia.

104. Tahmasebi, E. 2016. *Simulation of Internal Flow in Fuel Injection Process*. Ph.D. Thesis, Energy and Nuclear Science and Technology, Politecnico di Milano.

105. Sussman, M. and Puckett, E. G. 2000. *A Coupled Level Set and Volume-of-Fluid Method for Computing 3D and Axisymmetric Incompressible Two-Phase Flows*. Journal of Computational Physics 162, 301–337.

106. Noh, V. F and Woodward, P. 1976. *SLIC (Simple Line Interface Calculation)*. In *Proc*., 5th International Conference on Numerical Methods in Fluid Dynamics. Twente University, Enschede. Lecture Notes in Physics 59. Springer, Berlin, Heidelberg.

107. Convergent Science. 2018. *Converge manual*. Technical Report.

108. Giussani, F., Piscaglia, F., Saez-Mischlich, G. and Helie, J. 2020. *A three-phase VOF solver for the simulation of in-nozzle cavitation effects on liquid atomization*. Journal of Computational Physics 406.

109. Schmidt, D., Rakshit, S., Neroorkar, K. 2012. *Thermal and inertial equilibrium in small, high-speed, cavitating nozzle simulations*. ILASS-Americas, 24th Annual Conference on Liquid Atomization and Spray Systems, San Antonio, TX, USA.

110. Dabiri, S., Sirignano, W. A., Joseph, D. D. 2007. *Cavitation in an orifice flow*. Physics of Fluids 19.

111. Bode, Falkenstein, M., Davidovic, M., Pitsch, H., Taniguchi, H., Murayama, K., Arima, S. Moon, T., Wang, J. and Arioka, A. 2017. *Effects of Cavitation and Hydraulic Flip in 3-Hole GDI Injectors*. SAE International, Journal of Fuels and Lubricants 10.

112. Berg, E. v., Alajbegovic, A., Tatschl, R., Krüger, C. and Michels, U. 2001. *Multiphase Modeling of High-Pressure Diesel Sprays with the Eulerian-Eulerian Approach*. In *Proc*. ILASS Europe 2001, Zürich, Switzerland.

113. Berg, E. v., Edelbauer, W., Alajbegovic, A., Tatschl, R., Vollmajer, M., Kegl, B. and Ganippa, L. 2005. *Coupled Simulations of Nozzle Flow, Primary Fuel Jet Breakup and Spray Formation.* Journal of Engineering for Gas Turbines and Power 127(4).

114. Mithun, M. G., Koukouvinis, P. and Gavaises, M. 2018. *Numerical simulation of cavitation and atomization using a fully compressible three-phase model*. Physical Review Fluids 3.

115. Giannadakis, E., Gavaises, M. and Arcoumanis, C. 2008. *Modelling of cavitation in diesel injector nozzles.* Journal of Fluid Mechanics 616, pp 153-193.

116. Gavaises, M., Villa, F., Koukouvinis, P., Marengo, M. and Franc, J-P. 2015. *Visualisation and les simulation of cavitation cloud formation and collapse in an axisymmetric geometry*. International Journal of Multiphase Flow 68, pp. 14-26.

117. Arai M. 2012. *Physics behind diesel sprays*. In *Proc.*, ICLASS, 12th Triennial International Conference on Liquid Atomization and Spray Systems Heidelberg, Germany.

118. Karimi K. 2007. *Characterization of Multiple-Injection Diesel Sprays at Elevated Pressures and Temperatures*. PhD Thesis, School of Engineering, University of Brighton.

119. Vuorinen V. 2010. *LES of certain droplet size effects in fuel sprays*. PhD Thesis, Department of Energy Technology, Aalto University.

120. Arcoumanis, C., Gavaises, M. and French, B. 1997. *Effect of fuel injection processes on the structure of diesel sprays*. Transactions Journal of Engines, SAE Paper 970799, 106-3.

121. Desjardins, O. and Pitsch, H. 2010. *Detailed Numerical Investigation of Turbulent Atomization of Liquid Jets*. Atomization and Sprays 20(4), 311–336.

122. Arcoumanis, C., Flora, H. and Gavaises M. 2000. *Cavitation in Real-Size Multi-Hole Diesel Injector Nozzles*. SAE International, SAE Technical Paper 2000-01-1249.

123. Schmidt, D. P., Rutland, C. J., Corradini, M. L., Roosen, P. and Genge, O. 1999. *Cavitation in Two-Dimensional Asymmetric Nozzles.* SAE International, SAE Technical Paper 1999-03-01.

124. Schmidt, D. P. and Corradini, M. L. 2001. *The internal flow of diesel fuel injector nozzles: a review.* Int. J. Eng. Res, 2(1), pp. 1–22.

125. Schneider, B. M. 2003. E*xperimentelle untersuchungen zur spraystruktur in transienten, verdampfenden und nicht verdampfenden brennstoffstrahlen unter hochdruck*. PhD Thesis, Department of Mechanical and Process Engineering, ETH Zürich.

126. Schmitz, C. D., 2011. *A turbulence-based model for the primary breakup of pressure atomized liquid jets*. Graduate Theses and Dissertations. Paper 10296, Mechanical Engineering, Iowa State University.

127. Som, S. and Aggarwal, S. K. 2010. *Effects of primary breakup modeling on spray and combustion characteristics of compression ignition engines*. Combustion and Flame 157, 1179–1193.

128. Gorokhovski, M. and Herrmann, M. 2000. *Modeling Primary Atomization*. Annual Review of Fluid Mechanics 40(1), pp. 343-366.

129. Wierzba, A. 1993. *Deformation and Breakup of Liquid Drops in a Gas Stream at Nearly Critical Weber Numbers*. Experiments in Fluids 9, pp. 59–64.

130. Fischer, F., Heine, B. and Tropea, C. 2010. *Primary Breakup Model Considering Spray Core Development*. ILASS Europe 2010, 23rd Annual Conference on Liquid Atomization and Spray Systems, Brno, Czech Republic.

131. Turner, M. R., Sazhin, S. S., Healey, J. J., Crua, C. and Martynov, S. B. 2012. *A breakup model for transient Diesel fuel sprays*. Fuel 97:288-305, DOI: 10.1016/j.fuel.2012.01.076.

132. Lefebvre, A. H. and McDonell, V. G. 2017. *Atomization and Sprays*. Second edition, Introduction, CRC Press, New York, USA.

133. Pilch, M. and Erdman, C. 1987. *Use of Breakup Time Data and Velocity History Data to Predict the Maximum Size of Stable Fragments for Acceleration-Induced Breakup of a Liquid Drop*. International Journal of Multiphase Flow, 13, 741-757.

134. Reitz, R.D., 1978. *Atomization and Other Breakup Regimes of a Liquid Jet*. Ph.D. thesis, Princeton University, Princeton, NJ, USA.

135. Baumgarten, C. 2006. *Mixture formation in internal combustion engines*. Berlin: Springer.

136. Stiesch G. 2008. *Modeling Engine Spray and Combustion Processes*. Berlin: Springer.

137. Reitz, R. D. 1987. *Modeling atomization processes in high-pressure vaporizing sprays*. Atomization and Spray Technology, Volume 3, no. 4, pp. 309-337.

138. Kuensberg, S. C., Kong, S. C and Reitz, R. D. 1999. *Modeling the Effects of Injector Nozzle Geometry on Diesel Sprays*. SAE International, SAE Technical paper 1999-01-0912.

139. Huh, K.Y. and Gosman, A. D. 1991. *A phenomenological model of Diesel spray atomisation.* In. *Proc.*, Int. Conf. on Multiphase Flows, Tsukuba, 24-27 September.

140. Schmidt, D. P., Nouar, I., Senecal, P. K., Rutland, P. K., Martin, J. K. and Reitz, R. D. 1999. *Pressure-Swirl Atomization in the Near Field*. SAE International, SAE Technical Papers 108(3).

141. Bravo, L. and Kweon, C. B. 2014. *A Review on Liquid Spray Models for Diesel Engine Computational Analysis.* United States Army Research Laboratory Technical Report Number 6932, USA.

142. Reitz, R. 1996. *Computer Modeling of Sprays*. Spray Technology Short Course, Pittsburgh, PA, USA.

143. Reitz, R. D. and Bracco, F. V. 1982. *Mechanism of Atomization of a Liquid Jet*. The Physics of Fluids 26, 1376.

144. Reitz, R. D. and Bracco, F. V. 1986. *Mechanisms of Breakup of Round Liquid Jets*. The Encyclopaedia of Fluid Mechanics. Vol. 3, 1986, pp. 223-249.

145. Sazhin, S., Crua, C., Kennaird, D., Heikal, M. 2002. *The initial stage of fuel spray penetration.* Fuel 82 (2003) 875–885.

146. Sazhin, S., Crua, C., Hwang, J-S., Nob, S-Y. and Heikal, M. 2005. *Models of fuel spray penetration.* In *Proc.*: Estonian Academy of Sciences 11, pp. 154-160.

147. Som, S. 2009. *Development and validation of spray models for investigating Diesel engine combustion and emissions*. PhD thesis, University of Illinois at Chicago, USA.

148. Som, S. and Aggarwal S. K., 2010. *Effects of primary breakup modeling on spray and combustion characteristics of compression ignition engines.* Combustion and Flame 157 (2010) 1179–1193.

149. Som, S., Ramirez, A. I., Longman, D. E. and Aggarwal S. K. 2011. *Effect of Nozzle Orifice Geometry on Spray, Combustion, and Emission Characteristics under Diesel Engine Conditions*. Fuel 90(3):1267-1276, DOI: 10.1016/j.fuel.2010.10.048.

150. O'Rourke, P. J. and Amsden, A. A. 1987. *The TAB method for numerical calculation of spray droplet break-up*. SAE International, SAE Technical paper 872089.

151. Tanner, F. X. 1997. *Liquid jet atomization and droplet break-up modeling of non-evaporating diesel fuel sprays*, SAE International, SAE Technical paper 970050.

152. Reitz, R. D. and Diwakar, R. 1987. *Structure of High-pressure Fuel Sprays*. SAE International, SAE Technical Paper 870598, Society of Automotive Engineers. Warrendale, PA.

153. Beale, J. C. and Reitz, R. D. 1999. *Modeling spray atomization with the Kelvin-Helmholtz / Rayleigh-Taylor hybrid model*. Atomization and Sprays. 9(6):623-650.

154. Senecal, P. K., Pomraning, E., Richards, K. J., Yang, T., Dai, M., Mcdavid, R. M., Patterson, M. A., Hou, S. and Shethaji, T. 2007. *A New Parallel Cut-Cell Cartesian CFD Code for Rapid Grid Generation Applied to In-Cylinder Diesel Engine Simulations*. SAE International, SAE Technical Paper, 2007-01-0159.

155. Patterson, M. and Reitz., R. 1998. *Modeling the effects of fuel spray characteristics on diesel engine combustion and emission*. SAE International, Vol. 107, Section 3: Journal of Engines (1998).

156. Taylor, G. I. 1963. *Generation of ripples by wind blowing over a viscous fluid*. Scientific Papers of Sir G.I. Taylor (Ed. G. K. Bachelor), 3, Cambridge University Press (Paper written for the Chemical Defence Research Department, Ministry of Supply, 1940).

157. von Rotz, B. 2015. *Experimental investigation of spray characteristics and ignition processes at conditions representative of large two-stroke marine diesel engines*. Ph.D. thesis, Dept. of Mechanical and Process Engineering, Swiss Federal Institute of Technology, Zurich, Switzerland.

158. Schmid, A., Habchi, C., Bohbot, J. and Herrmann, K. 2014. *Influence of in-nozzle flow on spray morphology*. ILASS 2014, Bremen, Germany, 8-10 September.

159. von Rotz, B., Herrmann, K. and Boulouchos, K. 2015. *Experimental Investigation on the Characteristics of Sprays Representative for Large 2-Stroke Marine Diesel Engine Combustion Systems*. SAE Technical Paper 2015-01-1825, doi:10.4271/2015-01-1825.

160. Arcoumanis, C., Gavaises, M. and French, B. 1997. *Effect of fuel injection processes on the structure of diesel sprays*. Warrendale, PA: Society of Automotive Engineers.

161. Heywood, J. B. 1988. *Internal combustion engine fundamentals*. USA: McGraw Hill.

162. Hiroyasu, H., and Arai, M. 1990. *Structures of fuel sprays in diesel engines*. Warrendale, PA: SAE.

163. Weisser, G. 2013. *Investigations into spray and combustion processes at conditions typical of large diesel engines making use of a spray combustion chamber specifically devised for this purpose*. Conference: 14. Tagung "Der Arbeitsprozess des Verbrennungsmotors / The Working Process of the Internal Combustion Engine".

164. Takasaki, K., Tajima, H., Nakashima, M., Ishida H. and Osafune, S. 2002. *Combustion characteristics of trouble-making bunker fuel oil*. In *Proc*., CIMAC Congress, 620–629. Frankfurt, Germany: International Council on Combustion Engines.

165. Pizza, G., Y. Wright, M., Weisser, G. and Boulouchos, K. 2007. *Evaporating and non-evaporating diesel spray simulation: comparison between the ETAB and wave break-up model*. Int. Journal of Vehicle Design, 45: 80-99.

166. Fink, C., Buchholz, B., Niendorf, M. and Harndorf, H. 2008. *Injection spray analyses from medium speed engines using marine fuels*. In *Proc*., 22nd European Conf. on Liquid Atomization and Spray Systems. Paris: ILASS – EUROPE.

167. Bolla, M., Cattin, M. A., Wright, Y. M., Boulouchos, K. and Schulz, R. 2012. *3D-CFD Lagrangian spray simulations for large two stroke marine diesel engines compared with experimental data of a spray combustion chamber*. In *Proc*., ASME 2012 Internal Combustion Engine Division Spring Technical Conference, ASME.

168. Bolla, M., Srna, A. and Wright, Y. M., von Rotz, B., Hermann, K. and Boulouchos, K. 2014. *Influence of Injector Diameter (0.2-1.2 mm range) on Diesel Spray Combustion: Measurements and CFD simulations*. SAE International, SAE Technical Paper 2014-01-1419. doi:10.4271/2014-01-1419.

169. Li, H., Verschaeren, R., Decan, G., Beji, T. and Verhelst, S. 2019. *Evaluation of breakup models for marine diesel spray simulations*. 29th Conference on Liquid Atomization and Spray Systems, ILASS-Europe, Paris, France, September 2-4.

170. Kontoulis, P., Kazangas, D., Doss, T. P. and Kaiktsis, L. 2018. *Development and CFD validation of an integrated model for marine heavy fuel oil thermophysical properties*. J. Energy Eng. 144(5), 04018059: https://doi.org/10.1061/(ASCE)EY.1943-7897.0000576.

171. Kontoulis, P., Kaiktsis, L., von Rotz, B. and Boulouchos, K. 2019. *CFD modeling and experimental spray studies for different heavy fuel oil qualities with respect to large two-stroke marine engines*. J. Energy Eng., 145(5): 04019014: 1-17.

172. Hensel S., Hermann, K., Schulz, R. and Weisser, G., *Numerical analysis, and statistical description of the primary breakup in fuel nozzles of large two stroke engines for the application in CFD engine simulations*. ILASS 2012, Fukuoka, 2012.

173. El Tahry, S. H. 1983. *k-ε equation for compressible reciprocating engine flows*. AIAA, Journal of Energy. 7(4), 345–353.

174. Weltens, H., Bressler, H., Terres, F., Neumaier, H. and Rammoser, D. 1993. *Optimisation of catalytic converter gas flow distribution by CFD prediction*. SAE International, SAE Technical Paper No. 930780.

175. Patankar, S.V. 1980. *Numerical Heat Transfer and Fluid Flow*. CRC Press.

176. Mitroglou, N., Gavaises M. and Nouri, J. M. 2011. *Cavitation inside enlarged and real-size fully transparent injector nozzles and its effect on near nozzle spray formation*. In *Proc*., 2011 DIPSI Workshop.

177. Balz, R., Nagy, I. G., Weisser, G. and Sedarsky, D. 2021. *Experimental and numerical investigation of cavitation in marine Diesel injectors.* International Journal of Heat and Mass Transfer 169.

178. International Maritime Organization (IMO). 2012. *International Shipping Facts and Figures-Information Resources on Trade, Safety, Security, Environment*. Technical Report.

179. Herrmann, K. 2007. *Development of a reference experiment for large diesel engine combustion system optimization*. In *Proc.*, Congress of the International Council on Combustion Engines (CIMAC), Vienna, Austria.

180. Nagy, I. G., Schmid, A., Hensel, S., Dahnz, C. 2015. *Computational analysis of spray primary breakup in 2-stroke marine diesel engines with different nozzle layouts*. In *Proc*., 13th Triennial International Conference on Liquid Atomization and Spray Systems, Tainan, Taiwan.

181. Nagy, I. G., Matrisciano, A., Lehtiniemi, H. and Mauss, F. 2017. *Influence of Nozzle Eccentricity on Spray Structures in Marine Diesel Sprays*. SAE International, SAE Technical paper 2017-24-0031.

182. Martynov, S., Mason, D., Heikal, M. R. 2006. *Modelling of Cavitation Flow in a Nozzle and Its Effect on Spray Development*. In *Proc*.,13th International Heat Transfer Conference. Begell House, Inc., Sydney, Australia.

183. Sou, A., Hosokawa, S. and Tomiyama, A. 2007. *Effects of cavitation in a nozzle on liquid jet atomization*. International Journal of Heat and Mass Transfer 50.

184. Jeshani, M. 2013. *Optical characterisation of cavitating flows in diesel fuel injection equipment*. PhD Thesis, School of Engineering & Mathematical Sciences, City University, London.

185. Sun, Y., Guan, Z. and Hooman, K. 2019. *Cavitation in Diesel Fuel Injector Nozzles and its Influence on Atomization and Spray*. Chemical Engineering and Technology 42.

186. Mirshahi, M., Nouri, J. and Yan, Y. 2013. *Link between in-nozzle cavitation and jet spray in a gasoline multi-hole injector*. ILASS Europe, 25th European Conference on Liquid Atomization and Spray Systems. Chania, Greece, pp. 1–4.

187. Lesnik, L., Kegl, B. and Bombek, G. 2018. *The influence of in-nozzle cavitation on flow characteristics and spray break-up*. Fuel 222: 550–560.

188. Payri, F., Bermudez, V. and Payri, R. 2004. *The influence of cavitation on the internal flow and the spray characteristics in diesel injection nozzles*. Fuel 83(4-5): 419–431.

189. Shervani-Tabar, M., Parsa, S. and Ghorbani, M. 2012. *Numerical study on the effect of the cavitation phenomenon on the characteristics of fuel spray*. Mathematical and Computer Modelling 56(5-6): 105–117.

190. Hutli, E., Nedeljkovic, M. and Bonyar, A. 2017. *Experimental study on the influence of geometrical parameters on the cavitation erosion characteristics of high-speed submerged jets*. Experimental Thermal and Fluid Science 80(August): 281–292.

191. Som, S., Aggarwal, S. K., El-Hannouny, E. M. 2010. *Investigation of Nozzle Flow and Cavitation Characteristics in a Diesel Injector*. Journal of Engineering for Gas Turbines and Power 132(4): 042802.

192. Nouri, J. M., Mitroglou, N., Yan, Y. and Arcoumanis, C. 2018. *Internal Flow and Cavitation in a Multi-Hole Injector for Gasoline Direct - Injection Engines*. SAE International, SAE Technical Paper.

193. Jia, M., Xie, M. and Liu, H. 2011. *Numerical simulation of cavitation in the conical-spray nozzle for diesel premixed charge compression ignition engines*. Fuel 90(8): 2652-2661.

194. Salvador, F. J., Carreres, M. and Jaramillo, D. 2015. *Analysis of the combined effect of hydrogrinding process and inclination angle on hydraulic performance of diesel injection nozzles*. Energy Conversion and Management 105: 1352–1365.

195. Desantes, J. M., Payri, R. and Salvador, F. J. 2003. *Measurements of Spray Momentum for the Study of Cavitation in Diesel Injection Nozzles*. SAE International, SAE Technical Paper 2003-01-0007.

196. Duke, D. J., Kastengren, A. L. and Swantek, A. B. 2016. *X-ray fluorescence measurements of dissolved gas and cavitation*. Experiments in Fluids 57(10): 1–14.

197. Duke, D. J., Matusik, K.E. and Kastengren, A. L. 2017. *X-ray radiography of cavitation in a beryllium alloy nozzle*. International Journal of Engine Research18(1-2): 39– 50.

198. Zhang, X., Moon, S. and Gao, J. 2016. *Experimental study on the effect of nozzle hole-to-hole angle on the near-field spray of diesel injector using fast X-ray phase-contrast imaging*. Fuel 185: 142–150.

199. Falgout, Z. and Linne, M. 2015. *Cavitation Inside High-Pressure Optically Transparent Fuel Injector Nozzles*. Journal of Physics: Conference Series 656.

200. Blessing, M., Konig, G. and Kruger, C. 2003. *Analysis of Flow and Cavitation Phenomena in Diesel Injection Nozzles and Its Effects on Spray and Mixture Formation*. SAE International, SAE Technical Paper 2003-01-0013.

201. Falgout, Z. and Linne, M. 2016. *Novel design for transparent high-pressure fuel injector nozzles*. Review of Scientific Instruments 87(8).

202. Aleiferis, P. G., Serras-Pereira, J., Augoye, A., Davies, T. J., Cracknell, R. F. and Richardson, D. 2010. *Effect of fuel temperature on in-nozzle cavitation and spray formation of liquid hydrocarbons and alcohols from a real-size optical injector for direct-injection spark-ignition engines*. International Journal of Heat and Mass Transfer 53.

203. Balz, R., Schmid, A. and Sedarsky, D. 2017. *In-Nozzle Flow Investigations of Marine Diesel Injectors*. ILASS – Americas, 29th Annual Conference on Liquid Atomization and Spray Systems. Atlanta, GA, USA.

204. Balz, R. and Sedarsky, D. 2019. *Temperature Dependent In-Nozzle Flow Investigations of Marine Diesel Injectors*. ILASS - Americas, 30th Annual Conference on Liquid Atomization and Spray Systems. Tempe, AZ, USA, pp. 1–7.

205. Schmidt, D. 2001. *The internal flow of diesel fuel injector nozzles: A review*. International Journal of Engine Research 2(1): 1–22.

206. Arcoumanis, C., Gavaises, M. and Nouri, J. 2008. *The role of cavitation in automotive fuel injection systems*. In *Proc*., 8th International Symposium on Internal Combustion Diagnostics, Baden-Baden, Germany.

207. Wang, C., Moro, A., Xue, F., Wu, X. and Luo, F. 2018. *The influence of eccentric needle movement on internal flow and injection characteristics of a multi-hole diesel nozzle*. International Journal of Heat and Mass Transfer 117.

208. Zhao, J., Liu, W., Zhao, J. and Grekhov, L. 2020. *Numerical investigation of gas/liquid two-phase flow in nozzle holes considering the fuel compressibility*. International Journal of Heat and Mass Transfer 147.

209. Marcer, R., Le Cottier, P., Chaves, H., Argueyrolles, B., Habchi, C. and Barbeau, B. 2000. *A Validated Numerical Simulation of Diesel Injector Flow Using a VOF Method*. SAE International. SAE International, SAE Technical Paper 2000-01-2932.

210. Gold, M., Pearson, R., Turner, J. Sykes, D., Stetsyuk, V., De Sercey, G., Crua, C., Koukouvinis, F. and Gavaises, M. 2019. *Simulation and Measurement of Transient Fluid Phenomena within Diesel Injection*. SAE International, SAE Technical Papers 2019-01-0066.

211. Waclawczyk, T. and Koronowicz, T. 2006. *Modeling of the Wave Breaking with CICSAM and HRIC High Resolution Schemes*. In *Proc.*, European Conference on Computational Fluid Dynamics, Egmond aan Zee, The Netherlands.

212. Zhao, H., Quan, S., Dai, M., Pomraning, E., Senecal, P. K., Xue, Q., Battistoni, M. and Som, S. 2014. *Validation of a Three-Dimensional Internal Nozzle Flow Model Including Automatic Mesh Generation and Cavitation Effects*. Journal of Engineering for Gas Turbines and Power 136.

213. Neroorkar, K., Shields, B., Grover, R. O., Torres, A. P. and Schmidt, D. P. 2012. *Application of the Homogeneous Relaxation Model to Simulating Cavitating Flow of a Diesel Fuel*. SAE International. SAE Technical Papers 2012-01-1269.

214. Neroorkar, K. and Schmidt, D. 2011. *A Computational Investigation of Flash-Boiling Multi-hole Injectors with Gasoline-Ethanol Blends*. SAE International, SAE Technical Paper 2011-01-0384.

215. Schmidt, D. P., Gopalakrishnan, S. and Jasak, H. 2010. *Multi-dimensional simulation of thermal non-equilibrium channel flow*. International Journal of Multiphase Flow 36(4):284-292.

216. Battistoni, M., Som, S., Longman, E. D. 2014. *Comparison of Mixture and Multi-Fluid Models for In-Nozzle Cavitation Prediction*. Journal of Engineering for Gas Turbines and Power 136(6):061506.

217. Shields, B., Neroorkar, K. and Schmidt, D. 2011. *Cavitation as rapid flash boiling*. ILASS-Americas, 23rd Annual Conference on Liquid Atomization and Spray Systems, Ventura, CA, USA.

218. Brusiani, F., Negro, S., Bianchi, G. M., Moulai, M., Neroorkar, K. and Schmidt, D. P. 2013. *Comparison of the Homogeneous Relaxation Model and a Rayleigh Plesset Cavitation Model in Predicting the Cavitating Flow Through Various Injector Hole Shapes*. SAE International, SAE Technical Paper 2013-01-1613.

219. Salvador, F. J., Pastor, J. M., De la Morena, J. and Martinez-Miracle, E. C. 2020. *Computational study on the influence of nozzle eccentricity in spray formation by means of Eulerian Σ - Y coupled simulations in diesel injection nozzles*. International Journal of Multiphase Flow 129.

220. Lee, J., Madabhushi, R., Fotache, C., Gopalakrishnan, S. and Schmidt, D. P. 2009. *Flashing flow of superheated jet fuel*. Proceedings of the Combustion Institute 32.

221. Lyras, K., Dembele, S., Vyazmina, E., Jallais, S. and Wen, J. 2018. *Numerical simulation of flash-boiling through sharp-edged orifices*. International Journal of Computational Methods and Experimental Measurements 6.

222. Gao, Y, Wei, M., Yan, F., Chen, L., Li, G. and Feng, L. 2017. *Effects of cavitation flow and stagnant bubbles on the initial temporal evolution of diesel spray*. Experimental Thermal and Fluid Science 87.

223. Sou, A. and Bicer, B. 2014. *Numerical Simulation of Turbulent Cavitating Flow in Diesel Fuel Injector*. Computers & Fluids 103.

224. Gavaises, M., Papouluas, D., Andritotis, A. and Giannadakis, E. 2007. *Link between cavitation development and erosion damage in diesel injector nozzles*. SAE International, SAE Technical Paper 2007-01-0246.

225. Koukouvinis, P., Gavaises, M., Li, J. and Wang, L. 2016. *Large eddy simulation of diesel injector including cavitation effects and correlation to erosion damage*. Fuel 175, pp. 26-39.

226. Edelbauer, W., Strucl, J. and Morozov, A. 2014. *Large eddy simulation of cavitating throttle flows*. Advances in Hydroinformatics, Springer, pp. 501-517.

227. Yuan, W., Schnerr, G. H. and Sauer, J. 2001. *Modeling and Computation of Unsteady Cavitation Flows in Injection Nozzles*. Mécanique and Industries, 2(5), pp. 383–394.

228. Wilcox D. C. 1998. *Turbulence Modeling for CFD*. DCW Industries, Inc., La Canada, CA.

229. Yakhot, V., Orszag, S. A. 1986. *Renormalization group analysis of turbulence. I. Basic theory*. Journal of Scientific Computing 1, 3–51 (1986).

230. Shyy W., Thakur S. S., Quyang H., Liu J., Blosch, E. 1997. *Two-Equation Turbulence Models with Nonequilibrium, Rotation, and Compressibility Effects*. In *Computational Techniques for Complex Transport Phenomena.* Cambridge University Press.

231. Martynov S. 2005. *Numerical Simulation of the Cavitation Process in Diesel Fuel Injectors*. PhD Thesis, The University of Brighton, UK.

232. Rakshit S. 2012. *High Speed Flow Simulation in Fuel Injector Nozzles*. Master Thesis. Mechanical and Industrial Engineering, University of Massachusetts Amherst, USA.

233. Winklhofer, E., Kull, E., Kelz E. and Morozov, A. 2001. *Comprehensive hydraulic and flow field documentation in model throttle experiments under cavitation conditions*. ILASS-Europe, 17th International Conference on Liquid Atomization and Spray Systems, Zurich, Switzerland.

234. Engine combustion network, http://www.sandia.gov/ecn.

235. Matlok, S. Hult, J., Simmank, P. and Meyer, S. 2016. *Investigation of cavitation in injection nozzles for two-stroke Diesel engines*. 28th CIMAC World Congress, Helsinki, Finland.

236. Papadopoulos, N. and Aleiferis, P. 2015. *Numerical Modelling of the In-Nozzle Flow of a Diesel Injector with Moving Needle during and after the End of a Full Injection Event*. SAE International, SAE Technical Paper 2015-24-2472.

237. Paciaroni, M., Linne, M. and Sedarsky, D. 2015. Ballistic Imaging: *An Emerging Dense Spray Imaging Technique*. SIAMUF SEMINAR, Lund, Sweden, Lund University.

238. von Terzi, D. A., Sandberg, R. D., Fasel, H. F. 2009. *Identification of large coherent structures in supersonic axisymmetric wakes*. Computers and Fluids 38(8), pp. 1638-1650.

239. Hunt, J. C. R., Wray, A. A. and Moin, P. 1988. *Eddies, Streams, and Convergence Zones in Turbulent Zones*. In *Proc.*, 1988 Summer Program, Stanford N.A.S.A. Centre for Turbulent Research. Palo Alto: Stanford University.

240. Askey, R. A. and Roy, R. 2010. *Gamma function*. In: National Institute of Standards and Technology Handbook of Mathematical Functions, Chapter 5., pp. 139, Cambridge University Press.

241. Lanczos, K. 1964. *A Precision Approximation of the Gamma Function*. Journal of the Society for Industrial and Applied Mathematics, Series B: Numerical Analysis. 1: 86–96. https://doi.org/10.1137/0701008.

242. Pugh, G. R. 2004. *An Analysis of The Lanczos Gamma Approximation*. PhD Thesis, Department of Mathematics, The University of British Columbia, Vancouver, Canada.

243. Askey, R. A. and Roy, R. 2010. *Gamma function*. In: National Institute of Standards and Technology Handbook of Mathematical Functions, Chapter 5., pp. 142, Cambridge University Press.

244. Press, H. W. and Flannery, B. P. 1988. *Numerical Recipes in C: The Art of Scientific Computing*. Chapter 6.1, Gamma Function, Beta Function, Factorials, Binomial Coefficients, Cambridge University Press, New York, USA.

245. Wu, K-J., Reitz, R. D. and Bracco, F. V. 1986. *Measurements of Drop Size at the Spray Edge near the Nozzle in Atomizing Liquid Jets*. The Physics of Fluids 29, pp. 941-951.

246. Schmitz, C. D. 2011. *A turbulence-based model for the primary breakup of pressure atomized liquid jets.* Master of Science Thesis, Mechanical Engineering, Iowa State University, Ames, Iowa, USA.

247. Meyer, K. E., Cavar, D. and Pedersen, J. M. 2007. *POD as Tool for Comparison of PIV and LES Data*. In *Proc*., 7th Int. Symp. Particle Image Velocimetry, Roma, Italy.

248. Kaiktsis, L. and Monkewitz, P. A. 2003. *Global destabilization of flow over a backward-facing step*. Physics of Fluids 15(12).

249. Narayanan, V., Lightfoot, M. D. A., Schumaker, S. A., Danczyk, S. A. and Eilers, B. 2011. *Use of Proper Orthogonal Decomposition Towards Time-Resolved Image Analysis of Sprays.* ILASS - Americas, 23rd Annual Conference on Liquid Atomization and Spray Systems, Ventura, CA.

250. Gamard, S., George, W. K., Jung, D., Woodward, S. 2002. *Application of a slice proper orthogonal decomposition to the far field of an axisymmetric turbulent jet*. Physics of Fluids 14(7).

251. Liu, K. and Haworth, D. C. 2011. *Development and Assessment of Proper Orthogonal Decomposition for Analysis of Turbulent Flow in Piston Engines*. Department of Mechanical and Nuclear Engineering, The Pennsylvania State University, University Park, PA, USA. DOI: 104271/2011-01-0830.

252. Qin, W., Xu, M., Yin, P. and Hung, David L. S. 2015. *Analysis of the Cycle-to-Cycle Variations of In-cylinder Vortex Structure and Vorticity using Phase-invariant Proper Orthogonal Decomposition*. SAE International, SAE Technical Paper, 2015-01-1904. DOI: 10.4271/2015-01-1904.

253. Raposo, J., Hentschel, W. and Merzkirch, W. 2000. *Analysis of the dynamical behavior of coherent structures in in-cylinder flows of internal combustion engines*. In-cylinder Flows of Internal Combustion Engines, In *Proc*., 10th International Symposium on Application of Laser Techniques to Fluid Mechanics, Lisbon, Portugal.

254. Pastur, L., Lusseyran, F., Faure, T., Podvin, B. and Fraigneau, Y. 2008. *POD-based technique for 3D flow reconstruction using 2D data set*. In *Proc.*, 13th International Symposium on Flow Visualization, 11(4):395-400, Nice, France, December 2008, DOI: 10.1007/BF03182208 Nice, France.

255. Regert, T., Rambaud, P., Riethmuller, M. R. 2005. *Investigation of the link between physics and POD modes*. In: Recent Developments in Non-Intrusive Measurement Technology for Military Application on Model-and Full-Scale Vehicles (pp. 4-1-4-12), Meeting Proceedings RTO-MP-AVT-124 paper 4, Neuilly-sur-Seine, France.

256. Kostas, J., Soria, J. and Chong, M. S. 2002. *Particle image velocimetry measurement of a backward-facing step flow*. Experiments in Fluids, 33 (2002) 838-853.

257. Qin, W., Hung, D. L. S. and Xu, M. 2015. *Investigation of the temporal evolution and spatial variation of in-cylinder engine fuel spray characteristics*. In: *Energy Conversion and Management*, 98(2015), pp. 430-439.

258. Bizon, K., Continillo, G., Leistner, K. C., Mancaruseo, E. and Vaglieco, B. M. 2009. *POD-based analysis of cycle-to-cycle variations in an optically accessible Diesel engine*. In *Proc*., The Combustion Institute, 32(2009) pp. 2809-2816.

259. Bizon, K., Continillo, G., Mancaruseo, E. and Merola, S. S. 2010. *POD-based analysis of combustion images in optically accessible engines*. Combustion and Flame 157, pp. 632-640.

260. Tirunagari, S., Hulkkonen, T., Vourinen, V., Kaario, O. and Larmi, M. 2012. *Proper Orthogonal Decomposition Analysis of Cross-Sectional Fuel Spray Data*. ICLASS 12th Triennial International Conference on Liquid Atomization and Spray Systems, Heidelberg, Germany, Sept. 2-6, 2012.

261. Tirunagari, S., Vourinen, V., Kaario, O. and Larmi, M. 2012. *Analysis of Proper Orthogonal Decomposition and Dynamic Mode Decomposition on LES of Subsonic Jets*. CSI Journal of Computing 1(3).

262. Chen, H., Xu, M., Hung, D. L. S., Yang, J. and Zhuang, H. 2013. *Development of a POD-based analysis approach for quantitative comparison of spray structure variations in a spar-ignition direct-injection engine*. SAE International Conference. DOI:10.4271/2013-01-2545.

263. Lumley, J. L. 1967. *The structure of inhomogeneous turbulent flows*. Atmospheric Turbulence and Radio Wave Propagation, 166-178.

264. Sirovich, L. 1987. *Turbulence and dynamics of coherent structures*. Part I-III, Quarterly of Applied Mathematics 45(3), pp. 561-571.

265. Holmen, V. 2012. *Methods for Vortex Identification*. Master Thesis, Numerical Methods and Fluid Mechanics, Lund University.

266. Chatterjee, A. 2000. *An introduction to the Proper Orthogonal Decomposition*. Current Science 78(7), pp. 808-817.

267. Siegel, S., Cohen, K., Seidel, J. and McLaughlin, T. 2007. *State estimation of transient flow fields using double Proper Orthogonal Decomposition (DPOD)*. Active Flow Control, NNFM 95, pp. 105-118.

268. Chen, H., Reuss, D. L. and Sick, V. 2012. *On the use and interpretation of Proper Orthogonal Decomposition of in-cylinder engine flows*. Measurement Science and Technology 23, 085302, pp. 14.

269. El-Adawy, M., Heikal, M. R., Aziz, A. Rashid, A., Adam, I. K., Ismael, M. A., Babiker, M. E., Baharom, M. B., Abidin, F. and Abidin, E. Z. Z. 2018. *On the application of Proper Orthogonal Decomposition (POD) for in-cylinder flow analysis*. Energies 11, 2261, DOI:10.3390/en11092261.

270. Berkooz, G., Holmes, P. and Lumley, J. L. 1993. *The proper orthogonal decomposition in the analysis of turbulent flows*. Annual Review of Fluid Mechanics 25, pp. 539-575. DOI:10.1146/annurev.fl.25.010193.002543.

271. Holmes, P., Lumley, J. L., Berkooz, G. and Rowely, C. 2012. *Turbulence, Coherent Structures, Dynamical Systems and Symmetry*. 2nd edition, Cambridge University Press.

272. Rowley, C. W. and Dawson, S. T. M. 2017. *Model Reduction for Flow Analysis and Control*. Annual Review of Fluid Mechanics 49, pp. 387-417.

273. Kerschen, G., Golinval, J-C., Vakakis, A. F. and Bergman, L. A. 2005. *The Method of Proper Orthogonal Decomposition for Dynamical Characteristics and Order Reduction of Mechanical Systems: An Overview*. Springer, Nonlinear Dynamics 41, pp. 147-169.

274. George, W. K. 1988. *Insight into the Dynamics of Coherent Structures from a Proper Orthogonal Decomposition*. International Seminar on Wall Turbulence, Dubrovnik, Croatia.

275. Taira, K., Brunton, S. L., Dawson, S. T. M., Rowley, C. W., Colonius, T., McKeon, B. J., Schmidt, O. T., Gordeyev, S., Theofilis, V. and Ukeiley, L. S. 2017. *Modal Analysis of Fluid Flows: An Overview*. American Institute of Aeronautics and Astronautics.

276. Holmes, P., Lumley, J. L., Berkooz, G., Mattingly, J. C. and Wittenberg, R. W. 1997. *Low-dimensional models of coherent structures in turbulence*. Physics Reports, Review Section of Physics Letters 287, N4:338-384.

277. Meyer, K. E., Pedersen, J. M. and Ozcan, O. 2007. *A turbulent jet in crossflow analyzed with proper orthogonal decomposition*. Journal of Fluid Mechanics 583, pp. 199-227, DOI: 10.1017/S0022112007006143.

278. Khare, P., Wang, S. and Yang, V. 2015. *Modeling of finite-size droplets and particles in multiphase flows*. Chinese Journal of Aeronautics 28(4), pp. 974-982.

279. Coltrin, S. 2012. *The Influence on Nozzle Spacing and Diameter on the Acoustic Emissions of Closely Spaced Supersonic Jet Arrays*. Master Thesis, Department of Mechanical Engineering, Brigham Young University, All theses and dissertations, Provo, Utah, USA.

280. Webster, D. R. and Longmire, E. K. 1997. *Vortex dynamics in jets from inclined nozzles*. Physics of Fluids 9(3). DOI: 10.1063/1.869223.

281. Duke, D. J., Swantek, A. B., Matusik, K. E. and Powell, C. F. 2016. *X-ray radiography measurements and numerical simulations of cavitation in a metal nozzle*. ILASS-Americas, 28th Annual Conference on Liquid Atomization and Spray Systems, Dearborn. MI, USA.

282. Ahmed, M. H. and Barber, T. J. 2004. *POD convergence criterion for numerically solved periodic flows*. WASE Transactions on Computer 5, 1167-1172.

283. Arienti, M. and Soteriou, M. C. 2009. *Time-resolved proper orthogonal decomposition of liquid jet dynamics*. Physics of Fluids 21(11). DOI: 10.1063/1.3263165.

284. Siegel, S., Cohen, K., Seidel, J. and McLaughlin, T. 2005. *Short time Proper Orthogonal Decomposition for state estimation of transient flow fields*. 43rd AIAA Aerospace Sciences Meeting and Exhibit, Reno, Nevada, USA.

285. Charalampous, G., Hadjiyiannis, C. and Hardalupas, Y. 2019. *Proper Orthogonal Decomposition of primary breakup and spray in co-axial airblast atomizers*. Physics of Fluids 31, 043304, DOI:10.1063/1.3263165, 2019.

286. Khan, M. M. and Sheikh, N. A. 2016. *Identification and characterization of coherent structures in gasoline injector nozzle flow using proper orthogonal decomposition*. Journal of Mechanical Science and Technology 30(8), pp. 3673-3680.

287. Guadard, E., Druault, P., Marchiano, R. and Van Herpe, F. 2017. *POD and Fourier analysis of a fluid-structure-acoustic interaction problem related to interior car noise*. Mechanics and Industry 18(2).

288. Kypraiou, M., Dowling, A., Mastorakos, E. and Karimi, N. 2015. *Proper orthogonal decomposition analysis of a turbulent swirling self-excited premixed flame*. 53rd AIAA Aerospace Sciences Meeting, Kissimmee, Florida, USA.

289. Charalampous, G. and Hardalupas, Y. 2014. *Application of Proper Orthogonal Decomposition to the morphological analysis of confined co-axial jets of immiscible liquids with comparable densities.* Physics of Fluids 26. DOI:10.1063/1.4900944.

290. Charalampous, G. and Hardalupas, Y. 2011. *Proper Orthogonal Decomposition analysis of photographic and optical connectivity time resolved images of an atomising liquid jet*. ILASS-Europe 2011, 24th Annual Conference on Liquid Atomization and Spray Systems, Estoril, Portugal.

291. Abani, N., A. Munnannur and R. D. Reitz. 2008. *Reduction of numerical parameter dependencies in diesel spray models*. Journal of Engineering for Gas Turbines and Power - Transactions of the ASME, 130: 032809-1-9.

292. Bravo, L., M. Kurman, C. Kweon, S. Wijeyakulasuriya and P. K. Senecal. 2014. *Lagrangian Modeling of Evaporating Sprays at Diesel Engine Conditions: Effects of Multi-Hole Injector Nozzles with JP-8 Surrogates.* ILASS Americas 26th Annual Conference on Liquid Atomization and Spray Systems. Portland, OR, USA.

293. Montgomery, D. C. 2005. *Design and Analysis of Experiments*. 6th Ed., John Wiley and Sons, New York, USA.

294. Al Sadi, J. 2018. *Designing Experiments: 3 Level Full Factorial Design and Variation of Processing Parameters Methods for Polymer Colors.* Advances in Science, Technology and Engineering Systems 3(5) 109-115.

295. Elkotb, M. 1982. *Fuel atomization for spray modelling*. Progress in Energy and Combustion Science, 8(1), 61–91.

296. Dos Santos, F. and Le Moyne, L. 2018. *Spray Atomization Models in Engine Applications, from Correlations to Direct Numerical Simulations.* Oil & Gas Science and Technology - Revue d'IFP Energies nouvelles, Institut Français du Pétrole, 66 (5), pp.801-822.

297. http://www.logesoft.com/Products/Products.html

298. Peters, N. 2000. *Turbulent Combustion*. Cambridge University Press, Cambridge.

299. Lehtiniemi, H., Zhang, Y., Rawat, R. and Mauss, F. 2008. *Efficient 3-D combustion modeling with transient flamelet models*. SAE Internationals, SAE Technical Paper 2008-01-0957.

300. Olguin, H. and Gutheil, E. 2014. *Influence of evaporation on spray flamelet structures*. Combustion and Flame 161(4):987–996. DOI: 10.1016/j.combustflame.2013.10.010.

301. Borghesi, G., Mastorakos, E., Devaud, C. B. and Bilger, R. W. 2011. *Modeling evaporation effects in conditional moment closure for spray autoignition*. Combust. Theor. Model. 15(5):725-752.

302. Hollmann, C. and Gutheil, E. 1996. *Modeling of turbulent spray diffusion flames including detailed chemistry*. Proc. Combust. Inst. 26:1731-1738.

303. Peters, N. 1984. *Combustion Theory*. RWTH Aachen University.